Geavanceerde discretisatie- en preconditioneringstechnieken
voor elektromagnetische randintegraalvergelijkingen

Advanced Discretization and Preconditioning Techniques
for Electromagnetic Boundary Integral Equations

Yves Beghein

Promotoren: prof. dr. ir. D. De Zutter, prof. dr. ir. K. Cools
Proefschrift ingediend tot het behalen van de graad van
Doctor in de Ingenieurswetenschappen: Toegepaste Natuurkunde

Vakgroep Informatietechnologie
Voorzitter: prof. dr. ir. D. De Zutter
Faculteit Ingenieurswetenschappen en Architectuur
Academiejaar 2015 - 2016

UNIVERSITEIT
GENT

ISBN 978-90-8578-849-2
NUR 928
Wettelijk depot: D/2015/10.500/93

Advanced Discretization and Preconditioning Techniques for Electromagnetic Boundary Integral Equations

Yves Beghein

Dissertation submitted to obtain the academic degree of
Doctor of Engineering Physics

Publicly defended at Ghent University on November 12th, 2015

Research funded by a doctoral grant from the
Agency for Innovation by Science and Technology in Flanders (IWT)

Supervisor:

prof. dr. ir. D. De Zutter
Electromagnetics Group
Department of Information Technology
Faculty of Engineering and Architecture
Ghent University
Sint-Pietersnieuwstraat 41
9000 Ghent, Belgium
emweb.intec.ugent.be

Co-supervisor:

prof. dr. ir. K. Cools
Electrical Systems and
Optics Research Division
Faculty of Engineering
University of Nottingham
Nottingham NG7 2RD, U.K.
www.nottingham.ac.uk/engineering/
research/electricalsystemsandoptics/

Members of the examination board:

prof. dr. ir. R. Van de Walle (chairman)	Ghent University, Belgium
prof. dr. ir. D. Vande Ginste (secretary)	Ghent University, Belgium
prof. dr. ir. D. De Zutter (supervisor)	Ghent University, Belgium
prof. dr. ir. K. Cools (supervisor)	University of Nottingham, U.K.
prof. dr. ir. F.P. Andriulli	Télécom Bretagne, France
dr. ir. J. Sercu	Keysight Technologies, Belgium
prof. dr. M. Slodička	Ghent University, Belgium

Dankwoord

Waarde lezer, in uw handen liggen een 200-tal bladzijden over elektromagnetische randintegraalvergelijkingen. Dat een twintiger plots besluit om hier vier jaar van zijn leven aan te wijden, lijkt u misschien een beetje vreemd. Dat hij er na afloop nog eens met veel plezier op terugblikt, al helemaal bizar. Voor een verklaring hoeft u echter enkel maar te kijken naar de mensen die, rechtstreeks of onrechtstreeks, betrokken waren bij dit project.

Om te beginnen wil ik hiervoor Daniël bedanken. Als promotor en vakgroepvoorzitter heeft hij me de kans gegeven om mijn onderzoek te verrichten in de elektromagnetismegroep. Vier jaar lang heeft hij mij alle vrijheid gegeven om mijn eigen weg te zoeken, maar stond hij steeds klaar om me te helpen met om het even welk academisch dan wel praktisch probleem. Ook wil ik Hendrik en Dries bedanken om mij te verwelkomen in de groep, en zeker ook Isabelle, die er telkens opnieuw voor zorgde dat de administratieve plichtplegingen zowel pijn- als vlekkeloos verliepen.

Hoewel mijn academische thuis in Gent lag, is mijn doctoraat voornamelijk tot stand gekomen dankzij begeleiding uit Nottingham. Ondanks de afstand heeft Kristof er alles aan gedaan om me met raad en daad bij te staan, zowel in meatspace als in cyberspace. Deze spreidstand over de Noordzee was allerminst evident, maar toch kon ik steeds rekenen op zijn hulp en advies. Vandaar dus een bijzonder groot dankjewel voor jou, Kristof!

Not only the U.K., but also France has played an important role in the research leading to this PhD dissertation. Although he was not officially my supervisor, Francesco has definitely acted as such. Especially during the last two years, his guidance has been invaluable. For this, Francesco, grazie mille and merci beaucoup!

In Gent heb ik het geluk gehad het bureau op +1 te mogen delen met Dieter en Ignace. Dieter en ik hebben bijna exact hetzelfde traject doorlopen: op dezelfde dag begonnen, op dezelfde dag ingediend, op dezelfde dag intern verdedigd, en nu vallen onze publieke verdedigingen ook vlak na elkaar. De eerste drie jaar hebben we doorgebracht in het gezelschap van Ignace. Als groentjes konden we het niet beter treffen: welke vraag we ook hadden over C++, elektromagnetisme, fysica in 't algemeen, of die ene vreemde wiskundige functie: Ignace had een antwoord of op z'n minst een paper voor ons. Hij en Dieter maakten van dat afgelegen bureau op +1 een gezellig eilandje van nerdiness. Heren, bedankt voor deze onvergetelijke jaren!

Op +1 waren we dan wel ietwat geïsoleerd van de rest van de groep, maar 's middags daalden we steevast af naar -T om de collega's er op te wijzen dat het

etenstijd was. Daar vonden we altijd goed gezelschap om naar de brug te gaan, tenzij het natuurlijk international day was, of pita woensdag (tradities moeten nu eenmaal in ere gehouden worden). Voor deze mooie tijden, waarde collega's, dank jullie wel!

Thomas Hobbes schreef het al in 1651: *Leisure is the mother of Philosophy.* Over mijn *Philosophy* kunnen de meningen misschien verdeeld zijn, maar aan een gebrek aan *Leisure* zal dat alvast niet liggen. Wanneer ik nood had aan (niet-elektromagnetische) verstrooiing, kon ik hiervoor steeds rekenen op een hele reeks mensen: compagnons op city-, road- en kampeertrips, squashtegenstanders en klimpartners, collega's-vrijwilligers op Gent Jazz, Jazz Middelheim en Student Kick-Off, studiegenoten, quizbuddy's, ... Vergeef me dat ik geen namen opnoem, maar vrienden, jullie weten wie jullie zijn. Bedankt voor de mooie herinneringen, en op naar nieuwe avonturen!

Verder wil ik ook mijn familie bedanken, in het bijzonder mijn moeder en mijn zus voor het immer warme nest. En tot slot: Jelke, bedankt om van het laatste jaar het mooiste van de afgelopen 4 (of zeg maar meteen 26) te maken.

Gent, oktober 2015
Yves Beghein

"There's something that doesn't make sense.
Let's go and poke it with a stick. "

The Eleventh Doctor (Doctor Who)

Contents

Samenvatting

De voorbije vijftig jaar zijn numerieke simulatietechnieken voor elektromagnetische velden onmisbaar geworden voor het ontwerp van moderne elektronica en communicatiesystemen. Vandaag bestaan er hiervoor veel verschillende technieken, elk met hun eigen sterktes en beperkingen. Deze doctoraatsthesis focust op de klasse van randintegraalvergelijkingstechnieken. Bij deze technieken worden de stromen op de (tweedimensionale) randen van homogene gebieden gemodelleerd, in plaats van de velden in de volledige (driedimensionale) ruimte. Hierdoor zijn deze technieken bijzonder efficiënt voor het oplossen van elektromagnetische verstrooiingsproblemen waarin grote (of zelfs oneindige) gebieden stukgewijs homogeen zijn.

Voor veel toepassingen kan de tijdsafhankelijkheid van de elektromagnetische velden als sinusoïdaal worden benaderd. De tijdsvariabele kan dan worden geëlimineerd met behulp van een frequentieparameter, wat het oplossingsproces vereenvoudigt. In homogene gebieden voldoen dergelijke velden aan frequentiedomeinrandintegraalvergelijkingen (*frequency domain boundary integral equations*, FD-BIE's). Simulatiesoftware gebaseerd op deze vergelijkingen is commercieel verkrijgbaar en wordt vaak gebruikt bij het ontwerp van bijvoorbeeld antennes en elektronica. De sinusoïdale benadering kan helaas niet worden gebruikt voor toepassingen waarin een brede frequentieband wordt gebruikt, of wanneer niet-lineaire materialen of componenten deel uitmaken van het systeem. In deze situaties kunnen tijdsdomeinrandintegraalvergelijkingen (*time domain boundary integral equations*, TD-BIE's) worden aangewend.

Om deze TD-BIE's numeriek op te lossen moeten de continue vergelijkingen omgevormd worden tot stelsels van discrete vergelijkingen die door een computer kunnen worden begrepen. Het discretiseren van de spatiale variatie van de elektromagnetische velden is theoretisch goed begrepen en kan worden gedaan zoals bij FD-BIE's. Het discretiseren van de temporele variatie van de velden is ingewikkelder. Meestal wordt de tijdsafhankelijkheid van de velden benaderd door een lineaire combinatie van een eindig aantal verschoven kopieën van een basisfunctie. Het resulterende discrete stelsel kan dan worden opgelost door middel van het *marching-on-in-time*- of MOT-algoritme: de velden op een bepaalde tijdstap kunnen worden berekend op basis van de velden in het verleden, en daarna gaat het algoritme over naar de volgende tijdstap.

Helaas blijken vele implementaties van dit algoritme onstabiel te zijn, en dus nutteloos voor praktische toepassingen. Deze instabiliteit vindt zijn oorsprong in twee factoren. Ten eerste bepalen de details van de temporele discretisatieprocedure of het resulterende MOT-algoritme al dan niet stabiel kan zijn. Sommige

MOT-vergelijkingen kunnen worden afgeleid van een coërcieve variationele beschrijving van het verstrooiingsprobleem en zijn stabiel omdat de energie van de numerieke oplossing begrensd is door de energie van de exacte oplossing. Veel populaire MOT-methoden passen echter niet in dit raamwerk, waardoor er geen theoretische resultaten over hun stabiliteit beschikbaar zijn. Ten tweede vereist het MOT-algoritme de berekening van vierdimensionale integralen, een taak die maar met een eindige precisie kan worden uitgevoerd. Numerieke fouten in deze berekeningen kunnen theoretisch stabiele MOT-algoritmen in de praktijk onstabiel maken.

Het startpunt van deze thesis is een verzameling gerelateerde temporele discretisatieprocedures die in de praktijk hebben geleid tot bruikbare MOT-algoritmes. Deze procedures worden toegepast op de *time domain electric field integral equation* (TD-EFIE), de *time domain magnetic field integral equation* (TD-MFIE) en de *time domain combined field integral equation* (TD-CFIE), vergelijkingen die verstrooiing aan perfecte geleiders beschrijven. Deze procedures worden vervolgens uitgebreid om een hogere-orde-benadering van de tijdsafhankelijkheid van de velden te kunnen leveren. Dit verbetert zowel de nauwkeurigheid als de efficiëntie van de numerieke oplossingsmethode, zonder de stabiliteit van het MOT-algoritme te schaden.

Hoewel de voorgestelde oplossingsmethode stabiel en nauwkeurig is, gaat de TD-EFIE gebukt onder een fundamenteel probleem: het laat statische regime-oplossingen toe die onvermijdelijk opduiken in de numerieke oplossing, ook al zijn ze fysisch niet toegelaten. In deze thesis worden de quasi-Helmholtz-componenten van de TD-EFIE gescheiden en vervolgens geïntegreerd in of afgeleid naar de tijd. Dit levert een vergelijking op die equivalent is aan de TD-EFIE, maar geen statische regime-oplossingen toelaat. Wanneer de standaard temporele discretisatiemethoden hierop toegepast worden, is het resulterende MOT-algoritme instabiel. Door verschillende discretisatiemethoden te gebruiken voor de verschillende quasi-Helmholtz-componenten kan de stabiliteit hersteld worden. De resulterende vergelijking, genaamd de qHP-TDEFIE, can efficiënt toegepast worden op zowel enkelvoudig als meervoudig samenhangende geometrieën.

Centraal in het MOT-algoritme staat de oplossing van een stelsel van lineaire vergelijkingen. Als dit stelsel goed geconditioneerd is, kan het efficiënt worden opgelost met iteratieve technieken. De standaard TD-EFIE en TD-CFIE lijden echter aan *low frequency breakdown*: de stelsels die van deze vergelijkingen worden afgeleid zijn slecht geconditioneerd bij grote tijdstappen. In deze thesis wordt aangetoond dat de qHP-TDEFIE traag variërende velden correct behandelt, waardoor het stelsel goed geconditioneerd blijft bij grote tijdstappen.

Bovendien lijden de TD-EFIE, de TD-CFIE en de qHP-TDEFIE aan *dense discretization breakdown*. De ruimtelijke afhankelijkheid van de velden wordt gediscretiseerd met basisfuncties die gedefinieerd worden op een verzameling driehoeken die de randen van de homogene gebieden benadert. Om nauwkeurige

resultaten op te leveren, moeten deze driehoeken voldoende klein zijn. Dit leidt echter tot slecht geconditioneerde stelsels. Voor zowel FD-BIE's als TD-BIE's kan dit probleem verholpen worden met behulp van zogenaamde Calderón-preconditioners. In deze thesis wordt een dergelijke preconditioner geconstrueerd voor de qHP-TDEFIE. De gepreconditioneerde qHP-TDEFIE is stabiel, laat geen statische regime-oplossingen toe, blijft goed geconditioneerd, en is onmiddellijk toepasbaar op zowel enkelvoudig als meervoudig samenhangende geometrieën.

De hierboven vermelde resultaten laten toe om verstrooiing aan perfecte geleiders efficiënt en nauwkeurig numeriek op te lossen. Voor indringbare media moeten andere TD-BIE's aangewend worden, zoals de *time domain Poggio-Miller-Chan-Harrington-Wu-Tsai-* of TD-PMCHWT-vergelijking. Het ontwikkelen van MOT-algoritmes voor indringbare media, gebaseerd op bijvoorbeeld de TD-PMCHWT-vergelijking, is nog uitdagender gebleken dan voor perfecte geleiders.

Net zoals de TD-EFIE laat ook de TD-PMCHWT-vergelijking statische regime-oplossingen toe. Bij de TD-EFIE worden deze oplossingen numeriek exact behouden door de discretisatieprocedure. Bij de TD-PMCHWT-vergelijking zijn ze echter afhankelijk van de numerieke opheffing van verschillende termen. Als alle interactie-integralen exact berekend zouden kunnen worden, zou het discrete systeem ook statische regime-oplossingen toelaten. In de praktijk worden ze echter exponentieel stijgend door de aanwezigheid van numerieke fouten, wat uiteindelijk leidt tot instabiele MOT-algoritmes.

De herschalingsmethode die tot de qHP-TDEFIE geleid heeft elimineert de statische regime-oplossingen van de TD-EFIE. Deze methode kan echter niet rechtstreeks toegepast worden op de TD-PMCHWT-vergelijking. Daarom wordt in deze thesis een alternatieve herschalingsmethode ontwikkeld die wel van toepassing is op de TD-PMCHWT-vergelijking, en zo meteen ook het instabiliteitsprobleem oplost. De resulterende vergelijking wordt de qHP-PMCHWT-vergelijking genoemd.

Net zoals de qHP-TDEFIE lijdt ook de qHP-PMCHWT niet aan *low frequency breakdown*. Ze lijdt echter wel aan *dense discretization breakdown*. Dit probleem kan opnieuw worden opgelost door een geschikte Calderón-preconditioner te ontwikkelen. De resulterende oplossingsmethode is in staat om efficiënt verstrooiingsproblemen met homogene indringbare media te behandelen.

Tenslotte wordt de aandacht verschoven naar chirale media. Deze media hebben een complexe microscopische structuur zonder spiegelsymmetrie. Hierdoor worden circulair gepolariseerde golven verschillend verstrooid naargelang ze linkshandig of rechtshandig gepolariseerd zijn. Doordat dit fenomeen voornamelijk optreedt in beperkte frequentiebanden, kunnen dergelijke verstrooiingsproblemen in het frequentiedomein behandeld worden met een uitbreiding van de *frequency domain PMCHWT-* of FD-PMCHWT-vergelijking. Deze vergelijking

lijdt echter ook aan *dense discretization breakdown*. Om dit te verhelpen, wordt ook voor deze vergelijking een Calderón-preconditioner afgeleid.

De resultaten die in deze thesis gepresenteerd worden dragen samen bij tot een dieper inzicht in randintegraalvergelijkingstechnieken, en laten toe om verstrooiingsproblemen met stuksgewijs homogene objecten nauwkeuriger en efficiënter numeriek te behandelen. In het bijzonder lossen ze een aantal problemen op die tot nu toe de populariteit van tijdsdomeinrandintegraalvergelijkingen hebben tegengehouden.

Summary

Over the past half century, numerical simulation methods for electromagnetic fields have become indispensable tools in the design of modern electronics and telecommunication systems. Today, many different techniques are available, each with their own strengths and weaknesses. This PhD thesis is concerned with the class of methods called boundary integral equation (BIE) methods. These methods model the currents on (two-dimensional) interfaces between homogeneous regions rather than the fields in the entire (three-dimensional) space. As a result, they are particularly efficient for solving electromagnetic problems involving large piecewise homogeneous regions.

In many applications, the electromagnetic fields can be approximated as harmonic in time. The time variable can then be eliminated in favor of a frequency parameter, which facilitates the solution process. In homogeneous domains, such time-harmonic fields satisfy frequency domain BIEs (FD-BIEs). Simulation software based on these equations is commercially available, and has been widely used in the design of antennas and electronics. The time-harmonic approximation is unfortunately not possible in applications where a multitude of frequencies are present, or when nonlinear materials or components are part of the system under study. In these situations, time domain BIEs (TD-BIEs) can be used.

In order to numerically solve TD-BIEs, these continuous equations must be transformed into systems of discrete equations which can be handled by a computer. Discretizing the spatial variation of the electromagnetic fields is well understood, and can be done similarly as in FD-BIE methods. Discretizing the temporal variation of the electromagnetic fields presents more difficulties. Most often, the temporal signature of the unknown field is approximated as a linear combination of a finite number of temporal basis functions, all shifted copies of a reference basis function. The TD-BIEs can then be solved using the marching-on-in-time (MOT) algorithm: the fields at a certain point in time are computed from those in the past, after which the algorithm proceeds to the next time step.

Unfortunately, many implementations of this algorithm turn out to be unstable and are therefore useless for real-world applications. This instability can be traced back to two separate issues. First, the specific details of the temporal discretization procedure determine whether or not a MOT scheme can be stable. Some schemes are derived from a coercive variational description of the scattering problem and are stable because the energy in the approximate solution is bounded by the energy in the exact solution. Many popular schemes,

however, do not fit in this framework, and no theoretical results about their stability are available. Second, implementing the MOT algorithm requires the evaluation of four-dimensional integrals, which can only be performed with finite accuracy. Numerical errors in these calculations can render a theoretically stable MOT scheme unstable in practice.

The starting point of this thesis is a set of related discretization procedures which have in practice shown to yield usable MOT schemes. They are applied to the time domain electric field integral equation (TD-EFIE), the time domain magnetic field integral equation (TD-MFIE), and the time domain combined field integral equation (TD-CFIE), which model scattering by perfect conductors. These discretization procedures are then extended to allow a higher-order representation of the temporal variation of the electromagnetic fields. This improves the accuracy and the efficiency of the numerical simulation method, without deteriorating its stability.

Although the proposed method leads to stable and accurate solution methods, the TD-EFIE suffers from a fundamental problem: it allows static regime solutions, which inevitably show up in the numerical solution, even though they are physically forbidden to exist. In this thesis, the quasi-Helmholtz components of the TD-EFIE are separated and judiciously integrated or differentiated with respect to time, resulting in an equation that is completely equivalent to the original one but does not support static regime solutions. Standard temporal discretization methods fail to transform this semi-discrete equation into a stable MOT system. By employing different temporal discretization strategies for each quasi-Helmholtz component, stability can be restored. The resulting equation is termed the qHP-TDEFIE, and can be applied effectively to both simply and multiply connected geometries.

The MOT algorithm requires the solution of a system of linear equations. If this system is well-conditioned, it can be solved efficiently using a Krylov type iterative solver. The standard TD-EFIE and TD-CFIE, however, suffer from low frequency breakdown: the discrete systems become ill-conditioned when the time step size is large. As shown in this thesis, the qHP-TDEFIE correctly handles slowly varying electromagnetic fields, and as a result remains well-conditioned for large time step sizes.

Additionally, the TD-EFIE, the TD-CFIE and the qHP-TDEFIE all suffer from dense discretization breakdown. The spatial variation of the electromagnetic fields is discretized using basis functions defined on meshes of triangles which approximate the interfaces between homogeneous media. In order to obtain accurate results, this mesh must be sufficiently dense (i.e., the triangles sufficiently small). However, dense meshes lead to ill-conditioned systems. Both for FD-BIE methods and TD-BIE methods, this can be solved using Calderón preconditioning techniques. In this thesis, a Calderón preconditioner is constructed for the qHP-TDEFIE. The resulting MOT scheme is stable, does not support spurious static regime solutions, remains well-conditioned for both dense meshes

and large time steps, and is directly applicable to both simply and multiply connected geometries.

The aforementioned results allow the efficient and accurate simulation of scattering problems involving perfect electric conductors. Penetrable scatterers can be handled using other TD-BIEs, such as the time domain Poggio-Miller-Chan-Harrington-Wu-Tsai (TD-PMCHWT) equation. However, successfully implementing a MOT algorithm has proven to be even more challenging for penetrable media than for perfect conductors.

Just like the TD-EFIE, the TD-PMCHWT equation allows static regime solutions. For the TD-EFIE, these static modes are conserved exactly by the discretization procedure. For the TD-PMCHWT equation, they are dependent on the numerical cancellation of different terms. If all interaction integrals could be computed with infinite accuracy, the discrete system would also support static regime solutions. However, these modes become exponentially increasing in the presence of numerical quadrature errors, leading to unstable MOT schemes.

The rescaling method leading to the qHP-TDEFIE eliminates the static regime solutions of the TD-EFIE. This procedure can, however, not be applied directly to the TD-PMCHWT equation. In this thesis, an alternative rescaling method is developed that does eliminate the static regime solutions of the TD-PMCHWT equation, and thus solves the instability problem. The resulting equation is termed the qHP-PMCHWT equation.

Just like the qHP-TDEFIE, the qHP-PMCHWT equation does not suffer from low frequency breakdown. It does, however, suffer from dense discretization breakdown. This problem is again solved by developing a suitable Calderón preconditioner. The resulting solution scheme is able to efficiently solve scattering problems involving homogeneous penetrable media.

Finally, the focus is shifted to chiral media. These media have a complex microscopic structure that lacks reflection symmetry. As a result, circularly polarized electromagnetic waves impinging on such a medium are scattered differently depending on whether they are right-handed or left-handed circularly polarized. This phenomenon however occurs in a limited frequency range. Therefore, such scattering problems can generally be treated in the frequency domain and can be modeled using an extension of the frequency domain PMCHWT equation. This equation also suffers from dense discretization breakdown. In order to combat this, a chiral Calderón preconditioner is constructed.

Together, the results presented in this thesis contribute to a deeper understanding of BIE methods, and lead to more accurate and more efficient simulation techniques for scattering problems involving piecewise homogeneous objects. In particular, a number of issues that have been holding back the widespread adoption of TD-BIE methods have been solved.

List of Abbreviations

BC	Buffa-Christiansen (functions)
BEM	Boundary Element Method
BIE	Boundary Integral Equation
CFIE	Combined Field Integral Equation
CMP	Calderón Multiplicative Preconditioner
CP	Calderón Preconditioned (e.g. CP TD-EFIE)
CQ	Convolution Quadrature
DBF	Drude-Born-Fedorov (model)
DC	Direct Current
EFIE	Electric Field Integral Equation
EFIO	Electric Field Integral Operator
FD	Frequency Domain (e.g. FD-EFIE)
MFIE	Magnetic Field Integral Equation
MFIO	Magnetic Field Integral Operator
MOD	Marching-on-in-Degree (algorithm, method)
MOO	Marching-on-in-Order (algorithm, method)
MOT	Marching-on-in-Time (algorithm, method)
PEC	Perfect Electric Conductor
PMCHWT	Poggio-Miller-Chan-Harrington-Wu-Tsai (equation)
PWTD	Plane Wave Time Domain (method)
qHP	Quasi-Helmholtz Projected (e.g. qHP-PMCHWT equation)
RMS	Root Mean Square
RP-BIE	Retarded Potential Boundary Integral Equation
RWG	Rao-Wilton-Glisson (functions)
TD	Time Domain (e.g. TD-EFIE)

List of Symbols

Geometrical Symbols

$\boldsymbol{r}$, $\boldsymbol{r}'$	position vector
Ω	bounded domain
Γ	bounded surface
$\hat{\boldsymbol{n}}$	unit vector normal to Γ
D	diameter of Γ or Ω
R	distance between $\boldsymbol{r}$ and $\boldsymbol{r}'$

Physical Quantities

c	speed of light
η	impedance
ω	angular frequency
t	time
k	wave number
$\boldsymbol{e}(\boldsymbol{r},t)$	electric field
$\boldsymbol{h}(\boldsymbol{r},t)$	magnetic field
$\boldsymbol{d}(\boldsymbol{r},t)$	electric induction or flux density
$\boldsymbol{b}(\boldsymbol{r},t)$	magnetic induction or flux density
$\boldsymbol{j}(\boldsymbol{r},t)$	electric current density
$\boldsymbol{m}(\boldsymbol{r},t)$	magnetic current density
$\rho(\boldsymbol{r},t)$	electric charge density
$\kappa(\boldsymbol{r},t)$	magnetic charge density
$\boldsymbol{E}(\boldsymbol{r},\omega)$, ...	Fourier transform of $\boldsymbol{e}(\boldsymbol{r},t)$, ...

Symbols Related to Chiral Media

κ	chirality (or Pasteur) parameter
γ_+	wave number of the right-handed mode
γ_-	wave number of the left-handed mode
$\mathcal{E}_+$	right-handed circularly polarized electric field
$\mathcal{E}_-$	left-handed circularly polarized electric field
$\mathcal{H}_+$	right-handed circularly polarized magnetic field
$\mathcal{H}_-$	left-handed circularly polarized magnetic field

Integral and Differential Operators

∂_t	temporal derivative
∂_t^{-1}	temporal integral
∇, ∇'	gradient (w.r.t. $\boldsymbol{r}$, $\boldsymbol{r}'$)
$\nabla\cdot$, $\nabla'\cdot$	divergence (w.r.t. $\boldsymbol{r}$, $\boldsymbol{r}'$)
$\nabla\times$, $\nabla'\times$	curl (w.r.t. $\boldsymbol{r}$, $\boldsymbol{r}'$)
$\mathcal{T}$	time domain EFIO
$\mathcal{K}$	time domain MFIO
$\mathcal{T}_k$	frequency domain EFIO (with wave number k)
$\mathcal{K}_k$	frequency domain MFIO (with wave number k)
$\int_\Gamma f(\boldsymbol{r})ds$	integral of $f(\boldsymbol{r})$ over Γ
$\int_{\mathbb{R}} f(t)dt$	integral of $f(t)$ over the real time axis

Temporal and Spatial Basis Functions

$\boldsymbol{f}_m(\boldsymbol{r})$	RWG function associated with the m-th edge
$\boldsymbol{g}_m(\boldsymbol{r})$	BC function associated with the m-th edge
h	mesh parameter
$\mathsf{P}^{\Lambda H}$	RWG loop projector
P^{Σ}	RWG star projector
$\mathbb{P}^{\Sigma H}$	BC loop projector
$\mathbb{P}^{\Lambda}$	BC star projector
$\delta(t)$	Dirac delta distribution
$p(t)$	pulse function
$h(t)$	hat function
$q(t)$	cubic spline basis function
Δt	time step size

List of Publications

Articles Published in International Journals

- Y. Beghein, K. Cools, F. P. Andriulli, D. De Zutter, and E. Michielssen, "A Calderón multiplicative preconditioner for the PMCHWT equation for scattering by chiral objects", *IEEE Transactions on Antennas and Propagation*, vol. 60, no. 9, pp. 4239–4248, Sep. 2012.
- Y. Beghein, K. Cools, H. Bağcı, and D. De Zutter, "A space-time mixed Galerkin marching-on-in-time scheme for the time-domain combined field integral equation", *IEEE Transactions on Antennas and Propagation*, vol. 61, no. 3, pp. 1228–1238, Mar. 2013.
- A. J. Pray, Y. Beghein, N. V. Nair, K. Cools, H. Bağcı, and B. Shanker, "A higher order space-time Galerkin scheme for time domain integral equations", *IEEE Transactions on Antennas and Propagation*, vol. 62, no. 12, pp. 6183–6191, Dec. 2014.
- Y. Beghein, K. Cools, and F. Andriulli, "A DC stable and large-time step well-balanced td-efie based on quasi-Helmholtz projectors", *IEEE Transactions on Antennas and Propagation*, vol. 63, no. 7, pp. 3087–3097, Jul. 2015.

Articles to Appear in International Journals

- Y. Beghein, K. Cools, and F. P. Andriulli, "A DC-stable, well balanced, Calderón preconditioned time domain electric field integral equation", *IEEE Transactions on Antennas and Propagation*, accepted for publication on October 1st, 2015.

Articles Published in Conference Proceedings

- Y. Beghein, K. Cools, F. P. Andriulli, D. De Zutter, and E. Michielssen, "Calderon multiplicative preconditioner for the PMCHWT equation applied to chiral media", in *2011 IEEE International Symposium on Antennas and Propagation (APSURSI)*, Jul. 2011, pp. 3203 –3206.
- Y. Beghein, K. Cools, F. P. Andriulli, D. De Zutter, and E. Michielssen, "Accurate and conforming mixed discretization of the chiral Müller equation", in *2012 IEEE Antennas and Propagation Society International Symposium (APSURSI)*, Jul. 2012.
- Y. Beghein, K. Cools, and D. De Zutter, "Accurate temporal discretization of time domain boundary integral equations", in *2012 IEEE Antennas and Propagation Society International Symposium (APSURSI)*, Jul. 2012.
- Y. Beghein, K. Cools, and D. De Zutter, "A higher order space-time Galerkin discretization for the time domain PMCHWT equation", in *29th Annual Review of Progress in Applied Computational Electromagnetics*, The Applied Computational Electromagnetics Society, Mar. 2013, pp. 274–279.
- Y. Beghein, K. Cools, and D. De Zutter, "A temporal Galerkin discretization of the charge-current continuity equation", in *2013 International Conference on Electromagnetics in Advanced Applications (ICEAA)*, Sep. 2013, pp. 628–631.
- Y. Beghein, K. Cools, and F. P. Andriulli, "Eliminating the DC instability of the time domainelectric field integral equation", in *9th European Conference on Antennas and Propagation (EuCAP)*, Apr. 2015.
- Y. Beghein, K. Cools, and F. P. Andriulli, "A well-conditioned time domain EFIE for densely discretized low frequency problems", in *International Conference on Electromagnetics in Advanced Applications (ICEAA)*, Sep. 2015, pp. 962–965.
- Y. Beghein, K. Cools, and F. P. Andriulli, "A robust and low frequency stable time domain PMCHWT equation", in *International Conference on Electromagnetics in Advanced Applications (ICEAA)*, Sep. 2015, pp. 954–957.
- Y. Beghein, R. Mitharwal, K. Cools, and F. P. Andriulli, "Handling the low-frequency breakdown of the PMCHWT integral equation with the quasi-Helmholtz projectors", in *International Conference on Electromagnetics in Advanced Applications (ICEAA)*, Sep. 2015, pp. 1534–1537.

Advanced Discretization and Preconditioning Techniques for Electromagnetic Boundary Integral Equations

1 Introduction

1.1 Introduction

Throughout history, both scientists and laymen have been puzzled by the phenomena which are now known to be different manifestations of the electromagnetic force, for instance lightning, static electricity and magnetism. In the late eighteenth and early nineteenth century, scientists such as Benjamin Franklin, Charles-Augustin de Coulomb, André-Marie Ampère, Michael Faraday and many others have contributed to the discovery of this force. In the second half of the nineteenth century, James Clerk Maxwell was able to combine all of the previous knowledge into a single set of differential equations – Maxwell's equations – and show that light is a particular form of electromagnetic radiation [1], [2]. Even though the quantum revolution of the twentieth century has resulted in an even more refined theoretical framework, the equations developed by Maxwell still determine our understanding of electromagnetism on all but the smallest microscopic levels.

This understanding has played no small part in the technological progress of the twentieth century. Indeed, inventions such as radio, television, RADAR, satellite navigation, microwave ovens, or any electronic device, would not have been possible without Maxwell's classical electromagnetism. This remains true up to today, as evidenced by e.g. high speed electronics and mobile communication technology.

The ever increasing technological complexity has necessitated the solution of Maxwell's equations in increasingly more complex situations. While some idealized problems can be treated analytically (with pen and paper), this is completely out of the question for even simple realistic technological applications. For the past few decades, engineers have increasingly made use of computers to aid them with their designs.

Computers cannot in general solve the set of continuous Maxwell equations. Instead they are tasked with the solution of a discrete problem that is related to the original continuous problem in a well-understood and controllable manner. Such a discrete problem can be obtained in many different ways. In this PhD thesis, electromagnetic fields are modeled using boundary integral equations (BIEs), which can be solved numerically using the boundary element method (BEM). This technique is particularly efficient for modeling electromagnetic fields in large or even infinite homogeneous domains. Furthermore, it can be applied to both transient as well as time-harmonic electromagnetic fields.

For time-harmonic electromagnetic fields, BEM-based solvers are widely used in both industry and academia. For transient electromagnetic fields, on the other hand, only a small number of implementations exist, which are all fraught with practical as well as theoretical problems. The main objective of the research presented in this work is to provide solutions to some of these problems. Additionally, the treatment of time-harmonic fields in complex materials using the BEM is studied.

This introductory chapter starts from Maxwell's equations and continues to develop the theory of boundary integral equations. It is intended as a relatively concise overview and definition of the concepts that will be used in the following chapters. For a more thorough discussion, the reader is referred to textbooks such as [3], [4].

1.2 Time Domain Electromagnetics

1.2.1 Maxwell's Equations

Electromagnetic phenomena are, typically, the result of interactions between matter and electromagnetic fields (i.e., the electric field $\boldsymbol{e}(\boldsymbol{r},t)$ and the magnetic field $\boldsymbol{h}(\boldsymbol{r},t)$). Physically, these fields are induced by electric currents $\boldsymbol{j}(\boldsymbol{r},t)$ and electric charges $\rho(\boldsymbol{r},t)$. Maxwell's equations describe the relations between these quantities:

$$\nabla \times \boldsymbol{e}(\boldsymbol{r},t) = -\partial_t \boldsymbol{b}(\boldsymbol{r},t) \tag{1.1a}$$
$$\nabla \times \boldsymbol{h}(\boldsymbol{r},t) = \partial_t \boldsymbol{d}(\boldsymbol{r},t) + \boldsymbol{j}(\boldsymbol{r},t) \tag{1.1b}$$
$$\nabla \cdot \boldsymbol{d}(\boldsymbol{r},t) = \rho(\boldsymbol{r},t) \tag{1.1c}$$
$$\nabla \cdot \boldsymbol{b}(\boldsymbol{r},t) = 0. \tag{1.1d}$$

The electric flux density $\boldsymbol{d}(\boldsymbol{r},t)$ and the magnetic flux density $\boldsymbol{b}(\boldsymbol{r},t)$ are related to the electric field $\boldsymbol{e}(\boldsymbol{r},t)$ and the magnetic field $\boldsymbol{h}(\boldsymbol{r},t)$ through constitutive equations that model the interaction between the electromagnetic fields and the medium in which they reside. This topic will be discussed in section 1.2.2.

In order to make (1.1a) – (1.1d) more symmetrical, a magnetic current density

$\boldsymbol{m}(\boldsymbol{r},t)$ and magnetic charge density $\kappa(\boldsymbol{r},t)$ are introduced:

$$\begin{aligned}
\nabla \times \boldsymbol{e}(\boldsymbol{r},t) &= -\partial_t \boldsymbol{b}(\boldsymbol{r},t) - \boldsymbol{m}(\boldsymbol{r},t) && \text{(1.2a)}\\
\nabla \times \boldsymbol{h}(\boldsymbol{r},t) &= \partial_t \boldsymbol{d}(\boldsymbol{r},t) + \boldsymbol{j}(\boldsymbol{r},t) && \text{(1.2b)}\\
\nabla \cdot \boldsymbol{d}(\boldsymbol{r},t) &= \rho(\boldsymbol{r},t) && \text{(1.2c)}\\
\nabla \cdot \boldsymbol{b}(\boldsymbol{r},t) &= \kappa(\boldsymbol{r},t). && \text{(1.2d)}
\end{aligned}$$

These quantities are physically zero, but are convenient for theoretical computations – see section 1.2.4.

Other useful relations are obtained by substituting (1.2c) into the divergence of (1.2b), and (1.2d) into the divergence of (1.2a). This yields the electric and magnetic charge-current continuity equations:

$$\begin{aligned}
0 &= \partial_t \rho(\boldsymbol{r},t) + \nabla \cdot \boldsymbol{j}(\boldsymbol{r},t) && \text{(1.3a)}\\
0 &= \partial_t \kappa(\boldsymbol{r},t) + \nabla \cdot \boldsymbol{m}(\boldsymbol{r},t). && \text{(1.3b)}
\end{aligned}$$

Therefore, the (electric or magnetic) charge density can be computed from the (electric or magnetic) current density:

$$\begin{aligned}
\rho(\boldsymbol{r},t) &= -\int_{-\infty}^{t} \nabla \cdot \boldsymbol{j}(\boldsymbol{r},\tau) d\tau && \text{(1.4a)}\\
\kappa(\boldsymbol{r},t) &= -\int_{-\infty}^{t} \nabla \cdot \boldsymbol{m}(\boldsymbol{r},\tau) d\tau. && \text{(1.4b)}
\end{aligned}$$

1.2.2 Constitutive Equations

The interaction between the electromagnetic fields and the medium in which they reside is modeled using constitutive equations. These equations relate the field quantities $\boldsymbol{e}(\boldsymbol{r},t)$ and $\boldsymbol{h}(\boldsymbol{r},t)$ to the flux densities $\boldsymbol{d}(\boldsymbol{r},t)$ and $\boldsymbol{b}(\boldsymbol{r},t)$. In vacuum, they are given by

$$\begin{aligned}
\boldsymbol{d}(\boldsymbol{r},t) &= \epsilon_0\, \boldsymbol{e}(\boldsymbol{r},t) && \text{(1.5a)}\\
\boldsymbol{b}(\boldsymbol{r},t) &= \mu_0\, \boldsymbol{h}(\boldsymbol{r},t). && \text{(1.5b)}
\end{aligned}$$

For many isotropic materials, the constitutive equations can be approximated as

$$\begin{aligned}
\boldsymbol{d}(\boldsymbol{r},t) &= (\epsilon * \boldsymbol{e})(\boldsymbol{r},t) && \text{(1.6a)}\\
\boldsymbol{b}(\boldsymbol{r},t) &= (\mu * \boldsymbol{h})(\boldsymbol{r},t) && \text{(1.6b)}
\end{aligned}$$

where the continuous convolution operator $*$ is defined as

$$(a * b)(\boldsymbol{r},t) = \int_{\mathbb{R}} a(\boldsymbol{r},t-\tau) b(\boldsymbol{r},\tau) d\tau. \qquad \text{(1.7)}$$

Equations (1.6a)–(1.6b) assume that the medium is time invariant. In particular, moving bodies cannot be modeled with these equations.

More complex materials require more complex constitutive equations. For instance, bi-isotropic materials are described by

$$\begin{aligned} \boldsymbol{d}(\boldsymbol{r},t) &= (\epsilon * \boldsymbol{e})(\boldsymbol{r},t) + (\xi * \boldsymbol{h})(\boldsymbol{r},t) && \text{(1.8a)} \\ \boldsymbol{b}(\boldsymbol{r},t) &= (\mu * \boldsymbol{h})(\boldsymbol{r},t) + (\zeta * \boldsymbol{e})(\boldsymbol{r},t). && \text{(1.8b)} \end{aligned}$$

Examples of bi-isotropic media are the chiral media discussed in section 1.4. Other types of constitutive equations incorporate e.g. anisotropic or nonlinear behavior.

If the temporal variation of the electromagnetic fields is sufficiently slow, the constitutive equations can be regarded as instantaneous:

$$\begin{aligned} \epsilon(\boldsymbol{r},t) &= \epsilon(\boldsymbol{r})\ \delta(t) && \text{(1.9a)} \\ \mu(\boldsymbol{r},t) &= \mu(\boldsymbol{r})\ \delta(t) && \text{(1.9b)} \\ &\ldots \end{aligned}$$

where $\delta(t)$ is the Dirac delta distribution. In other words: the electric and magnetic flux densities $\boldsymbol{d}$ and $\boldsymbol{b}$ at time t depend only on the electric and magnetic fields $\boldsymbol{e}$ and $\boldsymbol{h}$ at the same time t.

Throughout most of this thesis, the material parameters will be assumed piecewise constant. Inside a domain $\Omega \subset \mathbb{R}^3$, the constitutive equations are then reduced to

$$\begin{aligned} \boldsymbol{d}(\boldsymbol{r},t) &= \epsilon\ \boldsymbol{e}(\boldsymbol{r},t) && \text{(1.10a)} \\ \boldsymbol{b}(\boldsymbol{r},t) &= \mu\ \boldsymbol{h}(\boldsymbol{r},t). && \text{(1.10b)} \end{aligned}$$

1.2.3 Jump Conditions

Consider a domain $\Omega \subset \mathbb{R}^3$. Its surface is denoted Γ, and the normal vector pointing outwards $\hat{\boldsymbol{n}}$ (see figure 1.1). Define for every $\boldsymbol{r} \in \Gamma$

$$\begin{aligned} \boldsymbol{e}^+(\boldsymbol{r},t) &= \lim_{\boldsymbol{r}' \to \boldsymbol{r}} \boldsymbol{e}(\boldsymbol{r}',t) \qquad \text{for } \boldsymbol{r}' \in \mathbb{R}^3 \backslash \Omega && \text{(1.11a)} \\ \boldsymbol{e}^-(\boldsymbol{r},t) &= \lim_{\boldsymbol{r}' \to \boldsymbol{r}} \boldsymbol{e}(\boldsymbol{r}',t) \qquad \text{for } \boldsymbol{r}' \in \Omega && \text{(1.11b)} \end{aligned}$$

and similarly for $\boldsymbol{h}$, $\boldsymbol{d}$ and $\boldsymbol{b}$. If no sources are present in Ω and $\mathbb{R}^3 \setminus \Omega$, the fields are continuous in both regions. If sources are present on Γ, then the following jump (or interface) conditions hold [5]:

$$\begin{aligned} \hat{\boldsymbol{n}} \times \boldsymbol{e}^+ - \hat{\boldsymbol{n}} \times \boldsymbol{e}^- &= -\boldsymbol{m} && \text{(1.12a)} \\ \hat{\boldsymbol{n}} \times \boldsymbol{h}^+ - \hat{\boldsymbol{n}} \times \boldsymbol{h}^- &= \boldsymbol{j} && \text{(1.12b)} \\ \hat{\boldsymbol{n}} \cdot \boldsymbol{d}^+ - \hat{\boldsymbol{n}} \cdot \boldsymbol{d}^- &= \rho && \text{(1.12c)} \\ \hat{\boldsymbol{n}} \cdot \boldsymbol{b}^+ - \hat{\boldsymbol{n}} \cdot \boldsymbol{b}^- &= \kappa. && \text{(1.12d)} \end{aligned}$$

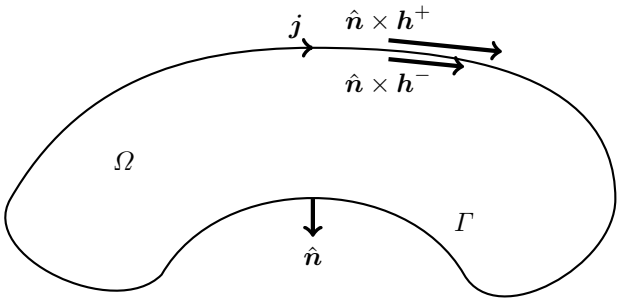

Figure 1.1: illustration of the jump condition (1.12b). A surface current $\boldsymbol{j}$ on Γ causes a discontinuity in the tangential trace of the magnetic field.

The jump in the tangential component of the magnetic field (1.12b) is illustrated in figure 1.1.

1.2.4 Equivalent Currents

Suppose that $\boldsymbol{e}(\boldsymbol{r},t)$ and $\boldsymbol{h}(\boldsymbol{r},t)$ are the electric and magnetic field generated by the electric and/or magnetic currents $\boldsymbol{j}_\Omega(\boldsymbol{r},t)$ and $\boldsymbol{m}_\Omega(\boldsymbol{r},t)$, which are located inside Ω. Then,

$$\tilde{\boldsymbol{e}}(\boldsymbol{r},t) = \begin{cases} \boldsymbol{e}(\boldsymbol{r},t) & \boldsymbol{r} \in \mathbb{R}^3 \backslash \Omega \\ \boldsymbol{0} & \boldsymbol{r} \in \Omega \end{cases} \tag{1.13a}$$

$$\tilde{\boldsymbol{h}}(\boldsymbol{r},t) = \begin{cases} \boldsymbol{h}(\boldsymbol{r},t) & \boldsymbol{r} \in \mathbb{R}^3 \backslash \Omega \\ \boldsymbol{0} & \boldsymbol{r} \in \Omega \end{cases} \tag{1.13b}$$

is a solution of the Maxwell equations (1.2a) – (1.2d) as well as the jump conditions (1.12a) – (1.12d) if the following equivalent surface currents are placed on the boundary of the domain:

$$\boldsymbol{j}_{\text{eq}}(\boldsymbol{r},t) = \hat{\boldsymbol{n}} \times \boldsymbol{h}(\boldsymbol{r},t) \qquad \boldsymbol{r} \in \Gamma \tag{1.14a}$$

$$\boldsymbol{m}_{\text{eq}}(\boldsymbol{r},t) = -\hat{\boldsymbol{n}} \times \boldsymbol{e}(\boldsymbol{r},t) \qquad \boldsymbol{r} \in \Gamma. \tag{1.14b}$$

In other words, the electromagnetic fields outside Ω generated by sources inside Ω, are identical to those generated by the equivalent surface currents $\boldsymbol{j}_{\text{eq}}(\boldsymbol{r},t)$ and $\boldsymbol{m}_{\text{eq}}(\boldsymbol{r},t)$ on Γ. This is illustrated in figure 1.2.

This principle can also be applied to the interior domain: the electromagnetic fields inside Ω generated by sources outside Ω, are identical to those generated by the equivalent surface currents $\boldsymbol{j}'_{\text{eq}}(\boldsymbol{r},t)$ and $\boldsymbol{m}'_{\text{eq}}(\boldsymbol{r},t)$ on Γ, with

$$\boldsymbol{j}'_{\text{eq}}(\boldsymbol{r},t) = -\hat{\boldsymbol{n}} \times \boldsymbol{h}(\boldsymbol{r},t) \qquad \boldsymbol{r} \in \Gamma \tag{1.15a}$$

$$\boldsymbol{m}'_{\text{eq}}(\boldsymbol{r},t) = \hat{\boldsymbol{n}} \times \boldsymbol{e}(\boldsymbol{r},t) \qquad \boldsymbol{r} \in \Gamma. \tag{1.15b}$$

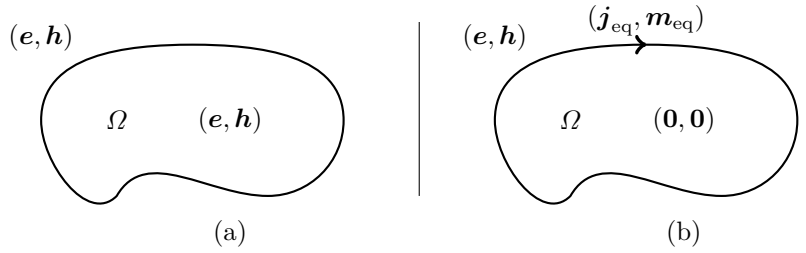

Figure 1.2: the electromagnetic fields outside Ω are identical in situations (a) and (b). The fields inside Ω can be set to zero if the equivalent surface currents (1.14a)–(1.14b) are introduced.

1.2.5 Electromagnetic Potentials

Consider a simply connected domain Ω. The medium in this domain is homogeneous, with permittivity ϵ and permeability μ. First, assume that no magnetic charges or currents are present in Ω: $\boldsymbol{m} = \boldsymbol{0}$ and $\kappa = 0$. Equation (1.2d) then implies that $\boldsymbol{b}(\boldsymbol{r}, t)$ is solenoidal. Therefore, there exists a vector potential $\boldsymbol{a}(\boldsymbol{r}, t)$ such that

$$\boldsymbol{b}(\boldsymbol{r}, t) = \nabla \times \boldsymbol{a}(\boldsymbol{r}, t). \tag{1.16}$$

Furthermore,

$$\nabla \times (\boldsymbol{e}(\boldsymbol{r}, t) + \partial_t \boldsymbol{a}(\boldsymbol{r}, t)) = 0. \tag{1.17}$$

Therefore, there exists a scalar potential $\phi(\boldsymbol{r}, t)$ such that

$$\boldsymbol{e}(\boldsymbol{r}, t) = -\partial_t \boldsymbol{a}(\boldsymbol{r}, t) - \nabla \phi(\boldsymbol{r}, t). \tag{1.18}$$

These potentials are not unique: for any given scalar field $\chi(\boldsymbol{r}, t)$, the potentials

$$\begin{aligned} \boldsymbol{a}'(\boldsymbol{r}, t) &= \boldsymbol{a}(\boldsymbol{r}, t) + \nabla \chi(\boldsymbol{r}, t) && \text{(1.19a)} \\ \phi'(\boldsymbol{r}, t) &= \phi(\boldsymbol{r}, t) - \partial_t \chi(\boldsymbol{r}, t) && \text{(1.19b)} \end{aligned}$$

give rise to the same electromagnetic fields. However, the potentials can be chosen such that they obey the Lorenz gauge condition

$$\nabla \cdot \boldsymbol{a}(\boldsymbol{r}, t) + \frac{\partial_t}{c^2} \phi(\boldsymbol{r}, t) = 0 \tag{1.20}$$

where the speed of light c equals $(\epsilon\mu)^{-1/2}$. Then, the potentials satisfy the following wave equations:

$$\begin{aligned} \nabla^2 \boldsymbol{a}(\boldsymbol{r}, t) - \frac{\partial_t^2}{c^2} \boldsymbol{a}(\boldsymbol{r}, t) &= -\mu \boldsymbol{j}(\boldsymbol{r}, t) && \text{(1.21a)} \\ \nabla^2 \phi(\boldsymbol{r}, t) - \frac{\partial_t^2}{c^2} \phi(\boldsymbol{r}, t) &= -\frac{1}{\epsilon} \rho(\boldsymbol{r}, t). && \text{(1.21b)} \end{aligned}$$

The case without electric charges or currents ($\boldsymbol{j} = \boldsymbol{0}$, $\rho = 0$) can be handled analogously. The electromagnetic fields generated by the magnetic charges and currents can be written as

$$\begin{aligned} \boldsymbol{d}(\boldsymbol{r},t) &= -\nabla \times \boldsymbol{f}(\boldsymbol{r},t) && \text{(1.22a)} \\ \boldsymbol{h}(\boldsymbol{r},t) &= -\partial_t \boldsymbol{f}(\boldsymbol{r},t) - \nabla\psi(\boldsymbol{r},t) && \text{(1.22b)} \end{aligned}$$

where the vector potential $\boldsymbol{f}(\boldsymbol{r},t)$ and the scalar potential $\psi(\boldsymbol{r},t)$ satisfy

$$\begin{aligned} \nabla^2 \boldsymbol{f}(\boldsymbol{r},t) - \frac{\partial_t^2}{c^2}\boldsymbol{f}(\boldsymbol{r},t) &= -\epsilon \boldsymbol{m}(\boldsymbol{r},t) && \text{(1.23a)} \\ \nabla^2 \psi(\boldsymbol{r},t) - \frac{\partial_t^2}{c^2}\psi(\boldsymbol{r},t) &= -\frac{1}{\mu}\kappa(\boldsymbol{r},t) && \text{(1.23b)} \\ \nabla \cdot \boldsymbol{f}(\boldsymbol{r},t) + \frac{\partial_t}{c^2}\psi(\boldsymbol{r},t) &= 0. && \text{(1.23c)} \end{aligned}$$

The general case can be regarded of a superposition of the electric case ($\boldsymbol{m} = \boldsymbol{0}$ and $\kappa = 0$) and the magnetic case ($\boldsymbol{j} = \boldsymbol{0}$, $\rho = 0$). The complete electromagnetic fields are then given by

$$\begin{aligned} \boldsymbol{e}(\boldsymbol{r},t) &= -\partial_t \boldsymbol{a}(\boldsymbol{r},t) - \nabla\phi(\boldsymbol{r},t) - \frac{1}{\epsilon}\nabla \times \boldsymbol{f}(\boldsymbol{r},t) && \text{(1.24a)} \\ \boldsymbol{h}(\boldsymbol{r},t) &= -\partial_t \boldsymbol{f}(\boldsymbol{r},t) - \nabla\psi(\boldsymbol{r},t) + \frac{1}{\mu}\nabla \times \boldsymbol{a}(\boldsymbol{r},t). && \text{(1.24b)} \end{aligned}$$

1.2.6 The Green's Function

Equations (1.24a) and (1.24b) relate the electromagnetic potentials to the electromagnetic fields. Up to now, the potentials have only been defined implicitly by the differential equations (1.21a), (1.21b), (1.23a) and (1.23b). An explicit solution can be obtained by studying the equation

$$\nabla^2 G(\boldsymbol{r},t) - \frac{\partial_t^2}{c^2} G(\boldsymbol{r},t) = -\delta(\boldsymbol{r})\delta(t). \tag{1.25}$$

In an infinite domain $\Omega = \mathbb{R}^3$, the solution to this differential equation is the Green's function

$$G(\boldsymbol{r},t) = \frac{\delta(t - |\boldsymbol{r}|/c)}{4\pi\,|\boldsymbol{r}|} \tag{1.26}$$

which represents a spherical wave, outgoing from $\boldsymbol{r} = \boldsymbol{0}$ at $t = 0$ (figure 1.3, left). Mathematically, a spherical wave incoming towards $\boldsymbol{r} = \boldsymbol{0}$ is also a solution to (1.25). However, it is anti-causal and thus does not represent the field generated by a point source (figure 1.3, right).

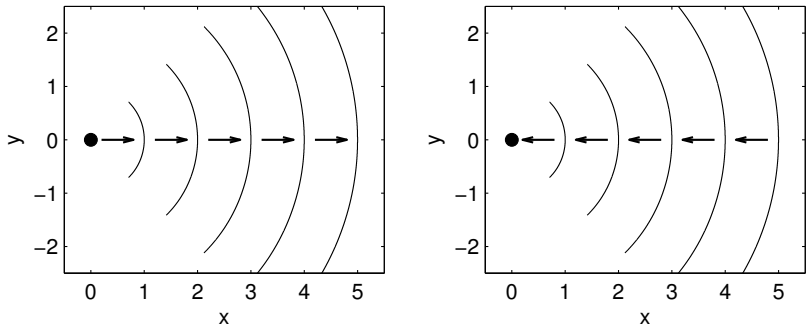

Figure 1.3: left: the Green's function (1.26) represents an outgoing spherical wave. Right: an incoming spherical wave is also a solution to (1.25), but is anti-causal and thus unphysical.

Using the Green's function (1.26), the following integral representations of the potentials are obtained:

$$\boldsymbol{a}(\boldsymbol{r},t) = \mu \int_{\mathbb{R}^3} dV' \int_{\mathbb{R}} dt' G\left(\boldsymbol{r}-\boldsymbol{r}', t-t'\right) \boldsymbol{j}(\boldsymbol{r}', t') \tag{1.27a}$$

$$\phi(\boldsymbol{r},t) = \frac{1}{\epsilon} \int_{\mathbb{R}^3} dV' \int_{\mathbb{R}} dt' G\left(\boldsymbol{r}-\boldsymbol{r}', t-t'\right) \rho(\boldsymbol{r}', t') \tag{1.27b}$$

$$\boldsymbol{f}(\boldsymbol{r},t) = \epsilon \int_{\mathbb{R}^3} dV' \int_{\mathbb{R}} dt' G\left(\boldsymbol{r}-\boldsymbol{r}', t-t'\right) \boldsymbol{m}(\boldsymbol{r}', t') \tag{1.27c}$$

$$\psi(\boldsymbol{r},t) = \frac{1}{\mu} \int_{\mathbb{R}^3} dV' \int_{\mathbb{R}} dt' G\left(\boldsymbol{r}-\boldsymbol{r}', t-t'\right) \kappa(\boldsymbol{r}', t') \tag{1.27d}$$

or

$$\boldsymbol{a}(\boldsymbol{r},t) = \mu \int_{\mathbb{R}^3} \frac{\boldsymbol{j}(\boldsymbol{r}', t-R/c)}{4\pi R} dV' \tag{1.28a}$$

$$\phi(\boldsymbol{r},t) = \frac{1}{\epsilon} \int_{\mathbb{R}^3} \frac{\rho(\boldsymbol{r}', t-R/c)}{4\pi R} dV' \tag{1.28b}$$

$$\boldsymbol{f}(\boldsymbol{r},t) = \epsilon \int_{\mathbb{R}^3} \frac{\boldsymbol{m}(\boldsymbol{r}', t-R/c)}{4\pi R} dV' \tag{1.28c}$$

$$\psi(\boldsymbol{r},t) = \frac{1}{\mu} \int_{\mathbb{R}^3} \frac{\kappa(\boldsymbol{r}', t-R/c)}{4\pi R} dV' \tag{1.28d}$$

where $R = |\boldsymbol{r} - \boldsymbol{r}'|$.

1.2.7 Representation Formulas

In boundary integral equation methods, the electromagnetic fields inside homogeneous domains are computed from surface currents on the boundaries of these domains. Consider such an electric surface current $\boldsymbol{j}(\boldsymbol{r},t)$ (either physical, or an equivalent current as in section 1.2.4) on Γ, immersed in an infinite homogeneous medium with permittivity ϵ and permeability μ. The electric and magnetic fields radiated by this current are

$$\begin{aligned}
\boldsymbol{e}(\boldsymbol{r},t) &= -\partial_t \boldsymbol{a}(\boldsymbol{r},t) - \nabla\phi(\boldsymbol{r},t) \\
&= -\mu\partial_t \int_\Gamma \frac{\boldsymbol{j}(\boldsymbol{r}',t-R/c)}{4\pi R} ds' \\
&\quad + \frac{1}{\epsilon}\nabla \int_\Gamma \frac{\int_{-\infty}^{t-R/c} \nabla'\cdot\boldsymbol{j}(\boldsymbol{r}',\tau)d\tau}{4\pi R} ds' \qquad (1.29) \\
\boldsymbol{h}(\boldsymbol{r},t) &= \frac{1}{\mu}\nabla\times\boldsymbol{a}(\boldsymbol{r},t) \\
&= \nabla\times\int_\Gamma \frac{\boldsymbol{j}(\boldsymbol{r}',t-R/c)}{4\pi R} ds'. \qquad (1.30)
\end{aligned}$$

Now, the limit of $\boldsymbol{r}$ going to Γ is studied as in (1.11a)–(1.11b). A careful analysis of the limits of the integral operators shows that

$$\hat{\boldsymbol{n}}\times\boldsymbol{e}^{\pm}(\boldsymbol{r},t) = \eta\left(\mathcal{T}\boldsymbol{j}\right)(\boldsymbol{r},t) \qquad (1.31)$$

$$\hat{\boldsymbol{n}}\times\boldsymbol{h}^{\pm}(\boldsymbol{r},t) = -\left(\mathcal{K}\boldsymbol{j}\right)(\boldsymbol{r},t) \pm \frac{1}{2}\boldsymbol{j}(\boldsymbol{r},t) \qquad (1.32)$$

where $\eta = \sqrt{\mu/\epsilon}$ is the characteristic impedance of the medium. The electric field integral operator (EFIO) $\mathcal{T}$ is defined as

$$\left(\mathcal{T}\boldsymbol{j}\right)(\boldsymbol{r},t) = \left(\mathcal{T}_s\boldsymbol{j}\right)(\boldsymbol{r},t) + \left(\mathcal{T}_h\boldsymbol{j}\right)(\boldsymbol{r},t) \qquad (1.33)$$

$$\left(\mathcal{T}_s\boldsymbol{j}\right)(\boldsymbol{r},t) = -\frac{1}{c}\hat{\boldsymbol{n}}\times\int_\Gamma \frac{\partial_t\boldsymbol{j}(\boldsymbol{r}',t-R/c)}{4\pi R} ds' \qquad (1.34)$$

$$\left(\mathcal{T}_h\boldsymbol{j}\right)(\boldsymbol{r},t) = c\,\hat{\boldsymbol{n}}\times p.v.\int_\Gamma \nabla\frac{\int_0^{t-R/c}\nabla'\cdot\boldsymbol{j}(\boldsymbol{r}',t')dt'}{4\pi R} ds' \qquad (1.35)$$

where $p.v.$ denotes the Cauchy principal value. The magnetic field integral operator (MFIO) $\mathcal{K}$ is defined as

$$\left(\mathcal{K}\boldsymbol{j}\right)(\boldsymbol{r},t) = -\hat{\boldsymbol{n}}\times p.v.\int_\Gamma \nabla\times\frac{\boldsymbol{j}(\boldsymbol{r}',t-R/c)}{4\pi R} ds'. \qquad (1.36)$$

The case of a magnetic surface current can be treated analogously. In general, the following equation holds (where the dependence on $\boldsymbol{r}$ and t have been omitted):

$$\begin{pmatrix} -\hat{\boldsymbol{n}}\times\boldsymbol{e}^{\pm} \\ \hat{\boldsymbol{n}}\times\boldsymbol{h}^{\pm}\end{pmatrix} = \begin{pmatrix} -\mathcal{K}\pm\frac{1}{2} & -\eta\mathcal{T} \\ \frac{1}{\eta}\mathcal{T} & -\mathcal{K}\pm\frac{1}{2}\end{pmatrix}\begin{pmatrix}\boldsymbol{m}\\ \boldsymbol{j}\end{pmatrix}. \qquad (1.37)$$

If the currents are equivalent currents as in section 1.2.4,

$$\begin{pmatrix} -\hat{\boldsymbol{n}} \times \boldsymbol{e}^{+} \\ \hat{\boldsymbol{n}} \times \boldsymbol{h}^{+} \end{pmatrix} = \begin{pmatrix} -\mathcal{K} + \frac{1}{2} & -\eta\mathcal{T} \\ \frac{1}{\eta}\mathcal{T} & -\mathcal{K} + \frac{1}{2} \end{pmatrix} \begin{pmatrix} -\hat{\boldsymbol{n}} \times \boldsymbol{e}^{+} \\ \hat{\boldsymbol{n}} \times \boldsymbol{h}^{+} \end{pmatrix} + \begin{pmatrix} -\hat{\boldsymbol{n}} \times \boldsymbol{e}^{i+} \\ \hat{\boldsymbol{n}} \times \boldsymbol{h}^{i+} \end{pmatrix} \tag{1.38}$$

where $\boldsymbol{e}^{i+}$ and $\boldsymbol{h}^{i+}$ are the electric and magnetic field radiated by the sources outside of Ω. Note that (1.38) only represents electromagnetic fields radiating in $\mathbb{R}^3 \setminus \Omega$. The traces of electromagnetic field distributions that correspond to resonances of the interior domain Ω reside in the null space of the operator in the right hand side of (1.38).

Similarly to (1.38),

$$\begin{pmatrix} -\hat{\boldsymbol{n}} \times \boldsymbol{e}^{-} \\ \hat{\boldsymbol{n}} \times \boldsymbol{h}^{-} \end{pmatrix} = \begin{pmatrix} \mathcal{K} + \frac{1}{2} & \eta\mathcal{T} \\ -\frac{1}{\eta}\mathcal{T} & \mathcal{K} + \frac{1}{2} \end{pmatrix} \begin{pmatrix} -\hat{\boldsymbol{n}} \times \boldsymbol{e}^{-} \\ \hat{\boldsymbol{n}} \times \boldsymbol{h}^{-} \end{pmatrix} + \begin{pmatrix} -\hat{\boldsymbol{n}} \times \boldsymbol{e}^{i-} \\ \hat{\boldsymbol{n}} \times \boldsymbol{h}^{i-} \end{pmatrix} \tag{1.39}$$

where $\boldsymbol{e}^{i-}$ and $\boldsymbol{h}^{i-}$ are the electric and magnetic field radiated by the sources inside Ω.

1.2.8 Calderón Identities

Consider an electric current density $\boldsymbol{j}$ and a magnetic current density $\boldsymbol{m}$ on a closed surface Γ. The electric and magnetic fields just outside Γ satisfy (1.37)

$$\begin{pmatrix} -\hat{\boldsymbol{n}} \times \boldsymbol{e}^{+} \\ \hat{\boldsymbol{n}} \times \boldsymbol{h}^{+} \end{pmatrix} = \begin{pmatrix} -\mathcal{K} + \frac{1}{2} & -\eta\mathcal{T} \\ \frac{1}{\eta}\mathcal{T} & -\mathcal{K} + \frac{1}{2} \end{pmatrix} \begin{pmatrix} \boldsymbol{m} \\ \boldsymbol{j} \end{pmatrix}. \tag{1.40}$$

Because these fields are a pair of traces belonging to a solution of Maxwell's equations in the domain, they fulfil the representation formulas (1.38) (with $\boldsymbol{h}^{i} = \boldsymbol{e}^{i} = \boldsymbol{0}$):

$$\begin{pmatrix} -\hat{\boldsymbol{n}} \times \boldsymbol{e}^{+} \\ \hat{\boldsymbol{n}} \times \boldsymbol{h}^{+} \end{pmatrix} = \begin{pmatrix} -\mathcal{K} + \frac{1}{2} & -\eta\mathcal{T} \\ \frac{1}{\eta}\mathcal{T} & -\mathcal{K} + \frac{1}{2} \end{pmatrix} \begin{pmatrix} -\hat{\boldsymbol{n}} \times \boldsymbol{e}^{+} \\ \hat{\boldsymbol{n}} \times \boldsymbol{h}^{+} \end{pmatrix}. \tag{1.41}$$

Therefore,

$$\begin{pmatrix} -\mathcal{K} + \frac{1}{2} & -\eta\mathcal{T} \\ \frac{1}{\eta}\mathcal{T} & -\mathcal{K} + \frac{1}{2} \end{pmatrix}^{2} \begin{pmatrix} \boldsymbol{m} \\ \boldsymbol{j} \end{pmatrix} = \begin{pmatrix} -\mathcal{K} + \frac{1}{2} & -\eta\mathcal{T} \\ \frac{1}{\eta}\mathcal{T} & -\mathcal{K} + \frac{1}{2} \end{pmatrix} \begin{pmatrix} \boldsymbol{m} \\ \boldsymbol{j} \end{pmatrix} \tag{1.42}$$

holds $\forall \boldsymbol{m}$ and $\forall \boldsymbol{j}$. From this identity, the Calderón identities are derived:

$$\mathcal{T}^2 - \mathcal{K}^2 = -\frac{1}{4} \tag{1.43}$$

$$\mathcal{K}\mathcal{T} + \mathcal{T}\mathcal{K} = 0. \tag{1.44}$$

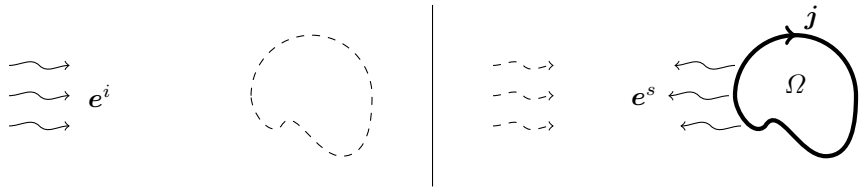

Figure 1.4: left: the incident electric field $\boldsymbol{e}^i$ is generated by external sources, in the absence of the conductor Ω. Right: when the conductor is present, a current $\boldsymbol{j}$ flows on its surface, generating the scattered field $\boldsymbol{e}^s$.

1.2.9 Scattering by PECs

Consider a domain Ω. Sources located outside Ω generate the incident fields $\boldsymbol{e}^i(\boldsymbol{r},t)$ and $\boldsymbol{h}^i(\boldsymbol{r},t)$ (see figure 1.4, left). Now, Ω is filled with a perfect electric conductor. On its surface Γ, a surface current $\boldsymbol{j}(\boldsymbol{r},t)$ can exist. Outside Ω, the total electric and magnetic field are

$$\begin{aligned} \boldsymbol{e}(\boldsymbol{r},t) &= \boldsymbol{e}^s(\boldsymbol{r},t)+\boldsymbol{e}^i(\boldsymbol{r},t) \quad \forall \boldsymbol{r}\in\mathbb{R}^3\backslash\Omega & (1.45)\\ \boldsymbol{h}(\boldsymbol{r},t) &= \boldsymbol{h}^s(\boldsymbol{r},t)+\boldsymbol{h}^i(\boldsymbol{r},t) \quad \forall \boldsymbol{r}\in\mathbb{R}^3\backslash\Omega & (1.46)\end{aligned}$$

where $\boldsymbol{e}^s$ and $\boldsymbol{h}^s$ are generated by the surface current on Γ (see figure 1.4, right).

The jump conditions (1.12a) and (1.12b) then imply that $\forall \boldsymbol{r}\in\Gamma$

$$\begin{aligned} \hat{\boldsymbol{n}}\times\boldsymbol{e}^s(\boldsymbol{r},t)+\hat{\boldsymbol{n}}\times\boldsymbol{e}^i(\boldsymbol{r},t) &= \boldsymbol{0} & (1.47)\\ \hat{\boldsymbol{n}}\times\boldsymbol{h}^s(\boldsymbol{r},t)+\hat{\boldsymbol{n}}\times\boldsymbol{h}^i(\boldsymbol{r},t) &= \boldsymbol{j} & (1.48)\end{aligned}$$

or with (1.37),

$$\begin{aligned} \eta\left(\mathcal{T}\boldsymbol{j}\right)(\boldsymbol{r},t) &= -\hat{\boldsymbol{n}}\times\boldsymbol{e}^i(\boldsymbol{r},t) & (1.49)\\ \left(\mathcal{K}\boldsymbol{j}\right)(\boldsymbol{r},t)+\frac{1}{2}\boldsymbol{j}(\boldsymbol{r},t) &= \hat{\boldsymbol{n}}\times\boldsymbol{h}^i(\boldsymbol{r},t). & (1.50)\end{aligned}$$

The boundary integral equation or BIE (1.49) is known as the time domain electric field integral equation or TD-EFIE, while (1.50) is known as the time domain magnetic field integral equation or TD-MFIE.

The TD-EFIE and the TD-MFIE are defined on the bounded two-dimensional surface Γ rather than on the unbounded three-dimensional domain $\mathbb{R}^3\setminus\Omega$. This restriction of the domain is particularly advantageous for the numerical solution of scattering problems.

As will be seen in the next chapters, the spectral properties of the TD-EFIE and TD-MFIE integral operators play an important role in the numerical solution of these equations. The singular values of the TD-EFIE operator are bounded

neither from above nor from below. As a result, discretizing the TD-EFIE will result in ill-conditioned systems. The singular values of the TD-MFIE operator, on the other hand, accumulate at $\frac{1}{2}$. As a result, correctly discretizing the TD-MFIE will yield well-conditioned systems. A more thorough discussion of the spectral properties of these operators can be found in [6], [7].

From its definition (1.33), it is clear that the operator $\mathcal{T}$ has a null space: constant-in-time solenoidal currents, for which $\partial_t \boldsymbol{j} = 0$ and $\nabla \cdot \boldsymbol{j} = 0$, do not generate an electric field. As such, the TD-EFIE (1.49) only defines $\boldsymbol{j}$ up to a constant solenoidal part. The TD-MFIE (1.50) suffers from a similar problem when it is applied to multiply connected geometries [8]. These spurious static modes can be eliminated by imposing causality:

$$\boldsymbol{e}(\boldsymbol{r},t) = 0, \quad \boldsymbol{h}(\boldsymbol{r},t) = 0, \quad \boldsymbol{j}(\boldsymbol{r},t) = 0 \tag{1.51}$$

for all $t < 0$ and $\boldsymbol{r}$ in a neighborhood of Γ.

Furthermore, even though (1.49) and (1.50) describe the electromagnetic fields outside Ω, they are still prone to the resonances of the interior problem [9]. In order to obtain a resonance free equation, the TD-EFIE and the TD-MFIE are combined into the TD-CFIE as follows [10]:

$$\begin{aligned} &-\alpha\eta\hat{\boldsymbol{n}} \times \mathcal{T}\boldsymbol{j}(\boldsymbol{r},t) + \eta\,(1-\alpha)\left\{\frac{1}{2}\mathcal{I} + \mathcal{K}\right\}\boldsymbol{j}(\boldsymbol{r},t) \\ &\quad = \alpha\hat{\boldsymbol{n}} \times \hat{\boldsymbol{n}} \times \boldsymbol{e}^i(\boldsymbol{r},t) + \eta\,(1-\alpha)\,\hat{\boldsymbol{n}} \times \boldsymbol{h}^i(\boldsymbol{r},t) \end{aligned} \tag{1.52}$$

where α is a dimensionless weighting parameter ranging from 0 (pure TD-MFIE) to 1 (pure TD-EFIE).

1.2.10 Scattering by Dielectrics

Consider a dielectric body Ω with permittivity ϵ' and permeability μ', immersed in a medium with permittivity ϵ and permeability μ. Furthermore assume that no sources exist inside Ω. The fields just outside Ω satisfy

$$\begin{pmatrix} -\hat{\boldsymbol{n}} \times \boldsymbol{e}^+ \\ \hat{\boldsymbol{n}} \times \boldsymbol{h}^+ \end{pmatrix} = \begin{pmatrix} -\mathcal{K} + \frac{1}{2} & -\eta\mathcal{T} \\ \frac{1}{\eta}\mathcal{T} & -\mathcal{K} + \frac{1}{2} \end{pmatrix} \begin{pmatrix} -\hat{\boldsymbol{n}} \times \boldsymbol{e}^+ \\ \hat{\boldsymbol{n}} \times \boldsymbol{h}^+ \end{pmatrix} + \begin{pmatrix} -\hat{\boldsymbol{n}} \times \boldsymbol{e}^{i+} \\ \hat{\boldsymbol{n}} \times \boldsymbol{h}^{i+} \end{pmatrix} \tag{1.53}$$

while the fields just inside Ω satisfy

$$\begin{pmatrix} -\hat{\boldsymbol{n}} \times \boldsymbol{e}^- \\ \hat{\boldsymbol{n}} \times \boldsymbol{h}^- \end{pmatrix} = \begin{pmatrix} \mathcal{K}' + \frac{1}{2} & \eta'\mathcal{T}' \\ -\frac{1}{\eta'}\mathcal{T}_2 & \mathcal{K}' + \frac{1}{2} \end{pmatrix} \begin{pmatrix} -\hat{\boldsymbol{n}} \times \boldsymbol{e}^+ \\ \hat{\boldsymbol{n}} \times \boldsymbol{h}^+ \end{pmatrix}. \tag{1.54}$$

The operators and quantities with a prime are defined with the material properties ϵ' and μ', whereas those without prime are defined with the material parameters ϵ and μ.

Since no physical current is allowed to flow on Γ, the jump conditions (1.12a) – (1.12b) imply that $\hat{\boldsymbol{n}} \times \boldsymbol{e}^+ = \hat{\boldsymbol{n}} \times \boldsymbol{e}^-$ and $\hat{\boldsymbol{n}} \times \boldsymbol{h}^+ = \hat{\boldsymbol{n}} \times \boldsymbol{h}^-$. Applying these

continuity conditions to (1.53)–(1.54) immediately yields the Poggio-Miller-Chan-Harrington-Wu-Tsai or PMCHWT equation

$$\begin{pmatrix} -\hat{\boldsymbol{n}} \times \boldsymbol{e}^{i+} \\ \hat{\boldsymbol{n}} \times \boldsymbol{h}^{i+} \end{pmatrix} = \begin{pmatrix} \mathcal{K} + \mathcal{K}' & \eta\mathcal{T} + \eta'\mathcal{T}' \\ -\frac{1}{\eta}\mathcal{T} - \frac{1}{\eta'}\mathcal{T}' & \mathcal{K} + \mathcal{K}' \end{pmatrix} \begin{pmatrix} -\hat{\boldsymbol{n}} \times \boldsymbol{e}^{+} \\ \hat{\boldsymbol{n}} \times \boldsymbol{h}^{+} \end{pmatrix}. \tag{1.55}$$

The PMCHWT operator is similar to the TD-EFIE operator in the sense that its spectrum is unbounded. Alternatively, (1.53) and (1.54) can be combined into the Müller equation

$$\begin{pmatrix} \frac{\epsilon+\epsilon'}{2} + \epsilon\mathcal{K} - \epsilon'\mathcal{K}' & \epsilon\eta\mathcal{T} - \epsilon'\eta'\mathcal{T}' \\ -\frac{\mu}{\eta}\mathcal{T} + \frac{\mu'}{\eta'}\mathcal{T}' & \frac{\mu+\mu'}{2} + \mu\mathcal{K} - \mu'\mathcal{K}' \end{pmatrix} \begin{pmatrix} -\hat{\boldsymbol{n}} \times \boldsymbol{e}^{+} \\ \hat{\boldsymbol{n}} \times \boldsymbol{h}^{+} \end{pmatrix} = \begin{pmatrix} -\epsilon\hat{\boldsymbol{n}} \times \boldsymbol{e}^{i+} \\ \mu\hat{\boldsymbol{n}} \times \boldsymbol{h}^{i+} \end{pmatrix}. \tag{1.56}$$

The Müller operator is similar to the TD-MFIE operator in the sense that its singular values accumulate at the finite nonzero values $(\epsilon + \epsilon')/2$ and $(\mu + \mu')/2$.

1.3 Frequency Domain Electromagnetics

In the previous section, the full time dependency of all fields was taken into account (although the background medium was assumed to be fixed in time). However, for many applications, the time dependency is (approximately) harmonic. Then, it is convenient to apply the Fourier transform to the electromagnetic fields and equations. For a quantity $x(t)$, its Fourier transform $X(\omega)$ is defined as

$$X(\omega) = \mathcal{F}\{x\}(\omega) = \frac{1}{\sqrt{2\pi}} \int_{\mathbb{R}} x(t) e^{-j\omega t} dt \tag{1.57}$$

$$x(t) = \mathcal{F}^{-1}\{x\}(t) = \frac{1}{\sqrt{2\pi}} \int_{\mathbb{R}} X(\omega) e^{j\omega t} dt. \tag{1.58}$$

Since $\mathcal{F}\{\partial_t x\}(\omega) = j\omega X(\omega)$, the Maxwell equations become

$$\nabla \times \boldsymbol{E}(\boldsymbol{r}) = -j\omega \boldsymbol{B}(\boldsymbol{r}) - \boldsymbol{M}(\boldsymbol{r}) \tag{1.59a}$$

$$\nabla \times \boldsymbol{H}(\boldsymbol{r}) = j\omega \boldsymbol{D}(\boldsymbol{r}) + \boldsymbol{J}(\boldsymbol{r}) \tag{1.59b}$$

$$\nabla \cdot \boldsymbol{D}(\boldsymbol{r}) = P(\boldsymbol{r}) \tag{1.59c}$$

$$\nabla \cdot \boldsymbol{B}(\boldsymbol{r}) = K(\boldsymbol{r}) \tag{1.59d}$$

where the dependence on ω is omitted for brevity. The charge-current continuity equations become

$$0 = j\omega P(\boldsymbol{r}) + \nabla \cdot \boldsymbol{J}(\boldsymbol{r}) \tag{1.60a}$$

$$0 = j\omega K(\boldsymbol{r}) + \nabla \cdot \boldsymbol{M}(\boldsymbol{r}). \tag{1.60b}$$

The constitutive equations (1.6a)–(1.6b) become

$$\boldsymbol{D}(\boldsymbol{r}) = \epsilon \boldsymbol{E}(\boldsymbol{r}) \tag{1.61a}$$

$$\boldsymbol{B}(\boldsymbol{r}) = \mu \boldsymbol{H}(\boldsymbol{r}) \tag{1.61b}$$

where ϵ and μ are in general functions of ω. They can often be approximated as constant, which is equivalent to (1.10a)–(1.10b).

Substituting the constitutive equations into Maxwell's equations yields

$$\begin{aligned} \nabla \times \boldsymbol{E}(\boldsymbol{r}) &= -j\omega\mu \boldsymbol{H}(\boldsymbol{r}) - \boldsymbol{M}(\boldsymbol{r}) && \text{(1.62a)} \\ \nabla \times \boldsymbol{H}(\boldsymbol{r}) &= j\omega\epsilon \boldsymbol{E}(\boldsymbol{r}) + \boldsymbol{J}(\boldsymbol{r}) && \text{(1.62b)} \\ \nabla \cdot \boldsymbol{D}(\boldsymbol{r}) &= P(\boldsymbol{r}) && \text{(1.62c)} \\ \nabla \cdot \boldsymbol{B}(\boldsymbol{r}) &= K(\boldsymbol{r}). && \text{(1.62d)} \end{aligned}$$

The derivation of the electromagnetic potentials and integral representation formulas is analogous to the time domain case. The major difference is that the Green's function now satisfies

$$\nabla^2 G(\boldsymbol{r}) + \frac{\omega^2}{c^2} G(\boldsymbol{r}) = -\delta(\boldsymbol{r}) \tag{1.63}$$

$$G(\boldsymbol{r}) = \frac{e^{-jk|\boldsymbol{r}|}}{4\pi\,|\boldsymbol{r}|} \tag{1.64}$$

with $k = \omega/c$.

The frequency domain boundary integral operators are defined by

$$\left(\mathcal{T}_k \boldsymbol{J}\right)(\boldsymbol{r}, \omega) = \mathcal{F}\left\{\mathcal{T}\boldsymbol{j}\right\}(\boldsymbol{r}, \omega) \tag{1.65}$$

or, explicitly,

$$\begin{aligned} \left(\mathcal{T}_k \boldsymbol{J}\right)(\boldsymbol{r}) &= \left(\mathcal{T}_{s,k} \boldsymbol{J}\right)(\boldsymbol{r}) + \left(\mathcal{T}_{h,k} \boldsymbol{J}\right)(\boldsymbol{r}) && \text{(1.66)} \\ \left(\mathcal{T}_{s,k} \boldsymbol{J}\right)(\boldsymbol{r}) &= -jk\hat{\boldsymbol{n}} \times \int_\Gamma \frac{e^{-jkR}}{4\pi R} \boldsymbol{J}(\boldsymbol{r'}) d\mathbf{s'} && \text{(1.67)} \\ \left(\mathcal{T}_{h,k} \boldsymbol{J}\right)(\boldsymbol{r}) &= \frac{1}{jk}\hat{\boldsymbol{n}} \times p.v. \int_\Gamma \nabla \frac{e^{-jkR}}{4\pi R} \nabla' \cdot \boldsymbol{J}(\boldsymbol{r'}) d\mathbf{s'} && \text{(1.68)} \\ \left(\mathcal{K}_k \boldsymbol{J}\right)(\boldsymbol{r}) &= -\hat{\boldsymbol{n}} \times p.v. \int_\Gamma \nabla \times \frac{e^{-jkR}}{4\pi R} \boldsymbol{J}(\boldsymbol{r}') d\mathbf{s}'. && \text{(1.69)} \end{aligned}$$

Scattering by perfect electric conductors is modeled by the frequency domain electric field integral equation (FD-EFIE)

$$\eta \left(\mathcal{T}_k \boldsymbol{J}\right)(\boldsymbol{r}) = -\hat{\boldsymbol{n}} \times \boldsymbol{E}^i(\boldsymbol{r}) \tag{1.70}$$

or the frequency domain magnetic field integral equation (FD-MFIE)

$$\left(\mathcal{K}_k \boldsymbol{J}\right)(\boldsymbol{r}) + \frac{1}{2}\boldsymbol{J}(\boldsymbol{r}) = \hat{\boldsymbol{n}} \times \boldsymbol{H}^i(\boldsymbol{r}). \tag{1.71}$$

The frequency domain PMCHWT (FD-PMCHWT) and Müller (FD-Müller) equations become

$$\begin{pmatrix} -\hat{\boldsymbol{n}} \times \boldsymbol{E}^{i+} \\ \hat{\boldsymbol{n}} \times \boldsymbol{H}^{i+} \end{pmatrix} = \begin{pmatrix} \mathcal{K}_k + \mathcal{K}_{k'} & \eta \mathcal{T}_k + \eta' \mathcal{T}_{k'} \\ -\frac{1}{\eta} \mathcal{T}_k - \frac{1}{\eta'} \mathcal{T}_{k'} & \mathcal{K}_k + \mathcal{K}_{k'} \end{pmatrix} \begin{pmatrix} -\hat{\boldsymbol{n}} \times \boldsymbol{E}^{+} \\ \hat{\boldsymbol{n}} \times \boldsymbol{H}^{+} \end{pmatrix} \tag{1.72}$$

and

$$\begin{pmatrix} \frac{\epsilon+\epsilon'}{2} + \epsilon \mathcal{K}_k - \epsilon' \mathcal{K}_{k'} & \epsilon \eta \mathcal{T}_{k'} - \epsilon' \eta' \mathcal{T}_{k'} \\ -\frac{\mu}{\eta} \mathcal{T}_k + \frac{\mu'}{\eta'} \mathcal{T}_{k'} & \frac{\mu+\mu'}{2} + \mu \mathcal{K}_k - \mu' \mathcal{K}_{k'} \end{pmatrix} \begin{pmatrix} -\hat{\boldsymbol{n}} \times \boldsymbol{E}^{+} \\ \hat{\boldsymbol{n}} \times \boldsymbol{H}^{+} \end{pmatrix} = \begin{pmatrix} -\epsilon \hat{\boldsymbol{n}} \times \boldsymbol{E}^{i+} \\ \mu \hat{\boldsymbol{n}} \times \boldsymbol{H}^{i+} \end{pmatrix} \tag{1.73}$$

respectively.

1.4 Chiral Media

1.4.1 Constitutive Equations

Section 1.2.2 described how the propagation medium is taken into account in Maxwell's equations. With the exception of vacuum, all media influence the electromagnetic fields on a microscopic level. The constitutive equations, however, provide a macroscopic description of the media, while taking into account certain properties of the microscopic structure. For instance, media with an anisotropic microscopic structure are described by anisotropic constitutive equations. Media which exhibit nonlinear behaviour are modeled using nonlinear constitutive equations.

In this section, another physical property is discussed: chirality. A geometrical entity (a set of points, lines, polygons, ...) is called chiral when it cannot be superposed onto its mirror image. A prime example are the human hands: the left hand is the mirror image of the right hand, but no amount of rotations or translations can turn a left hand into a right hand. In fact, the term chiral stems from the Greek word for hand. Another example are helices: a left-handed helix cannot be turned into a right-handed one without geometrical reflections.

Chemical molecules can also exhibit chirality. A well-known example is the DNA molecule, which has the structure of a double right-handed helix. Many more (and much simpler) molecules are chiral. Their left- and right-handed forms are called enantiomers. The lack of reflection symmetry has implications for the propagation of electromagnetic waves through a medium composed of chiral molecules. In particular, circularly polarized waves behave differently depending on whether they are right-handed or left-handed. This phenomenon is called optical activity.

Optical activity is a property of the propagation medium. Therefore, it should be present (in one way or another) in the constitutive equations. This is

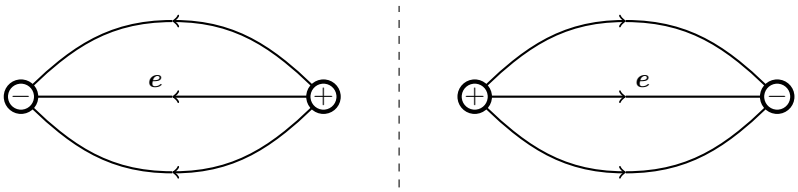

Figure 1.5: left: electric field lines between two opposite charges. Right: upon geometric reflection of the charges, the electric field is itself reflected. This is characteristic of a polar vector quantity.

however not the case for the standard constitutive equations (1.10a)–(1.10b). To see how these equations should be altered, it is instructive to examine how electromagnetic fields transform under reflection. The electric field $\boldsymbol{e}$ is said to be a polar vector: upon geometrical reflection of the position of its sources, the field is itself reflected – see figure 1.5. The magnetic field $\boldsymbol{h}$, on the other hand, is reflected and reversed, and is said to be an axial vector (or a pseudovector) – see figure 1.6. In mathematical terms,

$$\boldsymbol{e}' = \mathsf{R}\boldsymbol{e} \tag{1.74a}$$
$$\boldsymbol{h}' = -\mathsf{R}\boldsymbol{h} \tag{1.74b}$$

where the prime denotes the physical quantities after reflection of the geometrical set-up, and R is the matrix describing the geometrical reflection. The standard constitutive equations

$$\boldsymbol{d} = \epsilon\, \boldsymbol{e} \tag{1.75a}$$
$$\boldsymbol{b} = \mu\, \boldsymbol{h} \tag{1.75b}$$

imply that $\boldsymbol{d}$ is polar and $\boldsymbol{b}$ is axial. Furthermore, the curl of a polar vector is axial and the curl of an axial vector is polar.

The asymmetry of chiral media can be modeled by mixing polar and axial vectors in the constitutive equations, for example using the Drude-Born-Fedorov (DBF) equations

$$\boldsymbol{d} = \tilde{\epsilon}\,(\boldsymbol{e} + \beta\nabla\times\boldsymbol{e}) \tag{1.76a}$$
$$\boldsymbol{b} = \tilde{\mu}\,(\boldsymbol{h} + \beta\nabla\times\boldsymbol{h})\,. \tag{1.76b}$$

After reflection, the right hand sides transform as

$$\text{right hand side of (1.76a)} \;\Rightarrow\; \mathsf{R}\,\tilde{\epsilon}\,(\boldsymbol{e} - \beta\nabla\times\boldsymbol{e}) \tag{1.77a}$$
$$\text{right hand side of (1.76b)} \;\Rightarrow\; \mathsf{R}\,\tilde{\mu}\,(-\boldsymbol{h} + \beta\nabla\times\boldsymbol{h})\,. \tag{1.77b}$$

In this way, reflection symmetry is broken. However, this symmetry is present at the microscopic level. This contradiction is resolved by defining β as a

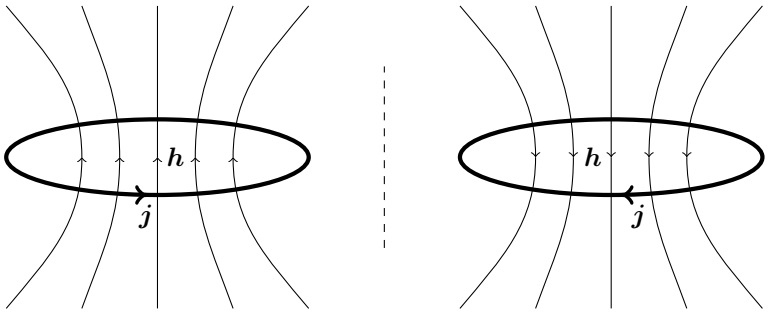

Figure 1.6: left: magnetic field lines generated by a current loop. Right: upon geometric reflection of the current loop, the magnetic field is reflected and reversed. This is characteristic of an axial vector quantity.

pseudoscalar: under geometrical reflection, it changes sign: $\beta' = -\beta$. In other words, consider a medium composed of left-handed molecules, which is described on a macroscopic level by the parameters (ϵ, μ, β). Its mirror image is composed of right-handed molecules, and is described by the parameters $(\epsilon, \mu, -\beta)$. In this way, chirality and optical activity can be incorporated into the constitutive equations.

The DBF model is not the only way to achieve this. Another possibility is given by the Condon model

$$\boldsymbol{d} = \tilde{\epsilon}\,(\boldsymbol{e} - \beta\partial_t \boldsymbol{h}) \tag{1.78a}$$

$$\boldsymbol{b} = \tilde{\mu}\,(\boldsymbol{h} + \beta\partial_t \boldsymbol{e}) \tag{1.78b}$$

and many other possibilities can model the same type of asymmetry. One could wonder which constitutive equations are correct. However, it is important to keep in mind that this is, in essence, a macroscopic approximation of microscopic behavior. Furthermore, which model best approximates a certain medium depends on the properties of this specific medium.

This ambiguity is removed in the frequency domain. Both the DBF and the Condon model then reduce to

$$\boldsymbol{D} = \epsilon\boldsymbol{E} - j\kappa\sqrt{\epsilon\mu}\boldsymbol{H} \tag{1.79a}$$

$$\boldsymbol{B} = \mu\boldsymbol{H} + j\kappa\sqrt{\epsilon\mu}\boldsymbol{E} \tag{1.79b}$$

where κ is the chirality or Pasteur parameter, which can depend on the frequency. In fact, it can be shown that this is the only correct form compatible with general physical properties such as covariance, reciprocity, and time-reversal symmetry – see [11] and references therein for a more thorough discussion. Therefore, it is acceptable to consider (1.79a)–(1.79b) as the correct constitutive equations for isotropic chiral media. If the frequency dependence of ϵ, μ and

κ can be measured or computed for a given material, then the correct time domain constitutive equations can be obtained by inverse Fourier (or Laplace) transforming (1.79a)–(1.79b).

In what follows, the discussion of chiral media will be restricted to the frequency domain. Optical activity only occurs in a relatively narrow frequency band. Therefore, this restriction does not limit the applicability of the theory.

1.4.2 The Bohren Transform

The constitutive equations (1.79a)–(1.79b) complicate Maxwell's equations by introducing additional coupling between the electromagnetic fields. However, the resulting equations can be simplified by defining

$$\begin{pmatrix} \mathcal{E}_\pm \\ \mathcal{H}_\pm \end{pmatrix} = \frac{1}{2} \begin{pmatrix} 1 & \mp j\eta \\ \pm j\eta & 1 \end{pmatrix} \begin{pmatrix} \boldsymbol{E} \\ \boldsymbol{H} \end{pmatrix} \tag{1.80}$$

and

$$\begin{pmatrix} \mathcal{J}_\pm \\ \mathcal{M}_\pm \end{pmatrix} = \frac{1}{2} \begin{pmatrix} 1 & \mp j/\eta \\ \pm j/\eta & 1 \end{pmatrix} \begin{pmatrix} \boldsymbol{J} \\ \boldsymbol{M} \end{pmatrix}. \tag{1.81}$$

These auxiliary quantities satisfy

$$\nabla \times \mathcal{E}_\pm = -j\omega\mu(1 \pm \kappa)\mathcal{H}_\pm - \mathcal{M}_\pm \tag{1.82a}$$

$$\nabla \times \mathcal{H}_\pm = j\omega\epsilon(1 \pm \kappa)\mathcal{H}_\pm + \mathcal{J}_\pm \tag{1.82b}$$

which is formally identical to (1.62a)–(1.62b). As such, two independent frequency domain Maxwellian problems are obtained: one with material parameters $\epsilon_+ = \epsilon(1 + \kappa)$ and $\mu_+ = \mu(1 + \kappa)$, and the other with material parameters $\epsilon_- = \epsilon(1 - \kappa)$ and $\mu_- = \mu(1 - \kappa)$. The wave numbers associated with these problems are, respectively,

$$\gamma_+ = \omega(1 + \kappa)\sqrt{\epsilon\mu} \tag{1.83}$$

$$\gamma_- = \omega(1 - \kappa)\sqrt{\epsilon\mu}. \tag{1.84}$$

All of the standard techniques can be applied to solve the two problems (1.82a)–(1.82b). After a solution has been obtained for $(\mathcal{E}_+, \mathcal{H}_+)$ and $(\mathcal{E}_-, \mathcal{H}_-)$, the physical electromagnetic fields are easily found to be

$$\boldsymbol{E} = \mathcal{E}_+ + \mathcal{E}_- \tag{1.85a}$$

$$\boldsymbol{H} = \mathcal{H}_+ + \mathcal{H}_-. \tag{1.85b}$$

1.4.3 Boundary Integral Equations

Consider a domain $\Omega \subset \mathbb{R}^3$, filled with a homogeneous isotropic chiral medium described by the material parameters ϵ, μ and κ. It is surrounded by a nonchiral medium (e.g. vacuum) with material parameters ϵ_0 and μ_0. No sources are present within Ω, and the electromagnetic fields radiated by the sources outside Ω are denoted $\boldsymbol{E}^i(\boldsymbol{r})$ and $\boldsymbol{H}^i(\boldsymbol{r})$.

All of the representation formulas and jump conditions derived earlier are applicable to the subproblems (1.82a)–(1.82b). As such, a chiral PMCHWT equation can be constructed:

$$\begin{pmatrix} \mathcal{K}_{k_0} + \mathcal{K}_+ + j\mathcal{T}_- & \eta_0\mathcal{T}_{k_0} + \eta\left(\mathcal{T}_+ - j\mathcal{K}_-\right) \\ -\frac{1}{\eta_0}\mathcal{T}_{k_0} - \frac{1}{\eta}\left(\mathcal{T}^+ + j\mathcal{K}^-\right) & \mathcal{K}_{k_0} + \mathcal{K}_+ + j\mathcal{T}_- \end{pmatrix} \begin{pmatrix} -\hat{\boldsymbol{n}} \times \boldsymbol{E}^+ \\ \hat{\boldsymbol{n}} \times \boldsymbol{H}^+ \end{pmatrix} = \begin{pmatrix} -\hat{\boldsymbol{n}} \times \boldsymbol{E}^i \\ \hat{\boldsymbol{n}} \times \boldsymbol{H}^i \end{pmatrix} \tag{1.86}$$

where

$$\mathcal{T}_+ = \frac{1}{2}\left(\mathcal{T}_{\gamma_+} + \mathcal{T}_{\gamma_-}\right) \qquad \mathcal{T}_- = \frac{1}{2}\left(\mathcal{T}_{\gamma_+} - \mathcal{T}_{\gamma_-}\right) \tag{1.87}$$

$$\mathcal{K}_+ = \frac{1}{2}\left(\mathcal{K}_{\gamma_+} + \mathcal{K}_{\gamma_-}\right) \qquad \mathcal{K}_- = \frac{1}{2}\left(\mathcal{K}_{\gamma_+} - \mathcal{K}_{\gamma_-}\right). \tag{1.88}$$

For nonchiral media ($\kappa = 0$), $\mathcal{T}_- = \mathcal{K}_- = 0$, and the chiral PMCHWT equation reduces to (1.72).

Similarly, a chiral Müller equation can be constructed:

$$\begin{pmatrix} \mathcal{M}_{11} & \mathcal{M}_{12} \\ \mathcal{M}_{21} & \mathcal{M}_{22} \end{pmatrix} \begin{pmatrix} -\hat{\boldsymbol{n}} \times \boldsymbol{E} \\ \hat{\boldsymbol{n}} \times \boldsymbol{H} \end{pmatrix} = \begin{pmatrix} \epsilon_0 & 0 \\ 0 & \mu_0 \end{pmatrix} \begin{pmatrix} -\hat{\boldsymbol{n}} \times \boldsymbol{E}^i \\ \hat{\boldsymbol{n}} \times \boldsymbol{H}^i \end{pmatrix} \tag{1.89}$$

where

$$\mathcal{M}_{11} = \epsilon_0\left(\frac{1}{2} + \mathcal{K}_0\right) + \epsilon\left(\frac{1}{2} - \mathcal{K}'_+ + j\mathcal{T}'_-\right) \tag{1.90}$$

$$\mathcal{M}_{12} = \sqrt{\epsilon_0\mu_0}\mathcal{T}_{k_0} - \sqrt{\epsilon\mu}\left(\mathcal{T}'_+ + j\left(\frac{\kappa}{2} + \mathcal{K}'_-\right)\right) \tag{1.91}$$

$$\mathcal{M}_{21} = -\mathcal{M}_{12} \tag{1.92}$$

$$\mathcal{M}_{22} = \mu_0\left(\frac{1}{2} + \mathcal{K}_0\right) + \mu\left(\frac{1}{2} - \mathcal{K}'_+ + j\mathcal{T}'_-\right) \tag{1.93}$$

$$\mathcal{T}'_+ = \frac{1}{2}\left((1+\kappa)\mathcal{T}_{\gamma_+} + (1-\kappa)\mathcal{T}_{\gamma_-}\right) \tag{1.94}$$

$$\mathcal{T}'_- = \frac{1}{2}\left((1+\kappa)\mathcal{T}_{\gamma_+} - (1-\kappa)\mathcal{T}_{\gamma_-}\right) \tag{1.95}$$

$$\mathcal{K}'_+ = \frac{1}{2}\left((1+\kappa)\mathcal{K}_{\gamma_+} + (1-\kappa)\mathcal{K}_{\gamma_-}\right) \tag{1.96}$$

$$\mathcal{K}'_- = \frac{1}{2}\left((1+\kappa)\mathcal{K}_{\gamma_+} - (1-\kappa)\mathcal{K}_{\gamma_-}\right). \tag{1.97}$$

1.5 Conclusion

In this chapter, the theory of electromagnetic boundary integral equations was developed. These equations efficiently model scattering by piecewise homogeneous objects, by restricting the domain on which the problem is defined to the interfaces between homogeneous regions. In particular, scattering by perfect conductors is described by the EFIE, the MFIE and the CFIE. The PMCHWT and Müller equations are applicable to dielectrics. All of these equations can be formulated in the time domain (for transient problems) and in the frequency domain (for time-harmonic problems). The PMCHWT and Müller equations can also be extended to deal with chiral media, but are here restricted to the frequency domain.

The next chapter deals with techniques to construct numerical solutions to these boundary integral equations using the boundary element method.

References

[1] J. C. Maxwell, *A treatise on electricity and magnetism*. Clarendon press, 1881, vol. 1.

[2] J. C. Maxwell, "A dynamical theory of the electromagnetic field", *Philosophical Transactions of the Royal Society of London*, vol. 155, pp. 459–512, 1865.

[3] J. Van Bladel, *Electromagnetic Fields*, 2nd ed., ser. IEEE press series on electromagnetic wave theory. Wiley-IEEE Press, 2007.

[4] J. D. Jackson, *Classical electrodynamics*, 3rd ed. Wiley, New York, 1998.

[5] J. R. Reitz, F. J. Milford, and R. W. Christy, *Foundations of electromagnetic theory*, 4th ed. Addison-Wesley Publishing Company, 2008.

[6] J.-C. Nédélec, *Acoustic and electromagnetic equations: Integral representations for harmonic problems*. Springer Science & Business Media, 2001, vol. 144.

[7] G. W. Hanson and A. B. Yakovlev, *Operator theory for electromagnetics: An introduction*. Springer Science & Business Media, 2001.

[8] K. Cools, F. P. Andriulli, F. Olyslager, and E. Michielssen, "Nullspaces of MFIE and Calderón preconditioned EFIE operators applied to toroidal surfaces", *IEEE Transactions on Antennas and Propagation*, vol. 57, no. 10, pp. 3205–3215, Oct. 2009.

[9] W. C. Chew and J. M. Song, "Gedanken experiments to understand the internal resonance problems of electromagnetic scattering.", *Electromagnetics*, vol. 27, no. 8, pp. 457 –471, 2007.

[10] B. Shanker, A. Ergin, K. Aygun, and E. Michielssen, "Analysis of transient electromagnetic scattering from closed surfaces using a combined field integral equation", *IEEE Transactions on Antennas and Propagation*, vol. 48, no. 7, pp. 1064 –1074, Jul. 2000.

[11] A. Lakhtakia, V. Varadan, and V. Varadan, *Time-Harmonic Electromagnetic Fields in Chiral Media*. Springer-Verlag, 1989.

2

Discretization of Boundary Integral Equations

2.1 Introduction

In chapter 1, the Maxwell equations were applied to scattering problems involving piecewise continuous media. This resulted in a number of boundary integral equations (BIEs) such as the EFIE and the MFIE, which are applicable to perfectly conducting scatterers, and the PMCHWT and Müller equations, which are applicable to penetrable media. These equations can be formulated in the time domain, in order to model transient scattering problems, or in the frequency domain, in order to model time-harmonic problems. The remainder of this thesis deals with the construction of numerical solutions to these BIEs using the boundary element method (BEM). In this chapter, the basic techniques for discretizing and solving these equations are discussed, as well as the most common difficulties encountered in practical situations.

2.2 The FD-EFIE and FD-MFIE

2.2.1 The FD-EFIE

As a first step, the discretization of the frequency domain electric and magnetic field integral equations (FD-EFIE and FD-MFIE, respectively) is studied. Recall the scattering problem in section 1.3: a perfect electric conductor Ω, with boundary Γ, is illuminated by an incident electromagnetic field distribution $\boldsymbol{E}^i$, $\boldsymbol{H}^i$, which is harmonic in time. As a result, an electric current density $\boldsymbol{J}$ is induced on Γ, which satisfies the FD-EFIE (1.70):

$$\eta \left(\mathcal{T}_k \boldsymbol{J}\right)(\boldsymbol{r}) = -\hat{\boldsymbol{n}} \times \boldsymbol{E}^i(\boldsymbol{r}) \quad \forall \boldsymbol{r} \in \Gamma. \tag{2.1}$$

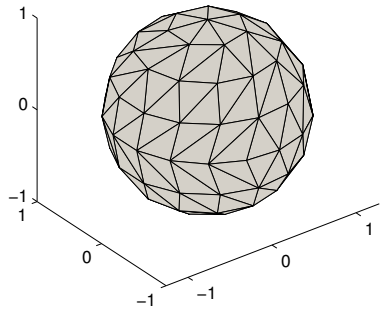

Figure 2.1: A mesh of triangles approximating a sphere with radius 1 m.

Here, $k = \omega\sqrt{\epsilon\mu}$, where ϵ and μ are, respectively, the permittivity and the permeability of the medium surrounding the scatterer, and ω is the angular frequency of the incident field distribution.

A numerical solution to (2.1) can be constructed using the boundary element method (BEM) [1], [2]. The standard approach is to approximate Γ by a mesh of triangles. An example of such a mesh is shown in figure 2.1. The number of edges on this mesh is denoted N_S, the number of faces N_F and the number of vertices N_V. Associated with each edge e_m, a Rao-Wilton-Glisson or RWG function $\boldsymbol{f}_m(\boldsymbol{r})$ [3] is defined on the two adjacent faces c_m^+ and c_m^- (see figure 2.2):

$$\boldsymbol{f}_m(\boldsymbol{r}) = \begin{cases} \frac{\boldsymbol{r}-\boldsymbol{r}_m^+}{2A_{c_m^+}} & \text{for } \boldsymbol{r} \in c_m^+ \\ \frac{\boldsymbol{r}_m^- - \boldsymbol{r}}{2A_{c_m^-}} & \text{for } \boldsymbol{r} \in c_m^- \\ 0 & \text{otherwise} \end{cases} \tag{2.2}$$

where $A_{c_m^-}$ is the area of c_m^-, and $A_{c_m^+}$ is the area of c_m^+[1].

The current on Γ is now approximated as an expansion in RWG functions:

$$\boldsymbol{J}(\boldsymbol{r}) = \sum_{m=1}^{N_S} \mathsf{j}_m \boldsymbol{f}_m(\boldsymbol{r}). \tag{2.3}$$

This expansion is inserted into (2.1). A Galerkin method is applied to the resulting equation, by spatially testing it using the rotated RWG functions $\hat{\boldsymbol{n}} \times \boldsymbol{f}_m$. This leads to the matrix equation

$$\mathsf{Z}\mathsf{j} = -\mathsf{e}^i \tag{2.4}$$

[1] In the original definition [3], the RWG functions are multiplied with l_m, i.e., the length of the m-th edge. In this thesis, the definition without edge length normalization is adopted in order to simplify the discussion of the quasi-Helmholtz projectors (section 2.2.6), and to maintain compatibility with [4].

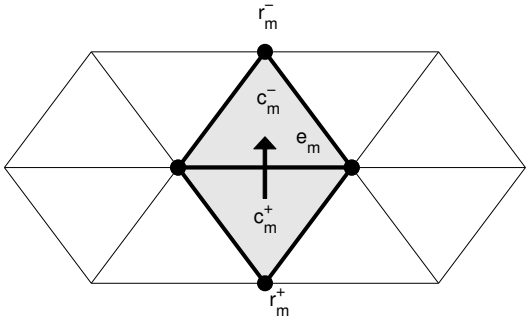

Figure 2.2: An RWG function $\boldsymbol{f}_m(\boldsymbol{r})$ is defined on a pair of triangles (c_m^+, c_m^-). It represents a current flowing across their common edge e_m.

where

$$[\mathsf{Z}]_{mn} = (\hat{\boldsymbol{n}} \times \boldsymbol{f}_m, \eta \mathcal{T}_k \boldsymbol{f}_n) \tag{2.5}$$

$$[\mathsf{j}]_m = \mathsf{j}_m \tag{2.6}$$

$$\left[\mathsf{e}^i\right]_m = \left(\hat{\boldsymbol{n}} \times \boldsymbol{f}_m, \hat{\boldsymbol{n}} \times \boldsymbol{E}^i\right) \tag{2.7}$$

with $m = 1, 2, ..., N_S$ and $n = 1, 2, ..., N_S$. The inner product $(\boldsymbol{a}, \boldsymbol{b})$ is defined as

$$(\boldsymbol{a}, \boldsymbol{b}) = \int_\Gamma \boldsymbol{a}(\boldsymbol{r}) \cdot \boldsymbol{b}(\boldsymbol{r}) \; ds. \tag{2.8}$$

Equation (2.4) can be solved using a standard matrix inversion:

$$\mathsf{j} = -\mathsf{Z}^{-1}\mathsf{e}^i. \tag{2.9}$$

Once the expansion coefficients j are known, the current $\boldsymbol{J}(\boldsymbol{r})$ on Γ is given by (2.3). The scattered fields generated by this current can be computed from (the frequency domain versions of) (1.29) and (1.30).

This presents a major advantage of the BEM, compared to other techniques such as the finite element method (FEM): the simulation domain is reduced to a two-dimensional bounded surface, leading to a significantly smaller number of unknowns.

Although (2.4) is conceptually simple, a number of points need to be discussed in more detail. First, the basis and testing functions used here are by no means the only possibility. Other choices are discussed in section 2.2.2. Second, the computation of the interaction elements (2.5) is studied in section 2.2.3. Third, solving the system (2.4) is computationally expensive, especially for large numbers of unknowns. Several ways to deal with this complexity are discussed in section 2.2.4.

2.2.2 Basis and Testing Functions

In the previous section, the current was expanded in a set of RWG functions. One advantage of these functions is that they are divergence-conforming: although they are discontinuous across edges, their (surface) divergence is well defined:

$$\nabla \cdot \boldsymbol{f}_m(\boldsymbol{r}) = \begin{cases} \frac{1}{2A_{c_m^+}} & \text{for } \boldsymbol{r} \in c_m^+ \\ -\frac{1}{2A_{c_m^-}} & \text{for } \boldsymbol{r} \in c_m^- \\ 0 & \text{otherwise.} \end{cases} \tag{2.10}$$

This means that the surface charge associated with the approximated current is piecewise continuous, and no Dirac delta distributions appear on the edges.

The rotated RWG functions $\hat{\boldsymbol{n}} \times \boldsymbol{f}_m(\boldsymbol{r})$ are used as testing functions. The interaction elements can be written as

$$\begin{aligned} [\mathsf{Z}]_{mn} &= \eta \int_\Gamma \left(\hat{\boldsymbol{n}} \times \boldsymbol{f}_m(\boldsymbol{r})\right) \cdot \left(\mathcal{T}_k \boldsymbol{f}_n\right)(\boldsymbol{r})\, ds \\ &= -jk\eta \int_\Gamma \left(\hat{\boldsymbol{n}} \times \boldsymbol{f}_m(\boldsymbol{r})\right) \cdot \left(\hat{\boldsymbol{n}} \times \int_\Gamma \frac{e^{-jkR}}{4\pi R} \boldsymbol{f}_n(\boldsymbol{r'}) ds'\right) ds \\ &\quad + \frac{1}{jk}\eta \int_\Gamma \left(\hat{\boldsymbol{n}} \times \boldsymbol{f}_m(\boldsymbol{r})\right) \cdot \left(\hat{\boldsymbol{n}} \times p.v. \int_\Gamma \nabla \frac{e^{-jkR}}{4\pi R} \nabla' \cdot \boldsymbol{f}_n(\boldsymbol{r'}) ds'\right) ds \\ &= -jk\eta \int_\Gamma \boldsymbol{f}_m(\boldsymbol{r}) \cdot \int_\Gamma \frac{e^{-jkR}}{4\pi R} \boldsymbol{f}_n(\boldsymbol{r'}) ds\, ds' \\ &\quad - \frac{1}{jk}\eta \int_\Gamma \int_\Gamma \left(\nabla \cdot \boldsymbol{f}_m(\boldsymbol{r})\right) \frac{e^{-jkR}}{4\pi R} \left(\nabla' \cdot \boldsymbol{f}_n(\boldsymbol{r'})\right) ds\, ds'. \end{aligned} \tag{2.11}$$

Thanks to the regularity of $\hat{\boldsymbol{n}} \times \boldsymbol{f}_m(\boldsymbol{r})$, the gradient can be transferred onto the testing function. The function is said to be curl-conforming, i.e., it is sufficiently regular for its surface curl to exist.

The RWG functions can be generalized to higher order: the resulting functions are known as the Graglia-Wilton-Peterson or GWP functions [5]. First, these functions provide a higher order approximation of the current. Second, they can be applied to curvilinear elements, allowing a better geometrical representation of curved scatterers.

Similar basis functions can be constructed for other types of cells, e.g. quadrilaterals. More information can be found in [6] and references therein.

Although much accuracy (and/or efficiency) can be gained by using higher order basis functions, these schemes are significantly more complicated to implement than the relatively simple RWG discretization. Therefore, the RWG scheme is the standard choice unless there is a specific demand for highly accurate results.

2.2.3 Computation of Interaction Elements

The interaction elements (2.11) are composed of four-dimensional integrals over pairs of triangles. Standard techniques such as Gaussian quadrature rules are insufficient for their numerical evaluation, due to the singularity of the integrand. One approach to overcome this, is to split the integral into a singular part which can be evaluated analytically, and a nonsingular part which can be evaluated numerically. This is the singularity extraction method – see e.g. [7]–[9].

An alternative is the singularity cancellation method, in which coordinate transforms are used in such a way that the Jacobian and the singularity cancel out. The inner two-dimensional integral is then performed analytically, and the outer two-dimensional integral numerically. See e.g. [10], [11] for details.

Recently, even more sophisticated computation methods have been proposed, e.g. [12]–[15]. The aim of these methods is to further increase the accuracy of the interaction elements, ideally up to machine precision, without sacrificing efficiency.

2.2.4 Efficient Solution of the Discrete System

Once the interaction matrix $\mathbf{Z}$ and the right hand side e^i have been computed, the system (2.4) needs to be solved. This is a computationally expensive operation: standard techniques such as Gaussian elimination or LU decomposition require $\mathcal{O}(N_S^3)$ operations, which severely limits the size of the largest feasible simulations.

Iterative Krylov subspace methods, such as the conjugate gradient method [16], can be used to reduce the complexity. At each iteration, these methods compute a new approximate solution that, ideally, converges to the exact solution. Under certain conditions on the system matrix, the number of iterations N_i needed to achieve a predefined level of precision ϵ is dependent on the condition number κ of the system matrix $\mathbf{Z}$. For a well-conditioned positive definite system matrix, an accurate solution can be obtained within $N_i \ll N_s$ iterations.

The most expensive step in each iteration is the multiplication of the matrix $\mathbf{Z}$ with a vector x. If $\mathbf{Z}$ is dense, this results in a total complexity of $\mathcal{O}\left(N_i N_S^2\right)$. If the condition number of the system is bounded for large N_S, the number of iterations N_i required by the iterative solution method is also bounded. In this case, the complexity is effectively $\mathcal{O}\left(N_S^2\right)$.

For large numbers of unknowns, the matrix-vector product can be accelerated using different techniques. In particular, the interactions between spatially well-separated groups of basis and testing functions can be computed more efficiently using the multilevel fast multipole algorithm (MLFMA). The complexity of a matrix-vector product accelerated with this algorithm is $\mathcal{O}(N_S \log N_S)$ [17]. Alternatively, the adaptive integration method (AIM) can be used, leading

to a complexity of $\mathcal{O}\left(N_S^{3/2}\log N_S\right)$ for general surface scatterers [18], and $\mathcal{O}\left(N_S \log N_S\right)$ for planar geometries [19].

Ideally, combining iterative solution methods with fast techniques such as the MLFMA results in quasi-linear complexity. This enables a single workstation to solve problems involving hundreds of thousands of unknowns. However, at some point, EFIE simulations become unfeasible due to either memory or time limitations. Parallel implementations on computer clusters can then be used. Distributing the work load over multiple computational nodes and balancing the communication between them is in itself a challenging task. If done correctly, however, it results in a scalable parallel algorithm: the number of computational nodes required to perform a certain EFIE simulation depends quasi-linearly on the number of unknowns [20].

The performance of this algorithm depends on the condition number κ of the system matrix for two reasons. First, the interaction elements and the right hand side can only be computed up to finite relative precision ϵ. This results in a relative error in the solution of order $\kappa\epsilon$ [21]. Second, the number of iterations required by the iterative solution method depends on κ. For these two reasons, it is of utmost important to obtain a well-conditioned system. Unfortunately, the EFIE is notorious for being ill-conditioned.

First, the condition number of the system matrix grows as the mesh density is increased. This dense discretization breakdown can be resolved using suitable preconditioning strategies, as detailed in section 2.2.5.

Second, at low frequencies, the equation decouples into an electrostatic part and a magnetostatic part, which scale differently. This leads to a condition number that grows proportionally to ω^{-2}. Methods to deal with this low frequency breakdown are discussed in section 2.2.6.

Third, when the EFIE is applied to closed scatterers, it is ill-posed at the resonant frequencies of the interior domain. As a result, the system matrix is ill-conditioned near these resonant frequencies. This can be avoided by switching to an equation that does not suffer from internal resonances, such as the CFIE – see section 2.2.7.

2.2.5 Calderón Preconditioning

The EFIE breaks down, i.e., its condition number increases without bound, when the spatial discretization density is increased. This is due to the fact that the singular values of the EFIE operator comprise two branches, one accumulating at zero and the other at infinity [22]. As the mesh density is increased, the eigenfunctions corresponding to larger and smaller eigenvalues can be resolved, leading to an increasingly higher condition number.

The Calderón identity (1.43) however states that for the time domain EFIE

and MFIE operators,

$$\mathcal{T}^2 = -\frac{1}{4} + \mathcal{K}^2. \tag{2.12}$$

The operator $\mathcal{K}$ is compact on smooth surfaces [22], i.e., its eigenvalues accumulate at 0. Therefore, the eigenvalues of $\mathcal{T}^2$ accumulate at $-\frac{1}{4}$. This indicates that a suitable discretization of $\mathcal{T}^2$ remains well-conditioned when the discretization density is increased and more eigenfunctions can be resolved. This conclusion also holds true for the frequency domain EFIE and MFIE operators $\mathcal{T}_k$ and $\mathcal{K}_k$.

The EFIE is now rewritten as

$$\eta \left(\mathcal{T}_k^2 \boldsymbol{J}\right)(\boldsymbol{r}) = -\left(\mathcal{T}_k \left\{\hat{\boldsymbol{n}} \times \boldsymbol{E}^i\right\}\right)(\boldsymbol{r}) \quad \forall \boldsymbol{r} \in \Gamma. \tag{2.13}$$

Discretizing it with RWG functions leads to

$$\mathsf{Z}\mathsf{G}^{-1}\mathsf{Z}\mathsf{j} = -\mathsf{Z}\mathsf{G}^{-1}\mathsf{e}^i \tag{2.14}$$

where the Gram matrix G is defined as

$$[\mathsf{G}]_{mn} = (\hat{\boldsymbol{n}} \times \boldsymbol{f}_m, \boldsymbol{f}_n). \tag{2.15}$$

Unfortunately, this Gram matrix is singular [23].

In order to obtain a well-conditioned equation, it is necessary to use a second set of basis functions $\boldsymbol{g}_m(\boldsymbol{r})$:

$$\mathbb{Z}\mathsf{G}_{\mathrm{mx}}^{-1}\mathsf{Z}\mathsf{j} = -\mathbb{Z}\mathsf{G}_{\mathrm{mx}}^{-1}\mathsf{e}^i \tag{2.16}$$

$$[\mathbb{Z}]_{mn} = (\hat{\boldsymbol{n}} \times \boldsymbol{g}_m, \eta\mathcal{T}_k \boldsymbol{g}_n) \tag{2.17}$$

$$[\mathsf{G}_{\mathrm{mx}}]_{mn} = (\hat{\boldsymbol{n}} \times \boldsymbol{f}_m, \boldsymbol{g}_m). \tag{2.18}$$

The functions $\boldsymbol{g}_m(\boldsymbol{r})$ are chosen such that the overlap matrix G_{mx} is well-conditioned. A common choice is the set of Buffa-Christiansen or BC basis functions [24]. These functions are linear combinations of the RWG functions defined on the barycentric refinement of the triangle mesh. The function $\boldsymbol{g}_m(\boldsymbol{r})$ represents a current flowing along edge e_m of the original mesh (see figure 2.3). It has been reported in e.g. [25] that this approach effectively solves dense discretization breakdown.

2.2.6 Loop-Star Decomposition

In the continuous case, (1.66) shows that for low frequencies, $\mathcal{T}_k \boldsymbol{f}(\boldsymbol{r})$ in general scales proportionally to ω^{-1}. However, if $\boldsymbol{f}(\boldsymbol{r})$ is solenoidal, $\mathcal{T}_k \boldsymbol{f}(\boldsymbol{r})$ scales proportionally to ω.

In the discrete case, a similar property holds. For $\omega \to 0$,

$$(\hat{\boldsymbol{n}} \times \boldsymbol{a}, \eta\mathcal{T}_k \boldsymbol{b}) \quad = \quad \begin{cases} \mathcal{O}(\omega) & \nabla \cdot \boldsymbol{a} = 0 \text{ and/or } \nabla \cdot \boldsymbol{b} = 0 \\ \mathcal{O}(\omega^{-1}) & \text{otherwise.} \end{cases} \tag{2.19}$$

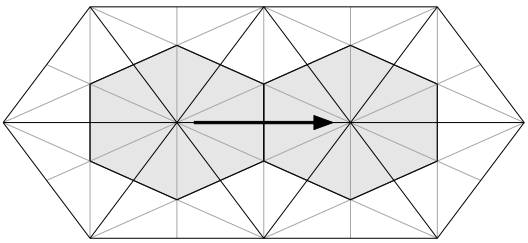

Figure 2.3: A BC function $\boldsymbol{g}_m(\boldsymbol{r})$ is defined on the barycentric refinement of the triangle mesh. It represents a current flowing along edge e_m of the original mesh.

The RWG functions themselves are not solenoidal, but can be combined into functions with zero divergence. More specifically, for a simply connected surface, the space spanned by the N_S RWG functions can be decomposed into the space of RWG loops (figure 2.4) and the space of RWG stars (figure 2.5). The $N_S \times N_V$ RWG (local) loop coefficient matrix (i.e., the matrix whose columns are the RWG expansion coefficients of the (local) loop functions) is given by

$$\Lambda_{m,i} = \begin{cases} 1 & \text{if node } i \text{ equals } \boldsymbol{r}_m^+ \\ -1 & \text{if node } i \text{ equals } \boldsymbol{r}_m^- \\ 0 & \text{otherwise.} \end{cases} \tag{2.20}$$

The matrix Λ has N_V columns, but its rank is $N_V - 1$: there are only $N_V - 1$ linearly independent RWG loops. The $N_S \times N_F$ RWG star coefficient matrix (i.e., the matrix whose columns are the RWG expansion coefficients of the star functions) is given by

$$\Sigma_{m,i} = \begin{cases} 1 & \text{if cell } i \text{ equals } c_m^+ \\ -1 & \text{if cell } i \text{ equals } c_m^- \\ 0 & \text{otherwise.} \end{cases} \tag{2.21}$$

The matrix Σ has N_F columns, but its rank is $N_F - 1$: there are only $N_F - 1$ linearly independent RWG stars.

For multiply connected surfaces with genus g, Euler's formula states that

$$N_S = (N_V - 1) + (N_F - 1) + 2g \tag{2.22}$$

meaning that $2g$ more linearly independent combinations can be constructed: these are the global loops, which span the so-called harmonic space H.

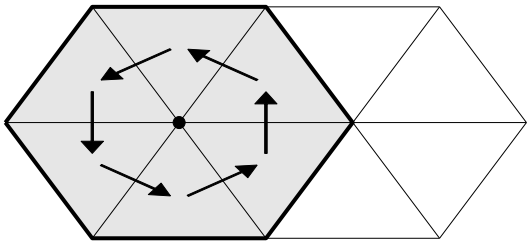

Figure 2.4: An RWG loop.

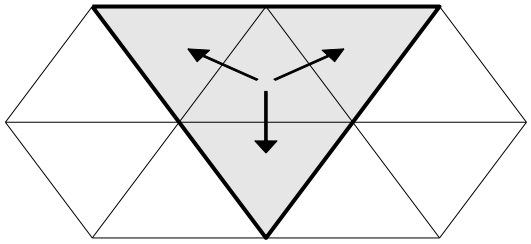

Figure 2.5: An RWG star.

Any combination $\boldsymbol{f}_i^{\Lambda H}$ of global and local loops is solenoidal. Any combination $\boldsymbol{f}_j^{\Sigma}$ of stars has nonzero divergence. Therefore,

$$\left(\hat{\boldsymbol{n}} \times \boldsymbol{f}_i^{\Lambda H}, \mathcal{T}_k \boldsymbol{f}_j^{\Lambda H}\right) = \mathcal{O}(\omega) \tag{2.23}$$

$$\left(\hat{\boldsymbol{n}} \times \boldsymbol{f}_i^{\Sigma}, \mathcal{T}_k \boldsymbol{f}_j^{\Lambda H}\right) = \mathcal{O}(\omega) \tag{2.24}$$

$$\left(\hat{\boldsymbol{n}} \times \boldsymbol{f}_i^{\Lambda H}, \mathcal{T}_k \boldsymbol{f}_j^{\Sigma}\right) = \mathcal{O}(\omega) \tag{2.25}$$

$$\left(\hat{\boldsymbol{n}} \times \boldsymbol{f}_i^{\Sigma}, \mathcal{T} \boldsymbol{f}_j^{\Sigma}\right) = \mathcal{O}(\omega^{-1}). \tag{2.26}$$

In other words, a basis transformation transforms Z into the block matrix form

$$\mathsf{T}^{-1}\mathsf{Z}\mathsf{T} = \begin{pmatrix} \mathcal{O}(\omega) & \mathcal{O}(\omega) \\ \mathcal{O}(\omega) & \mathcal{O}(\omega^{-1}) \end{pmatrix} \tag{2.27}$$

whose condition number grows proportionally to ω^{-2}. As a result, also the condition number of Z itself grows proportionally to ω^{-2}. This is low frequency breakdown.

A possible remedy for this ill-conditioning consists of explicitly switching to the basis of loops and stars, and rescaling the basis and testing functions with appropriate powers of ω or k, see e.g. [26].

One drawback of this approach is that for multiply connected geometries, it requires the detection of global loops. This is a computationally expensive operation. Furthermore, when applied to the Calderón preconditioned EFIE, the matrix G_{mx} becomes ill-conditioned when expressed in the basis of loops and stars [27].

An alternative approach has been suggested in [4], in which the projectors

$$\mathsf{P}^{\Sigma} = \Sigma \left(\Sigma^T \Sigma\right)^+ \Sigma^T \tag{2.28}$$

$$\mathsf{P}^{\Lambda H} = 1 - \mathsf{P}^{\Sigma} \tag{2.29}$$

were introduced (where $\left(\Sigma^T \Sigma\right)^+$ denotes the pseudo-inverse of $\Sigma^T \Sigma$). While computing a pseudo-inverse is in general a computationally expensive operation, it is argued in [27] and [4] that in this particular case, it can be computed in quasi-linear complexity. Furthermore, the matrix Σ is sparse, therefore multiplication with Σ is also $\mathcal{O}(N_S)$. This all leads to the conclusion that $\mathsf{P}^{\Lambda H}$ and P^{Σ} offer access to the loop and star part of an RWG coefficient vector in quasi-linear complexity. By correctly rescaling these components, as has been done in [4], low frequency breakdown can also be solved. This approach is also compatible with Calderón preconditioning.

2.2.7 The FD-MFIE and the FD-CFIE

As an alternative to the FD-EFIE, the FD-MFIE can be used:

$$\left(\mathcal{K}_k \boldsymbol{J}\right)(\boldsymbol{r}) + \frac{1}{2}\boldsymbol{J}(\boldsymbol{r}) = \hat{\boldsymbol{n}} \times \boldsymbol{H}^i(\boldsymbol{r}). \tag{2.30}$$

The FD-MFIE can be solved similarly to the FD-EFIE, although attention must be paid to the correct choice of basis and testing functions. The unknown current is again expanded in RWG functions $\boldsymbol{f}_m(\boldsymbol{r})$. For a general set of testing functions $\boldsymbol{t}_m(\boldsymbol{r})$, the discretized FD-MFIE becomes

$$\left(\frac{1}{2}\mathsf{G}_{\boldsymbol{t},\boldsymbol{f}} + \mathsf{K}\right)\mathsf{j} = \mathsf{h}^i \tag{2.31}$$

with

$$\left[\mathsf{G}_{\boldsymbol{t},\boldsymbol{f}}\right]_{mn} = \left(\boldsymbol{t}_m, \boldsymbol{f}_n\right) \tag{2.32}$$

$$\left[\mathsf{K}\right]_{mn} = \left(\boldsymbol{t}_m, \mathcal{K}_k \boldsymbol{f}_n\right) \tag{2.33}$$

$$\left[\mathsf{h}^i\right]_m = \left(\boldsymbol{t}_m, \hat{\boldsymbol{n}} \times \boldsymbol{h}^i\right). \tag{2.34}$$

If the testing functions are chosen as for the FD-EFIE, $\boldsymbol{t}_m = \hat{\boldsymbol{n}} \times \boldsymbol{f}_m$, the matrix $\mathsf{G}_{\boldsymbol{t},\boldsymbol{f}}$ is singular [23], rendering the discretized FD-MFIE ill-conditioned.

A well-conditioned equation can be obtained by setting $\boldsymbol{t}_m = \boldsymbol{f}_m$. However, results obtained from this scheme are less accurate than those obtained with the FD-EFIE. An alternative approach is to use the rotated BC functions as testing functions: $\boldsymbol{t}_m = \hat{\boldsymbol{n}} \times \boldsymbol{g}_m$. The accuracy of this mixed discretization scheme is comparable to that of the FD-EFIE [28], [29].

The spectrum of the continuous FD-MFIE operator is bounded from above and from below. Therefore, the discretized FD-MFIE does not suffer from dense discretization breakdown. Furthermore, the mixed FD-MFIE remains well-conditioned at low frequencies [30] (although the picture is somewhat complicated for multiply connected geometries [31]). A drawback of the FD-MFIE is that it is, in contrast to the FD-EFIE, only applicable to closed scatterers.

On closed scatterers, both the FD-EFIE and the FD-MFIE become singular at the resonance frequencies of the interior domain [32]. This can be resolved by combining the FD-EFIE and the FD-MFIE into the frequency domain combined field integral equation or FD-CFIE (see equation (1.52)) [33]. Due to the presence of the FD-EFIE operator, the equation is susceptible to low frequency and dense discretization breakdown. Due to the presence of the FD-MFIE operator, care must be taken to correctly discretize the two components [34]. Efforts to develop an accurate and well-conditioned FD-CFIE have been made in, amongst others, [34]–[38].

2.2.8 The FD-PMCHWT and FD-Müller Equations

The discussion up to now has focused on scattering by perfect conductors. Penetrable media can be treated similarly, using either the PMCHWT or the Müller equation.

The frequency domain PMCHWT equation is similar to the FD-EFIE in that the PMCHWT operator has an unbounded spectrum. As a result, it also suffers from dense discretization breakdown. This can again be resolved using a Calderón preconditioner [39]. Furthermore, the PMCHWT equation becomes ill-conditioned for low frequencies [40] and specific choices of material parameters [41].

The frequency domain Müller equation is similar to the FD-MFIE in that its discretization using only RWG functions yields inaccurate results. It has been shown in [29] that accurate results can be obtained using a mixed RWG-BC discretization strategy. Furthermore, the FD-Müller equation does not suffer from dense discretization breakdown [29]. Its low frequency stability has been demonstrated in [42] – albeit only for simply connected geometries.

2.3 The TD-EFIE

2.3.1 Spatial Discretization of the TD-EFIE

Consider the TD-EFIE (1.49):

$$\eta\left(\mathcal{T}\boldsymbol{j}\right)(\boldsymbol{r},t) = -\hat{\boldsymbol{n}}\times\boldsymbol{e}^{i}(\boldsymbol{r},t). \tag{2.35}$$

The spatial discretization of this equation can be done just as in the frequency domain, using RWG functions:

$$\boldsymbol{j}(\boldsymbol{r},t) = \sum_{m=1}^{N_S} \mathsf{j}_m(t)\boldsymbol{f}_m(\boldsymbol{r}) \tag{2.36}$$

$$\left(\mathcal{Z}\mathsf{j}\right)(t) = -\mathsf{e}(t). \tag{2.37}$$

The time dependent vector $\mathsf{j}(t)$ contains the RWG expansion coefficients of the current at all times t. The operator $\mathcal{Z}$ maps this vector onto the RWG testing coefficients of the TD-EFIE operator:

$$\left[\left(\mathcal{Z}\mathsf{j}\right)(t)\right]_n = \sum_{m=1}^{N_S}\left(\hat{\boldsymbol{n}}\times\boldsymbol{f}_n(\boldsymbol{r}), \eta\mathcal{T}\left\{\mathsf{j}_m(t)\boldsymbol{f}_m(\boldsymbol{r})\right\}\right). \tag{2.38}$$

Finally,

$$\left[\mathsf{e}(t)\right]_m = \left(\hat{\boldsymbol{n}}\times\boldsymbol{f}_n(\boldsymbol{r}), \hat{\boldsymbol{n}}\times\boldsymbol{e}^{i}(\boldsymbol{r},t)\right). \tag{2.39}$$

Equation (2.37) is discrete in space, but continuous in time. In order to construct a numerical solution to the TD-EFIE, (2.37) must be discretized in time.

2.3.2 Temporal Petrov-Galerkin Discretization of the TD-EFIE

In this thesis, the TD-EFIE and other TD-BIEs are temporally discretized in time using Petrov-Galerkin (PG) methods. In these methods, the unknown current is approximated by an expansion in a general family of expansion functions $T_i(t)$:

$$\boldsymbol{j}(\boldsymbol{r},t) = \sum_{m=1}^{N_S}\sum_{i}\mathsf{j}_{m,i}\; T_i(t)\;\boldsymbol{f}_m(\boldsymbol{r}). \tag{2.40}$$

The TD-EFIE is then weakly enforced by testing (2.37) (or its temporal derivative) with a set of temporal testing functions $U_j(t)$ (not necessarily equal to $T_i(t)$):

$$\int_{\mathbb{R}} U_j(t)\left[\text{Equation (2.37)}\right](t)\; dt \tag{2.41}$$

$$\text{- or -}\quad \int_{\mathbb{R}} U_j(t)\partial_t\left[\text{Equation (2.37)}\right](t)\; dt. \tag{2.42}$$

This results in a set of discrete linear equations. Depending on the choice of basis and testing functions, numerical solution schemes with different properties can be constructed. Three different possibilities are now explored.

Frequency Domain EFIE

If the electromagnetic fields are periodic in time, with period P, the current can be represented by a Fourier series:

$$\boldsymbol{j}(\boldsymbol{r},t) = \sum_{m=1}^{N_S} \sum_{k=-\infty}^{+\infty} \mathsf{j}_{m,k}\ e^{jt\frac{2\pi k}{P}}\ \boldsymbol{f}_m(\boldsymbol{r}) \tag{2.43}$$

i.e., $T_k(t) = e^{jt\frac{2\pi k}{P}}$. If the testing functions are chosen as $U_k(t) = e^{-jt\frac{2\pi k}{P}}$, the Petrov-Galerkin equations (2.41) (or (2.42)) yield nothing but the frequency domain EFIE evaluated at angular frequencies $\omega_k = 2\pi k/P$, $k \in \mathbb{Z}$. This particular choice of basis and testing functions results in a block diagonal system: the problems corresponding to different values of ω_k are independent.

Marching-on-in-Degree

For transient problems, the electromagnetic fields can be assumed to decay exponentially. This can be imposed by setting

$$\boldsymbol{j}(\boldsymbol{r},t) = \sum_{m=1}^{N_S} \sum_{i=0}^{+\infty} \mathsf{j}_{m,i}\ e^{-st/2} L_i(st)\ \boldsymbol{f}_m(\boldsymbol{r}) \tag{2.44}$$

$$T_i(t) = e^{-st/2} L_i(st) \quad i = 0, 1, 2, ... \tag{2.45}$$

where $L_i(t)$ is the Laguerre polynomial of degree i, and s is a temporal scaling factor. Setting $U_i(t) = T_i(t)$ results in a system of equations that allows the computation of $\mathsf{j}_{m,i}$ from $\mathsf{j}_{m,i-1}$, $\mathsf{j}_{m,i-2}$, ... This is the marching-on-in-order (MOO) or marching-on-in-degree (MOD) method [43]. This choice of basis and testing functions results in a block triangular system: the problem corresponding to a certain order i depends on the solution of the lower order problems, but not on that of the higher order problems.

Marching-on-in-Time

Assume that the current is expanded in a set of shifted basis functions $T_i(t) = T(t - i\Delta t)$, with $T(t) = 0\ \forall t < -\Delta t$:

$$\boldsymbol{j}(\boldsymbol{r},t) = \sum_{m=1}^{N_S} \sum_{i} \mathsf{j}_{m,i}\ T(t - i\Delta t)\ \boldsymbol{f}_m(\boldsymbol{r}). \tag{2.46}$$

The TD-EFIE is tested with a set of shifted testing functions $U_i(t) = U(t - i\Delta t)$, with $U(t) = 0\ \forall t > 0$. Due to causality and time invariance,

$$\int_{\mathbb{R}} U_j(t)\,(\mathcal{Z}\mathsf{j})\,(t)\ dt = \sum_{i=1}^{j} \mathsf{Z}_{j-i}\mathsf{j}_i \tag{2.47}$$

with

$$[\mathsf{Z}_j]_{nm} = \int_{\mathbb{R}} U(t-j\Delta t)\,(\hat{\boldsymbol{n}}\times\boldsymbol{f}_n(\boldsymbol{r}),\eta\mathcal{T}\{T(t)\boldsymbol{f}_m(\boldsymbol{r})\})\,dt \tag{2.48}$$

$$= (\hat{\boldsymbol{n}}\times\boldsymbol{f}_n(\boldsymbol{r}),\eta\mathcal{T}\{\xi(t)\boldsymbol{f}_m(\boldsymbol{r})\})|_{t=j\Delta t} \tag{2.49}$$

$$\xi(t) = \int_{\mathbb{R}} U(\tau)T(t+\tau)d\tau \tag{2.50}$$

and similarly for the time-differentiated scheme (2.42). As such, (2.37) becomes

$$\begin{pmatrix} \mathsf{Z}_0 & 0 & 0 & 0 & \cdots \\ \mathsf{Z}_1 & \mathsf{Z}_0 & 0 & 0 & \cdots \\ \mathsf{Z}_2 & \mathsf{Z}_1 & \mathsf{Z}_0 & 0 & \cdots \\ \cdots & \cdots & \cdots & \cdots & \cdots \end{pmatrix} \begin{pmatrix} \mathsf{j}_1 \\ \mathsf{j}_2 \\ \mathsf{j}_3 \\ \cdots \end{pmatrix} = - \begin{pmatrix} \mathsf{e}_1 \\ \mathsf{e}_2 \\ \mathsf{e}_3 \\ \cdots \end{pmatrix} \tag{2.51}$$

with

$$[\mathsf{j}_i]_m = \mathsf{j}_{m,i} \tag{2.52}$$

$$[\mathsf{e}_j]_n = \int_{\mathbb{R}} U(t-j\Delta t)\left(\hat{\boldsymbol{n}}\times\boldsymbol{f}_n(\boldsymbol{r}),\hat{\boldsymbol{n}}\times\boldsymbol{e}^i(\boldsymbol{r},t)\right)dt. \tag{2.53}$$

The system (2.51) is again block triangular: the problem corresponding to a certain value of j only depends on the solution of the previous problems. Therefore, it can be solved by forward substitution:

$$-\mathsf{Z}_0\mathsf{j}_j = \sum_{i=1}^{j} \mathsf{Z}_i\mathsf{j}_{j-i} + \mathsf{e}_j. \tag{2.54}$$

Equation (2.54) is the marching-on-in-time (MOT) equation.

The MOT algorithm is often applied with $U(t) = \delta(t)$, the Dirac delta distribution. Equation (2.54) is then nothing but the evaluation of (2.37) at $t = j\Delta t$. This approach is termed collocation-in-time. In this thesis, however, more general choices will be considered.

It is often claimed that general temporal Galerkin methods are inherently more difficult to implement than collocation methods, due to the additional temporal integral. However, (2.49) implies that the interaction matrices Z_j of a scheme with basis functions $T(t-i\Delta t)$ and testing functions $U(t-j\Delta t)$ are identical to those of a collocation scheme with basis functions $\xi(t-i\Delta t)$. In the following chapters, this property will be used to simplify many calculations.

2.3.3 Stability of the MOT Scheme

The MOT algorithm has first been developed in 1968 [44], and has long held a reputation of being unstable. One factor contributing to this instability has been the choice of basis and testing functions. Even if all computations could be carried out with extremely high accuracy, some choices would lead to stable simulations whereas other would not. Examples of a stable and an unstable simulation are shown in figure 2.6.

A limited number of theoretical results exist on the stability of MOT schemes [45], [46]. Some schemes can be derived from a coercive variational formulation of the scattering problem. If the energy of the approximate solution can be proven to be bounded by the energy of the exact solution, the scheme is theoretically stable. These results offer valuable theoretical insight, but are only available for a limited number of BIEs, and have mainly been applied to acoustic wave problems.

In this thesis, a more ad-hoc approach is taken. A number of schemes have shown in practice to be stable for a wide range of geometries and time step sizes. Even though no rigorous proof has been given for their stability, they will serve as a starting point for most of the work presented in the following chapters.

For any given time step size Δt, define the following temporal basis and testing functions (figure 2.7):

$$\delta(t) \quad = \quad \text{the Dirac delta distribution} \tag{2.55}$$

$$p(t) \quad = \quad \begin{cases} 1 & -\Delta t < t < 0 \\ 0 & \text{otherwise} \end{cases} \tag{2.56}$$

$$h(t) \quad = \quad \begin{cases} 1 + \frac{t}{\Delta t} & -\Delta t < t < 0 \\ 1 - \frac{t}{\Delta t} & 0 \leq t < \Delta t \\ 0 & \text{otherwise} \end{cases} \tag{2.57}$$

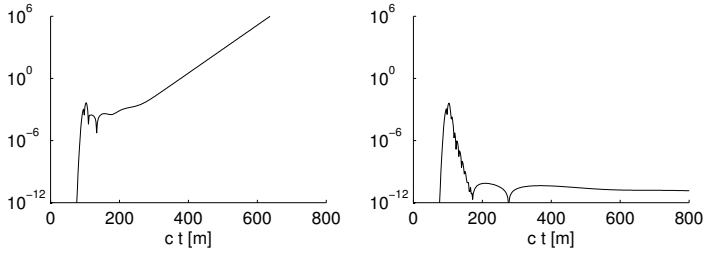

Figure 2.6: The current expansion coefficient $j_1(t)$ obtained from an unstable MOT scheme (left), and obtained from a stable MOT scheme (right).

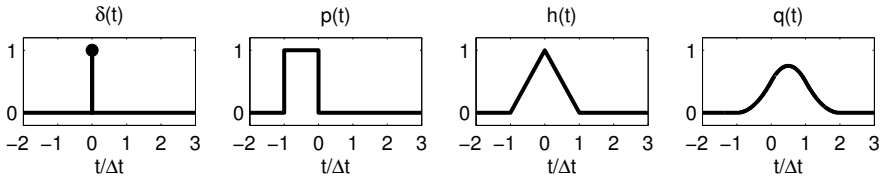

Figure 2.7: Functions used for the temporal discretization of the TD-EFIE.

$$q(t) \quad = \quad \begin{cases} \frac{1}{2}\left(\frac{t}{\Delta t}+1\right)^2 & -\Delta t < t < 0 \\ \frac{1}{2} - \frac{t^2}{\Delta t^2} + \frac{t}{\Delta t} & 0 < t < \Delta t \\ \frac{1}{2}\left(\frac{t}{\Delta t}-2\right)^2 & \Delta t < t < 2\Delta t \\ 0 & \text{otherwise.} \end{cases} \tag{2.58}$$

These functions have the following properties:

$$\frac{1}{\Delta t}\int_{\mathbb{R}} p(\tau)p(t+\tau)d\tau \quad = \quad \int_{\mathbb{R}} \delta(\tau)h(t+\tau)d\tau = h(t) \tag{2.59}$$

$$\frac{1}{\Delta t}\int_{\mathbb{R}} p(\tau)h(t+\tau)d\tau \quad = \quad \int_{\mathbb{R}} \delta(\tau)q(t+\tau)d\tau = q(t). \tag{2.60}$$

All of these functions are infinitely differentiable on each open interval $k\Delta t < t < (k+1)\Delta t$, for $k \in \mathbb{Z}$. The function $q(t)$ is continuously differentiable on the entire time axis ($C^1(\mathbb{R})$), while $h(t)$ is continuous on the entire time axis ($C^0(\mathbb{R})$). Additionally,

$$\partial_t p(t) \quad = \quad \frac{1}{\Delta t}\left(\delta(t+\Delta t) - \delta(t)\right) \tag{2.61}$$

$$\partial_t h(t) \quad = \quad \frac{1}{\Delta t}\left(p(t) - p(t-\Delta t)\right) \tag{2.62}$$

$$\partial_t q(t) \quad = \quad \frac{1}{\Delta t}\left(h(t) - h(t-\Delta t)\right). \tag{2.63}$$

On the condition that all numerical integrals can be performed with sufficiently high accuracy, the following schemes have been found to yield stable MOT schemes regardless of the chosen time step and geometrical discretization:

	Testing Scheme	**Testing function** $U_j(t)$	**Basis function** $T_i(t)$
1a	$\int_{\mathbb{R}} U(t)\partial_t \mathcal{T}\{...\}\,dt$	$\delta(t-j\Delta t)$	$q(t-i\Delta t)$
1b	$\int_{\mathbb{R}} U(t)\partial_t \mathcal{T}\{...\}\,dt$	$p(t-j\Delta t)$	$h(t-i\Delta t)$
2a	$\int_{\mathbb{R}} U(t)\mathcal{T}\{...\}\,dt$	$\delta(t-j\Delta t)$	$h(t-i\Delta t)$
2b	$\int_{\mathbb{R}} U(t)\mathcal{T}\{...\}\,dt$	$p(t-j\Delta t)$	$p(t-i\Delta t)$

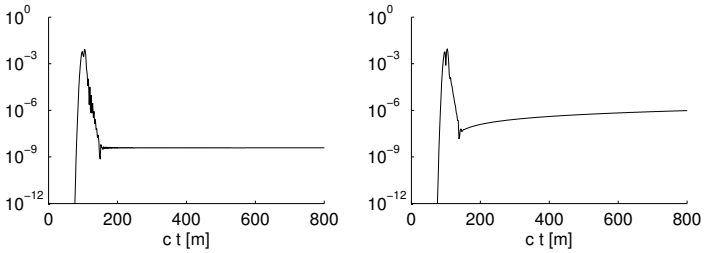

Figure 2.8: The current expansion coefficient $\mathrm{j}_1(t)$ obtained from a MOT scheme that supports constant-in-time spurious currents (left), and from a MOT scheme that supports linear-in-time spurious currents (right).

The schemes 1a and 1b result in identical interaction matrix elements due to (2.60). However, the right hand side as well as the interpretation of the unknowns are different. The same holds for schemes 2a and 2b, due to (2.59). Furthermore,

$$\int_{\mathbb{R}} \delta(t - i\Delta t)x(t)dt = \sum_{j=-\infty}^{i} \int_{\mathbb{R}} p(t - j\Delta t)\partial_t x(t)dt \tag{2.64}$$

which relates 1b to 2a. Nevertheless, these schemes differ on two important points.

First, schemes 2a and 2b require the computation of a temporal integral, whereas 1a and 1b do not. As a result, the number of nonzero matrices $\mathbf{Z}_i$ is finite in schemes 1a and 1b, but infinite in 2a and 2b. In practice, this technical complication is solved by introducing an additional variable for the integrated current, see section 2.3.5.

Second, it was noted in section 1.2.9 that the operator $\mathcal{T}$ has a null space consisting of contant-in-time solenoidal currents. Moreover, the operator $\partial_t\mathcal{T}$ has a null space consisting of both contant-in-time and linear-in-time solenoidal currents. As a result, schemes 2a and 2b allow for constant-in-time regime solutions (see figure 2.8, left), whereas schemes 1a and 1b allow for both constant-in-time and linear-in-time regime solutions (see figure 2.8, right).

It was noted in section 2.2.2 that for frequency domain simulations, the use of higher order spatial basis functions can increase the accuracy of the numerical solution. Similarly, it is possible to use higher order temporal basis functions. Chapter 3 introduces a higher order extension of scheme 1b. In [47], a higher order extension to scheme 2b is presented. The scheme developed in [48] can be regarded as a higher order extension of scheme 2a.

2.3.4 Stability and Null Spaces

The MOT system (2.54) can be written as

$$\begin{pmatrix} \mathsf{j}_j \\ \mathsf{j}_{j-1} \\ \mathsf{j}_{j-2} \\ \cdots \end{pmatrix} = \mathbf{Z}_c \begin{pmatrix} \mathsf{j}_{j-1} \\ \mathsf{j}_{j-2} \\ \mathsf{j}_{j-3} \\ \cdots \end{pmatrix} - \begin{pmatrix} \mathbf{Z}_0^{-1}\mathsf{e}_j \\ 0 \\ 0 \\ \cdots \end{pmatrix} \tag{2.65}$$

where the companion matrix $\mathbf{Z}_c$ is defined as

$$\mathbf{Z}_c = \begin{pmatrix} -\mathbf{Z}_0^{-1}\mathbf{Z}_1 & -\mathbf{Z}_0^{-1}\mathbf{Z}_2 & -\mathbf{Z}_0^{-1}\mathbf{Z}_3 & \cdots \\ \mathbf{1} & \mathbf{0} & \mathbf{0} & \cdots \\ \mathbf{0} & \mathbf{1} & \mathbf{0} & \cdots \\ \mathbf{0} & \mathbf{0} & \mathbf{1} & \cdots \\ \cdots & \cdots & \cdots & \cdots \end{pmatrix}. \tag{2.66}$$

The stability of the MOT algorithm is determined by the polynomial eigenvalues λ_i of $\mathbf{Z}_c$. If any of the eigenvalues is located outside the unit circle ($\exists\lambda_i : |\lambda_i| > 1$), the current will grow exponentially, rendering the simulation unstable. This is shown in figure 2.9, left. If all eigenvalues are located inside the unit circle ($\forall\lambda_i : |\lambda_i| < 1$), the current will decay exponentially, and the simulation will remain stable (figure 2.9, right). If there are poles on the unit circle ($\exists\lambda_i : |\lambda_i| = 1$), the current will grow at most polynomially (figure 2.9, middle).

Poles that are equal to 1 represent static regime solutions. To gain more insight into these solutions, consider the schemes 1a or 1b, which have only a finite number $N_m + 1$ of nonzero interaction matrices $\mathbf{Z}_i$. A current which is constant in time,

$$\mathsf{j}_i = \mathsf{j}_1 \tag{2.67}$$

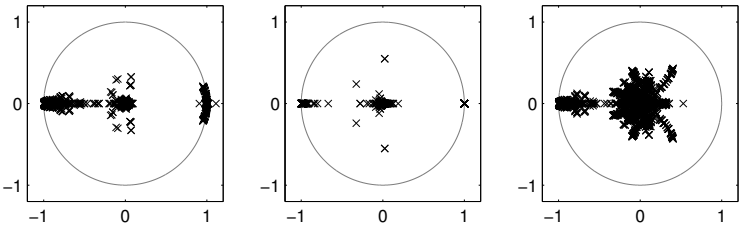

Figure 2.9: Polynomial eigenvalue distributions of $\mathbf{Z}_c$, obtained with different MOT schemes. The eigenvalues can be located both inside and outside the unit circle (left), inside or on the unit circle (middle), or strictly inside the unit circle (right).

is a regime solution of the sourceless equation if

$$\sum_{i=0}^{N_m} \mathbf{Z}_i \mathsf{j}_{j-i} = \left(\sum_{i=0}^{N_m} \mathbf{Z}_i \right) \mathsf{j}_1 = 0. \tag{2.68}$$

A current which is linear in time,

$$\mathsf{j}_i = i \cdot \mathsf{j}_1 \tag{2.69}$$

is a regime solution if

$$\sum_{i=0}^{N_m} \mathbf{Z}_i \mathsf{j}_{j-i} = \left(\sum_{i=0}^{N_m} \mathbf{Z}_i (N_m - i) \right) \mathsf{j}_1 = 0. \tag{2.70}$$

Therefore, the constant and linear eigenfunctions reside in the null space of

$$\mathbf{Z}_{\text{const}} = \sum_{i=0}^{N_m} \mathbf{Z}_i \tag{2.71}$$

$$\mathbf{Z}_{\text{lin}} = \sum_{i=0}^{N_m} \mathbf{Z}_i (N_m - i) \tag{2.72}$$

respectively, and can be obtained from an eigenvalue or singular value analysis.

Together, the matrices $\mathbf{Z}_c$, $\mathbf{Z}_{\text{const}}$ and $\mathbf{Z}_{\text{lin}}$ provide valuable information about the behavior of the MOT schemes 1a and 1b. For the schemes 2a and 2b, these techniques cannot be applied directly due to the infinite number of nonzero interaction matrices. This is only a technical complication, which will be dealt with in section 2.3.5.

2.3.5 Dealing with the Charge Accumulation

In section 2.3.3, it was noted that schemes 2a and 2b require the computation of a temporal integral, resulting in an infinite number of nonzero $\mathbf{Z}$ matrices. In practice, this is resolved by introducing an additional unknown for the integral of the current.

As mentioned in section 2.3.3, the interaction matrices of these two schemes are identical. Therefore, it suffices to consider the scheme 2b, in which the current is expanded as

$$\boldsymbol{j}(\boldsymbol{r}, t) = \sum_{m=1}^{N_S} \sum_i \mathsf{j}_{m,i} \; p(t - i\Delta t) \; \boldsymbol{f}_m(\boldsymbol{r}). \tag{2.73}$$

Its integral can be written as

$$\partial_t^{-1}\boldsymbol{j}(\boldsymbol{r},t) = \sum_{m=1}^{N_S}\sum_i \mathsf{j}_{m,i}^{\text{int}}\; h(t-i\Delta t)\;\boldsymbol{f}_m(\boldsymbol{r}) \tag{2.74}$$

$$\mathsf{j}_{m,i}^{\text{int}} = \Delta t\sum_{j\le i}\mathsf{j}_{m,i} \tag{2.75}$$

$$= \mathsf{j}_{m,i-1}^{\text{int}} + \Delta t\;\mathsf{j}_i^{\text{int}}. \tag{2.76}$$

Then,

$$\mathcal{T}\boldsymbol{j} = \mathcal{T}_s\boldsymbol{j} + (\partial_t\mathcal{T}_h)\left(\partial_t^{-1}\boldsymbol{j}\right) \tag{2.77}$$

and as a result,

$$\sum_{i=0}^{j}\mathsf{Z}_i\;\mathsf{j}_{j-i} = \sum_{i=0}^{j}\mathsf{Z}_i^s\;\mathsf{j}_{j-i} + \sum_{i=0}^{j}\dot{\mathsf{Z}}_i^h\;\mathsf{j}_{j-i}^{\text{int}} \tag{2.78}$$

where

$$\left[\mathsf{Z}_j^s\right]_{nm} = \int_{\mathbb{R}} p(t-j\Delta t)\left(\hat{\boldsymbol{n}}\times\boldsymbol{f}_n(\boldsymbol{r}),\eta\mathcal{T}_s\left\{p(t)\boldsymbol{f}_m(\boldsymbol{r})\right\}\right)dt \tag{2.79}$$

$$\left[\dot{\mathsf{Z}}_j^h\right]_{nm} = \int_{\mathbb{R}} p(t-j\Delta t)\left(\hat{\boldsymbol{n}}\times\boldsymbol{f}_n(\boldsymbol{r}),\eta\partial_t\mathcal{T}_h\left\{h(t)\boldsymbol{f}_m(\boldsymbol{r})\right\}\right)dt. \tag{2.80}$$

The number of nonzero matrices Z_j^s and $\dot{\mathsf{Z}}_j^h$ is finite. The MOT equation becomes

$$-\mathsf{Z}_0^s\;\mathsf{j}_j - \dot{\mathsf{Z}}_0^h\;\mathsf{j}_0^{\text{int}} = \sum_{i=1}^{j}\mathsf{Z}_i^s\;\mathsf{j}_{j-i} + \sum_{i=1}^{j}\dot{\mathsf{Z}}_i^h\;\mathsf{j}_{j-i}^{\text{int}} + \mathsf{e}_j \tag{2.81}$$

or with (2.76),

$$-\left(\mathsf{Z}_0^s + \Delta t\dot{\mathsf{Z}}_0^h\right)\mathsf{j}_j = \sum_{i=1}^{j}\mathsf{Z}_i^s\;\mathsf{j}_{j-i} + \sum_{i=1}^{j}\dot{\mathsf{Z}}_i^h\;\mathsf{j}_{j-i}^{\text{int}} + \dot{\mathsf{Z}}_0^h\;\mathsf{j}_{j-1}^{\text{int}} + \mathsf{e}_j. \tag{2.82}$$

The stability of the MOT algorithm $\{(2.82),(2.76)\}$ can now also be investigated using an eigenvalue analysis of a matrix similar to (2.66). Furthermore, the constant and linear regime solutions reside in the null space of

$$\mathsf{Z}_{\text{const}} = \sum_i\mathsf{Z}_i^s + \Delta t\sum_i(N_m-i+1)\dot{\mathsf{Z}}_i^h \tag{2.83}$$

$$\mathsf{Z}_{\text{lin}} = \sum_i(N_m-i+1)\mathsf{Z}_i^s + \Delta t\sum_i\frac{(N_m-i+1)(N_m-i+2)}{2}\dot{\mathsf{Z}}_i^h \tag{2.84}$$

respectively. The derivation of these expressions can be found in section 4.B.

2.3.6 Computation of the Interaction Elements

As was also the case for the FD-EFIE (see section 2.2.3), accurately computing the TD-EFIE interaction elements presents significant difficulties. In particular, the following integrals must be evaluated:

$$I_1 = \int_{\Gamma\times\Gamma} \frac{\boldsymbol{f}_m(\boldsymbol{r})\cdot\boldsymbol{f}_n(\boldsymbol{r'})}{4\pi R}\,\xi(j\Delta t - R/c)\;ds\;ds' \tag{2.85}$$

$$I_2 = \int_{\Gamma\times\Gamma} \frac{(\nabla\cdot\boldsymbol{f}_m(\boldsymbol{r}))\,(\nabla'\cdot\boldsymbol{f}_n(\boldsymbol{r'}))}{4\pi R}\,\xi(j\Delta t - R/c)\;ds\;ds' \tag{2.86}$$

where $\xi(t)$ is a piecewise polynomial. Different techniques for a direct evaluation have been proposed in e.g. [7], [49], [50].

The accurate evaluation of these integrals is not only important for the accuracy of the solution. Errors in the interaction matrices $\mathbf{Z}_j$ influence the eigenvalue spectrum of the companion matrix $\mathbf{Z}_c$ (2.66). As a result, theoretically stable MOT schemes can become unstable due to an inaccurate evaluation of the integrals (2.85)–(2.86). Robustness of stability in the presence of numerical errors is an important property for an algorithm. To date, no mathematical and only a limited amount of experimental results are available on this topic. In chapter 6, it will be shown that this is a crucial issue for the TD-PMCHWT equation.

2.3.7 Efficient Solution of the MOT System

The following approach is used to solve the MOT equation.

At a certain time step j, the right hand side of (2.54) must be computed. This involves a convolution of (sparse) matrices with vectors, which can be performed in $\mathcal{O}(N_S^2)$ operations. Then, the equation is solved for the unknown j_j. If the system matrix is well-conditioned, this can be done in $\mathcal{O}(N_S^2)$ operations using iterative solution methods (see section 2.2.4). Once j_j is known, the MOT algorithm then proceeds to the $(j+1)$th time step. The number of time steps is N_T. The complexity of the full solution method therefore is $\mathcal{O}(N_T N_S^2)$.

As was the case for the FD-EFIE, the most costly operation is the computation of the field generated by $\mathcal{O}(N_S)$ source points, evaluated at $\mathcal{O}(N_S)$ observer points. This can be accelerated using different techniques. The plane wave time domain or PWTD method [51]–[53] is the time domain counterpart of the fast multipole method. The adaptive integration method (AIM) can also be applied in the time domain [18], [54]. Alternatively, the accelerated cartesian expansion (ACE) method [55] can be used.

The efficiency and accuracy of the MOT scheme also hinges on the condition number of the system matrix $\mathbf{Z}_0$. As the TD-EFIE is related to the FD-EFIE through the Fourier transform, it is not surprising that it also suffers from both low frequency breakdown and dense discretization breakdown.

Low frequency breakdown is encountered when the time step Δt is large. It can be resolved by performing an explicit loop-star decomposition, and scaling the components with the correct powers of Δt [56]. As was the case in the frequency domain, this approach would lead to ill-conditioning of the mixed Gram matrix when used in conjunction with Calderón preconditioning, and requires the detection of global loops. In chapter 4, the qHP-TDEFIE is introduced, which is a TD-EFIE formulation that is immune to low frequency breakdown. It is based on the quasi-Helmholtz projectors and hence does not require an explicit loop-star decomposition.

Dense discretization breakdown is again encountered when the spatial discretization is dense, and can be resolved using Calderón preconditioning [57], [58]. Furthermore, by discretizing the operator

$$\mathcal{T}^2 = \mathcal{T}_s\mathcal{T}_s + (\partial_t\mathcal{T}_h)\left(\partial_t^{-1}\mathcal{T}_s\right) + \left(\partial_t^{-1}\mathcal{T}_s\right)(\partial_t\mathcal{T}_h) \tag{2.87}$$

the dottrick TD-EFIE [59] is obtained. This formulation does not require the computation of a charge integral. Additionally, it is immune to DC instability when applied to simply connected geometries, but not when applied to multiply connected geometries [60]. In chapter 5, a Calderón preconditioner is developed for the qHP-TDEFIE. the resulting equation is immune to DC instability, low frequency breakdown and dense discretization breakdown, for both simply and multiply connected geometries.

2.3.8 The TD-PMCHWT and TD-Müller Equations

Transient scattering by penetrable media can be treated using the TD-PMCHWT and the TD-Müller equations. Although conceptually similar to the TD-EFIE and the TD-MFIE, respectively, implementations of these equations are not frequently encountered in literature. A notable exception is [61], where it was noted that obtaining stable MOT systems for the TD-PMCHWT equation has proven more difficult than for the TD-EFIE. Chapter 6 will shed light on this problem, and provide an alternative formulation which results in stable MOT systems. This formulation, termed the qHP-PMCHWT equation, is also free of low frequency breakdown and can be Calderón preconditioned in order to mitigate dense discretization breakdown.

2.3.9 Convolution Quadrature Methods

The most commonly encountered temporal discretization techniques, including collocation methods, can be formulated within the framework of the temporal Petrov-Galerkin (PG) methods described in section 2.3.2. This is also the case for the discretization techniques that will be presented and studied in this work. However, other methods can also be used to discretize TD-BIEs. Especially convolution quadrature (CQ) methods [62], [63] show promising results. These

methods were first applied to the scalar Helmholtz equation in [64], and then to the TD-EFIE in [65]–[68].

The essential feature of CQ is that convolutions such as

$$\boldsymbol{x}(t) = \int_0^t \boldsymbol{f}(\tau)\boldsymbol{j}(t-\tau)d\tau \tag{2.88}$$

are approximated as

$$\boldsymbol{x}(i\Delta t) \approx \sum_{j=0}^{i} \omega_j \boldsymbol{j}((i-j)\Delta t). \tag{2.89}$$

The weights ω_j are here determined by

$$\sum_{j=0}^{\infty} \omega_j \zeta^j = F\left(\frac{P(\zeta)}{\Delta t}\right) \tag{2.90}$$

where $F(s)$ is the Laplace transform of $f(t)$, and $P(\zeta)$ is the product of the generating polynomials of a linear multistep method [69]. In other words, the discretization is done not by selecting appropriate temporal basis and testing functions, but by choosing a linear multistep method. The stability and convergence properties of such methods are mathematically well understood. Also for the convergence and stability of (2.89), theoretical results are available.

Using the CQ method, continuous equations such as

$$\int_0^t \boldsymbol{f}(\tau)\boldsymbol{j}(t-\tau)d\tau = \boldsymbol{g}(t) \tag{2.91}$$

can also be solved using the marching-on-in-time algorithm:

$$-\omega_0 \boldsymbol{j}(i\Delta t) = \sum_{j=1}^{i} \omega_j \boldsymbol{j}((i-j)\Delta t) - \boldsymbol{g}(i\Delta t). \tag{2.92}$$

The CQ method has certain advantages over the PG method. First, its theoretical foundations are better understood. Second, it only requires the Laplace transform of the Green's function, which might be easier to obtain than the time domain Green's function for, e.g., lossy media. On the other hand, the CQ method exhibits dispersion (which can be reduced but not eliminated by employing more accurate multistep methods), whereas the PG method does not. Additionally, the convolution matrices resulting from the CQ method are dense, whereas those obtained from the PG method are, typically, sparse.

The results presented in this thesis are concerned only with MOT systems stemming from temporal PG methods. As such, they are not immediately applicable

to CQ MOT systems. However, issues such as dense discretization breakdown, low frequency breakdown and DC instability originate from the mathematical properties of the continuous TD-BIEs. DC instability was encountered in CQ methods in [65]. It can be expected that also low frequency breakdown and dense discretization breakdown occur in CQ methods, but no research on this has been published to date. It is then reasonable to believe that the techniques developed in this PhD thesis can be adapted to the CQ method, or at least that they can serve as a starting point for further developments in this area.

2.4 Conclusion

In this chapter, the numerical solution of boundary integral equations was discussed. In comparison to other electromagnetic simulation techniques such as the finite difference time domain (FDTD) method or the finite element method (FEM), BIE methods are particularly effective for modeling scattering problems involving large or unbounded homogeneous regions.

In order to successfully implement frequency domain BIE methods, attention must be paid to:

- the correct choice of spatial basis and testing functions,
- the accurate computation of the near interactions,
- the efficient computation of the far interactions (matrix-vector product),
- parallelization,
- using an iterative solver,
- avoiding internal resonances,
- regularization of the low frequency breakdown,
- regularization of the dense discretization breakdown.

The measures required to deal with these issues depend on factors such as the size of the simulation, the desired accuracy, the intended frequency range, etc. For time domain BIE methods, this list is also applicable and must be complemented with

- the correct choice of temporal discretization method,
- DC instability.

This thesis focuses on discretization and preconditioning techniques for a number of boundary integral equations, both in the time domain and in the frequency domain, and their influence on the aforementioned issues.

Part I is concerned with time domain scattering problems involving only perfect conductors. In chapter 3, a set of higher order temporal basis and testing functions is presented and applied to the TD-EFIE, the TD-MFIE and the TD-CFIE. This results in a more accurate representation of the time dependence

of the electromagnetic fields and currents. In chapter 4, the qHP-TDEFIE is introduced, an alternative formulation of the TD-EFIE which is immune to both low frequency breakdown and DC instability. It does suffer from dense discretization breakdown, which can be solved using the Calderón preconditioner derived in chapter 5.

Part II is concerned with scattering problems involving penetrable media, both in the time domain and in the frequency domain. Chapter 6 extends the techniques introduced in chapters 4 and 5 to the time domain PMCHWT equation. In chapter 7, a Calderón preconditioner for the frequency domain chiral PMCHWT equation is presented.

References

[1] S. Sauter and C. Schwab, *Boundary Element Methods*. Springer, 2010, isbn: 3540680926.

[2] R. F. Harrington, *Field Computation by Moment Methods*. Wiley-IEEE Press, 1993, isbn: 0780310144.

[3] S. Rao, D. Wilton, and A. Glisson, "Electromagnetic scattering by surfaces of arbitrary shape", *IEEE Transactions on Antennas and Propagation*, vol. 30, no. 3, pp. 409 –418, May 1982.

[4] F. P. Andriulli, K. Cools, I. Bogaert, and E. Michielssen, "On a well-conditioned electric field integral operator for multiply connected geometries", *IEEE Transactions on Antennas and Propagation*, vol. 61, no. 4, pp. 2077–2087, Apr. 2013.

[5] R. D. Graglia, D. R. Wilton, and A. F. Peterson, "Higher order interpolatory vector bases for computational electromagnetics", *IEEE Transactions on Antennas and Propagation*, vol. 45, no. 3, pp. 329–342, 1997.

[6] A. F. Peterson, "Mapped vector basis functions for electromagnetic integral equations", *Synthesis Lectures on Computational Electromagnetics*, vol. 1, no. 1, pp. 1–124, 2005.

[7] D. R. Wilton, A. Glisson, D. Schaubert, O. Al-Bundak, and C. M. Butler, "Potentials integrals for uniform and linear source distributions on polygonal and polyhedral domains", *IEEE Transactions on Antennas and Propagation*, vol. 32, no. 3, pp. 276–281, 1984.

[8] R. D. Graglia, "On the numerical integration of the linear shape functions times the 3-D Green's function or its gradient on a plane triangle", *IEEE Transactions on Antennas and Propagation*, vol. 41, no. 10, pp. 1448–1455, 1993.

[9] P. Arcioni, M. Bressan, and L. Perregrini, "On the evaluation of the double surface integrals arising in the application of the boundary integral method to 3-D problems", *IEEE Transactions on Microwave Theory and Techniques*, vol. 45, no. 3, pp. 436–439, 1997.

[10] M. A. Khayat and D. R. Wilton, "Numerical evaluation of singular and near-singular potential integrals", *IEEE Transactions on Antennas and Propagation*, vol. 53, no. 10, pp. 3180–3190, 2005.

[11] L. Rossi and P. J. Cullen, "On the fully numerical evaluation of the linear-shape function times the 3D Green's function on a plane triangle", *IEEE Transactions onMicrowave Theory and Techniques*, vol. 47, no. 4, pp. 398–402, 1999.

[12] A. G. Polimeridis, J. M. Tamayo, J. M. Rius, and J. R. Mosig, "Fast and accurate computation of hypersingular integrals in Galerkin surface integral equation formulations via the direct evaluation method", *IEEE Transactions on Antennas and Propagation*, vol. 59, no. 6, pp. 2329–2340, 2011.

[13] A. G. Polimeridis and J. R. Mosig, "Complete semi-analytical treatment of weakly singular integrals on planar triangles via the direct evaluation method", *International Journal for Numerical Methods in Engineering*, vol. 83, no. 12, pp. 1625–1650, 2010.

[14] I. Bogaert, "Analytical computation of impedance integrals with power-law Green's functions", in *2012 International Conference on Electromagnetics in Advanced Applications (ICEAA)*, IEEE, 2012, pp. 117–120.

[15] I. Bogaert, "On the analytical treatment of singular impedance integrals in electromagnetics", in *International Conference on Electromagnetics in Advanced Applications (ICEAA 2013)*, IEEE, 2013, pp. 624–627.

[16] J. R. Shewchuk, *An introduction to the conjugate gradient method without the agonizing pain*, `http://www.cs.cmu.edu/~quake-papers/painless-conjugate-gradient.pdf`, 1994.

[17] W. Chew, E. Michielssen, J. M. Song, and J. M. Jin, Eds., *Fast and Efficient Algorithms in Computational Electromagnetics*. Norwood, MA, USA: Artech House, Inc., 2001, isbn: 1580531520.

[18] E Bleszynski, M Bleszynski, and T Jaroszewicz, "Aim: Adaptive integral method for solving large-scale electromagnetic scattering and radiation problems", *Radio Science*, vol. 31, no. 5, pp. 1225–1251, 1996.

[19] S. S. Bindiganavale, J. L. Volakis, and H. Anastassiu, "Scattering from planar structures containing small features using the adaptive integral method (AIM)", *IEEE Transactions on Antennas and Propagation*, vol. 46, no. 12, pp. 1867–1878, Dec. 1998.

[20] B. Michiels, J. Fostier, I. Bogaert, and D. De Zutter, "Weak scalability analysis of the distributed-memory parallel MLFMA", *IEEE Transactions on Antennas and Propagation*, vol. 61, no. 11, pp. 5567–5574, Nov. 2013.

[21] E Cheney and D. Kincaid, *Numerical mathematics and computing*. Cengage Learning, 2012.

[22] J.-C. Nédélec, *Acoustic and electromagnetic equations: Integral representations for harmonic problems*. Springer Science & Business Media, 2001, vol. 144.

[23] S. H. Christiansen and J.-C. Nédélec, "A preconditioner for the electric field integral equation based on Calderón formulas", *SIAM journal on numerical analysis*, vol. 40, no. 3, pp. 1100–1135, 2002.

[24] A. Buffa and S. H. Christiansen, "A dual finite element complex on the barycentric refinement", *Comptes Rendus Mathematique*, vol. 340, no. 6, pp. 461 –464, 2005.

[25] F. P. Andriulli, K. Cools, H. Bağcı, F. Olyslager, A. Buffa, S. Christiansen, and E. Michielssen, "A multiplicative Calderón preconditioner for the electric field integral equation", *IEEE Transactions on Antennas and Propagation*, vol. 56, no. 8, pp. 2398–2412, Aug. 2008.

[26] J.-S. Zhao and W. C. Chew, "Integral equation solution of Maxwell's equations from zero frequency to microwave frequencies", *IEEE Transactions on Antennas and Propagation*, vol. 48, no. 10, pp. 1635–1645, Oct. 2000.

[27] F. P. Andriulli, "Loop-star and loop-tree decompositions: Analysis and efficient algorithms", *IEEE Transactions on Antennas and Propagation*, vol. 60, no. 5, pp. 2347–2356, May 2012.

[28] K. Cools, F. P. Andriulli, D. De Zutter, and E. Michielssen, "Accurate and conforming mixed discretization of the MFIE", *IEEE Antennas and Wireless Propagation Letters*, vol. 10, pp. 528 –531, Oct. 2011.

[29] S. Yan, J.-M. Jin, and Z. Nie, "Improving the accuracy of the second-kind Fredholm integral equations by using the Buffa-Christiansen functions", *IEEE Transactions on Antennas and Propagation*, vol. 59, no. 4, pp. 1299 –1310, Apr. 2011.

[30] I. Bogaert, K. Cools, F. Andriulli, J. Peeters, and D. De Zutter, "Low frequency stability of the mixed discretization of the MFIE", in *Proceedings of the 5th European Conference on Antennas and Propagation (EuCAP)*, IEEE, 2011, pp. 2463–2465.

[31] I. Bogaert, K. Cools, F. Andriulli, and D. De Zutter, "Low frequency scaling of the mixed MFIE for scatterers with a non-simply connected surface", in *International Conference on Electromagnetics in Advanced Applications (ICEAA)*, IEEE, Sep. 2011, pp. 951–954.

[32] W. C. Chew and J. M. Song, "Gedanken experiments to understand the internal resonance problems of electromagnetic scattering.", *Electromagnetics*, vol. 27, no. 8, pp. 457 –471, 2007.

[33] B. Shanker, A. Ergin, K. Aygun, and E. Michielssen, "Analysis of transient electromagnetic scattering from closed surfaces using a combined field integral equation", *IEEE Transactions on Antennas and Propagation*, vol. 48, no. 7, pp. 1064 –1074, Jul. 2000.

[34] L. Gurel and O. Ergul, "Contamination of the accuracy of the combined-field integral equation with the discretization error of the magnetic-field integral equation", *IEEE Transactions on Antennas and Propagation*, vol. 57, no. 9, pp. 2650 –2657, Sep. 2009.

[35] H. Bağcı, F. P. Andriulli, K. Cools, F. Olyslager, and E. Michielssen, "A calderón multiplicative preconditioner for the combined field integral equation", *IEEE transactions on antennas and propagation*, vol. 57, no. 10, pp. 3387–3392, 2009.

[36] K. Cools, F. Andriulli, P Ylä-Oijala, H Bağci, D. De Zutter, and E Michielssen, "Improving the accuracy of the Calderón preconditioned CFIE by using a mixed discretization", in *2010 IEEE Antennas and Propagation Society International Symposium (APSURSI)*, IEEE, 2010, pp. 1–4.

[37] P. Ylä-Oijala, S. Kiminki, and S. Jä Andrvenpää, "Solving IBC-CFIE with dual basis functions", *IEEE Transactions on Antennas and Propagation*, vol. 58, no. 12, pp. 3997 –4004, Dec. 2010.

[38] F. P. Andriulli, I. Bogaert, K. Cools, and E. Michielssen, "A well-conditioned combined field integral equation based on quasi-Helmholtz projectors", in *2013 International Conference on Electromagnetics in Advanced Applications (ICEAA)*, IEEE, 2013, pp. 644–647.

[39] K. Cools, F. Andriulli, and E. Michielssen, "A Calderón multiplicative preconditioner for the PMCHWT integral equation", *IEEE Transactions on Antennas and Propagation*, vol. 59, no. 12, pp. 4579–4587, Dec. 2011.

[40] S. Chen, W. C. Chew, J. Song, and J.-S. Zhao, "Analysis of low frequency scattering from penetrable scatterers", *IEEE Transactions on Geoscience and Remote Sensing*, vol. 39, no. 4, pp. 726–735, Apr. 2001.

[41] Y. Liu and W. Chew, "Stability of surface integral equation for left-handed materials", *Microwaves, Antennas Propagation, IET*, vol. 1, no. 1, pp. 84–89, Feb. 2007.

[42] P. Yla-Oijala and M. Taskinen, "Well-conditioned Müller formulation for electromagnetic scattering by dielectric objects", *IEEE Transactions on Antennas and Propagation*, vol. 53, no. 10, pp. 3316–3323, Oct. 2005.

[43] Y.-s. Chung, T. K. Sarkar, and B. H. Jung, "Solution of a time-domain magnetic-field integral equation for arbitrarily closed conducting bodies using an unconditionally stable methodology", *Microwave and Optical Technology Letters*, vol. 35, no. 6, pp. 493–499, Jun. 2002.

[44] C. L. Bennett and W. L. Weeks, "A technique for computing approximate electromagnetic impulse response of conducting bodies", PhD thesis, Purdue University, 1968.

[45] I. Terrasse, "Résolution mathématique et numérique des équations de Maxwell instationnaires par une méthode de potentiels retardés", PhD thesis, 1993.

[46] T. Ha-Duong, "On retarded potential boundary integral equations and their discretisation", in *Topics in Computational Wave Propagation*, ser. Lecture Notes in Computational Science and Engineering, M. Ainsworth, P. Davies, D. Duncan, B. Rynne, and P. Martin, Eds., vol. 31, Springer Berlin Heidelberg, 2003, pp. 301–336, isbn: 978-3-642-55483-4.

[47] A. J. Pray, Y. Beghein, N. V. Nair, K. Cools, H. Bağcı, and B. Shanker, "A higher order space-time Galerkin scheme for time domain integral equations", *IEEE Transactions on Antennas and Propagation*, vol. 62, no. 12, pp. 6183–6191, Dec. 2014.

[48] Y. Beghein, K. Cools, and D. De Zutter, "A temporal Galerkin discretization of the charge-current continuity equation", in *2013 International Conference on Electromagnetics in Advanced Applications (ICEAA)*, Sep. 2013, pp. 628–631.

[49] T. Eibert and V. Hansen, "On the calculation of potential integrals for linear source distributions on triangular domains", *IEEE Transactions on Antennas and Propagation*, vol. 43, no. 12, pp. 1499–1502, Dec. 1995.

[50] A. Yucel and A. Ergin, "Exact evaluation of retarded-time potential integrals for the RWG bases", *IEEE Transactions on Antennas and Propagation*, vol. 54, no. 5, pp. 1496 –1502, May 2006.

[51] B. Shanker, A. Ergin, K. Aygun, and E. Michielssen, "Analysis of transient electromagnetic scattering phenomena using a two-level plane wave time-domain algorithm", *IEEE Transactions on Antennas and Propagation*, vol. 48, no. 4, pp. 510 –523, Apr. 2000.

[52] B. Shanker, A. A. Ergin, M. Lu, and E. Michielssen, "Fast analysis of transient electromagnetic scattering phenomena using the multilevel plane wave time domain algorithm", *IEEE Transactions on Antennas and Propagation*, vol. 51, no. 3, pp. 628–641, 2003.

[53] A. A. Ergin, B. Shanker, and E. Michielssen, "The plane-wave time-domain algorithm for the fast analysis of transient wave phenomena", *IEEE Antennas and Propagation Magazine*, vol. 41, no. 4, pp. 39–52, Apr. 1999.

[54] A. E. Yilmaz, J.-M. Jin, and E. Michielssen, "Time domain adaptive integral method for surface integral equations", *IEEE Transactions on Antennas and Propagation*, vol. 52, no. 10, pp. 2692–2708, 2004.

[55] M. Vikram and B. Shanker, "Fast evaluation of time domain fields in sub-wavelength source/observer distributions using accelerated cartesian expansions (ACE)", *Journal of Computational Physics*, vol. 227, no. 2, pp. 1007 –1023, 2007.

[56] N.-W. Chen, K. Aygun, and E. Michielssen, "Integral-equation-based analysis of transient scattering and radiation from conducting bodies at very low frequencies", *IEE Proceedings Microwaves, Antennas and Propagation*, vol. 148, no. 6, pp. 381–387, Dec. 2001.

[57] K. Cools, F. P. Andriulli, F. Olyslager, and E. Michielssen, "Time domain Calderón identities and their application to the integral equation analysis of scattering by PEC objects part I: Preconditioning", *IEEE Transactions on Antennas and Propagation*, vol. 57, no. 8, pp. 2352–2364, Aug. 2009.

[58] F. Valdes, M. Ghaffari-Miab, F. P. Andriulli, K. Cools, J. Kotulski, and E. Michielssen, "High-order Calderón multiplicative preconditioner for time domain electric field integral equations", in *2011 IEEE International Symposium on Antennas and Propagation (APSURSI)*, Jul. 2011, pp. 2362–2362.

[59] F. P. Andriulli, K. Cools, F. Olyslager, and E. Michielssen, "Time domain Calderón identities and their application to the integral equation analysis of scattering by PEC objects part II: Stability", *IEEE Transactions on Antennas and Propagation*, vol. 57, no. 8, pp. 2365–2375, Aug. 2009.

[60] K. Cools, F. P. Andriulli, F. Olyslager, and E. Michielssen, "Nullspaces of MFIE and Calderón preconditioned EFIE operators applied to toroidal surfaces", *IEEE Transactions on Antennas and Propagation*, vol. 57, no. 10, pp. 3205–3215, Oct. 2009.

[61] B. Shanker, M. Lu, J. Yuan, and E. Michielssen, "Time domain integral equation analysis of scattering from composite bodies via exact evaluation of radiation fields", *IEEE Transactions on Antennas and Propagation*, vol. 57, no. 5, pp. 1506 –1520, May 2009.

[62] C. Lubich, "Convolution quadrature and discretized operational calculus. I", *Numerische Mathematik*, vol. 52, no. 2, pp. 129–145, 1988.

[63] C. Lubich, "Convolution quadrature and discretized operational calculus II", *Numerische Mathematik*, vol. 52, no. 4, pp. 413–425, 1988.

[64] C. Lubich, "On the multistep time discretization of linear initial-boundary value problems and their boundary integral equations", *Numerische Mathematik*, vol. 67, no. 3, pp. 365–389, 1994.

[65] X. Wang, R. A. Wildman, D. S. Weile, and P. Monk, "A finite difference delay modeling approach to the discretization of the time domain integral equations of electromagnetics", *IEEE Transactions on Antennas and Propagation*, vol. 56, no. 8, pp. 2442–2452, 2008.

[66] X. Wang and D. S. Weile, "Implicit Runge-Kutta methods for the discretization of time domain integral equations", *IEEE Transactions on Antennas and Propagation*, vol. 59, no. 12, pp. 4651–4663, 2011.

[67] Q Chen, P Monk, X Wang, and D Weile, "Analysis of convolution quadrature applied to the time-domain electric field integral equation", *Communications in Computational Physics*, vol. 11, no. 2, p. 383, 2012.

[68] L. Banjai and M. Schanz, "Wave propagation problems treated with convolution quadrature and bem", in *Fast boundary element methods in engineering and industrial applications*, Springer, 2012, pp. 145–184.

[69] C. Lubich, "Convolution quadrature revisited", *BIT Numerical Mathematics*, vol. 44, no. 3, pp. 503–514, 2004.

Part I

Scattering by Perfect Electric Conductors

In this first part, transient scattering by perfect electric conductors is investigated. In chapter 3, a set of higher order temporal basis and testing functions is presented and applied to the TD-EFIE, the TD-MFIE and the TD-CFIE. In chapter 4, the qHP-TDEFIE is introduced, an alternative formulation of the TD-EFIE which is immune to both low frequency breakdown and DC instability. In chapter 5, the dense discretization breakdown of the qHP-TDEFIE is solved using a Calderón preconditioner.

3

A Space-Time Mixed Galerkin Marching-on-in-Time Scheme for the Time Domain Combined Field Integral Equation

Y. Beghein, K. Cools, H. Bağcı, and D. De Zutter

This chapter is based on an article published in
IEEE Transactions on Antennas and Propagation [1].

★ ★ ★

The time domain combined field integral equation (TD-CFIE), which is constructed from a weighted sum of the time domain electric and magnetic field integral equations (TD-EFIE and TD-MFIE) for analyzing transient scattering from closed perfect electrically conducting bodies, is free from spurious resonances. The standard marching-on-in-time technique for discretizing the TD-CFIE uses Galerkin and collocation schemes in space and time, respectively. Unfortunately, the standard scheme is theoretically not well understood: stability and convergence have been proven for only one class of space-time Galerkin discretizations. Moreover, existing discretization schemes are non-conforming, i.e., the TD-MFIE contribution is tested with divergence-conforming functions instead of curl-conforming functions. We therefore introduce a novel space-time mixed Galerkin

discretization for the TD-CFIE. A family of temporal basis and testing functions with arbitrary order is introduced. It is explained how the corresponding interactions can be computed efficiently by existing collocation-in-time codes. The spatial mixed discretization is made fully conforming and consistent by leveraging both Rao-Wilton-Glisson and Buffa-Christiansen basis functions and by applying the appropriate bi-orthogonalization procedures. The combination of both techniques is essential when high accuracy over a broad frequency band is required.

3.1 Introduction

The time domain electric and magnetic field integral equations (TD-EFIE and TD-MFIE, respectively) belong to the family of retarded potential boundary integral equations (RP-BIEs), which are specifically constructed for analyzing transient scattering from perfect electric conductors (PECs). Both the TD-EFIE and the TD-MFIE are susceptible to resonant instabilities, originating in internal resonances that are regime solutions to these equations. However, the time domain combined field integral equation (TD-CFIE), which is a weighted sum of the TD-EFIE and the TD-MFIE, does not support such regime solutions, and thus is not susceptible to resonant instabilities [2].

The TD-CFIE usually is discretized using the standard marching-on-in-time (MOT) technique, which makes use of Galerkin and collocation schemes in space and time, respectively. First, the current density is approximated by an expansion in spatial and temporal basis functions (usually the Rao-Wilton-Glisson (RWG) functions [3] and the Lagrange interpolators [4], respectively), which is inserted in the TD-CFIE. Next, the resulting equation is tested by a set of spatial testing functions (Galerkin-in-space) and evaluated at equidistant time steps (collocation-in-time). The temporal basis functions fulfil the discrete causality constraint, i.e., upon discretization, the TD-CFIE yields a system that can be solved for the unknown current expansion coefficients at successive time steps.

The solutions to this classically discretized TD-CFIE are free from resonant instabilities, but are often found to be less accurate compared to solutions to the frequency domain EFIE, which is regarded to be the benchmark when it comes to accuracy (away from resonant frequencies). The reasons for this are:

1) Although the classical discretization of the TD-CFIE is a spatial Galerkin scheme, it is a collocation-in-time scheme. This implies that it cannot be expected to benefit from the enhanced accuracy and convergence properties enjoyed by e.g. finite element methods.

2) The classical discretization of the TD-CFIE is spatially non-conforming in that the TD-MFIE contribution is tested by divergence-conforming functions

instead of curl-conforming functions, and therefore yields inaccurate results. This has also been observed for both the frequency domain MFIE and CFIE [5]–[7].

In this chapter, a space-time mixed Galerkin scheme for discretizing the TD-CFIE is introduced. The resulting MOT scheme does not suffer from the problems listed above; it improves on the accuracy of the classical MOT scheme for the TD-CFIE by:

1) Introducing a higher order temporal mixed Galerkin scheme. For any order p, families of basis and testing functions for the temporal discretization of the TD-CFIE are presented. These families fulfil the discrete causality constraint and thus give rise to a discrete system amenable to marching-on-in-time. Numerical results demonstrate that the accuracy of the resulting scheme is superior to that of the classical collocation-in-time schemes.

2) Applying a conforming spatial Galerkin scheme. A conforming mixed discretization of the frequency domain MFIE, leveraging both RWG and Buffa-Christiansen (BC) [8], [9] functions, has been introduced in [5]. It has also been applied to the frequency domain CFIE [6] and the frequency domain Calderón preconditioned CFIE [10]. This scheme is now applied to the TD-MFIE contribution in the TD-CFIE. This renders the discretization of both the TD-EFIE and the TD-MFIE contributions in the TD-CFIE conforming and well-tested. In the earliest implementations of spatially mixed frequency domain CFIEs [6], the RWG-RWG discretized EFIE and BC-RWG discretized MFIE were simply added. This scheme is not consistent, because it adds RWG and BC tested values in the same equation. In [10], this inconsistency has been removed by applying a Calderón preconditioner to the EFIE contribution. Here, consistency in the TD-CFIE is restored by insertion of the appropriate Gram matrices in the TD-MFIE contribution. Numerical results confirm the necessity of this operation.

The scheme introduced here can easily be incorporated in existing MOT solvers, because the required integrations are equivalent to those employed in collocation schemes. For the same reason, the scheme is amenable to acceleration by the PWTD algorithm [11] or the TD-AIM [12].

This chapter is organized as follows. In section 3.2, the standard Galerkin-in-space / collocation-in-time discretization of the TD-CFIE is revisited, and its shortcomings are highlighted.

In section 3.3, the temporal mixed Galerkin discretization is introduced. It is based on a first order temporal Galerkin scheme that was proven to be both stable and convergent for acoustic RP-BIEs [13] and for the TD-EFIE [14]. While this first order scheme is already more accurate than collocation-in-time schemes, its accuracy is still limited by the first order expansion in time. Higher order Galerkin-in-time schemes can be employed to increase the accuracy for a

given value of the time step size. In section 3.3, a general order extension to the first order scheme which also maintains discrete causality is presented.

In section 3.4, the spatial discretization is studied. Specifically, the non-conforming discretization of the TD-MFIE contribution, which deteriorates the accuracy of the TD-CFIE, is replaced by the conforming mixed discretization scheme proposed in [5]. Consistency with the TD-EFIE contribution is restored by insertion of the appropriate Gram matrices.

Finally, numerical results are presented in section 3.5, demonstrating the applicability of the proposed schemes, and providing insight into the gain of accuracy, both on smooth and non-smooth geometries.

3.2 The Time Domain Combined Field Integral Equation

Consider a scattering problem as in section 1.2.9. A PEC body occupies a domain Ω with boundary Γ and exterior normal vector $\hat{\boldsymbol{n}}$. It resides in a background medium with permittivity ϵ and permeability μ. Initially, the electromagnetic fields in the neighbourhood of Ω vanish. For $t > 0$, an incident electromagnetic field $\boldsymbol{e}^i(\boldsymbol{r},t)$, $\boldsymbol{h}^i(\boldsymbol{r},t)$ induces an unknown electric current $\boldsymbol{j}(\boldsymbol{r},t)$ on Γ, which satisfies both the TD-EFIE and the TD-MFIE:

$$-\eta\left(\mathcal{T}\boldsymbol{j}\right)(\boldsymbol{r},t) = \hat{\boldsymbol{n}}\times\boldsymbol{e}^i(\boldsymbol{r},t) \tag{3.1}$$

$$\left(\left\{\frac{1}{2}\mathcal{I}+\mathcal{K}\right\}\boldsymbol{j}\right)(\boldsymbol{r},t) = \hat{\boldsymbol{n}}\times\boldsymbol{h}^i(\boldsymbol{r},t) \tag{3.2}$$

$\forall t > 0$ and $\forall \boldsymbol{r} \in \Gamma$, where

$$\begin{aligned}
\left(\mathcal{T}\boldsymbol{j}\right)(\boldsymbol{r},t) &= \left(\mathcal{T}_s\boldsymbol{j}\right)(\boldsymbol{r},t) + \left(\mathcal{T}_h\boldsymbol{j}\right)(\boldsymbol{r},t)\\
\left(\mathcal{T}_s\boldsymbol{j}\right)(\boldsymbol{r},t) &= -\frac{1}{4\pi c}\hat{\boldsymbol{n}}\times\int_\Gamma \frac{\partial_t\boldsymbol{j}(\boldsymbol{r'},t_r)}{R}ds'\\
\left(\mathcal{T}_h\boldsymbol{j}\right)(\boldsymbol{r},t) &= \frac{c}{4\pi}\hat{\boldsymbol{n}}\times p.v.\int_\Gamma \nabla\frac{\int_0^{t_r}\nabla'\cdot\boldsymbol{j}(\boldsymbol{r'},t')dt'}{R}ds'\\
\left(\mathcal{K}\boldsymbol{j}\right)(\boldsymbol{r},t) &= -\frac{1}{4\pi}\hat{\boldsymbol{n}}\times p.v.\int_\Gamma \nabla\times\frac{\boldsymbol{j}(\boldsymbol{r'},t_r)}{R}ds'
\end{aligned}$$

$\mathcal{I}$ is the identity operator, $c = (\epsilon\mu)^{-1/2}$ is the speed of light in the background medium, $R = |\boldsymbol{r}-\boldsymbol{r'}|$ and $t_r = t - R/c$.

The TD-EFIE (3.1) and the TD-MFIE (3.2) are, however, plagued by spurious resonances [15]. In order to obtain a resonance free equation, the TD-EFIE and

the TD-MFIE are combined into the TD-CFIE as follows [16]:

$$\begin{aligned} -\alpha\eta\hat{\boldsymbol{n}}\times\left(\mathcal{T}\boldsymbol{j}\right)(\boldsymbol{r},t)+\eta\left(1-\alpha\right)\left(\left\{\frac{1}{2}\mathcal{I}+\mathcal{K}\right\}\boldsymbol{j}\right)(\boldsymbol{r},t) \\ =\alpha\hat{\boldsymbol{n}}\times\hat{\boldsymbol{n}}\times\boldsymbol{e}^{i}(\boldsymbol{r},t)+\eta\left(1-\alpha\right)\hat{\boldsymbol{n}}\times\boldsymbol{h}^{i}(\boldsymbol{r},t) \end{aligned} \tag{3.3}$$

where α is a dimensionless weighting parameter ranging from 0 (pure TD-MFIE) to 1 (pure TD-EFIE).

The temporal integration in $\mathcal{T}_h$ complicates the numerical solution of the TD-CFIE, and can be handled as detailed in section 2.3.5. However, here it is eliminated by differentiating the TD-CFIE with respect to time:

$$\begin{aligned} -\alpha\eta\hat{\boldsymbol{n}}\times\left(\dot{\mathcal{T}}\boldsymbol{j}\right)(\boldsymbol{r},t)+\eta\left(1-\alpha\right)\left(\left\{\frac{1}{2}\dot{\mathcal{I}}+\dot{\mathcal{K}}\right\}\boldsymbol{j}\right)(\boldsymbol{r},t) \\ =\alpha\hat{\boldsymbol{n}}\times\hat{\boldsymbol{n}}\times\dot{\boldsymbol{e}}^{i}(\boldsymbol{r},t)+\eta\left(1-\alpha\right)\hat{\boldsymbol{n}}\times\dot{\boldsymbol{h}}^{i}(\boldsymbol{r},t) \end{aligned} \tag{3.4}$$

where the dot on the operators and fields represents temporal differentiation. This equation can easily be discretized by expanding the unknown current $\boldsymbol{j}(\boldsymbol{r},t)$ in a set of N_S spatial basis functions $\boldsymbol{f}_i(\boldsymbol{r})$, and a set of shifted temporal basis functions $T_j(t)=T(t-j\Delta t)$:

$$\boldsymbol{j}(\boldsymbol{r},t)=\sum_{i=1}^{N_S}\sum_{j=1}^{\infty}\mathsf{x}_i^{(j)}\boldsymbol{f}_i(\boldsymbol{r})T_j(t). \tag{3.5}$$

Traditionally, $\boldsymbol{f}_i(\boldsymbol{r})$ are chosen to be the RWG basis functions [3], while $T_j(t)$ are shifted piecewise polynomial Lagrange interpolators of order p (figure 3.1, top panels) [4]. Next, the expansion (3.5) is inserted into the TD-CFIE (3.4). This equation is then spatially tested with the RWG functions $\boldsymbol{f}_i$, and evaluated at N_T subsequent time steps $t=k\Delta t$, $k=1,2,...,N_T$. Due to time translation symmetry, this results in the following system of equations:

$$\mathsf{Z}^{(0)}\mathsf{x}^{(j)}=\mathsf{v}^{(j)}-\sum_{i=0}^{j-1}\mathsf{Z}^{(j-i)}\mathsf{x}^{(i)} \tag{3.6}$$

where

$$\begin{aligned} \mathsf{v}_m^{(j)} &= -\alpha\left(\hat{\boldsymbol{n}}\times\boldsymbol{f}_m,\hat{\boldsymbol{n}}\times\dot{\boldsymbol{e}}^{i}\right)_{t=j\Delta t}+\eta\left(1-\alpha\right)\left(\boldsymbol{f}_m,\hat{\boldsymbol{n}}\times\dot{\boldsymbol{h}}^{i}\right)_{t=j\Delta t} \\ \mathsf{Z}_{mn}^{(j)} &= \alpha\eta\left(\hat{\boldsymbol{n}}\times\boldsymbol{f}_m,\dot{\mathcal{T}}\left[\boldsymbol{f}_n T\right]\right)_{t=j\Delta t}+ \\ &\quad \eta\left(1-\alpha\right)\left(\boldsymbol{f}_m,\left\{\frac{1}{2}\dot{\mathcal{I}}+\dot{\mathcal{K}}\right\}\left[\boldsymbol{f}_n T\right]\right)_{t=j\Delta t} \\ \left(\boldsymbol{a},\boldsymbol{b}\right)_{t=j\Delta t} &= \left[\int_{\Gamma}\boldsymbol{a}(\boldsymbol{r},t)\cdot\boldsymbol{b}(\boldsymbol{r},t)\;ds\right]_{t=j\Delta t}. \end{aligned}$$

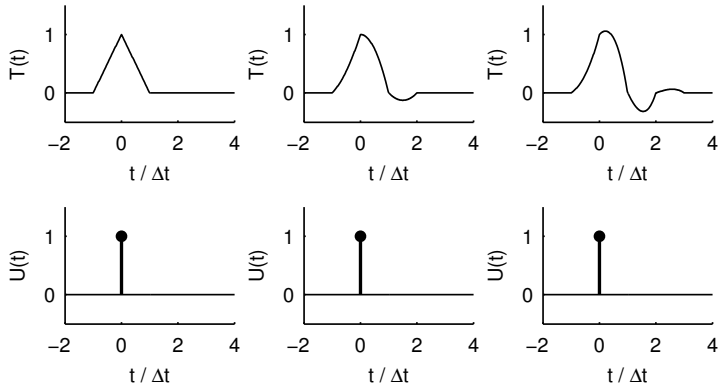

Figure 3.1: Top: first (left), second (middle) and third (right) degree piecewise polynomial Lagrange interpolators. Bottom: the collocation-in-time method is equivalent to the space-time mixed Galerkin method with $U(t) = \delta(t)$.

The system (3.6) is causal: for every time step j, the right hand side only depends on $\mathsf{x}^{(i)}$, $i < j$. It can therefore be solved successively for $\mathsf{x}^{(j)}$, $j = 1, 2, 3, ..., N_T$, yielding the samples of the current $\boldsymbol{j}(\boldsymbol{r}, t)$ for $t \in [0, N_T \Delta t]$. This is the marching-on-in-time algorithm.

Different schemes exist for the numerical evaluation of the four-dimensional integrals in $\mathbf{Z}^{(j)}$, see e.g. [17]–[22]. In general, more accurate integration schemes give rise to algorithms that are stable for an increasingly broader range of geometries, material parameters, and discretization parameters.

The complexity of this MOT scheme scales as $\mathcal{O}(N_T N_S^2)$. However, this can be reduced to $\mathcal{O}(N_T N_S^{3/2} \log N_S)$ and even $\mathcal{O}(N_T N_S \log^2 N_S)$ using the two-level and multilevel plane wave time domain (PWTD) algorithms, respectively [11], or to $\mathcal{O}(N_T N_S^{3/2} \log^2 N_S)$ using the time domain adaptive integration method (TD-AIM) [12].

While the Galerkin-in-space / collocation-in-time scheme has been widely applied, its soundness remains questionable. First, the collocation-in-time scheme is not well understood. As it does not fit in the general finite element theoretical framework, classical coercivity arguments cannot be used to establish its stability. While convergence proofs have been formulated, they remain limited to specific collocation schemes applied to the scalar single layer potential equation for acoustic scattering [23], [24].

Furthermore, the spatial testing procedure is well understood from frequency domain applications (see e.g. [25]). It is known that the spatial discretization of the TD-MFIE employed in (3.6) is non-conforming and inaccurate [7], [26].

Finally, the expansion of the current in piecewise Lagrange interpolators of order

p limits the accuracy. Band-limited signals can be more accurately approximated using band-limited interpolation functions (BLIFs, [27]) [28]. The resulting scheme is however not causal and requires an extrapolation procedure which introduces another source of errors.

3.3 Temporal Mixed Galerkin Discretization of the TD-CFIE

3.3.1 The Temporal Galerkin Method

The concerns raised above motivate the search for another temporal discretization scheme for the TD-CFIE. The resulting system must be causal (to allow for time-stepping), general-order, stable and convergent. Such a scheme is now constructed within the framework of temporal Galerkin methods, as described in section 2.3.2.

Consider an RP-BIE (such as the TD-CFIE) of the form

$$\mathcal{O}\boldsymbol{j}(\boldsymbol{r},t) = \boldsymbol{q}(\boldsymbol{r},t) \tag{3.7}$$

where the unknown current $\boldsymbol{j}(\boldsymbol{r},t)$ is expanded as in (3.5). Equation (3.7) is now multiplied by a spatial testing function $\boldsymbol{f}_m(\boldsymbol{r})$ as well as a temporal testing function $U_k(t) = U(t - k\Delta t)$. The resulting equation is integrated over both space and time:

$$\begin{aligned}\sum_{n,i} \mathsf{x}_n^{(i)} \int_{\Gamma\times\mathbb{R}} U_k(t)\boldsymbol{f}_m(\boldsymbol{r}) \cdot \mathcal{O}\left[\boldsymbol{f}_n T_i\right](\boldsymbol{r},t)\; ds\; dt \\ = \int_{\Gamma\times\mathbb{R}} U_k(t)\boldsymbol{f}_m(\boldsymbol{r}) \cdot \boldsymbol{q}(\boldsymbol{r},t)\; ds\; dt.\end{aligned} \tag{3.8}$$

Due to time translation symmetry, this expression depends on i and k only through the difference $k - i$. Furthermore, if the support of $T(t)$ is bounded below, and the support of $U(t)$ is bounded above, the integrals in the left hand side of (3.8) vanish for sufficiently small values of $k - i$. Specifically, assume that $T(t) = 0\ \forall t < -\Delta t$ and $U(t) = 0\ \forall t > 0$ (this can be accomplished by shifting the basis and testing functions, or shifting the temporal indices). Now the integrals with $k < i$ vanish, and the MOT equation becomes

$$\mathsf{Z}^{(0)}\mathsf{x}^{(j)} = \mathsf{v}^{(j)} - \sum_{i=0}^{j-1} \mathsf{Z}^{(j-i)}\mathsf{x}^{(i)} \tag{3.9}$$

where

$$\begin{aligned}\mathsf{v}_m^{(j)} &= (\boldsymbol{f}_m U_j, \boldsymbol{q}) \\ \mathsf{Z}_{mn}^{(j)} &= (\boldsymbol{f}_m U_j, \mathcal{O}\left[\boldsymbol{f}_n T\right]) \\ (\boldsymbol{a},\boldsymbol{b}) &= \int_{\Gamma\times\mathbb{R}} \boldsymbol{a}(\boldsymbol{r},t)\cdot\boldsymbol{b}(\boldsymbol{r},t)\; ds\; dt.\end{aligned}$$

The collocation scheme described in the previous section can be recovered by setting $U(t) = \delta(t)$, the Dirac delta function (figure 3.1, bottom panels).

There is another relation between the interaction matrices $\mathbf{Z}^{(i)}$ of the temporal collocation and Galerkin schemes. By inverting the order of the temporal testing and the temporal convolution of the Green function with the temporal basis function, one obtains the equivalence between the matrix elements of a temporal Galerkin scheme with basis and testing functions

$$T_i(t) = T(t - i\Delta t), \quad U_i(t) = U(t - i\Delta t) \tag{3.10a}$$

respectively, and those of a collocation scheme with basis functions

$$\xi_i(t) = \int_{-\infty}^{\infty} U(\tau)T(t - i\Delta t + \tau)d\tau. \tag{3.10b}$$

This equivalence greatly simplifies the implementation of the space-time mixed Galerkin method in existing solvers, even when fast techniques or special integration routines are used. Note however that only the matrix elements are equal, whereas the excitation $\mathbf{v}^{(j)}$ and the current expansion (3.5) are not. The stability only depends on the matrix elements. Thus, if the temporal Galerkin scheme is stable, the equivalent collocation scheme will also be stable. This has been exploited to construct a stable collocation scheme in [29].

Finally, it must be noted that the boundedness of the support of the basis and testing functions is not sufficient to obtain a usable scheme. For example, the BLIFs [27] of order M are defined on the interval $[-M\Delta t, M\Delta t]$. After shifting these basis functions to the interval $[-\Delta t, (2M-1)\Delta t]$, one can obtain a causal scheme with a piecewise constant testing function that is one on the interval $[-\Delta t, 0]$ and zero everywhere else. However, the system matrix will contain interactions of the fields radiated by the first time segment in the BLIF's support, which are multiple orders of magnitude smaller than those radiated in the center segments of its support. This will result in large numerical errors leading to unstable results. This example illustrates that the temporal basis and testing functions must be carefully selected. The fields radiated by the basis function $T_i(t)$ must strongly overlap with the testing function $U_i(t)$ (in comparison to $U_{i+1}(t)$, $U_{i+2}(t)$, ...) in time, so that the matrix $\mathbf{Z}^{(0)}$ accounts for most of the near interactions. This can be achieved if both $T(t)$ and $U(t)$ are (approximately) localized in the interval $[-\Delta t, 0]$.

3.3.2 First Order Basis and Testing Functions

In [13], it is proven that a temporal Galerkin scheme, which makes use of first order basis functions and piecewise constant testing functions, yields a stable system when applied to the time-differentiated scalar first and second kind RP-BIEs for acoustic scattering, if the span of the testing functions is equal

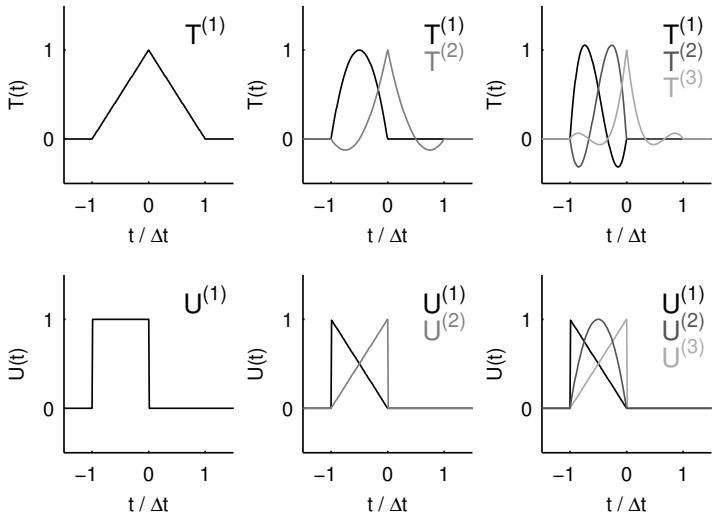

Figure 3.2: Top: temporal current basis functions for first (left), second (middle) and third (right) order temporally mixed Galerkin scheme. Bottom: corresponding testing functions.

to the span of the temporal derivatives of the basis functions. Therefore, the author of [13] chose continuous, piecewise linear basis functions

$$T(t) = \begin{cases} 1 + t/\Delta t & -\Delta t \leq t < 0 \\ 1 - t/\Delta t & 0 \leq t \leq \Delta t \\ 0 & \text{otherwise} \end{cases} \tag{3.11a}$$

and piecewise constant testing functions

$$U(t) = \begin{cases} 1 & -\Delta t \leq t < 0 \\ 0 & \text{otherwise} \end{cases} . \tag{3.11b}$$

$T(t)$ and $U(t)$ are shown in the left panels of figure 3.2. In [14], a similar first order in time scheme was applied to the TD-EFIE. This corresponds to scheme 1b in section 2.3.3.

This scheme is only defined for lowest order approximations. As will be shown in the numerical results section, this limits the maximal achievable accuracy for a fixed time step size Δt. A higher-order generalization is presented in the next section.

3.3.3 Definition of Higher Order Temporal Basis and Testing Functions

Now, in order to span all continuous, piecewise p-th order polynomial functions, introduce a set of p basis functions $T^{(\mu)}(t)$, $\mu = 1, ..., p$ that are globally continuous, piecewise polynomials of order p, achieve the value one at $t = (\mu/p - 1)\Delta t$, and zero at $t = (\nu/p - 1)\Delta t$, $\nu \neq \mu$. The support of $T^{(\mu)}$ is chosen to be $[-\Delta t, \Delta t]$ for $\mu = p$, and $[-\Delta t, 0]$ for $\mu \neq p$. For example, for $p = 2$ (figure 3.2, top middle panel):

$$T^{(1)}(t) = \begin{cases} -4\frac{t}{\Delta t}\left(\frac{t}{\Delta t} + 1\right) & -\Delta t < t < 0 \\ 0 & \text{otherwise} \end{cases} \tag{3.12a}$$

$$T^{(2)}(t) = \begin{cases} 2\left(\frac{t}{\Delta t} + 1\right)\left(\frac{t}{\Delta t} + \frac{1}{2}\right) & -\Delta t < t < 0 \\ 2\left(\frac{t}{\Delta t} - 1\right)\left(\frac{t}{\Delta t} - \frac{1}{2}\right) & 0 \leq t < \Delta t \\ 0 & \text{otherwise} \end{cases} . \tag{3.12b}$$

This introduces p degrees of freedom per time step. The current expansion (3.5) then becomes

$$\boldsymbol{j}(\boldsymbol{r}, t) = \sum_{i=1}^{N_S} \sum_{j=1}^{\infty} \sum_{\mu=1}^{p} \mathsf{x}_i^{(j,\mu)} \boldsymbol{f}_i(\boldsymbol{r}) T_j^{(\mu)}(t). \tag{3.13}$$

Next, a set of p testing functions $U^{(\mu)}(t)$, $\mu = 1, ..., p$ must be defined, that spans the space of the time derivatives of the basis functions. These can be chosen as the piecewise polynomials of order $p - 1$ on the interval $[-\Delta t, 0]$, achieving the value one at $t = (\mu - p)/(p - 1)\Delta t$, and zero on $t = (\nu - p)/(p - 1)\Delta t$, $\nu \neq \mu$. For $p = 2$ (figure 3.2, bottom middle panel):

$$U^{(1)}(t) = \begin{cases} -\frac{t}{\Delta t} & -\Delta t < t < 0 \\ 0 & \text{otherwise} \end{cases} \tag{3.14a}$$

$$U^{(2)}(t) = \begin{cases} \frac{t}{\Delta t} + 1 & -\Delta t < t < 0 \\ 0 & \text{otherwise} \end{cases} . \tag{3.14b}$$

Note that the testing functions are not continuous at the boundary between adjacent time segments, whereas the basis functions are.

Since the higher order basis and testing functions associated to the same time step do not fulfil the discrete causality condition among each other, the MOT system needs to be solved simultaneously for the corresponding unknowns. In other words, the presence of higher order basis and testing functions introduces block structure in the system matrix. More explicitly, the marching-on-in-time

equations become:

$$\begin{pmatrix} \mathsf{Z}_{11}^{(0)} & \dots & \mathsf{Z}_{1p}^{(0)} \\ \dots & \dots & \dots \\ \mathsf{Z}_{p1}^{(0)} & \dots & \mathsf{Z}_{pp}^{(0)} \end{pmatrix} \begin{pmatrix} \mathsf{x}^{(j,1)} \\ \dots \\ \mathsf{x}^{(j,p)} \end{pmatrix}$$
$$= \begin{pmatrix} \mathsf{v}^{(j,1)} \\ \dots \\ \mathsf{v}^{(j,p)} \end{pmatrix} - \sum_{i=0}^{j-1} \begin{pmatrix} \mathsf{Z}_{11}^{(i)} & \dots & \mathsf{Z}_{1p}^{(i)} \\ \dots & \dots & \dots \\ \mathsf{Z}_{p1}^{(i)} & \dots & \mathsf{Z}_{pp}^{(i)} \end{pmatrix} \begin{pmatrix} \mathsf{x}^{(j-i,1)} \\ \dots \\ \mathsf{x}^{(j-i,p)} \end{pmatrix} \tag{3.15}$$

with

$$\mathsf{v}_m^{(j,\mu)} = \left(\boldsymbol{f}_m U_j^{(\mu)}, \boldsymbol{q} \right) \tag{3.16}$$

$$\left(\mathsf{Z}_{\mu\nu}^{(j)} \right)_{mn} = \left(\boldsymbol{f}_m U_j^{(\mu)}, \mathcal{O}\left[\boldsymbol{f}_n T^{(\nu)}(t) \right] \right). \tag{3.17}$$

$\mathsf{Z}_{\mu\nu}^{(j)}$, $\mu, \nu = 1, 2, .., p$ are block matrices of dimension $N_S \times N_S$. Thus, pN_S unknowns are treated at each time step, increasing the order of the system to be inverted at every time step with a factor p. Note, however, that this is in no way different from the increase of nonzero matrix entries associated with an increase in order in e.g. classic finite element methods.

3.4 Mixed Spatial Discretization of the TD-CFIE

It is well known that the frequency domain MFIE discretized using RWG basis and testing functions yields inaccurate results [5], [26]. The spatial discretization of the TD-CFIE used in section 3.2

$$\eta\alpha \left(\hat{\boldsymbol{n}} \times \boldsymbol{f}, \dot{\mathcal{T}} \boldsymbol{j} \right) + \eta (1-\alpha) \left(\boldsymbol{f}, \left\{ \frac{1}{2} \dot{\mathcal{I}} + \dot{\mathcal{K}} \right\} \boldsymbol{j} \right)$$
$$= -\alpha \left(\hat{\boldsymbol{n}} \times \boldsymbol{f}, \hat{\boldsymbol{n}} \times \dot{\boldsymbol{e}}^i \right) + \eta (1-\alpha) \left(\boldsymbol{f}, \hat{\boldsymbol{n}} \times \dot{\boldsymbol{h}}^i \right) \tag{3.18}$$

incorporates the time domain version of this non-conforming discretization scheme for the MFIE contribution. In the numerical results section, it will be illustrated that this non-conforming scheme indeed deteriorates the accuracy of the results. A similar phenomenon has been observed in the frequency domain CFIE [7].

In [5] a mixed discretization scheme using RWG functions as basis functions and BC functions as testing functions for the frequency domain MFIE has been introduced. This scheme is conforming and leads to well-conditioned system matrices. The accuracy of this scheme's solution has been shown to be competitive with that of the EFIE [5], [30].

The accuracy of the TD-CFIE can thus be improved by incorporating this conforming discretization scheme for the MFIE. By testing the TD-EFIE using

RWG functions, testing the TD-MFIE using the rotated BC functions $\hat{\boldsymbol{n}} \times \boldsymbol{g}_m$, and adding both contributions, one obtains:

$$\begin{aligned} &\eta\alpha \left(\hat{\boldsymbol{n}} \times \boldsymbol{f}, \dot{\mathcal{T}} \boldsymbol{j}\right) + \eta\,(1-\alpha) \left(\hat{\boldsymbol{n}} \times \boldsymbol{g}, \left\{\tfrac{1}{2}\dot{\mathcal{I}} + \dot{\mathcal{K}}\right\} \boldsymbol{j}\right) \\ &= -\alpha \left(\hat{\boldsymbol{n}} \times \boldsymbol{f}, \hat{\boldsymbol{n}} \times \dot{\boldsymbol{e}}^i\right) + \eta\,(1-\alpha) \left(\hat{\boldsymbol{n}} \times \boldsymbol{g}, \hat{\boldsymbol{n}} \times \dot{\boldsymbol{h}}^i\right). \end{aligned} \tag{3.19}$$

A frequency domain version of this discretization scheme has been suggested in [6]. Although a significant increase in accuracy was reported, this is not a consistent discretization of the CFIE, since the EFIE and MFIE contributions are tested using different functions. In the numerical results section, it will be shown that it is still prone to spurious resonances.

A consistent conforming discretization of the frequency domain CFIE was obtained in [10] by applying the Calderón multiplicative preconditioner to the EFIE contribution. A mixed discretization was applied to the Calderón preconditioned EFIE (CP-EFIE), such that both the CP-EFIE and the MFIE are tested using BC functions. However, for geometries discretized with moderately dense meshes, the introduction of a Calderón preconditioner introduces unnecessary overhead.

A consistent and resonance free mixed discretization of the TD-CFIE (3.4) can be obtained without applying a Calderón multiplicative preconditioner by projecting the range of the TD-MFIE contribution onto the RWG basis:

$$\left\{\frac{1}{2}\dot{\mathcal{I}} + \dot{\mathcal{K}}\right\} \boldsymbol{j}(\boldsymbol{r}, t) \approx \sum_m \mathsf{b}_m(t) \boldsymbol{f}_m(\boldsymbol{r}) \quad \forall t. \tag{3.20}$$

This equation can be solved for $\mathsf{b}(t)$ by spatially testing it with the rotated BC functions $\hat{\boldsymbol{n}} \times \boldsymbol{g}_n(\boldsymbol{r})$. In matrix form:

$$\mathsf{b}(t) = \mathsf{G}^{-1}_{\hat{\boldsymbol{n}} \times \boldsymbol{g}, \boldsymbol{f}} \cdot \left(\hat{\boldsymbol{n}} \times \boldsymbol{g}, \left\{\frac{1}{2}\dot{\mathcal{I}} + \dot{\mathcal{K}}\right\} \boldsymbol{j}(t)\right)$$

where the Gram matrix $\mathsf{G}_{\hat{\boldsymbol{n}} \times \boldsymbol{g}, \boldsymbol{f}}$ is given by

$$\left(\mathsf{G}_{\hat{\boldsymbol{n}} \times \boldsymbol{g}, \boldsymbol{f}}\right)_{mn} = \left(\hat{\boldsymbol{n}} \times \boldsymbol{g}_m, \boldsymbol{f}_n\right). \tag{3.21}$$

The expansion (3.20) is inserted into the TD-CFIE (3.4). A similar projection is applied to the incoming magnetic field $\boldsymbol{h}^i(\boldsymbol{r}, t)$. Finally, the resulting equation is tested with the RWG functions $\boldsymbol{f}_m(\boldsymbol{r})$. This results in

$$\begin{aligned} &\eta\alpha \left(\hat{\boldsymbol{n}} \times \boldsymbol{f}, \dot{\mathcal{T}} \boldsymbol{j}\right) + \eta\,(1-\alpha)\, \mathsf{G}_{\boldsymbol{f}, \boldsymbol{f}} \mathsf{G}^{-1}_{\hat{\boldsymbol{n}} \times \boldsymbol{g}, \boldsymbol{f}} \left(\hat{\boldsymbol{n}} \times \boldsymbol{g}, \left\{\frac{1}{2}\dot{\mathcal{I}} + \dot{\mathcal{K}}\right\} \boldsymbol{j}\right) \\ = \quad &-\alpha \left(\hat{\boldsymbol{n}} \times \boldsymbol{f}, \hat{\boldsymbol{n}} \times \dot{\boldsymbol{e}}^i\right) + \eta\,(1-\alpha)\, \mathsf{G}_{\boldsymbol{f}, \boldsymbol{f}} \mathsf{G}^{-1}_{\hat{\boldsymbol{n}} \times \boldsymbol{g}, \boldsymbol{f}} \left(\hat{\boldsymbol{n}} \times \boldsymbol{g}, \hat{\boldsymbol{n}} \times \dot{\boldsymbol{h}}^i\right) \end{aligned} \tag{3.22}$$

where the Gram matrix $\mathsf{G}_{\boldsymbol{f}, \boldsymbol{f}}$ results from testing the expansion (3.20) with the RWG functions $\boldsymbol{f}_m(\boldsymbol{r})$:

$$\left(\mathsf{G}_{\boldsymbol{f}, \boldsymbol{f}}\right)_{mn} = \left(\boldsymbol{f}_m, \boldsymbol{f}_n\right). \tag{3.23}$$

Equation (3.22) is a combination of spatially conforming discretizations of the TD-EFIE and the TD-MFIE, but also a consistent spatial discretization of the TD-CFIE as a whole (3.4). Finally, the full discretization is achieved by applying either the classical collocation-in-time scheme or the temporal mixed Galerkin scheme introduced above.

Alternatively, the range of the TD-EFIE operator can be projected onto the BC basis:

$$\dot{\mathcal{T}}\boldsymbol{j}(\boldsymbol{r},t) \approx \sum_m \mathsf{c}_m(t)\boldsymbol{g}_m(\boldsymbol{r}). \tag{3.24}$$

This equation can be solved for $\mathsf{c}(t)$ by spatially testing it with the rotated RWG functions $\hat{\boldsymbol{n}} \times \boldsymbol{f}_m(\boldsymbol{r})$:

$$\mathsf{c}(t) = \mathbf{G}^{-1}_{\hat{\boldsymbol{n}}\times\boldsymbol{f},\boldsymbol{g}} \cdot \left(\hat{\boldsymbol{n}} \times \boldsymbol{f}, \dot{\mathcal{T}}\boldsymbol{j}(t)\right) \tag{3.25}$$

where the Gram matrix $\mathbf{G}_{\hat{\boldsymbol{n}}\times\boldsymbol{f},\boldsymbol{g}}$ is given by

$$\left(\mathbf{G}_{\hat{\boldsymbol{n}}\times\boldsymbol{f},\boldsymbol{g}}\right)_{mn} = \left(\hat{\boldsymbol{n}} \times \boldsymbol{f}_m, \boldsymbol{g}_n\right). \tag{3.26}$$

The expansion (3.24) is inserted into the TD-CFIE (3.4). A similar projection is applied to the incoming electric field $\boldsymbol{e}^i(\boldsymbol{r},t)$. Finally, the equation is tested with the BC functions $\boldsymbol{g}_m(\boldsymbol{r})$. This results in

$$\begin{aligned} & \eta\alpha\mathbf{G}_{\boldsymbol{g},\boldsymbol{g}}\mathbf{G}^{-1}_{\hat{\boldsymbol{n}}\times\boldsymbol{f},\boldsymbol{g}}\left(\hat{\boldsymbol{n}} \times \boldsymbol{f}, \dot{\mathcal{T}}\boldsymbol{j}\right) + \eta\left(1-\alpha\right)\left(\hat{\boldsymbol{n}} \times \boldsymbol{g}, \left\{\frac{1}{2}\dot{\mathcal{I}} + \dot{\mathcal{K}}\right\}\boldsymbol{j}\right) \\ = \quad & -\alpha\mathbf{G}_{\boldsymbol{g},\boldsymbol{g}}\mathbf{G}^{-1}_{\hat{\boldsymbol{n}}\times\boldsymbol{f},\boldsymbol{g}}\left(\hat{\boldsymbol{n}} \times \boldsymbol{f}, \hat{\boldsymbol{n}} \times \dot{\boldsymbol{e}}^i\right) + \eta\left(1-\alpha\right)\left(\hat{\boldsymbol{n}} \times \boldsymbol{g}, \hat{\boldsymbol{n}} \times \dot{\boldsymbol{h}}^i\right) \end{aligned} \tag{3.27}$$

where the Gram matrix $\mathbf{G}_{\boldsymbol{g},\boldsymbol{g}}$ results from testing the expansion (3.24) with the BC functions $\boldsymbol{g}_m(\boldsymbol{r})$:

$$\left(\mathbf{G}_{\boldsymbol{g},\boldsymbol{g}}\right)_{mn} = \left(\boldsymbol{g}_m, \boldsymbol{g}_n\right). \tag{3.28}$$

Both (3.22) and (3.27) have been implemented and tested, but no significant difference in performance has been found. In the next parts, the first version (3.22) will be used.

The projection operators in (3.22) and (3.27) have been introduced ad hoc, i.e., to allow for the inclusion of the conforming discretization of the MFIE contribution. Concatenation of the MFIE operator with another operator, as in (3.22), has however been used to develop a rigorous variational analysis of the CFIE, applicable to non-smooth surfaces [31]. Concatenation of the EFIE operator with another operator, as in (3.27), has been used to improve the spectral properties of the CFIE operator [10], [32].

3.5 Numerical Examples

In this section, numerical results demonstrating the accuracy and stability of the scheme introduced in the previous sections will be presented. First, the error estimation scheme used will detailed. To clearly indicate that both the spatial and temporal compartments of the scheme are needed in order to obtain accurate solutions, results will be shown obtained using all four combinations of temporal and spatial discretization schemes.

3.5.1 Error Estimation Scheme and Rationale

In order to assess the accuracy of an MOT solution, it will be compared to a known frequency domain reference solution $\boldsymbol{j}_{\mathrm{ref}}(\boldsymbol{r},\omega)$. In all the examples presented here, the scatterer is illuminated by a Gaussian pulse:

$$\begin{aligned}\boldsymbol{e}^i(\boldsymbol{r},t) &= \frac{4A}{w\sqrt{\pi}}\hat{\boldsymbol{p}}\exp\left(-\left(\frac{4}{w}\left(c(t-t_0)-\hat{\boldsymbol{k}}\cdot\boldsymbol{r}\right)\right)^2\right)\\ &= \frac{A\hat{\boldsymbol{p}}}{2\pi c}\int_{-\infty}^{\infty}d\omega\exp\left(j\omega\left(t-t_0\right)-j\frac{\omega}{c}\hat{\boldsymbol{k}}\cdot\boldsymbol{r}-\left(\frac{\omega w}{8c}\right)^2\right)\end{aligned}$$

where A is the amplitude, w is the width of the pulse, $\hat{\boldsymbol{p}}$ is the polarization vector, c is the speed of light in vacuum, $\hat{\boldsymbol{k}}$ is the direction in which the pulse is propagating, and t_0 is the time of arrival of the pulse at $\boldsymbol{r}=\boldsymbol{0}$. It can be interpreted as a superposition of plane waves with angular frequency ω and amplitude $\frac{A}{2\pi c}\exp\left(-\left(\frac{\omega w}{8c}\right)^2\right)$.

The current induced on a PEC surface by this incident wave is then computed using the MOT algorithm. To obtain the frequency response $\boldsymbol{j}_{\mathrm{MOT}}(\boldsymbol{r},\omega)$, the current is Fourier transformed, and divided by $\frac{A}{c}\cdot\exp\left(-j\omega t_0-\left(\frac{\omega w}{8c}\right)^2\right)$.

Now, $\boldsymbol{j}_{\mathrm{MOT}}(\boldsymbol{r},\omega)$ can be compared with the reference solution $\boldsymbol{j}_{\mathrm{ref}}(\boldsymbol{r},\omega)$. An often used measure for the error is the maximum error or the RMS error in the radar cross section. However, this does not account for errors in the near field. Here, another error measure is chosen: the $H_{\mathrm{div}}^{-1/2}$ norm on Γ. Since the operator

$$\left(\mathcal{S}\boldsymbol{j}\right)(\boldsymbol{r},\omega)=\frac{\omega}{c}\int_{\Gamma}ds'\frac{\boldsymbol{j}(\boldsymbol{r}',\omega)}{|\boldsymbol{r}-\boldsymbol{r}'|}-\frac{c}{\omega}\nabla\int_{\Gamma}ds'\frac{\nabla'\cdot\boldsymbol{j}(\boldsymbol{r}',\omega)}{|\boldsymbol{r}-\boldsymbol{r}'|}\tag{3.29}$$

is self-adjoint, positive, continuous and coercive with regard to the standard Sobolev-Slobodeckij norm on $H_{\mathrm{div}}^{-1/2}$, it furnishes a norm on $H_{\mathrm{div}}^{-1/2}$. As follows from the trace theorems for electromagnetic fields [33], this norm is a measure for the near field energy of the error. Here, the discretization of $\mathcal{S}$ with respect to the triangle mesh is used to estimate the error in near field energy.

For each frequency $f = \omega/2\pi$, the relative error is defined as:

$$e_r(\omega) = \|\boldsymbol{j}_{\mathrm{MOT}} - \boldsymbol{j}_{\mathrm{ref}}\|_{H^{-1/2}_{\mathrm{div}}} \Big/ \|\boldsymbol{j}_{\mathrm{ref}}\|_{H^{-1/2}_{\mathrm{div}}} \tag{3.30}$$

$$\begin{aligned} \|\boldsymbol{j}\|^2_{H^{-1/2}_{\mathrm{div}}} &= \frac{c}{\omega}\int_\Gamma ds \int_\Gamma ds' \frac{\nabla\cdot\boldsymbol{j}(\boldsymbol{r},\omega)\nabla'\cdot\boldsymbol{j}(\boldsymbol{r}',\omega)}{|\boldsymbol{r}-\boldsymbol{r}'|} \\ &\quad + \frac{\omega}{c}\int_\Gamma ds \int_\Gamma ds' \frac{\boldsymbol{j}(\boldsymbol{r},\omega)\cdot\boldsymbol{j}(\boldsymbol{r}',\omega)}{|\boldsymbol{r}-\boldsymbol{r}'|}. \end{aligned}$$

This provides a physically meaningful estimate of the quality of a MOT solution.

For spherical scatterers, the solution can be computed analytically using the Mie series [34]. As the Mie series is defined on the sphere, whereas the MOT solution is defined on the triangle mesh, the projection of the Mie series $\boldsymbol{j}_{\mathrm{Mie}}(\boldsymbol{r},\omega)$ onto the RWG basis is needed:

$$\tilde{\boldsymbol{j}}_{\mathrm{Mie}}(\boldsymbol{r},\omega) = \sum_i \mathsf{a}_i(\omega)\boldsymbol{f}_i(\boldsymbol{r}). \tag{3.31}$$

The expansion coefficients a_i are found by testing with rotated BC functions $\hat{\boldsymbol{n}}\times\boldsymbol{g}_m$, in order to conformingly discretize the unit operator [6]:

$$\mathsf{a}(\omega) = \left(G_{\hat{\boldsymbol{n}}\times\boldsymbol{g},\boldsymbol{f}}\right)^{-1}\left(\hat{\boldsymbol{n}}\times\boldsymbol{g}, \boldsymbol{j}_{\mathrm{Mie}}(\boldsymbol{r},\omega)\right). \tag{3.32}$$

This projection is used as the reference solution in section 3.5.2.

For non-spherical scatterers, for which no analytical solution is available, one can instead use a simulation, of which the reliability is already established, as a reference solution. In sections 3.5.3 and 3.5.4, frequency domain EFIE simulations will be used for this purpose. The frequency domain EFIE is known to be reliable away from resonant frequencies.

3.5.2 Scattering by a Sphere

Consider a PEC sphere of radius 0.3 meters, approximated using an equilateral triangle mesh with edge length 4.5 cm. It is illuminated by a Gaussian pulse (with $w = 3.33$ ns, $t_0 = 20$ ns). The induced current is approximated by an expansion in 1887 RWG basis functions. The CFIE weighting coefficient is $\alpha = 0.5$, unless specified otherwise.

Temporal Discretization Scheme

First, the temporal discretization scheme is investigated. In figure 3.3, the following schemes are compared:

(a) collocation-in-time; second degree Lagrange interpolators ($\Delta t = 0.1$ ns),
(b) collocation-in-time; third degree Lagrange interpolators ($\Delta t = 0.1$ ns),
(c) first order temporal mixed Galerkin ($\Delta t = 0.1$ ns),
(d) second order temporal mixed Galerkin ($\Delta t = 0.2$ ns).

The spatial discretization is performed using the mixed scheme (3.22). In (d), the time step is doubled, as there are $p = 2$ degrees of freedom at each time step. Thus, simulations with an equal number of temporal degrees of freedom per unit of time are compared.

The $H_{\text{div}}^{-1/2}$ error on the currents with respect to the Mie series are computed as outlined in the previous section (figure 3.3). Temporal mixed Galerkin schemes outperform collocation schemes using an equal number of temporal degrees of freedom per unit of time. Using higher order temporal basis functions increases the accuracy even further.

In addition to the improved accuracy, the second order temporal Galerkin method exhibits faster convergence than the other schemes when the time step is decreased. In figure 3.4, the relative error as a function of $\Delta t/p$ (the inverse of the number of degrees of freedom per unit of time) at a fixed frequency of 500 MHz is shown for the four temporal discretization types under investigation; all four types of temporal discretization make use of the mixed discretization scheme in space. Indeed, the second order temporal mixed Galerkin method exhibits faster convergence (approx. $\mathcal{O}(\Delta t^4)$) than both the first order Galerkin scheme and the second and third degree collocation schemes (approx. $\mathcal{O}(\Delta t^2)$, $\mathcal{O}(\Delta t^1)$ and $\mathcal{O}(\Delta t^2)$, respectively). For small time steps, the error saturates toward a value determined by the density of the triangle mesh.

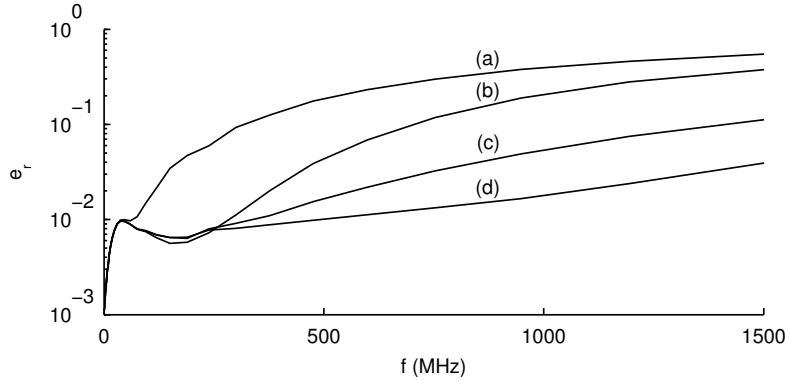

Figure 3.3: Relative $H_{\mathrm{div}}^{-1/2}$ error for different temporal discretizations: (a) collocation-in-time using second degree Lagrange interpolators, (b) collocation-in-time using third degree Lagrange interpolators, (c) first order temporal mixed Galerkin, and (d) second order temporal mixed Galerkin.

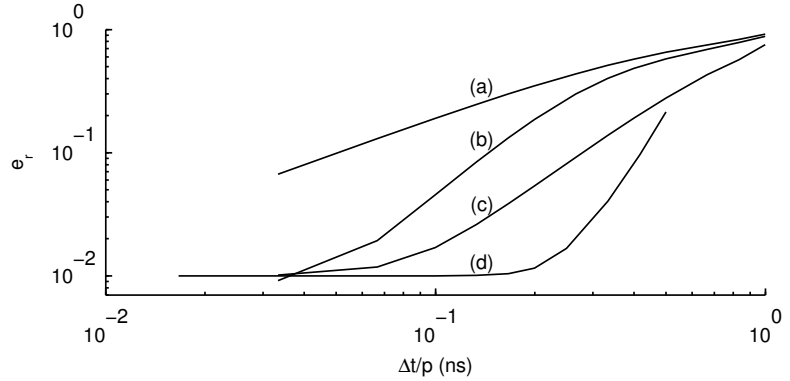

Figure 3.4: The relative error at 500 MHz, for varying time step Δt: (a) collocation-in-time using second degree Lagrange interpolators, (b) collocation-in-time using third degree Lagrange interpolators, (c) first order temporal mixed Galerkin, and (d) second order temporal mixed Galerkin.

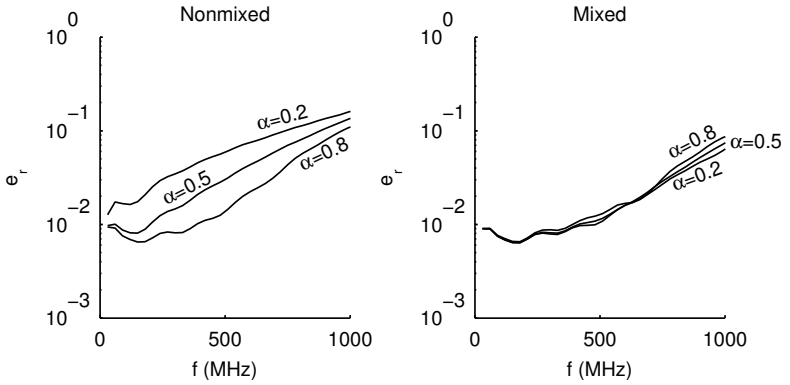

Figure 3.5: The relative error for $\alpha = 0.2$, $\alpha = 0.5$ and $\alpha = 0.8$. Left: non-mixed spatial discretization; right: mixed spatial discretization.

Spatial Discretization Scheme

In section 3.4, it was claimed that the non-conforming discretization of the TD-MFIE is responsible for the loss of accuracy, but that it can be remedied by the mixed spatial discretization. This becomes apparent when the errors are plotted for different values of the TD-CFIE weighting parameter α. This is done in figure 3.5 for a second order temporal mixed Galerkin simulation with $\Delta t = 0.4$ ns. For a spatial non-mixed discretization (left panel), the simulation becomes more accurate as α is increased, because the TD-MFIE contribution becomes smaller. For a spatial mixed discretization (right panel), the value of α does not significantly affect the accuracy. The complete range of values for α thus becomes available, whereas classic schemes are subject to a stability/accuracy trade-off.

Next, it is demonstrated that the restoration of consistency between the EFIE and MFIE contributions by multiplication with the appropriate Gram matrices is essential to arrive at a resonance-free scheme. Results of the following schemes are compared:

(1) the consistent non-mixed discretization (3.18),
(2) the inconsistent mixed discretization (3.19),
(3) the consistent mixed discretization (3.22).

The temporal discretization is performed using a first order temporal mixed Galerkin scheme with $\Delta t = 0.1$ ns. The relative $H_{\text{div}}^{-1/2}$ error is plotted in figure 3.6.

The consistent schemes (1) and (3) give rise to smooth error curves, whereas the inconsistent scheme (2) picks up the resonant frequencies of the sphere. Indeed,

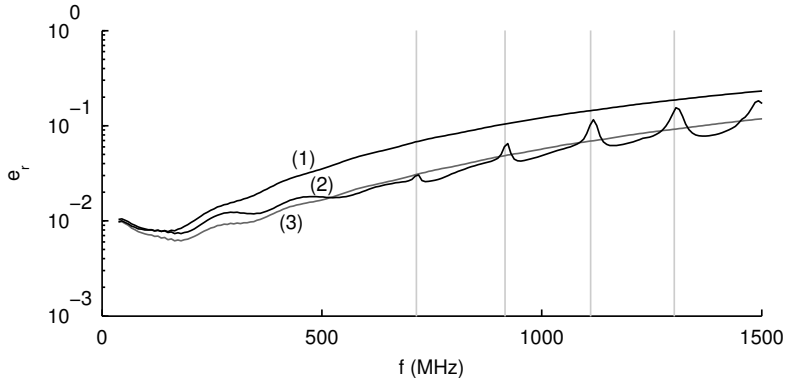

Figure 3.6: The relative error for (1) the consistent non-mixed discretization (3.18), (2) the inconsistent mixed discretization (3.19), and (3), the consistent mixed discretization (3.22). The error in (2) shows distinct peaks at the resonance frequencies of the sphere, which are denoted by the vertical lines.

the resonant frequencies of a sphere with radius r are determined by [35]:

$$J_{n+1/2}\left(\frac{2\pi fr}{c}\right) = 0 \qquad \text{(TE modes)} \tag{3.33}$$

$$J'_{n+1/2}\left(\frac{2\pi fr}{c}\right) = 0 \qquad \text{(TM modes)} \tag{3.34}$$

where n is an integer, J_n is the Bessel function of order n, and J'_n is its derivative. The peaks are found at the TE resonances at 715 MHz ($n = 1$), 917 MHz ($n = 2$), 1111 MHz ($n = 3$) and 1301 MHz ($n = 4$), which are represented as vertical lines in figure 3.6.

Away from these resonant frequencies, the mixed schemes (2) and (3) both are more accurate than the nonmixed scheme (1). In the neighbourhood of the resonant frequencies, the increased accuracy of (2) is partly lost due to the presence of spurious resonances. Therefore, an accurate solution over a broad frequency band can only be obtained using the consistent mixed scheme (3).

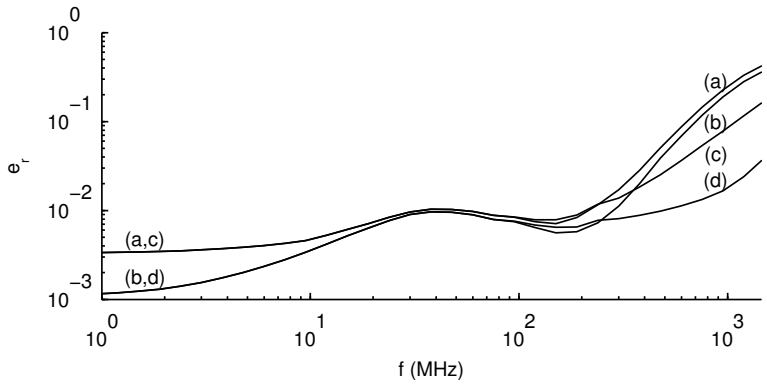

Figure 3.7: The relative error for (a) collocation-in-time using third degree Lagrange interpolators and nonmixed spatial discretization, (b) collocation-in-time using third degree Lagrange interpolators and mixed spatial discretization, (c) second order Galerkin-in-time and nonmixed spatial discretization, and (d) second order Galerkin-in-time and mixed spatial discretization.

Space-Time Mixed Scheme

The importance of using the mixed spatial discretization scheme in conjunction with the higher order mixed temporal discretization scheme, is illustrated in figure 3.7. Here, the following simulations are compared:

(a) collocation-in-time (third degree Lagrange interpolators, $\Delta t = 0.2$ ns) with nonmixed spatial discretization,
(b) collocation-in-time (third degree Lagrange interpolators, $\Delta t = 0.2$ ns) with mixed spatial discretization,
(c) second order Galerkin-in-time ($\Delta t = 0.4$ ns) with nonmixed spatial discretization,
(d) second order Galerkin-in-time ($\Delta t = 0.4$ ns) with mixed spatial discretization.

At low frequencies, the error is dominated by the spatial discretization scheme. At high frequencies, the error is dominated by the temporal discretization scheme. To achieve a high accuracy over a broad frequency band, the space-time mixed Galerkin scheme is needed.

3.5.3 Scattering by a Cuboid

As a second example, consider a PEC cuboid with dimensions 0.25 by 1 by 0.5 meters (figure 3.8). It is illuminated by a Gaussian pulse propagating along the positive z-axis, with the electric field linearly polarized along the x-axis. The induced current is approximated by an expansion in 1344 RWG basis functions. This scattering problem is simulated in the time domain using the following MOT schemes:

(a) collocation-in-time (second degree Lagrange interpolators, $\Delta t = 0.1$ ns) with nonmixed spatial discretization,
(b) collocation-in-time (second degree Lagrange interpolators, $\Delta t = 0.1$ ns) with mixed spatial discretization,
(c) second order Galerkin-in-time ($\Delta t = 0.2$ ns) with nonmixed spatial discretization,
(d) second order Galerkin-in-time ($\Delta t = 0.2$ ns) with mixed spatial discretization.

As no analytical solution is available, frequency domain EFIE simulations are performed for frequencies ranging from 30 to 1000 MHz, with steps of 30 MHz, and used as a reference solution. The relative $H_{div}^{-1/2}$ error e_r is computed for each of these frequencies (figure 3.9). For a number of discrete frequencies, the error peaks. This is due to the spurious resonances that plague the frequency domain EFIE. Indeed, the resonance frequencies of a cuboid with dimensions $x \times y \times z$ are [34]

$$f_{mnl} = c\sqrt{\left(\frac{m}{2x}\right)^2 + \left(\frac{n}{2y}\right)^2 + \left(\frac{l}{2z}\right)^2} \tag{3.35}$$

where m, n and l are integers. The largest peaks are located at 540 and 750 MHz, which are very close to the resonant frequencies of 540.46 and 749.48 MHz, respectively. Two small peaks are located at 420 and 630 MHz, which are due to the resonances at 423.97 and 618.04 MHz, respectively.

For low frequencies ($f < 200$ MHz), the error is dominated by the spatial discretization. In this frequency range, the mixed spatial discretization schemes are more accurate than the non-mixed ones. For higher frequencies, the error is dominated by the temporal discretization, and the temporal mixed Galerkin schemes are more accurate than the collocation schemes. Over the whole frequency range, the space-time mixed Galerkin scheme yields the most accurate results.

These results further support the conclusions drawn in sections 3.3 and 3.4: even for non-smooth geometries, the space-time mixed Galerkin scheme is significantly more accurate than the tradititial non-mixed collocation scheme.

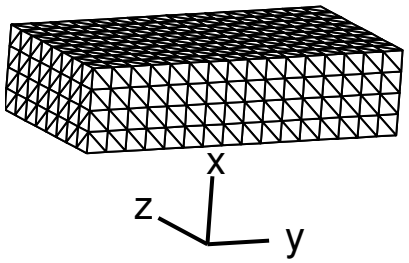

Figure 3.8: A cuboid with dimensions 0.25 by 1 by 0.5 meters, discretized using 896 right triangles. The incident electromagnetic field is propagating in the z-direction, while the electric field is polarized along the x-axis.

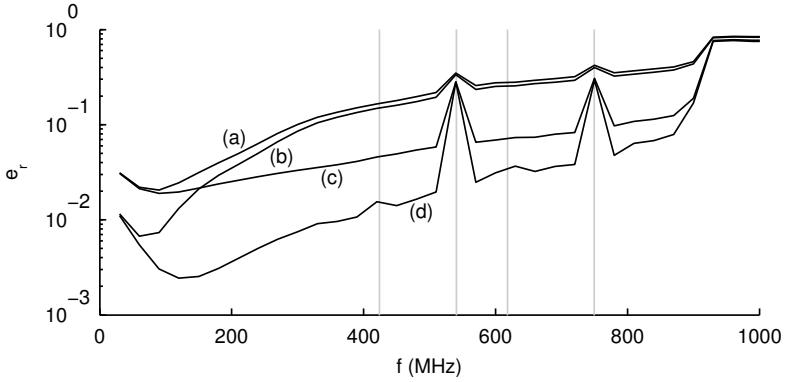

Figure 3.9: Relative $H_{\mathrm{div}}^{-1/2}$ error of the TD-CFIE simulations for scattering by a cuboid with respect to the frequency domain EFIE. The error peaks at the resonance frequencies of the cuboid, indicated by the vertical lines.

3.5.4 Scattering by an Ice Cream Cone

As a third example, scattering by the PEC ice cream cone depicted in figure 3.10 is simulated. Due to the sharp point, the geometry is even more singular than the cuboid. Again, the electric field is polarized along the x-axis, while the wave propagates along the z-axis. The current is approximated by an expansion in 1845 RWG basis functions.

The following time domain simulations were performed, with mesh parameter 3.14 cm, and time step $\Delta t = 0.5$ ns:

(a) collocation-in-time (third degree Lagrange interpolators) with nonmixed spatial discretization,
(b) collocation-in-time (third degree Lagrange interpolators) with mixed spatial discretization,
(c) first order Galerkin-in-time (third degree Lagrange interpolators) with nonmixed spatial discretization,
(d) first order Galerkin-in-time (third degree Lagrange interpolators) with mixed spatial discretization.

The relative $H_{\mathrm{div}}^{-1/2}$ error of the time domain results with respect to the frequency domain EFIE results is plotted in figure 3.11. In this frequency range, the FD-EFIE does not pick up any internal resonances. Similarly to the case of the cuboid, the accuracy at low frequencies is dominated by the spatial discretization. At high frequencies, it is dominated by the temporal discretization. Over the entire frequency range, the space-time mixed Galerkin scheme yields the most accurate results.

3.6 Conclusions

In this chapter, a space-time mixed Galerkin discretization for the TD-CFIE has been introduced. It is spatially a mixed Galerkin discretization in that both RWG and BC functions are used in order to obtain an accurate and conforming spatial discretization of the TD-CFIE. It is temporally a mixed Galerkin discretization in that different temporal basis and testing functions are used. The temporal mixed discretization has been defined for arbitrary order. The combination of the spatial and temporal mixed Galerkin discretization is essential in order to obtain accurate results over a broad frequency band. This was demonstrated for different numerical examples. Moreover, it has been shown that in order for the space-time mixed Galerkin discretization of the TD-CFIE to be immune to resonances, the TD-EFIE and TD-MFIE contributions need be made consistent by insertion of the appropriate Gram matrices.

Since the interactions in a temporally mixed Galerkin scheme can be identified with interactions in a collocation-in-time scheme, the space-time mixed Galerkin

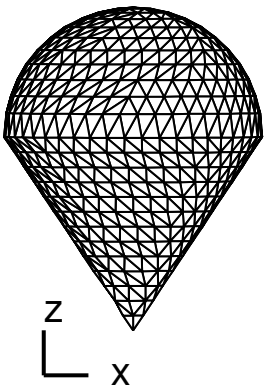

Figure 3.10: An ice cream cone discretized using 1230 triangles, with minimal edge length 3.14 cm. The radius of the top hemisphere is 0.3 m, the height of the cone is 0.4 m. The incident electromagnetic field is propagating in the z-direction, while the electric field is polarized along the x-axis.

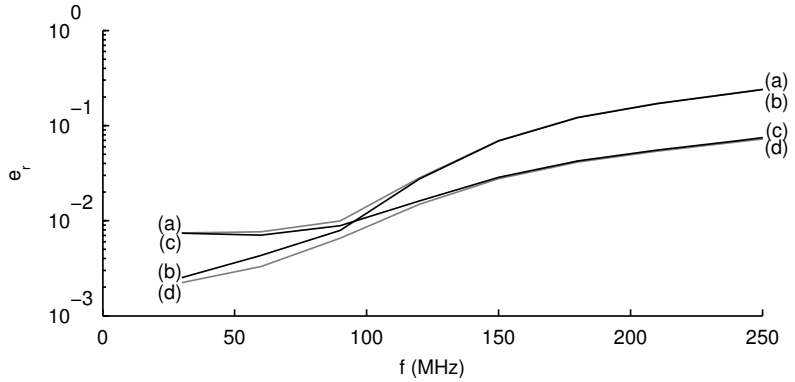

Figure 3.11: Relative $H_{\mathrm{div}}^{-1/2}$ error of the TD-CFIE simulations for scattering by an ice cream cone with respect to the frequency domain EFIE.

discretization can easily be incorporated in existing solvers. Furthermore, the scheme introduced in this chapter is amenable to acceleration by e.g. the PWTD algorithm [11].

References

[1] Y. Beghein, K. Cools, H. Bağcı, and D. De Zutter, "A space-time mixed Galerkin marching-on-in-time scheme for the time-domain combined field integral equation", *IEEE Transactions on Antennas and Propagation*, vol. 61, no. 3, pp. 1228–1238, Mar. 2013.

[2] J. R. Mautz and R. F. Harrington, "H-field, E-field, and combined-field solutions for conducting bodies of revolution", *Archiv Elektronik und Uebertragungstechnik*, vol. 32, pp. 157–164, Apr. 1978.

[3] S. Rao, D. Wilton, and A. Glisson, "Electromagnetic scattering by surfaces of arbitrary shape", *IEEE Transactions on Antennas and Propagation*, vol. 30, no. 3, pp. 409 –418, May 1982.

[4] B. Shanker, A. Ergin, K. Aygun, and E. Michielssen, "Analysis of transient electromagnetic scattering phenomena using a two-level plane wave time-domain algorithm", *IEEE Transactions on Antennas and Propagation*, vol. 48, no. 4, pp. 510 –523, Apr. 2000.

[5] K. Cools, F. P. Andriulli, D. De Zutter, and E. Michielssen, "Accurate and conforming mixed discretization of the MFIE", *IEEE Antennas and Wireless Propagation Letters*, vol. 10, pp. 528 –531, Oct. 2011.

[6] S. Yan, J.-M. Jin, and Z. Nie, "Improving the accuracy of the second-kind Fredholm integral equations by using the Buffa-Christiansen functions", *IEEE Transactions on Antennas and Propagation*, vol. 59, no. 4, pp. 1299 –1310, Apr. 2011.

[7] L. Gurel and O. Ergul, "Contamination of the accuracy of the combined-field integral equation with the discretization error of the magnetic-field integral equation", *IEEE Transactions on Antennas and Propagation*, vol. 57, no. 9, pp. 2650 –2657, Sep. 2009.

[8] A. Buffa and S. H. Christiansen, "A dual finite element complex on the barycentric refinement", *Comptes Rendus Mathematique*, vol. 340, no. 6, pp. 461 –464, 2005.

[9] F. P. Andriulli, K. Cools, H. Bağci, F. Olyslager, A. Buffa, S. Christiansen, and E. Michielssen, "A multiplicative Calderón preconditioner for the electric field integral equation", *IEEE Transactions on Antennas and Propagation*, vol. 56, pp. 2398–1930, Aug. 2008.

[10] K. Cools, F. P. Andriulli, P. Ylä-Oijala, H. Bağci, D. D. Zutter, and E. Michielssen, "Improving the accuracy of the Calderón preconditioned cfie by using a mixed discretization", in *IEEE International Symposium on Antennas and Propagation and CNC/USNC/URSI Radio Science Meeting*, Toronto, Canada, Jul. 2010.

[11] W. Chew, E. Michielssen, J. M. Song, and J. M. Jin, Eds., *Fast and Efficient Algorithms in Computational Electromagnetics*. Norwood, MA, USA: Artech House, Inc., 2001, isbn: 1580531520.

[12] A. Yilmaz, J.-M. Jin, and E. Michielssen, "Time domain adaptive integral method for surface integral equations", *IEEE Transactions on Antennas and Propagation*, vol. 52, no. 10, pp. 2692 –2708, Oct. 2004.

[13] T. Ha-Duong, "On retarded potential boundary integral equations and their discretisation", in *Topics in Computational Wave Propagation*, ser. Lecture Notes in Computational Science and Engineering, M. Ainsworth, P. Davies, D. Duncan, B. Rynne, and P. Martin, Eds., vol. 31, Springer Berlin Heidelberg, 2003, pp. 301–336, isbn: 978-3-642-55483-4.

[14] I. Terrasse, "Résolution mathématique et numérique des équations de Maxwell instationnaires par une méthode de potentiels retardés", PhD thesis, Ecole Polytechnique, 1993.

[15] W. C. Chew and J. M. Song, "Gedanken experiments to understand the internal resonance problems of electromagnetic scattering.", *Electromagnetics*, vol. 27, no. 8, pp. 457 –471, 2007.

[16] B. Shanker, A. Ergin, K. Aygun, and E. Michielssen, "Analysis of transient electromagnetic scattering from closed surfaces using a combined field integral equation", *IEEE Transactions on Antennas and Propagation*, vol. 48, no. 7, pp. 1064 –1074, Jul. 2000.

[17] B. Shanker, M. Lu, J. Yuan, and E. Michielssen, "Time domain integral equation analysis of scattering from composite bodies via exact evaluation of radiation fields", *IEEE Transactions on Antennas and Propagation*, vol. 57, no. 5, pp. 1506 –1520, May 2009.

[18] R. E. Hodges and Y. Rahmat-Samii, "The evaluation of MFIE integrals with the use of vector triangle basis functions", *Microwave and Optical Technology Letters*, vol. 14, no. 1, pp. 9–14, 1997.

[19] Y. Shi, M.-Y. Xia, R.-S. Chen, E. Michielssen, and M. Lu, "Stable electric field TDIE solvers via quasi-exact evaluation of MOT matrix elements", *IEEE Transactions on Antennas and Propagation*, vol. 59, no. 2, pp. 574 –585, Feb. 2011.

[20] A. G. Polimeridis and J. R. Mosig, "Complete semi-analytical treatment of weakly singular integrals on planar triangles via the direct evaluation method", *International Journal for Numerical Methods in Engineering*, vol. 83, no. 12, pp. 1625–1650, 2010.

[21] A. Yucel and A. Ergin, "Exact evaluation of retarded-time potential integrals for the RWG bases", *IEEE Transactions on Antennas and Propagation*, vol. 54, no. 5, pp. 1496 –1502, May 2006.

[22] H. Ulku and A. Ergin, "Application of analytical retarded-time potential expressions to the solution of time domain integral equations", *IEEE Transactions on Antennas and Propagation*, vol. 59, no. 11, pp. 4123 –4131, Nov. 2011.

[23] P. J. Davies, "Numerical stability and convergence of approximations of retarded potential integral equations", *SIAM Journal on Numerical Analysis*, vol. 31, no. 3, pp. 856–875, 1994.

[24] P. Davies and D. Duncan, "Numerical stability of collocation schemes for time domain boundary integral equations", in *Computational Electromagnetics*, ser. Lecture Notes in Computational Science and Engineering, C. Carstensen, S. Funken, W. Hackbusch, R. H. W. Hoppe, and P. Monk, Eds., vol. 28, Springer Berlin Heidelberg, 2003, pp. 51–67, isbn: 978-3-642-55745-3.

[25] S. Sauter and C. Schwab, *Boundary Element Methods*. Springer, 2010, isbn: 3540680926.

[26] O. Ergul and L. Gurel, "Investigation of the inaccuracy of the MFIE discretized with the RWG basis functions", in *Antennas and Propagation Society International Symposium, 2004. IEEE*, vol. 3, Jun. 2004, 3393 –3396 Vol.3.

[27] D. Weile, G. Pisharody, N.-W. Chen, B. Shanker, and E. Michielssen, "A novel scheme for the solution of the time-domain integral equations of electromagnetics", *IEEE Transactions on Antennas and Propagation*, vol. 52, no. 1, pp. 283 –295, Jan. 2004.

[28] G. Kaur and A. E. Yilmaz, "Accuracy - efficiency tradeoff of temporal basis functions for time-marching solvers", *Microwave and Optical Technology Letters*, vol. 53, no. 6, pp. 1343–1348, 2011.

[29] E. van 't Wout, H. van der Ven, D. R. van der Heul, and C. Vuik, "A provably stable MoT scheme based on quadratic spline basis functions", in *Antennas and Propagation Society International Symposium, 2012. APS '12. IEEE*, Jul. 2012.

[30] H. Arda Ülkü, I. Bogaert, K. Cools, F. P. Andriulli, and H. Bağcı, "On the low frequency behavior of the mixed discretized time domain magnetic field integral equation", in *USNC-URSI National Radio Science Meeting, 2012. USNC-URSI '12. IEEE*, Jul. 2012.

[31] A. Buffa and R. Hiptmair, "Regularized combined field integral equations", *Numer. Math.*, vol. 100, no. 1, pp. 1–19, Mar. 2005.

[32] O. Bruno, T. Elling, R. Paffenroth, and C. Turc, "Electromagnetic integral equations requiring small numbers of Krylov-subspace iterations", *J. Comput. Phys.*, vol. 228, no. 17, pp. 6169–6183, Sep. 2009.

[33] A. Buffa and P. Ciarlet, "On traces for functional spaces related to Maxwell's equations part I: An integration by parts formula in Lipschitz polyhedra", *Mathematical Methods in the Applied Sciences*, vol. 24, no. 1, pp. 9–30, 2001.

[34] J. Van Bladel, *Electromagnetic Fields*, 2nd ed., ser. IEEE press series on electromagnetic wave theory. Wiley-IEEE Press, 2007.

[35] R. F. Harrington, *Time-harmonic Electromagnetic Fields*. McGraw-Hill, 1961, pp. 269–270.

4

A DC Stable and Large Time Step Well-Balanced TD-EFIE Based on Quasi-Helmholtz Projectors

Y. Beghein, K. Cools and F.P. Andriulli

This chapter is based on an article published in
IEEE Transactions on Antennas and Propagation [1].

★ ★ ★

The marching-on-in-time solution of the time domain electric field integral equation (TD-EFIE) has traditionally suffered from a number of issues, including the emergence of spurious static currents (DC instability) and ill-conditioning at large time steps (low frequencies). In this contribution, a space-time Galerkin discretization of the TD-EFIE is proposed, which separates the loop and star components of both the equation and the unknown. Judiciously integrating or differentiating these components with respect to time leads to an equation which is free from DC instability. By choosing the correct temporal basis and testing functions for each of the components, a stable marching-on-in-time system is obtained. Furthermore, the scaling of these basis and testing functions ensures that the system

remains well-conditioned for large time steps. The loop-star decomposition is performed using quasi-Helmholtz projectors in order to avoid the explicit transformation to the unstable bases of loops and stars (or trees), and to avoid the search for global loops, which is a computationally expensive operation.

4.1 Introduction

Electromagnetic scattering by perfect electric conductors (PECs) can be modeled efficiently using boundary integral equations (BIEs). The two most prominent formulations are the electric field integral equation (EFIE) and the magnetic field integral equation (MFIE). This chapter focusses on the properties of the EFIE.

The EFIE can be formulated in either the frequency domain (FD-EFIE, for time-harmonic electromagnetic fields) or the time domain (TD-EFIE, for general time dependence). Whereas the FD-EFIE is solved at a single point on the frequency axis, the TD-EFIE requires a discretization of the time axis. Most often, a causal discretization scheme is chosen such that the resulting system of equations can be solved using the marching-on-in-time (MOT) algorithm [2], [3] (other approaches such as marching-on-in-order have been suggested, see e.g. [4]). The stability of the MOT algorithm hinges on both the accurate evaluation of the interaction integrals [5]–[8] and the choice of temporal discretization scheme [9]–[12]. Space-time Galerkin schemes have been found to produce good results in terms of stability, accuracy and extensibility to higher order in both space and time [11], [13]–[15].

Unfortunately, these schemes suffer from at least one of the following problems.

First, the TD-EFIE allows sourceless harmonic-in-time regime solutions. When the scatterer is closed, interior resonances can be excited (resonant instabilities) [16], [17]. Furthermore, it supports sourceless constant-in-time or linear-in-time divergence-free solutions (DC instabilities) [17], [18]. For simply connected geometries, DC instabilities can be eliminated by switching to the Calderón preconditioned TD-EFIE [19] and applying the so-called dot-trick [17]. However, for multiply connected geometries, the dot-trick EFIE still supports static solutions [20] and is therefore susceptible to DC instability.

Second, for large time steps Δt, the scaling of the blocks of the TD-EFIE operator that describe the electrostatic and and magnetostatic problems differs by a factor Δt^2, leading to an ill conditioned system matrix. The resulting system cannot be solved efficiently (using e.g. iterative techniques), which drastically increases the solution time. This phenomenon is termed low frequency breakdown [21], [22], and also occurs in the frequency domain, see e.g. [23], [24] and references therein.

Finally, the standard TD-EFIE involves the computation of the charge as the temporal integral of the current divergence at every time step. This computationally costly operation is often avoided by introducing an additional charge variable (at the cost of greater memory requirements), or by switching to the time-differentiated TD-EFIE (at the cost of introducing linear-in-time spurious loop currents to the solution).

Low frequency breakdown can be mitigated by applying a loop-star or loop-tree decomposition to the EFIE, and rescaling the components with the correct powers of Δt [22]. However, explicitly constructing a basis of loops and stars (or trees) leads to ill-conditioning [25]. Furthermore, for multiply connected surfaces, global loops must be detected, which is computationally expensive.

Linear-in-time spurious currents have also been tackled by applying a loop-tree decomposition to the time-differentiated TD-EFIE in [26]. While this does result in the elimination of the linear-in-time spurious currents, it does not solve constant-in-time DC instability. In [27], a loop-tree decomposition is used to filter out static loop modes after they emerge.

In this chapter, a novel formulation termed the quasi-Helmholtz Projected TD-EFIE (qHP-TDEFIE) is obtained by separating the quasi-Helmholtz components of both spatial basis and testing functions using the loop and star projectors introduced in [23], thereby eliminating the need to explicitly construct a loop-star basis. The loop and star parts of both the equation and the unknown are temporally integrated or differentiated in such a way that the resulting equation does not possess a static null space, and is therefore not susceptible to DC instability. Furthermore, it does not require the computation of the temporal integral of the current.

Next, the quasi-Helmholtz components of both the unknown and the equation are separately discretized in time using Galerkin methods. More specifically, the order of regularity of the basis and testing functions is matched to the order of differentiation of each component. This is necessary in order to obtain a stable MOT scheme. Furthermore, the scaling of the basis and testing functions is chosen such that system has a well-defined and well-conditioned low frequency limit. In addition, the interaction matrix elements needed in this scheme are compatible with matrix-vector product accelerators such as the PWTD method [28], [29].

This chapter is organized as follows. In section 4.2, the standard TD-EFIE is presented in order to fix the notations and definitions that will be used throughout the chapter. The properties of the resulting MOT algorithm are summarily reviewed. In section 4.3, the derivation of the new qHP-TDEFIE is presented and discussed. In section 4.4, the low frequency (large time step) limit of the resulting numerical scheme is investigated. Finally, a number of numerical experiments are performed in section 4.5 to demonstrate the favourable properties of the qHP-TDEFIE formulation, both in terms of DC stability and independence of the condition number on the time step size.

4.2 The Standard EFIE and Its Properties

4.2.1 The Time Domain EFIE

Consider the scattering problem discussed in section 1.2.9, featuring a perfectly conducting body Ω, whose boundary is denoted Γ. When an incident electric field $\boldsymbol{e}^i(\boldsymbol{r},t)$ impinges on it at $t>0$, a surface current $\boldsymbol{j}(\boldsymbol{r},t)$ is induced on Γ, that satisfies the time domain EFIE

$$\eta\left(\mathcal{T}\boldsymbol{j}\right)(\boldsymbol{r},t) = -\hat{\boldsymbol{n}}\times\boldsymbol{e}^i(\boldsymbol{r},t) \quad \forall \boldsymbol{r}\in\Gamma, t>0 \tag{4.1}$$

where the electric field integral operator (EFIO) $\mathcal{T}$ is defined as

$$\left(\mathcal{T}\boldsymbol{j}\right)(\boldsymbol{r},t) = \left(\mathcal{T}_s\boldsymbol{j}\right)(\boldsymbol{r},t) + \left(\mathcal{T}_h\boldsymbol{j}\right)(\boldsymbol{r},t) \tag{4.2}$$

$$\left(\mathcal{T}_s\boldsymbol{j}\right)(\boldsymbol{r},t) = -\frac{1}{c}\hat{\boldsymbol{n}}\times\int_\Gamma \frac{\partial_t\boldsymbol{j}(\boldsymbol{r}',\tau)}{4\pi R}ds' \tag{4.3}$$

$$\left(\mathcal{T}_h\boldsymbol{j}\right)(\boldsymbol{r},t) = c\;\hat{\boldsymbol{n}}\times p.v.\int_\Gamma \nabla\frac{\partial_t^{-1}\nabla'\cdot\boldsymbol{j}(\boldsymbol{r}',\tau)}{4\pi R}ds' \tag{4.4}$$

$\eta=\sqrt{\mu_0/\epsilon_0}$, $c=1/\sqrt{\epsilon_0\mu_0}$, $R=|\boldsymbol{r}-\boldsymbol{r}'|$, $\tau=t-R/c$, and $\hat{\boldsymbol{n}}$ is the exterior normal vector to Γ. Define $\partial_t^{-1}f(t)=\int_{-\infty}^t f(\tau)d\tau$.

Note that (4.1) in itself only defines the current $\boldsymbol{j}$ up to a constant solenoidal part. Uniqueness is achieved by imposing causality, i.e., all fields are assumed to vanish for $t<0$ in a neighborhood of Ω. Causality also guarantees that $\partial_t^{-1}f(t)=\int_{-\infty}^t f(\tau)d\tau$ is well defined.

4.2.2 Standard Galerkin Discretization

Following the procedure outlined in section 2.3.1, the surface Γ is now approximated by a triangle mesh with N_V vertices, N_S edges, and N_C cells. On this mesh, N_S Rao-Wilton-Glisson (RWG) functions are constructed [30]. Each RWG function $\boldsymbol{f}_m(\boldsymbol{r})$ is associated with one edge e_m (see figure 4.1), and is defined on the two adjacent cells c_m^+ and c_m^-:

$$\boldsymbol{f}_m(\boldsymbol{r}) = \begin{cases} \frac{\boldsymbol{r}-\boldsymbol{r}_m^+}{2A_{c_m^+}} & \text{for } \boldsymbol{r}\in c_m^+ \\ \frac{\boldsymbol{r}_m^- -\boldsymbol{r}}{2A_{c_m^-}} & \text{for } \boldsymbol{r}\in c_m^- \end{cases} \tag{4.5}$$

where $A_{c_m^+}$ and $A_{c_m^-}$ denote the area of cell c_m^+ and c_m^-, respectively. Note that this definition does not include edge length normalization as in [30], in order to simplify the notation in what follows.

The current $\boldsymbol{j}(\boldsymbol{r},t)$ is approximated as an expansion in these RWG functions:

$$\boldsymbol{j}(\boldsymbol{r},t) = \sum_{m=1}^{N_S} \mathsf{j}_m(t)\boldsymbol{f}_m(\boldsymbol{r}). \tag{4.6}$$

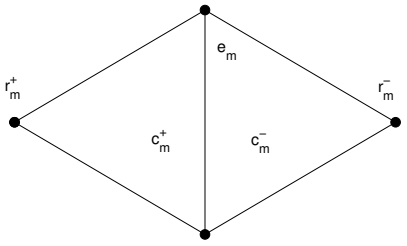

Figure 4.1: Two adjacent cells on which an RWG function is defined.

Next, (4.1) is spatially tested with the rotated RWG functions $\hat{\boldsymbol{n}} \times \boldsymbol{f}_m(\boldsymbol{r})$, $m = 1, 2, ..., N_S$:

$$\int_\Gamma (\hat{\boldsymbol{n}} \times \boldsymbol{f}_m(\boldsymbol{r})) \cdot (\text{equation (4.1)})\, ds. \tag{4.7}$$

By defining the following quantities:

$$\mathcal{Z} = \mathcal{Z}_s + \mathcal{Z}_h \tag{4.8a}$$

$$[(\mathcal{Z}_s \mathsf{j})(t)]_m = -\sum_n \frac{\eta}{c} \int_\Gamma ds\ \boldsymbol{f}_m \cdot \int_\Gamma ds'\ \frac{\partial_t \mathsf{j}_n(\tau) \boldsymbol{f}_n(\boldsymbol{r}')}{4\pi R} \tag{4.8b}$$

$$[(\mathcal{Z}_h \mathsf{j})(t)]_m = -\sum_n \eta c \int_\Gamma ds\ (\nabla \cdot \boldsymbol{f}_m(\boldsymbol{r})) \cdot \int_\Gamma ds'\ \frac{\partial_t^{-1} \mathsf{j}_n(\tau)\ \nabla' \cdot \boldsymbol{f}_n(\boldsymbol{r}')}{4\pi R} \tag{4.8c}$$

$$[\mathsf{e}(t)]_m = \int_\Gamma \boldsymbol{f}_m(\boldsymbol{r}) \cdot \boldsymbol{e}^i(\boldsymbol{r}, t)\ ds \tag{4.8d}$$

equation (4.7) can be concisely stated as

$$\mathcal{Z}\mathsf{j}(t) = -\mathsf{e}(t) \qquad \forall t > 0. \tag{4.9}$$

This equation is temporally discretized using a Galerkin method. More specifically, scheme 2b of section 2.3.3 is used. Alternatively, scheme 2a can also be used – see appendix 4.A. The RWG expansion coefficients $\mathsf{j}_m(t)$ are approximated by an expansion in pulse functions $p(t - i\Delta t)$ (figure 4.2, middle)

$$\mathsf{j}(t) = \sum_{i=1}^{N_T} \mathsf{j}_i p(t - i\Delta t) \tag{4.10}$$

$$p(t) = \begin{cases} 1 & t \in (-\Delta t, 0) \\ 0 & \text{otherwise} \end{cases} \tag{4.11}$$

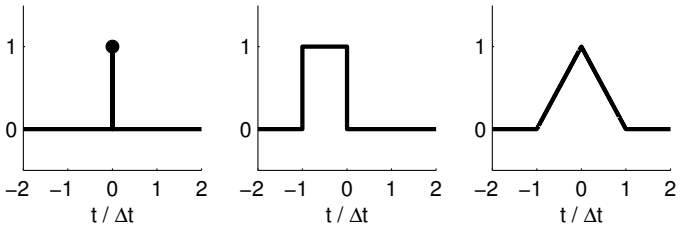

Figure 4.2: Temporal basis and testing functions: Dirac delta distribution $\delta(t)$ (left), pulse $p(t)$ (middle) and hat $h(t)$ (right).

and (4.9) is tested with pulses $p(t - j\Delta t)$:

$$\int_{\mathbb{R}} p(t - j\Delta t)\,(\text{equation (4.9)})\,dt \qquad j = 1, 2, 3, ..., N_T. \tag{4.12}$$

This can be written as

$$\sum_{i=0}^{j} \mathbf{Z}_i \mathsf{j}_{j-i} = -\mathsf{e}_j \qquad j = 1, 2, 3, ..., N_T \tag{4.13}$$

where

$$\mathsf{e}_j = \int_{\mathbb{R}} p(t - j\Delta t)\ \mathsf{e}(t) dt \tag{4.14}$$

and

$$\begin{aligned} [\mathbf{Z}_i]_{mn} &= \eta \int_{\mathbb{R}} dt\ p(t - i\Delta t) \int_{\Gamma} (\hat{\boldsymbol{n}} \times \boldsymbol{f}_m(\boldsymbol{r})) \cdot \mathcal{T}\left\{\boldsymbol{f}_n p\right\}(\boldsymbol{r}, t) ds \\ &= \Delta t \int_{\Gamma} (\hat{\boldsymbol{n}} \times \boldsymbol{f}_m(\boldsymbol{r})) \cdot \mathcal{T}\left\{\boldsymbol{f}_n h\right\}(\boldsymbol{r}, i\Delta t) ds. \end{aligned} \tag{4.15}$$

The hat function $h(t)$ (figure 4.2, right) is defined as

$$h(t) = \begin{cases} 1 + \frac{t}{\Delta t} & t \in (-\Delta t, 0) \\ 1 - \frac{t}{\Delta t} & t \in (0, \Delta t) \\ 0 & \text{otherwise} \end{cases}. \tag{4.16}$$

In (4.15), the interaction elements are transformed into the form encountered in traditional collocation-in-time methods. These integrals can be evaluated using techniques outlined in e.g. [5]–[8]. It is also possible to accelerate these computations using fast techniques such as PWTD [28], [29]. The system of linear equations (4.13) can be solved using the marching-on-in-time (MOT) method, as in section 2.3.1. To this end, it is recasted in the following form:

$$-\mathbf{Z}_0 \mathsf{j}_i = \sum_{j=1}^{i} \mathbf{Z}_j \mathsf{j}_{i-j} + \mathsf{e}_i \tag{4.17}$$

which is then successively solved for j_i, $i = 1, 2, ..., N_T$.

Because of the temporal integral in the hypersingular contribution, there are an unlimited number of matrices $\mathsf{Z}_i \neq 0$. The number of nonzero terms in the summation in the right hand side therefore grows without bound when the MOT algorithm progresses. The unbounded summation can be avoided by introducing the charge as an additional variable, see section 2.3.5 or e.g. [12] or [31]. This however leads to overhead in both memory requirements and computation time.

4.2.3 Null Space of the Discretized EFIO

In sections 2.3.4 and 4.2.1, it was noted that the sourceless EFIE supports constant solenoidal regime solutions. This property is conserved by the discretization procedure: if j_L is a solenoidal current,

$$\sum_{j=0}^{\infty} \mathsf{Z}_j \mathsf{j}_L = 0. \tag{4.18}$$

In the continuous case, an energy argument shows that late time constant signals cannot be part of the solution. Indeed, all energy in the incident wave is reflected during scattering, leaving no energy to sustain a residual magnetostatic field. In the discrete case, the finite precision of the numerical scheme allows static loop currents to creep into the solution, after which they persist throughout the simulation [18].

Even though the solution to the discrete EFIE will always be an approximation of the exact solution, it is possible to design a scheme that explicitly coerces late time energy conservation and thus cannot support DC signals in the tail of the approximate solution. In practice this property can be checked by inspecting the expressions for the interaction elements and keeping track of the explicit appearance of divergence and differentation operators. In the next section, the EFIE is rewritten and discretized in such a way that the resulting discrete system does not sustain constant-in-time regime solutions.

4.3 The Quasi-Helmholtz Projected TD-EFIE

4.3.1 Separation of the Quasi-Helmholtz Components

In [23], the quasi-Helmholtz components (i.e., the divergence-free and weakly curl-free components) of the FD-EFIE are separated not by explicitly constructing a loop-star basis, but using projectors $\mathsf{P}^{\Lambda H}$ and P^{Σ}, as discussed in section 2.2.6.

Consider a triangle mesh consisting of N_C cells, on which N_S RWG functions $\boldsymbol{f}_m(\boldsymbol{r})$ are defined. Each RWG function $\boldsymbol{f}_m(\boldsymbol{r})$ is defined on two cells, c_m^+ and c_m^- (see figure 4.1), and represents a current flowing from c_m^+ to c_m^-. The $N_S \times N_C$ star coefficient matrix is given by

$$\Sigma_{ij} = \begin{cases} 1 & \text{if cell } j \text{ equals } c_i^+ \\ -1 & \text{if cell } j \text{ equals } c_i^- \\ 0 & \text{otherwise} \end{cases}. \tag{4.19}$$

Note that Σ^T is the discrete divergence operator in a basis of RWG functions for the current, and cellwise constant functions for the charge. Projection onto the star space is then achieved using the projector

$$\mathsf{P}^{\Sigma} = \Sigma \left(\Sigma^T \Sigma\right)^+ \Sigma^T \tag{4.20}$$

where $\left(\Sigma^T \Sigma\right)^+$ denotes the pseudoinverse of $\Sigma^T \Sigma$. A pseudoinverse is required because the vector $(1\ 1\ ...\ 1)^T$ is in the kernel of Σ. Computing this pseudoinverse using standard techniques would require $\mathcal{O}(N_c^3)$ operations. Section V of [23], however, explains how this computation can be done in linear time using techniques developed in [25]. As a result, for any $N_S \times 1$ vector c, the matrix-vector product $\mathsf{P}^{\Sigma}\mathsf{c}$ can be computed in $\mathcal{O}(N_S)$ operations.

The operator $\mathsf{P}^{\Lambda H}$ projects onto the space of divergence-free expansion coefficients: $\Sigma^T \mathsf{P}^{\Lambda H} = 0$. Therefore, $\mathsf{P}^{\Sigma}\mathsf{P}^{\Lambda H} = \mathsf{P}^{\Lambda H}\mathsf{P}^{\Sigma} = 0$. This also means that the loop-star decomposition is coefficient-wise orthogonal. $\mathsf{P}^{\Lambda H}$ can easily be found as

$$\mathsf{P}^{\Lambda H} = 1 - \mathsf{P}^{\Sigma}. \tag{4.21}$$

In this way, the detection of global loops is avoided.

4.3.2 Elimination of the Static Null Space

The quasi-Helmholtz projectors $\mathbf{P}^{\Lambda H}$ and $\mathbf{P}^{\Sigma}$ are now applied to both the test and trial side of the semi-discrete TD-EFIE (4.9):

$$\begin{pmatrix}\mathbf{P}^{\Lambda H} & \mathbf{P}^{\Sigma}\end{pmatrix}\begin{pmatrix}\mathcal{Z}_s & \mathcal{Z}_s\\ \mathcal{Z}_s & \mathcal{Z}_s+\mathcal{Z}_h\end{pmatrix}\begin{pmatrix}\mathbf{P}^{\Lambda H}\\ \mathbf{P}^{\Sigma}\end{pmatrix}\mathsf{j}(t)=-\mathsf{e}(t) \tag{4.22}$$

where the property $\mathcal{Z}_h\mathbf{P}^{\Lambda H}=\mathbf{P}^{\Lambda H}\mathcal{Z}_h=0$ has been used. The operator $\mathcal{Z}_h$ (equation (4.8c)) requires the evaluation of a temporal integral. This is avoided by introducing an auxiliary unknown $\mathsf{y}(t)$:

$$\begin{aligned}&\mathsf{y}(t)=\left(\partial_t^{-1}\mathbf{P}^{\Sigma}+\mathbf{P}^{\Lambda H}\right)\mathsf{j}(t)\\ \iff\quad &\mathsf{j}(t)=\left(\partial_t\mathbf{P}^{\Sigma}+\mathbf{P}^{\Lambda H}\right)\mathsf{y}(t)\end{aligned} \tag{4.23}$$

satisfying

$$\begin{pmatrix}\mathbf{P}^{\Lambda H} & \mathbf{P}^{\Sigma}\end{pmatrix}\begin{pmatrix}\mathcal{Z}_s & \partial_t\mathcal{Z}_s\\ \mathcal{Z}_s & \partial_t\mathcal{Z}_s+\partial_t\mathcal{Z}_h\end{pmatrix}\begin{pmatrix}\mathbf{P}^{\Lambda H}\\ \mathbf{P}^{\Sigma}\end{pmatrix}\mathsf{y}(t)=-\mathsf{e}(t). \tag{4.24}$$

The operator $\mathcal{Z}_s$ involves a temporal differentiation, which annihilates constant-in-time currents. Therefore, constant loop currents reside in the null space of the operator on the left hand side of (4.24). This is resolved by temporally integrating the loop part of (4.24):

$$\mathcal{Z}'\mathsf{y}(t)=-\left(\partial_t^{-1}\mathbf{P}^{\Lambda H}+\mathbf{P}^{\Sigma}\right)\mathsf{e}(t) \tag{4.25}$$

$$\mathcal{Z}' = \begin{pmatrix}\mathbf{P}^{\Lambda H} & \mathbf{P}^{\Sigma}\end{pmatrix}\begin{pmatrix}\partial_t^{-1}\mathcal{Z}_s & \mathcal{Z}_s\\ \mathcal{Z}_s & \partial_t\mathcal{Z}_s+\partial_t\mathcal{Z}_h\end{pmatrix}\begin{pmatrix}\mathbf{P}^{\Lambda H}\\ \mathbf{P}^{\Sigma}\end{pmatrix} \tag{4.26}$$

$$= \left(\partial_t^{-1}\mathbf{P}^{\Lambda H}+\mathbf{P}^{\Sigma}\right)\mathcal{Z}\left(\mathbf{P}^{\Lambda H}+\partial_t\mathbf{P}^{\Sigma}\right). \tag{4.27}$$

Equation (4.25) is the semi-discrete quasi-Helmholtz projected TD-EFIE or qHP-TDEFIE. Note, however, that it is still continuous in time. A suitable discretization strategy is developed in the next section.

The operator $\mathcal{Z}'$ is constructed in such way that it does not require the evaluation of a temporal integral, and it does not annihilate static loop currents. It is, in essence, the inverse Fourier transform of the modified EFIE operator proposed in [23], up to irrelevant sign conventions. An alternative method to obtain this operator is explored in appendix 4.A.

For slowly varying fields, the off-diagonal components as well as $\partial_t\mathcal{Z}_s$ in the lower right block of (4.26) become negligible. The remaining dominant contributions ($\partial_t^{-1}\mathcal{Z}_s$ and $\partial_t\mathcal{Z}_h$) do neither contain explicit temporal differentiations or integrations. These diagonal terms have a physical meaning: $\partial_t^{-1}\mathcal{Z}_s$ represents the electromagnetic vector potential, and $\partial_t\mathcal{Z}_h$ the electromagnetic scalar potential.

4.3.3 Temporal Discretization

Next, the qHP-TDEFIE (4.25) is discretized in time. In section 4.2, $\mathsf{j}(t)$ was expanded in pulses. This implies that

$$\begin{aligned} \mathsf{y}(t) &= \left(\partial_t^{-1}\mathbf{P}^{\Sigma} + \mathbf{P}^{\Lambda H}\right)\mathsf{j}(t) && (4.28)\\ &= \sum_{i=1}^{N_T}\left(p(t-i\Delta t)\mathbf{P}^{\Lambda H} + \partial_t^{-1}p(t-i\Delta t)\mathbf{P}^{\Sigma}\right)\mathsf{j}_i. && (4.29)\end{aligned}$$

The testing coefficients are transformed in a similar way.

$$\begin{aligned} \mathsf{t}_i &= \int_{\mathbb{R}} p(t-i\Delta t)\mathcal{Z}\mathsf{j}(t)\ dt && (4.30)\\ &= \int_{\mathbb{R}} p(t-i\Delta t)\left(\partial_t\mathbf{P}^{\Lambda H} + \mathbf{P}^{\Sigma}\right)\mathcal{Z}'\mathsf{y}(t)dt && (4.31)\\ &= \int_{\mathbb{R}}\left(-\partial_t p(t-i\Delta t)\mathbf{P}^{\Lambda H} + p(t-i\Delta t)\mathbf{P}^{\Sigma}\right)\mathcal{Z}'\mathsf{y}(t)dt. && (4.32)\end{aligned}$$

Applying this discretization scheme to the qHP-TDEFIE would, however, result in the same system as in section 4.2. In particular, the resulting MOT algorithm would also suffer from DC instability. This is due to the testing functions

$$-\partial_t p(t-i\Delta t) = \delta\left(t-(i-1)\Delta t\right) - \delta\left(t-i\Delta t\right)$$

which act as discrete derivatives. Furthermore, the number of nonzero $\mathbf{Z}$-matrices would be infinite due to the infinite support of the expansion function $\partial_t^{-1}p(t-i\Delta t)$. Finally also the scaling of the two blocks remains unchanged and leads to a condition number that scales like Δt^2 at large time steps (see section 4.4).

All these issues can be solved by directly discretizing (4.25) rather than inheriting the discretization of the classic TD-EFIE (4.9). More specifically:

$$\begin{aligned} \mathsf{y}(t) &= \sum_{i=1}^{N_T}\left(p(t-i\Delta t)\mathbf{P}^{\Lambda H} + h(t-i\Delta t)\mathbf{P}^{\Sigma}\right)\mathsf{y}_i && (4.33)\\ \mathsf{y}_i &= \Delta t\sum_{j=1}^{i}\mathbf{P}^{\Sigma}\mathsf{j}_j + \mathbf{P}^{\Lambda H}\mathsf{j}_i && (4.34)\\ \mathsf{r}_i &= \int_{\mathbb{R}}\left(\delta(t-i\Delta t)\mathbf{P}^{\Lambda H} + \frac{1}{\Delta t}p(t-i\Delta t)\mathbf{P}^{\Sigma}\right)\mathcal{Z}'\mathsf{y}(t)dt\\ &= \frac{1}{\Delta t}\mathbf{P}^{\Sigma}\mathsf{t}_i - \sum_{j=1}^{i}\mathbf{P}^{\Lambda H}\mathsf{t}_j. && (4.35)\end{aligned}$$

In this discretization scheme, the loop part and the star part of $\mathsf{y}(t)$ are expanded in pulse functions $p(t-i\Delta t)$ (figure 4.2, middle) and hat functions $h(t-i\Delta t)$

(figure 4.2, right), respectively. The loop part and the star part of $\mathcal{Z}'$ are tested with Dirac delta distributions $\delta(t - i\Delta t)$ (figure 4.2, left) and pulses, respectively. Note that the basis functions of both Helmholtz components can represent the constant-in-time function and that the testing functions of neither of the Helmholtz components disappears when applied to constant-in-time functions. The basis functions of both Helmholtz components of $\mathsf{y}(t)$ are normalized to 1. The testing functions of both Helmholtz components are also scaled equally in the sense that both $\int_{\mathbb{R}} \delta(t)dt$ and $\int_{\mathbb{R}} \frac{1}{\Delta t} p(t)dt$ equal 1. This is the origin of the factor $\frac{1}{\Delta t}$ in (4.35). The global factor Δt in (4.34) is not necessary for balancing, but results in a well defined limit for the system matrices at large time steps, as will be detailed in section 4.4.

This expansion and testing scheme is now applied to the qHP-TDEFIE (4.25).

$$\int_{\mathbb{R}} \left(\delta(t - j\Delta t)\mathbf{P}^{\Lambda H} + \frac{1}{\Delta t} p(t - j\Delta t)\mathbf{P}^{\Sigma} \right) (\text{equation (4.25)}) \; dt \tag{4.36}$$

for $j = 1, 2, ..., N_T$, or

$$-\mathbf{Z}'_0 \mathsf{y}_j = \sum_{i=1}^{j} \mathbf{Z}'_i \mathsf{y}_{j-i} + \mathsf{e}'_j \tag{4.37}$$

where the matrices $\mathbf{Z}'_i$ are constructed from four components

$$\mathbf{Z}'_i = \begin{pmatrix} \mathbf{P}^{\Lambda H} & \mathbf{P}^{\Sigma} \end{pmatrix} \begin{pmatrix} \mathbf{Z}'^{LL}_i & \mathbf{Z}'^{LS}_i \\ \mathbf{Z}'^{SL}_i & \mathbf{Z}'^{SS}_i \end{pmatrix} \begin{pmatrix} \mathbf{P}^{\Lambda H} \\ \mathbf{P}^{\Sigma} \end{pmatrix} \tag{4.38}$$

$$\begin{aligned} \left[\mathbf{Z}'^{SS}_i\right]_{mn} &= \frac{\eta}{\Delta t} \int_{\mathbb{R}} dt \; p(t - i\Delta t) \int_{\Gamma} ds \; (\hat{\boldsymbol{n}} \times \boldsymbol{f}_m(\boldsymbol{r})) \cdot \partial_t \mathcal{T} \{\boldsymbol{f}_n h\} (\boldsymbol{r}, t) \\ &= \eta \int_{\Gamma} ds \; (\hat{\boldsymbol{n}} \times \boldsymbol{f}_m(\boldsymbol{r})) \cdot \partial_t \mathcal{T} \{\boldsymbol{f}_n q\} (\boldsymbol{r}, i\Delta t) \end{aligned} \tag{4.39a}$$

$$\begin{aligned} \left[\mathbf{Z}'^{SL}_i\right]_{mn} &= \frac{\eta}{\Delta t} \int_{\mathbb{R}} dt \; p(t - i\Delta t) \int_{\Gamma} ds \; (\hat{\boldsymbol{n}} \times \boldsymbol{f}_m(\boldsymbol{r})) \cdot \mathcal{T}_s \{\boldsymbol{f}_n p\} (\boldsymbol{r}, t) \\ &= \eta \int_{\Gamma} ds \; (\hat{\boldsymbol{n}} \times \boldsymbol{f}_m(\boldsymbol{r})) \cdot \mathcal{T}_s \{\boldsymbol{f}_n h\} (\boldsymbol{r}, i\Delta t) \end{aligned} \tag{4.39b}$$

$$\begin{aligned} \left[\mathbf{Z}'^{LS}_i\right]_{mn} &= \eta \int_{\mathbb{R}} dt \; \delta(t - i\Delta t) \int_{\Gamma} ds \; (\hat{\boldsymbol{n}} \times \boldsymbol{f}_m(\boldsymbol{r})) \cdot \mathcal{T}_s \{\boldsymbol{f}_n h\} (\boldsymbol{r}, t) \\ &= \eta \int_{\Gamma} ds \; (\hat{\boldsymbol{n}} \times \boldsymbol{f}_m(\boldsymbol{r})) \cdot \mathcal{T}_s \{\boldsymbol{f}_n h\} (\boldsymbol{r}, i\Delta t) \end{aligned} \tag{4.39c}$$

$$\begin{aligned} \left[\mathbf{Z}'^{LL}_i\right]_{mn} &= \eta \int_{\mathbb{R}} dt \; \delta(t - i\Delta t) \int_{\Gamma} ds \; (\hat{\boldsymbol{n}} \times \boldsymbol{f}_m(\boldsymbol{r})) \cdot \partial_t^{-1} \mathcal{T}_s \{\boldsymbol{f}_n p\} (\boldsymbol{r}, t) \\ &= \eta \int_{\Gamma} ds \; (\hat{\boldsymbol{n}} \times \boldsymbol{f}_m(\boldsymbol{r})) \cdot \partial_t^{-1} \mathcal{T}_s \{\boldsymbol{f}_n p\} (\boldsymbol{r}, i\Delta t) \end{aligned} \tag{4.39d}$$

$$q(t) \quad = \quad \frac{1}{\Delta t}\int_{\mathbb{R}} p(\tau)h(t+\tau)d\tau. \tag{4.39e}$$

The excitation vector e'_j is given by

$$\mathsf{e}'_j = \int_{\mathbb{R}} \left(\delta(t-j\Delta t)\partial_t^{-1}\mathbf{P}^{\Lambda H} + \frac{1}{\Delta t}p(t-j\Delta t)\mathbf{P}^{\Sigma}\right)\mathsf{e}(t)\ dt. \tag{4.40}$$

Once the expansion coefficients y_i are found, the physical current $\boldsymbol{j}(\boldsymbol{r},t)$ on Γ can be computed as

$$\boldsymbol{j}(\boldsymbol{r},t) \quad = \quad \sum_{m=1}^{N_S}\sum_{i=1}^{N_T}[\mathsf{j}_i]_m\ \ p(t-j\Delta t)\boldsymbol{f}_m(\boldsymbol{r}) \tag{4.41}$$

$$\mathsf{j}_i \quad = \quad \mathbf{P}^{\Lambda H}\mathsf{y}_i + \mathbf{P}^{\Sigma}\frac{1}{\Delta t}\left(\mathsf{y}_i - \mathsf{y}_{i-1}\right). \tag{4.42}$$

The use of different temporal basis and testing functions for the loop and star components is necessary to obtain a stable MOT scheme. If $y(t)$ is expanded in a single set of basis functions ($h(t-i\Delta t)$ or $p(t-i\Delta t)$), and (4.25) is tested with a single set of testing functions ($p(t-i\Delta t)$ or $\delta(t-i\Delta t)$), high frequency instabilities are encountered. When a stability analysis is conducted as in [17], the eigenvalues of the companion matrix are not confined to the unit circle, indicating that the scheme is unstable.

The discretization scheme in (4.39a) corresponds to scheme 1b in section 2.3.3. Likewise, (4.39b) corresponds to scheme 2b and (4.39c) to scheme 2a. The discretization procedure used in (4.39d) is a logical extension of these schemes.

In contrast to $\mathcal{Z}$, $\mathcal{Z}'$ does not contain a temporal integral. As a consequence, the number of nonzero matrices $\mathbf{Z}'_i$ is finite in this scheme. No further manipulations or auxiliary quantities are required.

The integrals (4.39a)-(4.39d) can be interpreted as the interactions which are also found in traditional collocation-in-time schemes, meaning that they can be accelerated using fast techniques such as PWTD [28], [29].

4.3.4 Static Null Space

Consider a constant solenoidal current $\boldsymbol{j}(\boldsymbol{r},t) = \boldsymbol{j}_L(\boldsymbol{r})$, $\nabla \cdot \boldsymbol{j}_L(\boldsymbol{r}) = 0$, with RWG expansion coefficients $\mathsf{j}_i = \mathsf{j}_L = \mathsf{P}^{\Lambda H}\mathsf{j}_L$. This current is annihilated by the TD-EFIE operator, in the continuous as well as the discrete setting:

$$\begin{aligned} (\mathcal{T}\boldsymbol{j})(\boldsymbol{r},t) &= 0 \quad \forall t>0, \forall \boldsymbol{r}\in\Gamma && (4.43)\\ (\mathcal{Z}\mathsf{j})(t) &= 0 \quad \forall t>0 && (4.44)\\ \sum_{j=0}^{i}\mathsf{Z}_j\mathsf{j}_{i-j} &= 0 \quad i=0,1,2,... && (4.45)\end{aligned}$$

This is the origin of the DC instability encountered in standard TD-EFIE simulations.

For solenoidal currents, $\mathsf{j}(t) = \mathsf{y}(t)$ and $\mathsf{j}_i = \mathsf{y}_i$. These functions are not annihilated by the qHP-TDEFIE operator:

$$(\mathcal{Z}'\mathsf{y})(t) \neq 0 \quad \forall t>0. \tag{4.46}$$

Moreover, because the trial functions can resolve constant-in-time functions, this property is conserved upon temporal discretization. Therefore, the qHP-TDEFIE does not allow constant-in-time solenoidal currents as sourceless regime solutions. This immediately implies that the qHP-TDEFIE is not susceptible to DC instabilities.

4.4 Low Frequency Limit

In this section, the low frequency limits of the system matrices Z_0 (standard TD-EFIE, section 4.2) and Z'_0 (qHP-TDEFIE, section 4.3) are investigated. For this, the scatterer is assumed to be small, i.e., with diameter $D \ll c\Delta t$.

4.4.1 Low Frequency Limit of the Standard TD-EFIE

The TD-EFIE system matrix is split into a singular and a hypersingular part

$$\begin{aligned} \mathsf{Z}_0 &= \mathsf{Z}_0^s + \mathsf{Z}_0^h && (4.47)\\ [\mathsf{Z}_0^s]_{mn} &= \eta\int_{\mathbb{R}} dt\; p(t)\int_\Gamma (\hat{\boldsymbol{n}}\times\boldsymbol{f}_m(\boldsymbol{r}))\cdot\mathcal{T}_s\{\boldsymbol{f}_n p\}(\boldsymbol{r},t)ds\\ &= \eta\,\Delta t\int_\Gamma (\hat{\boldsymbol{n}}\times\boldsymbol{f}_m(\boldsymbol{r}))\cdot\mathcal{T}_s\{\boldsymbol{f}_n h\}(\boldsymbol{r},0)ds && (4.48)\\ \left[\mathsf{Z}_0^h\right]_{mn} &= \eta\int_{\mathbb{R}} dt\; p(t)\int_\Gamma (\hat{\boldsymbol{n}}\times\boldsymbol{f}_m(\boldsymbol{r}))\cdot\mathcal{T}_h\{\boldsymbol{f}_n p\}(\boldsymbol{r},t)ds\\ &= \eta\,\Delta t\int_\Gamma (\hat{\boldsymbol{n}}\times\boldsymbol{f}_m(\boldsymbol{r}))\cdot\mathcal{T}_h\{\boldsymbol{f}_n h\}(\boldsymbol{r},0)ds. && (4.49)\end{aligned}$$

Here we used the fact that a temporal Galerkin scheme is equivalent to a collocation scheme with as effective basis function the anti-convolution of the basis and testing function of the Galerkin scheme (see (4.15)). Assuming that $D \ll c\Delta t$, the integrand of (4.48) is constant in time:

$$\partial_t h(0 - R/c) = \frac{1}{\Delta t} \quad \text{for} \quad R < c\Delta t. \tag{4.50}$$

Therefore,

$$\begin{aligned} [\mathbf{Z}_0^s]_{mn} &= -\mu\ \Delta t \int_\Gamma ds \boldsymbol{f}_m(\boldsymbol{r}) \cdot \int_\Gamma ds' \frac{\boldsymbol{f}_n(\boldsymbol{r}')\partial_t h(-R/c)}{4\pi R} \\ &= -\mu \int_\Gamma ds\ \boldsymbol{f}_m(\boldsymbol{r}) \cdot \int_\Gamma ds'\ \frac{\boldsymbol{f}_n(\boldsymbol{r}')}{4\pi R} \\ &= [\mathbf{Z}_{\text{stat}}^s]_{mn} \end{aligned} \tag{4.51}$$

where $\mathbf{Z}_{\text{stat}}^s$ is the RWG discretization of the static vector potential, which is independent of Δt. For the hypersingular part, the time dependence of the integrand of (4.49) can be approximated by a Taylor series:

$$\partial_t^{-1} h(0 - R/c) = \Delta t \left(\frac{1}{2} + \mathcal{O}\left(\frac{R}{c\Delta t} \right) \right) \tag{4.52}$$

leading to

$$\begin{aligned} \left[\mathbf{Z}_0^h\right]_{mn} &= -\frac{\Delta t}{\epsilon} \int_\Gamma ds\ \nabla \cdot \boldsymbol{f}_m(\boldsymbol{r})\ p.v. \int_\Gamma ds' \frac{\nabla' \cdot \boldsymbol{f}_n(\boldsymbol{r}')\partial_t^{-1} h(-R/c)}{4\pi R} \\ &= \Delta t^2 \left(\frac{1}{2} \left[\mathbf{Z}_{\text{stat}}^h\right]_{mn} + \mathcal{O}\left(\frac{D}{c\Delta t} \right) \right) \end{aligned} \tag{4.53}$$

$$\left[\mathbf{Z}_{\text{stat}}^h\right]_{mn} = -\frac{1}{\epsilon} \int_\Gamma ds\ \nabla \cdot \boldsymbol{f}_m(\boldsymbol{r}) \int_\Gamma ds'\ \frac{\nabla' \cdot \boldsymbol{f}_n(\boldsymbol{r}')}{4\pi R} \tag{4.54}$$

where $\mathbf{Z}_{\text{stat}}^h$ is the RWG discretization of the static scalar potential, which is also independent of Δt.

Thus, for $c\Delta t \to +\infty$, and considering that $\mathbf{Z}_0^h = \mathbf{P}^\Sigma \mathbf{Z}_0^h \mathbf{P}^\Sigma$,

$$\mathbf{Z}_0 \quad \to \quad \mathbf{Z}_{\text{stat}}^s + \mathcal{O}\left(\frac{D}{c\Delta t} \right) + \Delta t^2 \mathbf{P}^\Sigma \left(\frac{1}{2} \mathbf{Z}_{\text{stat}}^h + \mathcal{O}\left(\frac{D}{c\Delta t} \right) \right) \mathbf{P}^\Sigma \tag{4.55}$$

or

$$\mathbf{Z}_0 \to \begin{pmatrix} \mathbf{P}^{\Lambda H} & \mathbf{P}^\Sigma \end{pmatrix} \begin{pmatrix} \mathcal{O}(1) & \mathcal{O}(1) \\ \mathcal{O}(1) & \mathcal{O}(\Delta t^2) \end{pmatrix} \begin{pmatrix} \mathbf{P}^{\Lambda H} \\ \mathbf{P}^\Sigma \end{pmatrix} \tag{4.56}$$

which leads to a condition number that grows proportionally to Δt^2. In [22], this ill-conditioning is resolved for simply connected structures by scaling the spatial local loop functions proportionally to Δt.

4.4.2 Low Frequency Limit of the qHP-TDEFIE

The same approach is applied to the four components of the qHP-TDEFIE. First, the loop-loop-part (4.39d):

$$\begin{aligned}\left[\mathbf{Z}_0'^{LL}\right]_{mn} &= \eta \int_\Gamma ds\ (\hat{\boldsymbol{n}} \times \boldsymbol{f}_m(\boldsymbol{r})) \cdot \partial_t^{-1} \mathcal{T}_s \left\{\boldsymbol{f}_n p\right\}(\boldsymbol{r}, 0) \\ &= -\mu \int_\Gamma ds\ \boldsymbol{f}_m(\boldsymbol{r}) \cdot \int_\Gamma ds'\ \frac{\boldsymbol{f}_n(\boldsymbol{r}')\ p(0 - R/c)}{4\pi R}. \end{aligned} \tag{4.57}$$

Since the scatterer has diameter $D < c\Delta t$,

$$\left[\mathbf{Z}_0'^{LL}\right]_{mn} = -\mu \int_\Gamma ds\ \boldsymbol{f}_m(\boldsymbol{r}) \cdot \int_\Gamma ds'\ \frac{\boldsymbol{f}_n(\boldsymbol{r}')}{4\pi R} \tag{4.58}$$

$$= [\mathbf{Z}^s_{\text{stat}}]_{mn}\,. \tag{4.59}$$

The star-loop part (4.39b) and loop-star part (4.39c) are, up to a factor Δt, equal to $\mathbf{Z}_0^s$ (4.51):

$$\left[\mathbf{Z}_0'^{LS}\right]_{mn} = \left[\mathbf{Z}_0'^{SL}\right]_{mn} = \frac{1}{\Delta t}\,[\mathbf{Z}^s_0]_{mn} = \frac{1}{\Delta t}\,[\mathbf{Z}^s_{\text{stat}}]_{mn}\,. \tag{4.60}$$

Finally, the star-star part is split in two contributions

$$\left[\mathbf{Z}_0'^{SS}\right]_{mn} = \left[\mathbf{Z}_{s,0}'^{SS}\right]_{mn} + \left[\mathbf{Z}_{h,0}'^{SS}\right]_{mn} \tag{4.61}$$

$$\left[\mathbf{Z}_{h,0}'^{SS}\right]_{mn} = \eta \int_\Gamma ds\ (\hat{\boldsymbol{n}} \times \boldsymbol{f}_m(\boldsymbol{r})) \cdot \partial_t \mathcal{T}_h \left\{\boldsymbol{f}_n q\right\}(\boldsymbol{r}, 0)$$

$$\left[\mathbf{Z}_{s,0}'^{SS}\right]_{mn} = \eta \int_\Gamma ds\ (\hat{\boldsymbol{n}} \times \boldsymbol{f}_m(\boldsymbol{r})) \cdot \partial_t \mathcal{T}_s \left\{\boldsymbol{f}_n q\right\}(\boldsymbol{r}, 0).$$

The time dependence of these integrands can be approximated as follows, for $R/c \ll \Delta t$:

$$q(0 - R/c) = \frac{1}{2} + \mathcal{O}\left(\frac{R}{c\Delta t}\right) \tag{4.62}$$

$$\partial_t^2 q(0 - R/c) = \frac{1}{\Delta t^2}. \tag{4.63}$$

Then,

$$\left[\mathbf{Z}_{s,0}'^{SS}\right]_{mn} = \frac{1}{\Delta t^2}\,[\mathbf{Z}^s_{\text{stat}}]_{mn} \tag{4.64}$$

$$\left[\mathbf{Z}_{h,0}'^{SS}\right]_{mn} = -\epsilon \int_\Gamma ds\ \nabla \cdot \boldsymbol{f}_m(\boldsymbol{r}) \int_\Gamma ds'\ \frac{\nabla' \cdot \boldsymbol{f}_n(\boldsymbol{r}')}{4\pi R} \left(\frac{1}{2} + \mathcal{O}\left(\frac{R}{c\ \Delta t}\right)\right)$$

$$= \frac{1}{2}\left[\mathbf{Z}^h_{\text{stat}}\right]_{mn} + \mathcal{O}(\Delta t^{-1}). \tag{4.65}$$

Thus, when $\Delta t \to +\infty$,

$$\mathbf{Z}'_0 \to \mathbf{P}^{\Lambda H}\mathbf{Z}^s_{\text{stat}}\mathbf{P}^{\Lambda H} + \frac{1}{2}\mathbf{P}^{\Sigma}\mathbf{Z}^h_{\text{stat}}\mathbf{P}^{\Sigma} + \mathcal{O}\left(\Delta t^{-1}\right) \tag{4.66}$$

or

$$\mathbf{Z}'_0 \to \begin{pmatrix}\mathbf{P}^{\Lambda H} & \mathbf{P}^{\Sigma}\end{pmatrix}\begin{pmatrix}\mathcal{O}(1) & \mathcal{O}\left(\Delta t^{-1}\right)\\ \mathcal{O}\left(\Delta t^{-1}\right) & \mathcal{O}(1)\end{pmatrix}\begin{pmatrix}\mathbf{P}^{\Lambda H}\\ \mathbf{P}^{\Sigma}\end{pmatrix} \tag{4.67}$$

which leads to a condition number that is asymptotically constant. This is the result of rescaling the temporal basis and testing functions associated with the star part with a factor $\frac{1}{\Delta t}$ (equations (4.34) and (4.35), respectively). This contrasts with the approach used in [22], where the spatial basis and testing functions were rescaled.

4.5 Numerical Results

4.5.1 Torus

As a first example, scattering by a torus with large radius 0.8 m and small radius 0.2 m (figure 4.3) is examined. The torus is illuminated by a Gaussian-in-time plane wave

$$\boldsymbol{e}^i(\boldsymbol{r},t) = \frac{4A}{w\sqrt{\pi}}\hat{\boldsymbol{p}}\exp\left(-\left(\frac{4}{w}\left(c(t-t_0)-\hat{\boldsymbol{k}}\cdot\boldsymbol{r}\right)\right)^2\right) \tag{4.68}$$

with amplitude $A = 1\ V$, polarization $\hat{\boldsymbol{p}} = \hat{\mathbf{1}}_x$, direction $\hat{\boldsymbol{k}} = \hat{\mathbf{1}}_z$, width $w = 10\ m$ and time of arrival $t_0 = 100\ ns$.

The torus is approximated by a triangle mesh on which $N_S = 918$ RWG functions are defined. The time step is chosen as 0.83 ns (or $c\Delta t = 0.25\ m$). The scattering problem is solved using the EFIE (section 4.2), the dot-trick Calderón preconditioned EFIE [17] and the qHP-TDEFIE (section 4.3).

The resulting current on the edge indicated by the arrow in figure 4.3 is shown in figure 4.4 for the three simulations. At early times ($ct < 75\ m$), the three simulations match very well. However, the EFIE simulation ends in a constant loop current, whereas the dot-trick EFIE simulation exhibits a linearly increasing loop current. With the qHP-TDEFIE, the current expansion coefficient goes down to 10^{-14}, at which point the machine precision comes into play. It has been verified that the resulting current is not a static loop current but random numerical noise.

Next, the time step is increased in order to study the low frequency limit of the matrix $\mathbf{Z}_0$. Its condition number is shown in figure 4.5 for the EFIE, the dot-trick EFIE and the qHP-TDEFIE. Whereas for the EFIE and the dot-trick EFIE, the condition number grows proportionally to Δt^2, the qHP-TDEFIE's condition number remains constant.

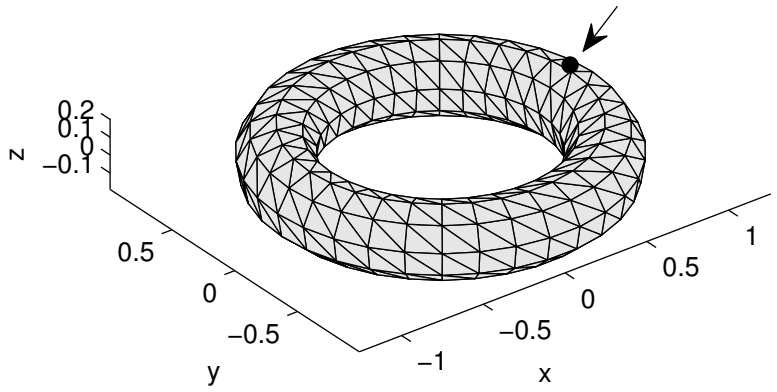

Figure 4.3: Triangle mesh for a torus. The arrow points toward the edge on which the current is observed in figure 4.4.

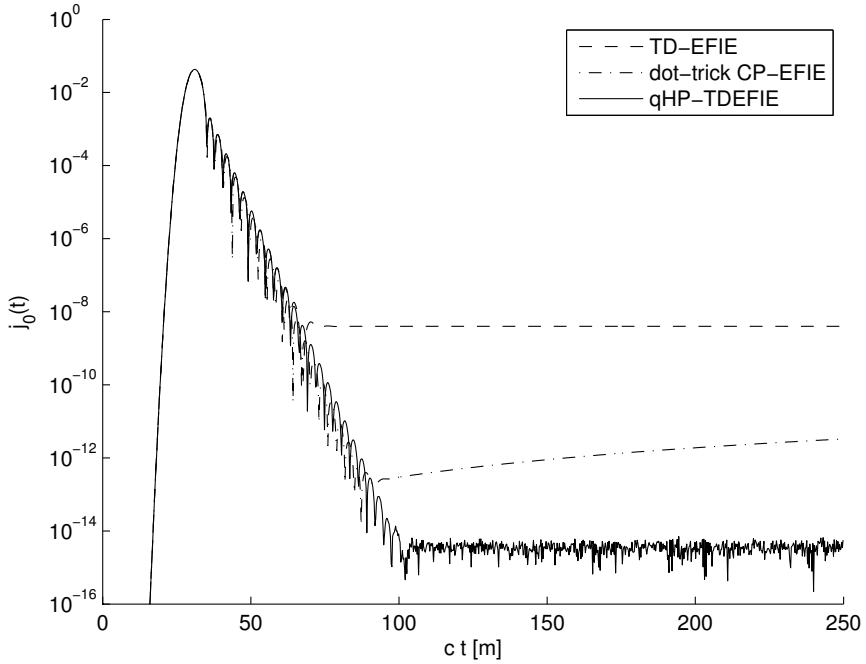

Figure 4.4: Current on the torus, obtained using three different formulations. The standard TD-EFIE exhibits a constant-in-time DC instablity. The dot-trick Calderón preconditioned EFIE suffers from a linear-in-time DC instability. The qHP-TDEFIE is immune to DC instability.

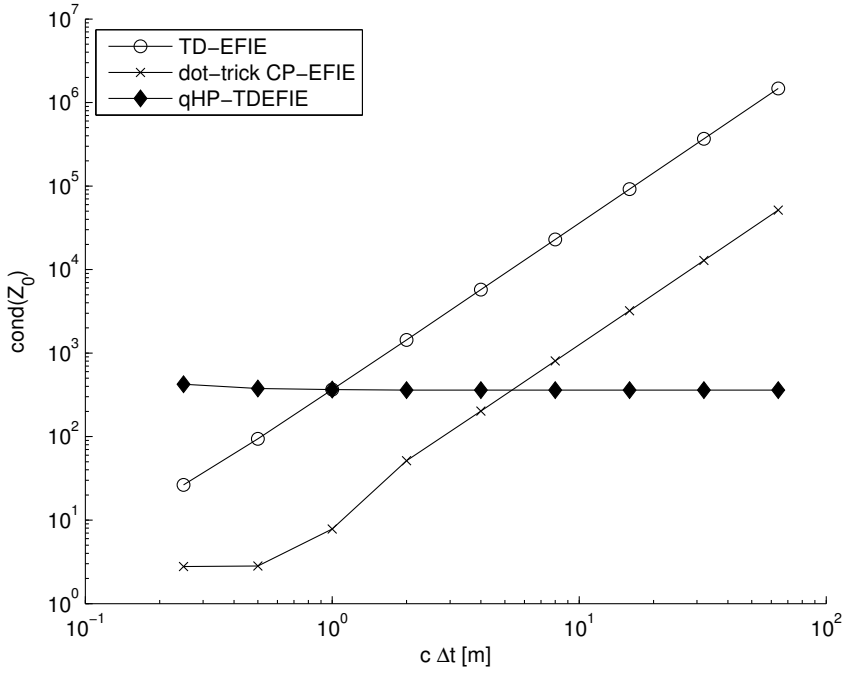

Figure 4.5: cond($\mathbf{Z}_0$) for the torus, as a function of the time step Δt.

4.5.2 Static Null Space

Consider an MOT system with a finite number N_X of nonzero interaction matrices

$$-\mathbf{X}_0 \mathsf{j}_i = \sum_{j=1}^{N_X} \mathbf{X}_j \mathsf{j}_{i-j} + \mathsf{e}_i. \tag{4.69}$$

As discussed in section 2.3.4, this equation allows constant-in-time regime solutions if

$$\exists \mathsf{j}_c : \sum_{i=0}^{N_X} \mathbf{X}_i \mathsf{j}_c = 0 \tag{4.70}$$

and linear-in-time regime solutions if

$$\exists \mathsf{j}_l : \sum_{i=0}^{N_X} \mathbf{X}_i (N_X - i + 1) \mathsf{j}_l = 0. \tag{4.71}$$

In other words, the constant and linear null spaces of the operator $\mathbf{X}_i$ can be investigated by computing the spectrum of

$$\mathbf{X}_c = \sum_{i=0}^{N_X} \mathbf{X}_i \tag{4.72}$$

$$\mathbf{X}_l = \sum_{i=0}^{N_X} (N_X - i + 1)\mathbf{X}_i. \tag{4.73}$$

This approach can readily be applied to the dot-trick EFIE and the qHP-TDEFIE. For the standard TD-EFIE, there are an unlimited number of nonzero interaction matrices. This is only a technical complication, which is resolved in appendix 4.B. This type of analysis is much cheaper than a full eigenvalue analysis on the system's companion matrix (see section 2.3.3).

Cuboid

Now consider the cuboid mesh with dimensions $2 \times 2 \times 2/3$ m in figure 4.6. On this mesh, $N_S = 360$ RWG functions are defined, which can be combined into 121 independent loops. The time step is fixed at $c\Delta t = 1$ m.

The singular values of $\mathbf{X}_c$ are shown in figure 4.7, top, for the standard TD-EFIE, the dot-trick CP-EFIE and the qHP-TDEFIE. The 121 singular values smaller than 10^{-14} correspond to the constant loop currents that reside in the null space of the EFIE operator. The dot-trick CP-EFIE and the qHP-TDEFIE do not exhibit a constant-in-time null space.

The singular values of $\mathbf{X}_l$ are shown in figure 4.7, bottom. The absence of very small singular values indicates that none of the three formulations exhibit a linear-in-time null space.

Rectangular Torus

The experiment is now repeated for the rectangular torus shown in figure 4.8. On this mesh, 384 RWG functions are defined, which can be combined into 127 local and 2 global loops.

Figure 4.9 shows that the constant-in-time loops (127 local loops, and 2 global loops) are again in the null space of the EFIE. The null space of the dot-trick EFIE encompasses both constant-in-time and linear-in-time global loops. The qHP-TDEFIE again does not exhibit a static null space.

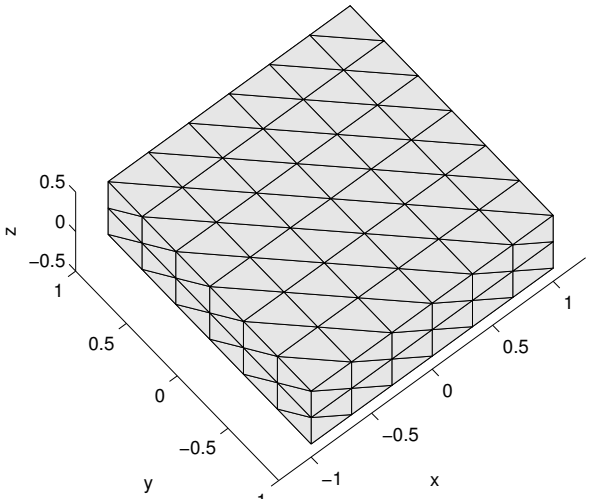

Figure 4.6: Cuboid ($2 \times 2 \times 2/3$ m) mesh, $N_S = 360$.

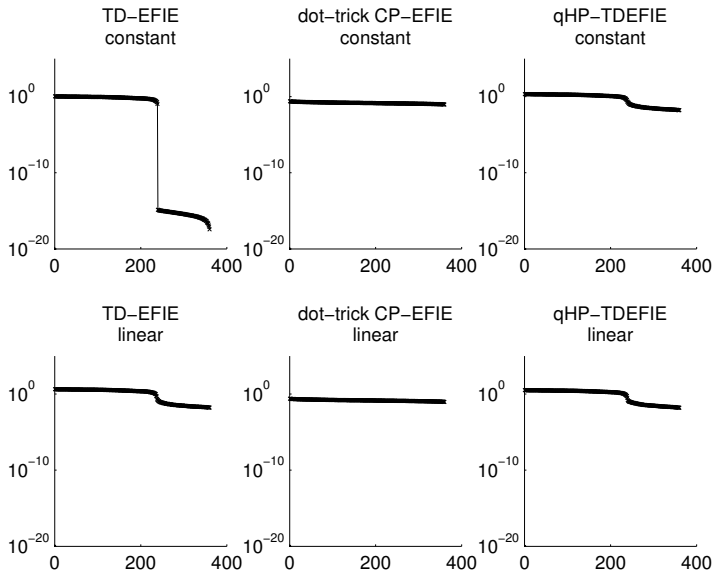

Figure 4.7: Spectral analysis of the static null space of the cuboid. Top: constant-in-time currents, bottom: linear-in-time currents.

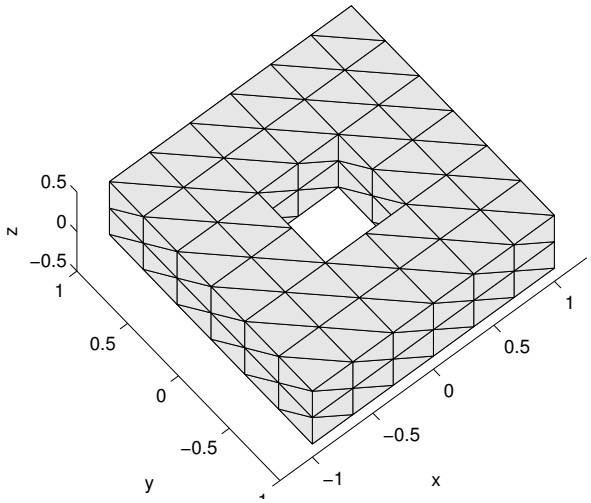

Figure 4.8: Rectangular torus mesh, $N_S = 384$.

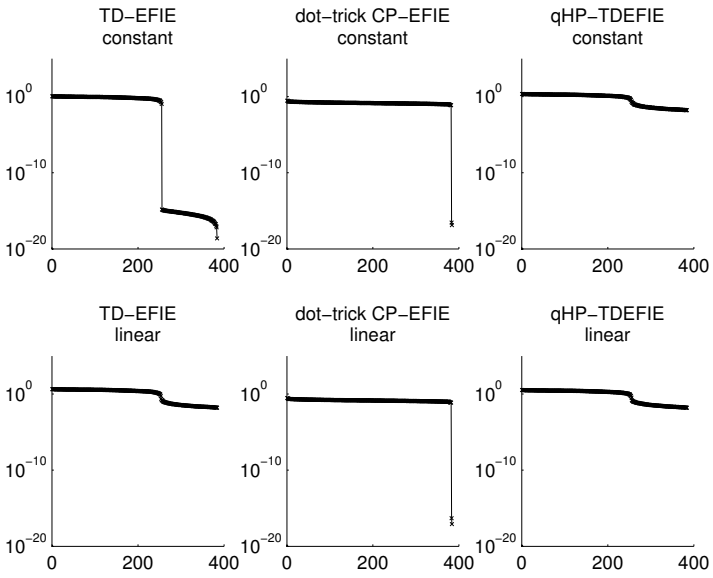

Figure 4.9: Spectral analysis of the static null space of the rectangular torus. Top: constant-in-time currents, bottom: linear-in-time currents.

4.6 Conclusion

The quasi-Helmholtz Projected TD-EFIE developed in this chapter is a novel formulation of the TD-EFIE that is immune to spurious static currents, on both simply and multiply connected structures. While it is based on the separation of quasi-Helmholtz components, it does not require the explicit construction of a loop-star or a loop-tree basis, nor the detection of global loops. The qHP-TDEFIE is discretized in time using a Galerkin method, with different basis and testing function combinations for each component. This is necessary in order to obtain a stable marching-on-in-time scheme. The temporal basis and testing functions are chosen such that the resulting system of equations is immune to low frequency breakdown, i.e., the system remains well-conditioned for large time steps.

4.A Alternative Form

4.A.1 Standard TD-EFIE

In section 4.2, a temporal Galerkin discretization of the TD-EFIE was proposed in which the temporal testing and trial functions are both pulses $p(t - i\Delta t)$. This corresponds to scheme 2b in section 2.3.3, and results in a current that is piecewise constant in time. Alternatively, it is also possible to expand the current in hat functions:

$$\mathsf{j}(t) = \sum_{i=1}^{N_T} \mathsf{j}_i \; h(t - i\Delta t). \tag{4.74}$$

A stable MOT scheme can be obtained by testing the TD-EFIE with Dirac delta distributions, as in scheme 2a in section 2.3.3:

$$\int_{\mathbb{R}} \delta(t - j\Delta t) \,(\text{equation (4.9)})\, dt \qquad j = 1, 2, 3, ..., N_T. \tag{4.75}$$

Since

$$\begin{aligned} & \eta \int_{\mathbb{R}} dt \; \delta(t - i\Delta t) \int_{\Gamma} (\hat{\boldsymbol{n}} \times \boldsymbol{f}_m(\boldsymbol{r})) \cdot \mathcal{T} \left\{ \boldsymbol{f}_n h \right\} (\boldsymbol{r}, t) ds \\ = \; & \frac{\eta}{\Delta t} \int_{\mathbb{R}} dt \; p(t - i\Delta t) \int_{\Gamma} (\hat{\boldsymbol{n}} \times \boldsymbol{f}_m(\boldsymbol{r})) \cdot \mathcal{T} \left\{ \boldsymbol{f}_n p \right\} (\boldsymbol{r}, t) ds \\ = \; & \frac{1}{\Delta t} \left[\mathbf{Z}_i \right]_{mn} \end{aligned} \tag{4.76}$$

the interaction matrices and therefore the properties concerning stability and null spaces are identical.

4.A.2 qHP-TDEFIE

A qHP-TDEFIE similar to this scheme can be developed by defining the auxiliary unknown $y(t)$ as

$$\begin{aligned} & \mathsf{y}(t) = \left(\mathbf{P}^{\Sigma} + \partial_t \mathbf{P}^{\Lambda H}\right) \mathsf{j}(t) \\ \iff \quad & \mathsf{j}(t) = \left(\mathbf{P}^{\Sigma} + \partial_t^{-1} \mathbf{P}^{\Lambda H}\right) \mathsf{y}(t) \end{aligned} \tag{4.77}$$

satisfying

$$\mathcal{Z}' \mathsf{y}(t) = -\left(\mathbf{P}^{\Lambda H} + \partial_t \mathbf{P}^{\Sigma}\right) \mathsf{e}(t). \tag{4.78}$$

The operator $\mathcal{Z}'$ is the same as in section 4.3.2, since

$$\begin{aligned} \mathcal{Z}' &= \left(\partial_t^{-1} \mathbf{P}^{\Lambda H} + \mathbf{P}^{\Sigma}\right) \mathcal{Z} \left(\mathbf{P}^{\Lambda H} + \partial_t \mathbf{P}^{\Sigma}\right) \\ &= \left(\mathbf{P}^{\Lambda H} + \partial_t \mathbf{P}^{\Sigma}\right) \mathcal{Z} \left(\partial_t^{-1} \mathbf{P}^{\Lambda H} + \mathbf{P}^{\Sigma}\right). \end{aligned} \tag{4.79}$$

The temporal discretization of (4.78) is similar as in section 4.3.3, with only minor modifications:

$$\mathsf{e'}_j = \int_{\mathbb{R}} \left(\delta(t - j\Delta t)\mathbf{P}^{\Lambda H} + \frac{1}{\Delta t} p(t - j\Delta t)\partial_t \mathbf{P}^{\Sigma}\right) \mathsf{e}(t)\, dt \tag{4.80}$$

$$\boldsymbol{j}(\boldsymbol{r}, t) = \sum_{m=1}^{N_S} \sum_{j=1}^{N_T} \left[\mathbf{P}^{\Sigma} \mathsf{y}_j + \Delta t \sum_{i=1}^{j} \mathbf{P}^{\Lambda H} \mathsf{y}_i\right]_m h(t - j\Delta t) \boldsymbol{f}_m(\boldsymbol{r}). \tag{4.81}$$

This results in a current that is also expanded in hats instead of pulses. The MOT matrices $\mathbf{Z}'_i$ are the same as in section 4.3. Therefore, this alternative scheme is also stable, and free of a static null space. Even though the numerical integration of $\mathbf{P}^{\Lambda H}\mathsf{y}(t)$ ($\Delta t \sum_{i=1}^{j} \mathbf{P}^{\Lambda H}\mathsf{y}_i$ in (4.81)) can result in a nonzero loop component in $\mathsf{j}(t)$, it can never lead to DC instabilities.

4.B Spectral Analysis of the Static Null Space for the EFIE

The hypersingular EFIO $\mathcal{T}_h$ contains a temporal integral, which corresponds to the integration of the current in order to obtain the electric charge on Γ. This integral is transformed into an infinite summation by the discretization procedure, i.e., an infinite number of matrices $\mathbf{Z}_i \neq 0$.

It is therefore convenient to introduce additional unknowns to discretize the temporal integral of $\mathsf{j}(t)$, as discussed in section 2.3.5:

$$\mathsf{s}(t) = \partial_t^{-1}\mathsf{j}(t) = \sum_{i=1}^{N_T} \mathsf{s}_i \; h(t - i\Delta t) \tag{4.82}$$

$$\mathsf{s}_i = \Delta t \sum_{j=0}^{i} \mathsf{j}_i. \tag{4.83}$$

Then,

$$\sum_{i=0}^{j} \mathbf{Z}_i \mathsf{j}_{j-i} = \sum_{i=0}^{j} \mathbf{Z}_i^s \mathsf{j}_{j-i} + \sum_{i=0}^{j} \dot{\mathbf{Z}}_i^h \mathsf{s}_{j-i} \tag{4.84}$$

$$\begin{aligned}
[\mathbf{Z}_i^s]_{mn} &= \eta \int_{\mathbb{R}} dt \; p(t - i\Delta t) \int_{\Gamma} (\hat{\boldsymbol{n}} \times \boldsymbol{f}_m(\boldsymbol{r})) \cdot \mathcal{T}_s \left\{ \boldsymbol{f}_n p \right\} (\boldsymbol{r}, t) ds \\
\left[\dot{\mathbf{Z}}_i^h\right]_{mn} &= \eta \int_{\mathbb{R}} dt \; p(t - i\Delta t) \int_{\Gamma} (\hat{\boldsymbol{n}} \times \boldsymbol{f}_m(\boldsymbol{r})) \cdot \partial_t \mathcal{T}_h \left\{ \boldsymbol{f}_n h \right\} (\boldsymbol{r}, t) ds
\end{aligned}$$

where $\mathbf{Z}_i^s = \dot{\mathbf{Z}}_i^h = 0$ for $i > N_Z$. Currents that are constant in time satisfy

$$\mathsf{j}_i = \mathsf{j}_c \tag{4.85}$$

$$\mathsf{s}_i = (i+1)\Delta t \; \mathsf{j}_c \tag{4.86}$$

and belong to the null space of the TD-EFIE operator if

$$\left(\sum_i \mathbf{Z}_i^s + \Delta t \sum_i (N_Z - i + 1) \dot{\mathbf{Z}}_i^h \right) \mathsf{j}_c = 0. \tag{4.87}$$

Currents that are linear in time satisfy

$$\mathsf{j}_i = (i+1)\mathsf{j}_l \tag{4.88}$$

$$\mathsf{s}_i = \Delta t \frac{(i+1)(i+2)}{2} \mathsf{j}_l \tag{4.89}$$

and belong to the null space of the TD-EFIE operator if

$$\left(\sum_i (N_Z - i + 1) \mathbf{Z}_i^s \right) \mathsf{j}_l + \Delta t \left(\sum_i \frac{(N_Z - i + 1)(N_Z - i + 2)}{2} \dot{\mathbf{Z}}_i^h \right) \mathsf{j}_l = 0. \tag{4.90}$$

Therefore, the static null space of the EFIE operator can be investigated by computing the spectrum of

$$\mathbf{X}_c = \sum_i \mathbf{Z}_i^s + \Delta t \sum_i (N_Z - i + 1)\dot{\mathbf{Z}}_i^h \tag{4.91}$$

$$\mathbf{X}_l = \sum_i (N_Z - i + 1)\mathbf{Z}_i^s + \Delta t \sum_i \frac{(N_Z - i + 1)(N_Z - i + 2)}{2}\dot{\mathbf{Z}}_i^h . \tag{4.92}$$

References

[1] Y. Beghein, K. Cools, and F. Andriulli, "A DC stable and large-time step well-balanced td-efie based on quasi-Helmholtz projectors", *IEEE Transactions on Antennas and Propagation*, vol. 63, no. 7, pp. 3087–3097, Jul. 2015.

[2] C. L. Bennett and W. L. Weeks, "A technique for computing approximate electromagnetic impulse response of conducting bodies", PhD thesis, Purdue University, 1968.

[3] S. M. Rao and D. R. Wilton, "Transient scattering by conducting surfaces of arbitrary shape", *IEEE Transactions on Antennas and Propagation*, vol. 39, no. 1, pp. 56–61, 1991.

[4] Y.-s. Chung, T. K. Sarkar, and B. H. Jung, "Solution of a time-domain magnetic-field integral equation for arbitrarily closed conducting bodies using an unconditionally stable methodology", *Microwave and Optical Technology Letters*, vol. 35, no. 6, pp. 493–499, Jun. 2002.

[5] M.-D. Zhu, X.-L. Zhou, and W.-Y. Yin, "Efficient evaluation of double surface integrals in time-domain integral equation formulations", *IEEE Transactions on Antennas and Propagation*, vol. 61, no. 9, pp. 4653–4664, Sep. 2013.

[6] B. Shanker, M. Lu, J. Yuan, and E. Michielssen, "Time domain integral equation analysis of scattering from composite bodies via exact evaluation of radiation fields", *IEEE Transactions on Antennas and Propagation*, vol. 57, no. 5, pp. 1506–1520, May 2009.

[7] A. Yucel and A. Ergin, "Exact evaluation of retarded-time potential integrals for the RWG bases", *IEEE Transactions on Antennas and Propagation*, vol. 54, no. 5, pp. 1496–1502, May 2006.

[8] Y. Shi, M.-Y. Xia, R. shan Chen, E. Michielssen, and M. Lu, "Stable electric field TDIE solvers via quasi-exact evaluation of MOT matrix elements", *IEEE Transactions on Antennas and Propagation*, vol. 59, no. 2, pp. 574–585, Feb. 2011.

[9] A. Geranmayeh, W. Ackermann, and T. Weiland, "Temporal discretization choices for stable boundary element methods in electromagnetic scattering problems", *Applied Numerical Mathematics*, vol. 59, no. 11, pp. 2751 –2773, Nov. 2009, Special Issue: Boundary Elements – Theory and Applications, {BETA} 2007 Dedicated to Professor Ernst P. Stephan on the Occasion of his 60th Birthday.

[10] E. van 't Wout, D. Van der Heul, H. van der Ven, and C. Vuik, "Design of temporal basis functions for time domain integral equation methods with predefined accuracy and smoothness", *IEEE Transactions on Antennas and Propagation*, vol. 61, no. 1, pp. 271–280, Jan. 2013.

[11] Y. Beghein, K. Cools, H. Bağcı, and D. De Zutter, "A space-time mixed Galerkin marching-on-in-time scheme for the time-domain combined field integral equation", *IEEE Transactions on Antennas and Propagation*, vol. 61, no. 3, pp. 1228–1238, Mar. 2013.

[12] Y. Beghein, K. Cools, and D. De Zutter, "A temporal Galerkin discretization of the charge-current continuity equation", in *2013 International Conference on Electromagnetics in Advanced Applications (ICEAA)*, Sep. 2013, pp. 628–631.

[13] I. Terrasse, "Résolution mathématique et numérique des équations de Maxwell instationnaires par une méthode de potentiels retardés", PhD thesis, 1993.

[14] A. J. Pray, Y. Beghein, N. V. Nair, K. Cools, H. Bağcı, and B. Shanker, "A higher order space-time Galerkin scheme for time domain integral equations", *IEEE Transactions on Antennas and Propagation*, vol. 62, no. 12, pp. 6183–6191, Dec. 2014.

[15] F. Valdes, M. Ghaffari-Miab, F. P. Andriulli, K. Cools, J. Kotulski, and E. Michielssen, "High-order Calderón multiplicative preconditioner for time domain electric field integral equations", in *2011 IEEE International Symposium on Antennas and Propagation (APSURSI)*, Jul. 2011, pp. 2362–2362.

[16] Y. Shi, H. Bağcı, and M. Lu, "On the internal resonant modes in marching-on-in-time solution of the time domain electric field integral equation", *IEEE Transactions on Antennas and Propagation*, vol. 61, no. 8, pp. 4389–4392, Aug. 2013.

[17] F. P. Andriulli, K. Cools, F. Olyslager, and E. Michielssen, "Time domain Calderón identities and their application to the integral equation analysis of scattering by PEC objects part II: Stability", *IEEE Transactions on Antennas and Propagation*, vol. 57, no. 8, pp. 2365–2375, Aug. 2009.

[18] Y. Shi, H. Bağcı, and M. Lu, "On the static loop modes in the marching-on-in-time solution of the time-domain electric field integral equation", *IEEE Antennas and Wireless Propagation Letters*, vol. 13, pp. 317–320, 2014.

[19] K. Cools, F. P. Andriulli, F. Olyslager, and E. Michielssen, "Time domain Calderón identities and their application to the integral equation analysis of scattering by PEC objects part I: Preconditioning", *IEEE Transactions on Antennas and Propagation*, vol. 57, no. 8, pp. 2352–2364, Aug. 2009.

[20] K. Cools, F. P. Andriulli, F. Olyslager, and E. Michielssen, "Nullspaces of MFIE and Calderón preconditioned EFIE operators applied to toroidal surfaces", *IEEE Transactions on Antennas and Propagation*, vol. 57, no. 10, pp. 3205–3215, Oct. 2009.

[21] F. P. Andriulli, H. Bağcı, F. Vipiana, G. Vecchi, and E. Michielssen, "Analysis and regularization of the TD-EFIE low-frequency breakdown", *IEEE Transactions on Antennas and Propagation*, vol. 57, no. 7, pp. 2034–2046, Jul. 2009.

[22] N.-W. Chen, K. Aygun, and E. Michielssen, "Integral-equation-based analysis of transient scattering and radiation from conducting bodies at very low frequencies", *IEE Proceedings Microwaves, Antennas and Propagation*, vol. 148, no. 6, pp. 381–387, Dec. 2001.

[23] F. P. Andriulli, K. Cools, I. Bogaert, and E. Michielssen, "On a well-conditioned electric field integral operator for multiply connected geometries", *IEEE Transactions on Antennas and Propagation*, vol. 61, no. 4, pp. 2077–2087, Apr. 2013.

[24] I. Bogaert, K. Cools, F. P. Andriulli, and H. Bağcı, "Low-frequency scaling of the standard and mixed magnetic field and müller integral equations", *IEEE Transactions on Antennas and Propagation*, vol. 62, no. 2, pp. 822–831, Feb. 2014.

[25] F. P. Andriulli, "Loop-star and loop-tree decompositions: Analysis and efficient algorithms", *IEEE Transactions on Antennas and Propagation*, vol. 60, no. 5, pp. 2347–2356, May 2012.

[26] G. Pisharody and D. S. Weile, "Robust solution of time-domain integral equations using loop-tree decomposition and bandlimited extrapolation", *IEEE Transactions on Antennas and Propagation*, vol. 53, no. 6, pp. 2089–2098, Jun. 2005.

[27] D. S. Weile, G. Pisharody, N.-W. Chen, B. Shanker, and E. Michielssen, "A novel scheme for the solution of the time-domain integral equations of electromagnetics", *IEEE Transactions on Antennas and Propagation*, vol. 52, no. 1, pp. 283–295, Jan. 2004.

[28] K. Aygun, B. Shanker, A. A. Ergin, and E. Michielssen, "A two-level plane wave time-domain algorithm for fast analysis of EMC/EMI problems", *IEEE Transactions on Electromagnetic Compatibility*, vol. 44, no. 1, pp. 152–164, 2002.

[29] A. A. Ergin, B. Shanker, and E. Michielssen, "The plane-wave time-domain algorithm for the fast analysis of transient wave phenomena", *IEEE Antennas and Propagation Magazine*, vol. 41, no. 4, pp. 39–52, Apr. 1999.

[30] S. Rao, D. Wilton, and A. Glisson, "Electromagnetic scattering by surfaces of arbitrary shape", *IEEE Transactions on Antennas and Propagation*, vol. 30, no. 3, pp. 409 –418, May 1982.

[31] A. Pray, N. Nair, and B. Shanker, "Stability properties of the time domain electric field integral equation using a separable approximation for the convolution with the retarded potential", *IEEE Transactions on Antennas and Propagation*, vol. 60, no. 8, pp. 3772–3781, Aug. 2012.

5

A DC-stable, Well Balanced, Calderón Preconditioned TD-EFIE

Y. Beghein, K. Cools and F.P. Andriulli

This chapter is based on an article that has been accepted for publication in *IEEE Transactions on Antennas and Propagation* [1].

★ ★ ★

The marching-on-in-time solution of the time domain electric field integral equation (TD-EFIE) has traditionally suffered from a number of problems, including (i) instability; (ii) spurious static contributions plaguing the solution; (iii) low frequency breakdown; (iv) dense discretization breakdown. The first issue can be resolved by employing proper space-time Galerkin discretization schemes and accurate quadrature methods. The second and the third issue have been resolved by the quasi-Helmholtz Projected TD-EFIE (qHP-TDEFIE). This chapter introduces a multiplicative preconditioner which can be applied to the qHP-TDEFIE, without further modifying the original scheme. This preconditioner is based on Calderón techniques and guarantees that the marching-on-in-time system can be solved efficiently using iterative methods, not only for large time step sizes but also for dense spatial discretizations, and for both simply and multiply connected geometries.

5.1 Introduction

The electric field integral equation (EFIE) efficiently models scattering of electromagnetic waves by perfect electric conductors. Its frequency domain formulation (FD-EFIE) is applicable to time-harmonic electromagnetic fields, whereas its time domain formulation (TD-EFIE) describes transient scattering problems. As both formulations are related through the Fourier transform, they share a number of properties.

First, upon discretization, the EFIE yields an ill-conditioned system of equations when the spatial discretization is dense. This phenomenon is termed dense discretization breakdown, and occurs both in the time domain [2] and in the frequency domain [3].

Second, the EFIE suffers from low frequency breakdown. In the frequency domain, this leads to ill-conditioned systems of equations at low frequencies, see e.g. [4], [5] and references therein. In the time domain, ill-conditioned systems are found at large time steps [6], [7].

In addition to this, the marching-on-in-time (MOT) solution of the TD-EFIE is prone to instability. A study of different types of instability has been performed in [8]. So-called high frequency (HF) instability can be avoided by carefully choosing the temporal discretization scheme, and by using accurate numerical integration methods [9]–[12]. Furthermore, the TD-EFIE allows static sourcefree regime solutions. Due to this phenomenon, the numerical solution is plagued by spurious static modes (DC instability) [13].

The first two issues have been extensively studied for the FD-EFIE. Dense discretization breakdown has been successfully remedied using Calderón preconditioning (CP) [3]. These schemes are also immune to low frequency breakdown, but only when the geometry is simply connected [14]. Another approach to combat low frequency breakdown is the use of quasi-Helmholtz (loop-star or loop-tree) decompositions [15]–[18]. While this works for both simply and multiply connected geometries, the latter case requires the detection of global loops, which is a computationally expensive operation. Recently, a modified FD-EFIE formulation has been proposed that tackles both low frequency and dense discretization breakdown, without resorting to an explicit quasi-Helmholtz decomposition [19]. This approach is applicable to both simply and multiply connected geometries.

Calderón preconditioning can also be applied to the TD-EFIE [8], [20]. The Calderón preconditioned TD-EFIE is immune to dense discretization breakdown. For simply connected geometries, it is also immune to LF breakdown and DC instability. Global topological loops, however, are not correctly handled by the Calderón preconditioned TD-EFIE, leading to LF breakdown and DC instability when applied to multiply connected geometries. This was previously studied in the frequency domain in [14], and also observed in the time domain in chapter 4.

In chapter 4, the quasi-Helmholtz projected TD-EFIE (qHP-TDEFIE) has been introduced. This TD-EFIE formulation is immune to both low frequency breakdown and DC instability, regardless of the topological properties of the geometry. It is related to the (unpreconditioned) modified FD-EFIE presented in [19], and suffers from dense discretization breakdown.

The aim of this chapter is to construct a multiplicative preconditioner for the qHP-TDEFIE, which effectively solves dense discretization breakdown. As in other Calderón preconditioners, this is achieved by leveraging the self-regularizing property of the EFIE operator. In contrast to other Calderón schemes, the preconditioner itself is rendered immune to low frequency breakdown by rescaling its quasi-Helmholtz components similarly as in chapter 4. All this needs to be combined with a consistent spatial and temporal discretization scheme, such that the resulting marching-on-in-time scheme is stable and can be implemented without further modifications to the original scheme presented in chapter 4. The resulting preconditioned scheme is immune to both dense discretization breakdown and low frequency breakdown, and can be applied to both simply connected and multiply connected geometries without requiring the detection of topological loops.

This chapter is organized as follows. In section 5.2, the spatial discretization of the TD-EFIE is discussed, and modified as in chapter 4. After extending this approach to a dual basis, a Calderón preconditioned equation is proposed which is discrete in space but continuous in time. In section 5.3, this equation is discretized in time and transformed into a multiplicative preconditioner for the original qHP-TDEFIE. In section 5.4, the low frequency limit of the preconditioned equation is studied. Finally, a number of numerical experiments are performed in section 5.5 in order to demonstrate the power of the proposed method.

5.2 Spatial Discretization of the CP qHP-TDEFIE

5.2.1 The Time Domain Electric Field Integral Equation

Consider a scattering problem as in section 1.2.9, involving a perfect electrically conducting body Ω whose boundary is denoted Γ. When an incident electric field $\boldsymbol{e}^i(\boldsymbol{r},t)$ impinges on it at $t>0$, a surface current $\boldsymbol{j}(\boldsymbol{r},t)$ is induced on Γ, which satisfies the time domain EFIE

$$\eta\left(\mathcal{T}\boldsymbol{j}\right)(\boldsymbol{r},t) = -\hat{\boldsymbol{n}}\times\boldsymbol{e}^i(\boldsymbol{r},t) \quad \forall \boldsymbol{r}\in\Gamma, t>0 \tag{5.1}$$

where

$$\begin{aligned}
\left(\mathcal{T}\boldsymbol{j}\right)(\boldsymbol{r},t) &= \left(\mathcal{T}_s\boldsymbol{j}\right)(\boldsymbol{r},t) + \left(\mathcal{T}_h\boldsymbol{j}\right)(\boldsymbol{r},t) &(5.2)\\
\left(\mathcal{T}_s\boldsymbol{j}\right)(\boldsymbol{r},t) &= -\frac{1}{c}\hat{\boldsymbol{n}}\times\int_\Gamma \frac{\partial_t\boldsymbol{j}(\boldsymbol{r}',\tau)}{4\pi R}ds' &(5.3)\\
\left(\mathcal{T}_h\boldsymbol{j}\right)(\boldsymbol{r},t) &= c\;\hat{\boldsymbol{n}}\times p.v.\int_\Gamma \nabla\frac{\partial_t^{-1}\nabla'\cdot\boldsymbol{j}(\boldsymbol{r}',\tau)}{4\pi R}ds' &(5.4)
\end{aligned}$$

and $\tau = t-R/c$, $\eta=\sqrt{\mu_0/\epsilon_0}$, $c=1/\sqrt{\epsilon_0\mu_0}$, $R=|\boldsymbol{r}-\boldsymbol{r}'|$, and $\hat{\boldsymbol{n}}$ is the exterior normal vector to Γ. Further define $\partial_t^{-1}f(t)=\int_{-\infty}^t f(\tau)d\tau$, which is well defined because all fields are assumed to vanish for $t<0$ in a neighborhood of Ω.

5.2.2 RWG Discretization and Rescaling

In order to construct a numerical solution to (5.1), the procedure described in section 2.3.1 is followed. The surface Γ is approximated by a triangle mesh with N_V vertices, N_S edges, and N_F faces. On this mesh, N_S Rao-Wilton-Glisson (RWG) functions $\boldsymbol{f}_m(\boldsymbol{r})$ are constructed [21], as defined in (2.2) (i.e., without edge length normalization). Each function is defined on a pair of triangles, and associated with their common edge e_m (see figure 5.1). The current $\boldsymbol{j}(\boldsymbol{r},t)$ is then approximated as

$$\boldsymbol{j}(\boldsymbol{r},t) = \sum_{m=1}^{N_S} \mathsf{j}_m(t)\boldsymbol{f}_m(\boldsymbol{r}). \tag{5.5}$$

Next, the TD-EFIE (5.1) is spatially tested with the rotated RWG functions $\hat{\boldsymbol{n}}\times\boldsymbol{f}_m(\boldsymbol{r})$, leading to

$$\mathcal{Z}\mathsf{j}(t) = -\mathsf{e}(t) \quad \forall t>0 \tag{5.6}$$

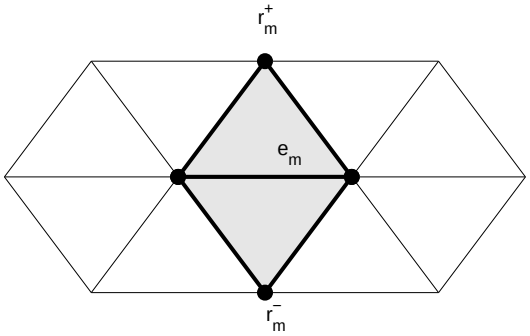

Figure 5.1: An RWG function $\boldsymbol{f}_m(\boldsymbol{r})$ is defined on a pair of triangles (grey). It represents a current flowing across the common edge e_m.

where $\mathsf{j}(t)$ and $\mathsf{e}(t)$ are time-dependent $N_S \times 1$ column vectors of RWG expansion and testing coefficients, respectively, and

$$\mathcal{Z} = \mathcal{Z}_s + \mathcal{Z}_h \tag{5.7}$$

$$[\mathcal{Z}_s \mathsf{j}(t)]_m = -\sum_n \frac{\eta}{c} \int_\Gamma ds\ \boldsymbol{f}_m(\boldsymbol{r}) \cdot \int_\Gamma ds'\ \frac{\partial_t \mathsf{j}_n(\tau) \boldsymbol{f}_n(\boldsymbol{r}')}{4\pi R} \tag{5.8}$$

$$[\mathcal{Z}_h \mathsf{j}(t)]_m = -\sum_n \eta c \int_\Gamma ds\ \nabla \cdot \boldsymbol{f}_m(\boldsymbol{r}) \int_\Gamma ds'\ \frac{\partial_t^{-1} \mathsf{j}_n(\tau)\ \nabla' \cdot \boldsymbol{f}_n(\boldsymbol{r}')}{4\pi R} \tag{5.9}$$

$$[\mathsf{e}(t)]_m = \int_\Gamma \boldsymbol{f}_m(\boldsymbol{r}) \cdot \boldsymbol{e}^i(\boldsymbol{r}, t)\ ds. \tag{5.10}$$

Just like static solenoidal currents reside in the null space of $\mathcal{T}$, the RWG expansion coefficients of such a current reside in the null space of the operator $\mathcal{Z}$. In chapter 4, this null space was eliminated using the quasi-Helmholtz projection operators introduced in [19]. The operator $\mathbf{P}^{\Sigma}$, defined in (4.20), projects a vector of RWG expansion coefficients onto the space of RWG stars. Its orthogonal complement $\mathbf{P}^{\Lambda H} = 1 - \mathbf{P}^{\Sigma}$ projects a vector of RWG expansion coefficients onto the space of (local and global) RWG loops, without requiring their explicit construction. Using these projectors, an auxiliary unknown $\mathsf{y}(t)$ is introduced:

$$\mathsf{y}(t) = \left(\mathbf{P}^{\Lambda H} + \frac{1}{T_0} \partial_t^{-1} \mathbf{P}^{\Sigma} \right) \mathsf{j}(t) \tag{5.11}$$

which is a time-dependent $N_S \times 1$ RWG expansion coefficient vector satisfying

$$\mathcal{Z}' \mathsf{y}(t) = -\left(\frac{1}{T_0} \partial_t^{-1} \mathbf{P}^{\Lambda H} + \mathbf{P}^{\Sigma} \right) \mathsf{e}(t) \tag{5.12}$$

where

$$\mathcal{Z}' = \begin{pmatrix} \mathbf{P}^{\Lambda H} & \mathbf{P}^{\Sigma} \end{pmatrix} \begin{pmatrix} \frac{1}{T_0} \partial_t^{-1} \mathcal{Z}_s & \mathcal{Z}_s \\ \mathcal{Z}_s & T_0 \partial_t \mathcal{Z} \end{pmatrix} \begin{pmatrix} \mathbf{P}^{\Lambda H} \\ \mathbf{P}^{\Sigma} \end{pmatrix}. \tag{5.13}$$

These definitions are identical to those in chapter 4, up to the factor T_0 which is introduced here to allow additional control over the scaling of the diagonal blocks. The scheme in chapter 4 is recovered by setting $T_0 = 1$.

In contrast to $\mathcal{Z}$, $\mathcal{Z}'$ does not have a static null space. In chapter 4, a suitable temporal discretization scheme is applied to (5.12), leading to a stable MOT scheme that is immune to DC instability. Additionally, the equation can be rendered immune to low frequency breakdown by correctly choosing and scaling the temporal basis and testing functions. A more thorough discussion of these operators and their properties can be found in chapter 4.

5.2.3 Choice of the Scaling Factor

The definitions in chapter 4 are equivalent to those in section 5.2.2 with $T_0 = 1$ *unit of time* (e.g. 1 second, or 1 meter/c, depending on the chosen units of measurement). By introducing this fixed time scale, the method stops being scale invariant.

In section 5.5, T_0 will be set to D/c, where D is the diameter of the scatterer. This is more natural in the sense that the properties of the resulting scheme (in particular the condition number) will depend only on the geometry of the scatterer, and not on the chosen units of measurement. In the following sections, however, T_0 will be kept as an explicit parameter in order to maintain compatibility with both choices.

5.2.4 Dual Discretization and Preconditioning

Standard Calderón preconditioning is based on the fact that the spectrum of $\mathcal{T}^2$ is bounded (in contrast to the spectrum of $\mathcal{T}$ itself), and will therefore yield a well-conditioned system of equations when a suitable spatial discretization scheme is employed – see section 2.2.5. This, however, requires the use of dual basis functions. In particular, the combination of RWG functions with Buffa-Christiansen (BC) functions [22] has widely been used for this purpose. A BC function $\boldsymbol{g}_m(\boldsymbol{r})$ is defined on a set of triangles of the barycentric refinement of the triangle mesh, as shown in figure 5.2, and is associated with an edge e_m of the original mesh.

A current $\boldsymbol{j}(\boldsymbol{r})$ expanded in BC functions, with expansion coefficients j, can again be decomposed into its quasi-Helmholtz components. Similarly to $\mathbf{P}^{\Sigma}$, define the projection operator [19]

$$\mathbb{P}^{\Lambda} = \Lambda \left(\Lambda^T \Lambda\right)^+ \Lambda^T \tag{5.14}$$

where $\left(\Lambda^T \Lambda\right)^+$ denotes the pseudo-inverse of $\Lambda^T \Lambda$. The $N_S \times N_V$ loop coefficient

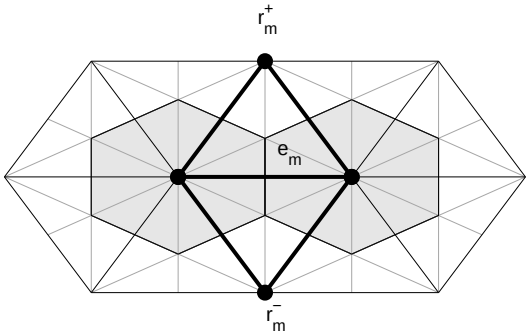

Figure 5.2: A BC function $\boldsymbol{g}_m(\boldsymbol{r})$ is defined on a set of triangles (grey) on the barycentric refinement of the triangle mesh. It represents a current flowing along the common edge e_m.

matrix is given by [19]

$$\Lambda_{m,j} = \begin{cases} 1 & \text{if node } j \text{ equals } r_m^+ \\ -1 & \text{if node } j \text{ equals } r_m^- \\ 0 & \text{otherwise} \end{cases}. \tag{5.15}$$

The vector $\mathsf{j}^\Lambda = \mathbb{P}^\Lambda \mathsf{j}$ contains the BC expansion coefficients of the weakly curl-free component of $\boldsymbol{j}(\boldsymbol{r})$. Similarly to $\mathbf{P}^{\Lambda H}$, define [19]

$$\mathbb{P}^{\Sigma H} = 1 - \mathbb{P}^\Lambda. \tag{5.16}$$

The vector $\mathsf{j}^{\Sigma H} = \mathbb{P}^{\Sigma H}\mathsf{j}$ contains the BC expansion coefficients of the divergence-free component of $\boldsymbol{j}(\boldsymbol{r})$.

With these projection operators, the rescaling procedure of the previous section can be applied to the dual discretization of the TD-EFIE. Define, analogously to (5.7)–(5.9):

$$\tilde{\mathcal{Z}} = \tilde{\mathcal{Z}}_s + \tilde{\mathcal{Z}}_h \tag{5.17}$$

$$\left[\tilde{\mathcal{Z}}_s \mathsf{j}(t)\right]_m = -\sum_n \frac{\eta}{c} \int_\Gamma ds\ \boldsymbol{g}_m(\boldsymbol{r}) \cdot \int_\Gamma ds'\ \frac{\partial_t \mathsf{j}_n(\tau) \boldsymbol{g}_n(\boldsymbol{r}')}{4\pi R} \tag{5.18}$$

$$\left[\tilde{\mathcal{Z}}_h \mathsf{j}(t)\right]_m = -\sum_n \eta c \int_\Gamma ds\ \nabla \cdot \boldsymbol{g}_m(\boldsymbol{r}) \int_\Gamma ds'\ \frac{\partial_t^{-1} \mathsf{j}_n(\tau)\ \nabla' \cdot \boldsymbol{g}_n(\boldsymbol{r}')}{4\pi R} \tag{5.19}$$

Further define, analogously to (5.13),

$$\tilde{\mathcal{Z}}' = \begin{pmatrix} \mathbb{P}^{\Sigma H} & \mathbb{P}^\Lambda \end{pmatrix} \begin{pmatrix} \frac{1}{T_0}\partial_t^{-1}\tilde{\mathcal{Z}}_s & \tilde{\mathcal{Z}}_s \\ \tilde{\mathcal{Z}}_s & T_0 \partial_t \tilde{\mathcal{Z}} \end{pmatrix} \begin{pmatrix} \mathbb{P}^{\Sigma H} \\ \mathbb{P}^\Lambda \end{pmatrix}. \tag{5.20}$$

With these definitions, the following semi-discrete Calderón preconditioned qHP-TDEFIE is proposed:

$$\tilde{\mathcal{Z}}' \, \mathbf{G}_{\mathrm{mx}}^{-1} \, \mathcal{Z}' \mathsf{y}(t) = -\tilde{\mathcal{Z}}' \, \mathbf{G}_{\mathrm{mx}}^{-1} \left(\frac{1}{T_0} \partial_t^{-1} \mathbf{P}^{\Lambda H} + \mathbf{P}^{\Sigma} \right) \mathsf{e}(t) \tag{5.21}$$

where the $N_S \times N_S$ Gram matrix $\mathbf{G}_{\mathrm{mx}}$ is defined as

$$[\mathbf{G}_{\mathrm{mx}}]_{mn} = \int_{\Gamma} (\hat{\boldsymbol{n}} \times \boldsymbol{f}_m(\boldsymbol{r})) \cdot \boldsymbol{g}_n(\boldsymbol{r}) ds. \tag{5.22}$$

Equation (5.21) is discrete in space, but continuous in time. It will be discretized in time, and further analyzed, in the following sections.

5.3 Temporal Discretization

5.3.1 Discretization of the Full Equation

In order to allow for a numerical solution, (5.21) needs to be discretized in time. Furthermore, the aim is to maintain compatibility with the original qHP-TDEFIE. To this end, the auxiliary unknown $\mathsf{y}(t)$ is expanded as in chapter 4:

$$\mathsf{y}(t) \quad \approx \quad \sum_i \left(p(t - i\Delta t) \mathbf{P}^{\Lambda H} + h(t - i\Delta t) \mathbf{P}^{\Sigma} \right) \mathsf{y}_i \tag{5.23}$$

where $p(t - i\Delta t)$ are pulse functions (figure 5.3, middle)

$$p(t) = \begin{cases} 1 & t \in (-\Delta t, 0) \\ 0 & \text{otherwise} \end{cases} \tag{5.24}$$

and $h(t)$ the hat functions (figure 5.3, right)

$$h(t) = \begin{cases} 1 + \frac{t}{\Delta t} & t \in (-\Delta t, 0) \\ 1 - \frac{t}{\Delta t} & t \in (0, \Delta t) \\ 0 & \text{otherwise} \end{cases} . \tag{5.25}$$

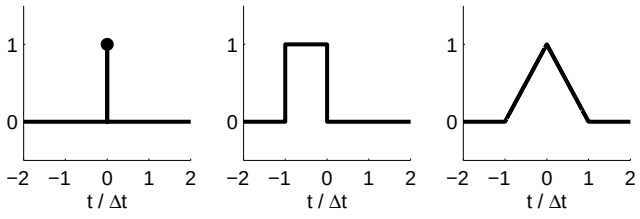

Figure 5.3: Temporal basis and testing functions: Dirac delta distribution $\delta(t)$ (left), pulse $p(t)$ (middle) and hat $h(t)$ (right).

A second auxiliary unknown $\mathsf{y}'(t)$ (a time-dependent $N_S \times 1$ column vector) is defined as

$$\begin{aligned} \mathsf{y}'(t) &= \mathcal{Z}'\mathsf{y}(t) \\ &\approx \sum_i \left(p(t - i\Delta t)\mathbf{P}^{\Sigma} + h(t - i\Delta t)\mathbf{P}^{\Lambda H} \right) \mathsf{y}'_i. \end{aligned} \tag{5.26}$$

An expression for its $N_S \times 1$ expansion coefficient vectors y'_i is obtained by applying a temporal Galerkin procedure to (5.26):

$$\int_{\mathbb{R}} \left(\delta(t - j\Delta t)\mathbf{P}^{\Lambda H} + \frac{1}{\Delta t} p(t - j\Delta t)\mathbf{P}^{\Sigma} \right) (\text{equation (5.26)}) \; dt \tag{5.27}$$

for $j = 1, 2, ..., N_T$, where $\delta(t - j\Delta t)$ denotes the Dirac delta distribution (figure 5.3, left). Since

$$\begin{aligned} \int_{\mathbb{R}} \delta(t - j\Delta t) h(t - i\Delta t) dt &= \int_{\mathbb{R}} \frac{1}{\Delta t} p(t - j\Delta t) p(t - i\Delta t) dt \\ &= \begin{cases} 1 & \text{if } i = j \\ 0 & \text{otherwise} \end{cases} \end{aligned} \tag{5.28}$$

the system of equations (5.27) is easily inverted:

$$\mathsf{y}'_i = \sum_{k=0}^{\infty} \mathbf{Z}'_k \mathsf{y}_{i-k} =: \left[\mathbf{Z}' * \mathsf{y} \right]_i \quad i = 1, 2, ..., N_T \tag{5.29}$$

with

$$\mathbf{Z}'_i = \begin{pmatrix} \mathbf{P}^{\Lambda H} & \mathbf{P}^{\Sigma} \end{pmatrix} \begin{pmatrix} \mathbf{Z}'^{LL}_i & \mathbf{Z}'^{LS}_i \\ \mathbf{Z}'^{SL}_i & \mathbf{Z}'^{SS}_i \end{pmatrix} \begin{pmatrix} \mathbf{P}^{\Lambda H} \\ \mathbf{P}^{\Sigma} \end{pmatrix}. \tag{5.30}$$

The quasi-Helmholtz components of this operator are defined as

$$\begin{aligned} \left[\mathbf{Z}'^{SS}_i \right]_{mn} &= T_0 \frac{\eta}{\Delta t} \int_{\mathbb{R}} dt \; p(t - i\Delta t) \int_{\Gamma} ds \; (\hat{\boldsymbol{n}} \times \boldsymbol{f}_m(\boldsymbol{r})) \cdot \partial_t \mathcal{T} \{ \boldsymbol{f}_n h \} (\boldsymbol{r}, t) \\ \left[\mathbf{Z}'^{SL}_i \right]_{mn} &= \frac{\eta}{\Delta t} \int_{\mathbb{R}} dt \; p(t - i\Delta t) \int_{\Gamma} ds \; (\hat{\boldsymbol{n}} \times \boldsymbol{f}_m(\boldsymbol{r})) \cdot \mathcal{T}_s \{ \boldsymbol{f}_n p \} (\boldsymbol{r}, t) \\ \left[\mathbf{Z}'^{LS}_i \right]_{mn} &= \eta \int_{\mathbb{R}} dt \; \delta(t - i\Delta t) \int_{\Gamma} ds \; (\hat{\boldsymbol{n}} \times \boldsymbol{f}_m(\boldsymbol{r})) \cdot \mathcal{T}_s \{ \boldsymbol{f}_n h \} (\boldsymbol{r}, t) \\ \left[\mathbf{Z}'^{LL}_i \right]_{mn} &= \frac{1}{T_0} \eta \int_{\mathbb{R}} dt \; \delta(t - i\Delta t) \int_{\Gamma} ds \; (\hat{\boldsymbol{n}} \times \boldsymbol{f}_m(\boldsymbol{r})) \cdot \partial_t^{-1} \mathcal{T}_s \{ \boldsymbol{f}_n p \} (\boldsymbol{r}, t). \end{aligned}$$

Note that this definition is identical to the one in chapter 4, if T_0 is set to 1. Furthermore, (5.29) defines the operator $*$ as the discrete convolution of a sequence of matrices and a sequence of vectors.

The RWG testing coefficients $\mathsf{y}'(t)$ are now transformed into BC expansion coefficients, through multiplication with the mixed Gram matrix

$$\begin{aligned} \mathsf{y}''(t) &= \mathbf{G}_{\mathrm{mx}}^{-1}\, \mathsf{y}'(t) \\ &\approx \sum_i \left(p(t-i\Delta t)\mathbb{P}^{\Sigma H} + h(t-i\Delta t)\mathbb{P}^{\Lambda}\right) \mathsf{y}_i''. \end{aligned} \tag{5.31}$$

A temporal Galerkin procedure is applied to (5.31):

$$\int_{\mathbb{R}} \left(\delta(t-j\Delta t)\mathbb{P}^{\Lambda} + \frac{1}{\Delta t} p(t-j\Delta t)\mathbb{P}^{\Sigma H}\right) (\text{equation (5.31)})\ dt \tag{5.32}$$

for $j = 1, 2, ..., N_T$, leading to

$$\mathsf{y}_j'' = \sum_{k=0}^{1} \mathbf{G}_k^{-1} \mathsf{y}_{j-k}' =: \left[\mathbf{G}^{-1} * \mathsf{y}'\right]_j \tag{5.33}$$

with

$$\begin{aligned} \mathbf{G}_0^{-1} &= \frac{1}{2}\mathbb{P}^{\Sigma H}\mathbf{G}_{\mathrm{mx}}^{-1}\mathbf{P}^{\Lambda H} + \mathbb{P}^{\Sigma H}\mathbf{G}_{\mathrm{mx}}^{-1}\mathbf{P}^{\Sigma} \\ &\quad + \mathbb{P}^{\Lambda}\mathbf{G}_{\mathrm{mx}}^{-1}\mathbf{P}^{\Lambda H} \qquad (5.34) \\ \mathbf{G}_1^{-1} &= \frac{1}{2}\mathbb{P}^{\Sigma H}\mathbf{G}_{\mathrm{mx}}^{-1}\mathbf{P}^{\Lambda H} \qquad (5.35) \\ \mathbf{G}_k^{-1} &= 0 \text{ for } k \neq 0 \text{ and } k \neq 1. \qquad (5.36) \end{aligned}$$

In this, $\mathbb{P}^{\Lambda}\mathbf{G}_{\mathrm{mx}}^{-1}\mathbf{P}^{\Sigma} = \mathbf{0}$ was used (for a proof, see appendix 5.A). This identity removes the otherwise ill-defined term $\int_{\mathbb{R}} \delta(t-j\Delta t)p(t-i\Delta)dt$ from the computation.

The right hand side is treated similarly. Define

$$\begin{aligned} \mathsf{e}'(t) &= \left(\frac{1}{T_0}\partial_t^{-1}\mathbf{P}^{\Lambda H} + \mathbf{P}^{\Sigma}\right) \mathsf{e}(t) \\ &\approx \sum_i \left(p(t-i\Delta t)\mathbf{P}^{\Sigma} + h(t-i\Delta t)\mathbf{P}^{\Lambda H}\right) \mathsf{e}_i' \qquad (5.37) \\ \mathsf{e}''(t) &= \mathbf{G}_{\mathrm{mx}}^{-1}\, \mathsf{e}'(t) \\ &\approx \sum_i \left(p(t-i\Delta t)\mathbb{P}^{\Sigma H} + h(t-i\Delta t)\mathbb{P}^{\Lambda}\right) \mathsf{e}_i''. \qquad (5.38) \end{aligned}$$

This leads to

$$\mathsf{e}_j'' = \left[\mathbf{G}^{-1} * \mathsf{e}\right]_j \tag{5.39}$$

for $j = 1, 2, ..., N_T$. Substituting (5.38) and (5.31) into (5.21):

$$\tilde{\mathcal{Z}}'\, \mathsf{y}''(t) = -\tilde{\mathcal{Z}}'\, \mathsf{e}''(t). \tag{5.40}$$

Again, a temporal Galerkin method is employed:

$$\int_{\mathbb{R}} \left(\delta(t - j\Delta t)\mathbb{P}^{\Sigma H} + \frac{1}{\Delta t} p(t - j\Delta t)\mathbb{P}^{\Lambda} \right) (\text{equation (5.40)}) \; dt \tag{5.41}$$

leading to

$$\left[\mathbb{Z}' * \mathsf{y}''\right]_j = -\left[\mathbb{Z}' * \mathsf{e}''\right]_j \tag{5.42}$$

for $j = 1, 2, ..., N_T$, where

$$\mathbb{Z}'_i = \begin{pmatrix} \mathbb{P}^{\Sigma H} & \mathbb{P}^{\Lambda} \end{pmatrix} \begin{pmatrix} \mathbb{Z}'^{SS}_i & \mathbb{Z}'^{SL}_i \\ \mathbb{Z}'^{SL}_i & \mathbb{Z}'^{LL}_i \end{pmatrix} \begin{pmatrix} \mathbb{P}^{\Sigma H} \\ \mathbb{P}^{\Lambda} \end{pmatrix}. \tag{5.43}$$

The quasi-Helmholtz components of this operator are given by

$$\begin{aligned}
\left[\mathbb{Z}'^{LL}_i\right]_{mn} &= T_0 \frac{\eta}{\Delta t} \int_{\mathbb{R}} dt \; p(t - i\Delta t) \int_{\Gamma} ds \; (\hat{\boldsymbol{n}} \times \boldsymbol{g}_m(\boldsymbol{r})) \cdot \partial_t \mathcal{T} \left\{ \boldsymbol{g}_n h \right\} (\boldsymbol{r}, t) \\
\left[\mathbb{Z}'^{LS}_i\right]_{mn} &= \frac{\eta}{\Delta t} \int_{\mathbb{R}} dt \; p(t - i\Delta t) \int_{\Gamma} ds \; (\hat{\boldsymbol{n}} \times \boldsymbol{g}_m(\boldsymbol{r})) \cdot \mathcal{T}_s \left\{ \boldsymbol{g}_n p \right\} (\boldsymbol{r}, t) \\
\left[\mathbb{Z}'^{SL}_i\right]_{mn} &= \eta \int_{\mathbb{R}} dt \; \delta(t - i\Delta t) \int_{\Gamma} ds \; (\hat{\boldsymbol{n}} \times \boldsymbol{g}_m(\boldsymbol{r})) \cdot \mathcal{T}_s \left\{ \boldsymbol{g}_n h \right\} (\boldsymbol{r}, t) \\
\left[\mathbb{Z}'^{SS}_i\right]_{mn} &= \frac{1}{T_0} \eta \int_{\mathbb{R}} dt \; \delta(t - i\Delta t) \int_{\Gamma} ds \; (\hat{\boldsymbol{n}} \times \boldsymbol{g}_m(\boldsymbol{r})) \cdot \partial_t^{-1} \mathcal{T}_s \left\{ \boldsymbol{g}_n p \right\} (\boldsymbol{r}, t).
\end{aligned}$$

The final discretized equation then becomes

$$\left[\mathbb{Z}' * \mathsf{G}^{-1} * \mathsf{Z}' * \mathsf{y}\right]_j = -\left[\mathbb{Z}' * \mathsf{G}^{-1} * \mathsf{e}\right]_j \tag{5.44}$$

for $j = 1, 2, ..., N_T$. Equation (5.44) is a preconditioned version of the qHP-TDEFIE developed in chapter 4. It can again be solved using the MOT algorithm:

$$-\mathsf{Q}_0 \mathsf{y}_j = \sum_{i=1}^{j} \mathsf{Q}_i \mathsf{y}_{j-i} + \sum_{i=0}^{j} \mathsf{R}_i \mathsf{e}_{j-i} \tag{5.45}$$

$$\mathsf{Q}_i = \sum_{l+m \leq i}^{l=0,m=0} \mathbb{Z}'_l \; \mathsf{G}_m^{-1} \; \mathsf{Z}'_{i-l-m} \tag{5.46}$$

$$\mathsf{R}_i = \sum_{l=0}^{i} \mathbb{Z}'_l \; \mathsf{G}_{i-l}^{-1}. \tag{5.47}$$

5.3.2 A Multiplicative Preconditioner

The full system (5.44) can be written in a lower triangular block matrix form:

$$\begin{pmatrix} \mathsf{Q}_0 & & & \\ \mathsf{Q}_1 & \mathsf{Q}_0 & & \\ \mathsf{Q}_2 & \mathsf{Q}_1 & \mathsf{Q}_0 & \\ \vdots & \vdots & \vdots & \ddots \end{pmatrix} \begin{pmatrix} \mathsf{y}_1 \\ \mathsf{y}_2 \\ \mathsf{y}_3 \\ \vdots \end{pmatrix} = - \begin{pmatrix} [\mathsf{R} * \mathsf{e}]_1 \\ [\mathsf{R} * \mathsf{e}]_2 \\ [\mathsf{R} * \mathsf{e}]_3 \\ \vdots \end{pmatrix}. \tag{5.48}$$

The MOT algorithm amounts to solving this equation through forward substitution. In order to be able to efficiently solve the MOT equations, it suffices that $\mathbf{Q}_0 = \mathbb{Z}'_0\mathbf{G}_0^{-1}\mathbf{Z}'_0$ is well-conditioned, rather than the full triangular block matrix. This means that $\mathbb{Z}'_0\mathbf{G}_0^{-1}$ can be used as a multiplicative preconditioner for the qHP-TDEFIE, instead of the convolution operator $\mathbb{Z}' * \mathbf{G}^{-1}$. The Calderón preconditioned qHP-TDEFIE then becomes

$$-\mathbb{Z}'_0\mathbf{G}_0^{-1}\mathbf{Z}'_0\mathsf{j}_j = \mathbb{Z}'_0\mathbf{G}_0^{-1}\left(\sum_{i=1}^{j}\mathbf{Z}'_i\mathsf{j}_{j-i} + \mathsf{e}_j\right). \tag{5.49}$$

5.3.3 Complexity Analysis

In practice, (5.49) is solved using iterative solution techniques which require only matrix-vector products. Applying the preconditioner requires the evaluation of the product of a vector with the matrix $\mathbb{Z}'_0\mathbf{G}_0^{-1}$.

The matrix $\mathbf{G}_0^{-1}$ is defined in (5.34). As argued in [19], multiplication with the projector matrices $\mathbf{P}^{\Lambda H}$, $\mathbf{P}^{\Sigma}$, $\mathbb{P}^{\Sigma H}$ and $\mathbb{P}^{\Lambda}$ requires $\mathcal{O}(N_S)$ time and memory. Furthermore, the Gram matrix $\mathbf{G}_{\mathrm{mx}}$ is sparse and well-conditioned [3], [22]. As a result, the complexity of multiplication with $\mathbf{G}_{\mathrm{mx}}^{-1}$ using iterative methods is also $\mathcal{O}(N_S)$.

Multiplication with $\mathbb{Z}'_0$ (5.43) also involves multiplication with the projector matrices, requiring $\mathcal{O}(N_S)$ operations.

For small time steps (i.e., in the high frequency regime), the matrices $\mathbb{Z}_0'^{LL}$, $\mathbb{Z}_0'^{LS}$, $\mathbb{Z}_0'^{SL}$ and $\mathbb{Z}_0'^{SS}$ contain $\mathcal{O}(N_S)$ elements representing interactions between nearby BC functions. The preconditioner can therefore be applied in $\mathcal{O}(N_S)$ operations.

For large time steps (i.e., in the low frequency regime), the matrices $\mathbb{Z}_0'^{LL}$, $\mathbb{Z}_0'^{LS}$, $\mathbb{Z}_0'^{SL}$ and $\mathbb{Z}_0'^{SS}$ contain $\mathcal{O}(N_S^2)$ elements representing (quasi-)static interactions between all BC functions. A direct computation of the product would then require $\mathcal{O}(N_S^2)$ operations. However, acceleration techniques for (quasi-)static kernels (see e.g. [23]) can be used to reduce the complexity to $\mathcal{O}(N_S)$.

In both regimes, multiplication with the preconditioner $\mathbb{Z}'_0\mathbf{G}_0^{-1}$ has the same computational complexity as multiplication with the qHP-TDEFIE system matrix $\mathbf{Z}'_0$. As a result, the computational complexity per iteration is the same for the standard qHP-TDEFIE and the CP qHP-TDEFIE. However, as will be shown in the numerical results section, the number of iterations required by the standard qHP-TDEFIE grows without bound for large N_S, while the CP qHP-TDEFIE can be solved in a small number of iterations regardless of N_S.

5.4 Low Frequency Limit

Now the low frequency limit of the Calderón preconditioned qHP-TDEFIE is investigated. The calculations made in section 4.4 show that for $\Delta t \to +\infty$,

$$\mathbf{Z}'_0 \to \frac{1}{T_0}\mathbf{P}^{\Lambda H}\mathbf{Z}^A_{\text{stat}}\mathbf{P}^{\Lambda H} + \frac{T_0}{2}\mathbf{P}^{\Sigma}\mathbf{Z}^{\phi}_{\text{stat}}\mathbf{P}^{\Sigma}. \tag{5.50}$$

where

$$\left[\mathbf{Z}^A_{\text{stat}}\right]_{mn} = -\mu\int_\Gamma ds\ \boldsymbol{f}_m(\boldsymbol{r})\cdot\int_\Gamma ds'\ \frac{\boldsymbol{f}_n(\boldsymbol{r}')}{4\pi R} \tag{5.51}$$

$$\left[\mathbf{Z}^{\phi}_{\text{stat}}\right]_{mn} = -\epsilon\int_\Gamma ds\ \nabla\cdot\boldsymbol{f}_m(\boldsymbol{r})\int_\Gamma ds'\ \frac{\nabla'\cdot\boldsymbol{f}_n(\boldsymbol{r}')}{4\pi R} \tag{5.52}$$

are the RWG discretizations of the static vector and scalar potentials, respectively. Similarly, for the BC discretized operators:

$$\mathbb{Z}'_0 \to \frac{1}{T_0}\mathbb{P}^{\Sigma H}\mathbb{Z}^A_{\text{stat}}\mathbb{P}^{\Sigma H} + \frac{T_0}{2}\mathbb{P}^{\Lambda}\mathbb{Z}^{\phi}_{\text{stat}}\mathbb{P}^{\Lambda} \tag{5.53}$$

$$\left[\mathbb{Z}^A_{\text{stat}}\right]_{mn} = -\mu\int_\Gamma ds\ \boldsymbol{g}_m(\boldsymbol{r})\cdot\int_\Gamma ds'\ \frac{\boldsymbol{g}_n(\boldsymbol{r}')}{4\pi R} \tag{5.54}$$

$$\left[\mathbb{Z}^{\phi}_{\text{stat}}\right]_{mn} = -\epsilon\int_\Gamma ds\ \nabla\cdot\boldsymbol{g}_m(\boldsymbol{r})\int_\Gamma ds'\frac{\nabla'\cdot\boldsymbol{g}_n(\boldsymbol{r}')}{4\pi R}. \tag{5.55}$$

The system matrix of the Calderón preconditioned qHP-TDEFIE is the product of three matrices with a well-defined and well-conditioned low frequency limit. Therefore, its low frequency limit is itself well-defined and well-conditioned. As a result, the the Calderón preconditioned qHP-TDEFIE is immune to low frequency breakdown.

Furthermore, the limit can be written as

$$\begin{aligned}
&\mathbb{Z}'_0\mathbf{G}_0^{-1}\mathbf{Z}'_0 \\
\to\ &\frac{1}{2}\left(\frac{1}{T_0}\mathbb{P}^{\Sigma H}\mathbb{Z}^A_{\text{stat}}\mathbb{P}^{\Sigma H} + T_0\mathbb{P}^{\Lambda}\mathbb{Z}^{\phi}_{\text{stat}}\mathbb{P}^{\Lambda}\right)\cdot\mathbf{G}_{\text{mx}}^{-1}\cdot \\
&\left(\frac{1}{T_0}\mathbf{P}^{\Lambda H}\mathbf{Z}^A_{\text{stat}}\mathbf{P}^{\Lambda H} + T_0\mathbf{P}^{\Sigma}\mathbf{Z}^{\phi}_{\text{stat}}\mathbf{P}^{\Sigma}\right) &(5.56)\\
=\ &\frac{1}{2}\mathbb{P}^{\Sigma H}\mathbb{Z}^A_{\text{stat}}\mathbb{P}^{\Sigma H}\mathbf{G}_{\text{mx}}^{-1}\mathbf{P}^{\Sigma}\mathbf{Z}^{\phi}_{\text{stat}}\mathbf{P}^{\Sigma} + \frac{1}{2}\mathbb{P}^{\Lambda}\mathbb{Z}^{\phi}_{\text{stat}}\mathbb{P}^{\Lambda}\mathbf{G}_{\text{mx}}^{-1}\mathbf{P}^{\Lambda H}\mathbf{Z}^A_{\text{stat}}\mathbf{P}^{\Lambda H} \\
&+\frac{1}{2T_0^2}\mathbb{P}^{\Sigma H}\mathbb{Z}^A_{\text{stat}}\mathbb{P}^{\Sigma H}\mathbf{G}_{\text{mx}}^{-1}\mathbf{P}^{\Lambda H}\mathbf{Z}^A_{\text{stat}}\mathbf{P}^{\Lambda H}. &(5.57)
\end{aligned}$$

For this, the property $\mathbb{P}^{\Lambda}\mathbf{G}_{\text{mx}}^{-1}\mathbf{P}^{\Sigma} = \mathbf{0}$ (see Appendix 5.A) has again been used. Up to the global factor $\frac{1}{2}$ and the scaling factor T_0, (5.57) is equal to the low frequency limit of the modified FD-EFIE [19]. It therefore enjoys the same

advantageous properties, in particular the absence of a kernel on both simply and multiply connected surfaces and a spectrum that admits efficient iterative solution even in the small mesh parameter limit.

5.5 Numerical Results

As mentioned in section 5.2.3, T_0 will be set to D/c (with D the diameter of the scatterer) in what follows. While this choice does influence the condition number of the system matrices, it does not influence its scaling as a function of h or Δt.

5.5.1 Sphere

Consider a perfectly conducting sphere with radius 1 m, approximated by a triangle mesh on which 771 RWG functions are defined (see figure 5.4, middle). It is illuminated by a Gaussian pulse

$$\boldsymbol{e}^i(\boldsymbol{r},t) = \frac{4A}{w\sqrt{\pi}}\hat{\boldsymbol{p}}\exp\left(-\left(\frac{4}{w}\left(c(t-t_0)-\hat{\boldsymbol{k}}\cdot\boldsymbol{r}\right)\right)^2\right), \tag{5.58}$$

with amplitude $A = 1\ V$, polarization $\hat{\boldsymbol{p}} = \hat{\mathbf{1}}_x$, direction $\hat{\boldsymbol{k}} = \hat{\mathbf{1}}_z$, width $w = 20\ m$ and time of arrival $t_0 = 200\ ns$ (or $ct_0 = 60\ m$). The induced surface current $\boldsymbol{j}(\boldsymbol{r},t)$ is computed using the following simulation techniques:

- the standard TD-EFIE ("TD-EFIE"),
- the standard Calderón preconditioned TD-EFIE ("CP TD-EFIE"),
- the dot-trick Calderón preconditioned TD-EFIE [8] ("dot-trick CP TD-EFIE"),
- the qHP-TDEFIE developed in chapter 4,
- the Calderón preconditioned qHP-TDEFIE developed in this chapter ("CP qHP-TDEFIE"),

each with $\Delta t = 0.83\ ns$ (or $c\Delta t = 0.25\ m$). The current at $(x,y,z) = (0.069\ m, 0.087\ m, 0.99\ m)$ is plotted in figure 5.5.

Up to $ct = 100\ m$, the five simulations match very well, with relative errors of the order of 10^{-4} and lower. After that point, however, DC instability comes into play for the TD-EFIE: a spurious constant-in-time loop current is observed. The CP TD-EFIE exhibits a linear-in-time DC instability. This is due to the fact that it is implemented as a convolution of two operators which are both susceptible to constant-in-time DC instability. The dot-trick CP TD-EFIE solves this problem: the current expansion coefficient goes down

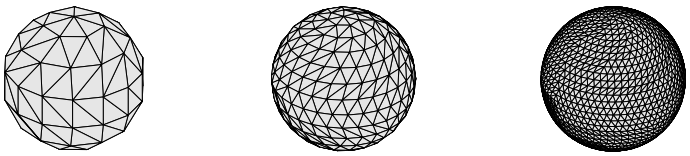

Figure 5.4: Spherical meshes with radius 1 m. Left: coarse mesh with $N_S = 192, h = 0.45\ m$. Middle: intermediate mesh with $N_S = 771, h = 0.22\ m$. Right: fine mesh with $N_S = 3963, h = 0.098\ m$.

to 10^{-14}, at which point the finite numerical precision comes into play: the solution becomes numerical noise. The same is observed for the qHP-TDEFIE and the CP qHP-TDEFIE. The last three schemes thus do not suffer from DC instability.

For each simulation method, the system matrix (i.e., $\mathbf{Z}'_0$ or $\mathbb{Z}'_0\mathbf{G}_{\text{mx}}^{-1}\mathbf{Z}'_0$ or equivalent, depending on the method) is now computed for different time step sizes, ranging from $c\Delta t = 0.25\ m$ to $c\Delta t = 64\ m$. The condition numbers of these matrices are plotted in figure 5.6. The condition number of the standard TD-EFIE grows proportionally to Δt^2: this is the low frequency breakdown. The other formulations are immune to LF breakdown. Note, however, that the condition number obtained by the qHP-TDEFIE (without preconditioner) is significantly higher than the condition number obtained using the Calderón preconditioned methods. This is due to dense discretization breakdown.

In order to study the effect of dense discretization breakdown, the time step is fixed at $c\Delta t = 1\ m$, and the discretization density is varied. The mesh parameter (i.e., the average edge length h) ranges from 0.098 m (figure 5.4, right) to 0.45 m (figure 5.4, left). The resulting condition numbers are plotted in figure 5.7. For dense spatial discretizations, the condition number of the schemes without preconditioner grow proportionally to h^{-2}, whereas the preconditioned schemes remain well-conditioned.

Next, each of these MOT simulations is carried out for $N_T = 300$ time steps. Figure 5.8 shows the average number of iterations required by the TFQMR iterative solver to reach a relative error of 10^{-6}. The number of iterations per time step is roughly constant for the Calderón preconditioned schemes, whereas a growth proportional to h^{-1} is observed for the schemes without preconditioner.

This shows that for simply connected geometries, the Calderón preconditioner developed in this chapter effectively eliminates the dense discretization breakdown of the qHP-TDEFIE. It performs just as well as the dot-trick Calderón preconditioned TD-EFIE, but does not require the evaluation of a double matrix-vector convolution, because the preconditioner is purely multiplicative.

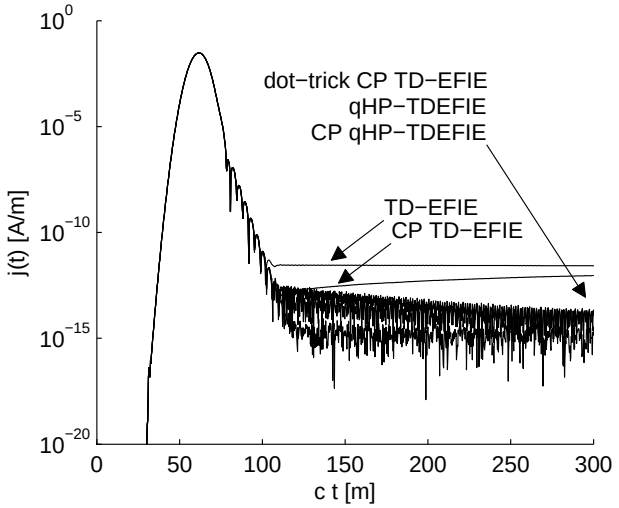

Figure 5.5: Induced current $\boldsymbol{j}(\boldsymbol{r}, t)$ on the sphere (figure 5.4, middle) at $\boldsymbol{r} = (0.069\ m, 0.087\ m, 0.99\ m)$, obtained using different simulation techniques.

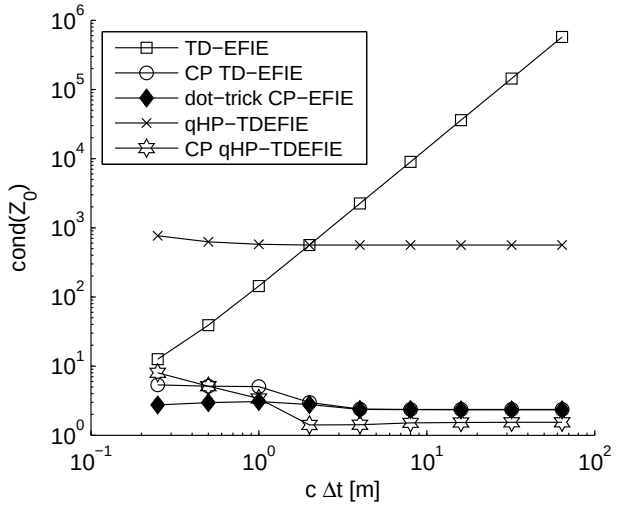

Figure 5.6: Condition number of the MOT system matrix for a sphere, obtained using different simulation types and parameters. The mesh parameters is fixed at $h = 0.22\ m$, while the time step is varied. The standard TD-EFIE simulations exhibit low frequency breakdown.

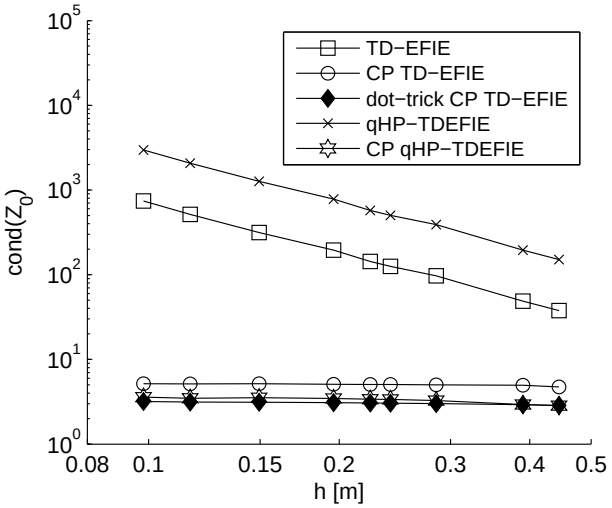

Figure 5.7: Condition number of the MOT system matrix for a sphere, obtained using different simulation types. The time step is fixed at $c\Delta t = 1\ m$, while the mesh parameter is varied. The standard TD-EFIE and the qHP-TDEFIE simulations exhibit dense discretization breakdown.

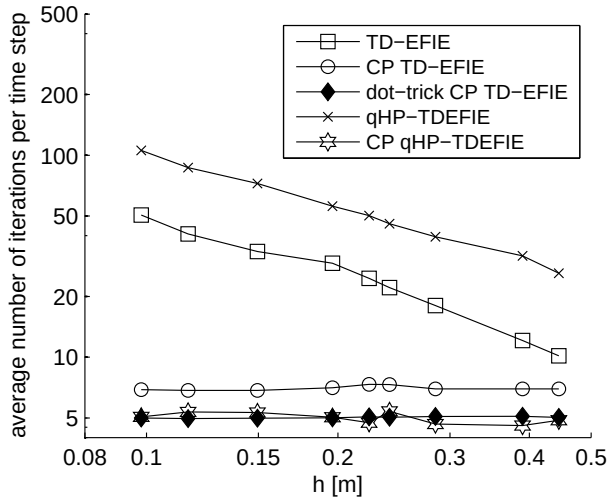

Figure 5.8: Average number of iterations required by the iterative solver at each time step, using different simulation types applied to a sphere. The time step is fixed at $c\Delta t = 1\ m$, while the mesh parameter is varied. The standard TD-EFIE and the qHP-TDEFIE simulations exhibit dense discretization breakdown.

5.5.2 Torus

The previous experiment is now repeated for a torus (which is multiply connected). First, the mesh parameter h is fixed at 0.14 m (figure 5.9, middle), and the time step at $c\Delta t = 0.25$ m. The torus is illuminated by the Gaussian pulse (5.58). The induced current at $(x, y, z) = (0.86\ m, 0.085\ m, 0.18\ m)$ obtained with the different simulation techniques is plotted in figure 5.10.

The results are roughly similar to the spherical case. Up to $ct \approx 100$ m, the five simulation techniques match up to a relative error of the order of 10^{-4}. After that, DC instability comes into play: the TD-EFIE and the CP TD-EFIE produce spurious static loop currents, whereas the qHP-TDEFIE and the CP qHP-TDEFIE do not. The major difference is that in this case, also the dot-trick CP TD-EFIE is prone to DC instability. This is due to the incorrect handling of global loops, as has been shown in the frequency domain in [14].

Next, the time step is increased from $c\Delta t = 0.25$ m up to $c\Delta t = 64$ m. The condition numbers of the system matrices for every simulation are plotted in figure 5.11. Low frequency breakdown is now also encountered in the CP TD-EFIE and the dot-trick CP TD-EFIE. This is again due to the incorrect handling of global loops. The qHP-TDEFIE and CP qHP-TDEFIE, however, remain well-conditioned at large time steps.

Finally, the time step is fixed at $c\Delta t = 4$ m, while the mesh parameter is varied from $h = 0.069$ m (figure 5.9, right) to $h = 0.28$ m (figure 5.9, left). As shown in figure 5.12, dense discretization breakdown is again encountered in the schemes without preconditioner, whereas the preconditioned schemes remain well-conditioned for dense spatial discretizations. Dense discretization breakdown is also apparent in the number of iterations required by the iterative solver to obtain a residual error lower than 10^{-6} at each time step. This is plotted in figure 5.13 for each of the simulation techniques under study.

Figure 5.9: Toroidal meshes with small radius 0.2 m and large radius 0.8 m. Left: coarse mesh with $N_S = 156, h = 0.28$ m. Middle: intermediate mesh with $N_S = 918, h = 0.14$ m. Right: fine mesh with $N_S = 3888, h = 0.069$ m.

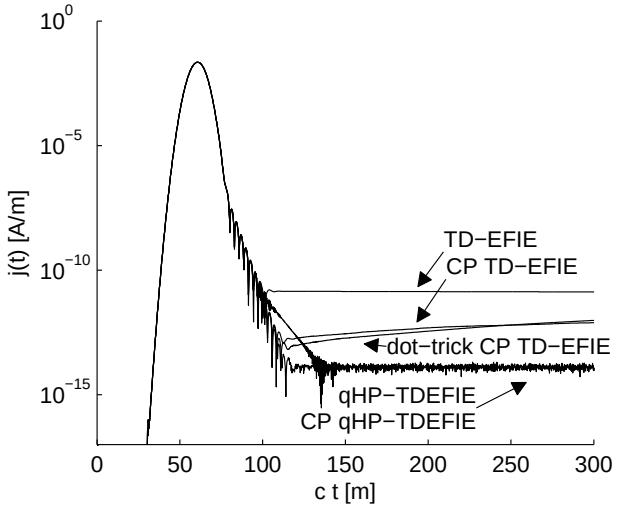

Figure 5.10: Induced current on the torus (figure 5.9, middle) at $(x, y, z) = (0.86\ m, 0.085\ m, 0.18\ m)$, obtained using different simulation techniques.

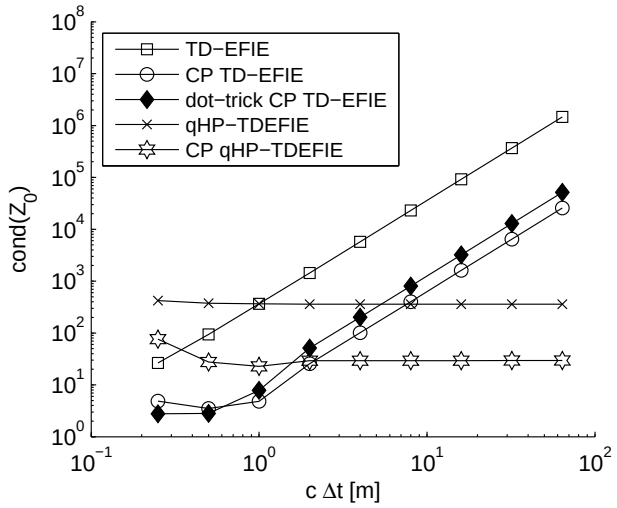

Figure 5.11: Condition number of the MOT system matrix for a torus, obtained using different simulation types and parameters. The mesh parameters is fixed at $h = 0.14\ m$, while the time step is varied. The TD-EFIE, CP TD-EFIE and dot-trick CP TD-EFIE all suffer from low frequency breakdown, whereas the (CP) qHP-TDEFIE does not.

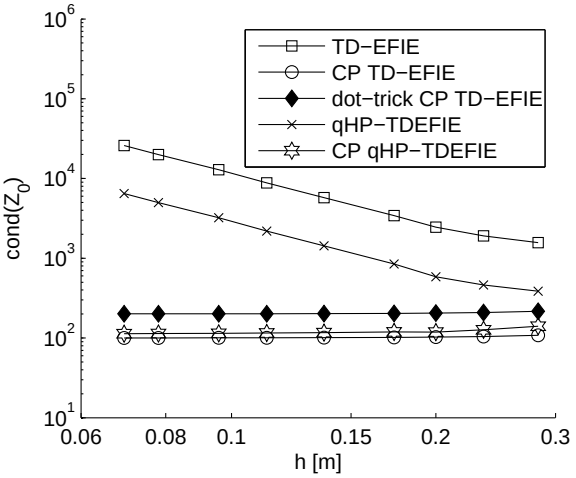

Figure 5.12: Condition number of the MOT system matrix for a torus, obtained using different simulation types. The time step is fixed at $c\Delta t = 4\ m$, while the mesh parameter is varied. The standard TD-EFIE and the qHP-TDEFIE simulations exhibit dense discretization breakdown, whereas the Calderón preconditioned (CP) schemes do not.

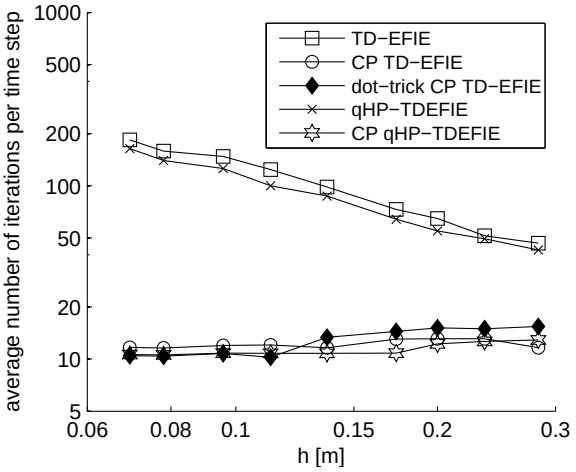

Figure 5.13: Average number of iterations required by the iterative solver at each time step, using different simulation types applied to a torus. The time step is fixed at $c\Delta t = 4\ m$, while the mesh parameter is varied. The standard TD-EFIE and the qHP-TDEFIE simulations exhibit dense discretization breakdown.

5.6 Conclusion

The qHP-TDEFIE developed in chapter 4 is, in itself, immune to low frequency breakdown and DC instability. However, it suffers from dense discretization breakdown: for dense spatial discretizations, the system matrix becomes ill-conditioned. In this contribution, a Calderón multiplicative preconditioner for this system matrix has been devised, which effectively solves the problem of dense discretization breakdown. It can be applied to the qHP-TDEFIE without making any further modifications to the original scheme. The preconditioned scheme is stable and well-conditioned both at large time steps and for dense spatial discretization.

For simply connected geometries, similar results can be obtained using the using the Calderón preconditioned TD-EFIE (with or without the dot-trick). However, for multiply connected structures, these methods solve neither DC instability nor low frequency breakdown due to the incorrect handling of global topological loops. The Calderón preconditioned qHP-TDEFIE on the other hand is effective for both simply and multiply connected geometries, without requiring the detection of global loops.

5.A The Mixed Gram Matrix

In section 5.3, the property $\mathbb{P}^{\Lambda}\mathbf{G}_{\mathrm{mx}}^{-1}\mathbf{P}^{\Sigma} = \mathbf{0}$ was used. In order to prove this, consider a scatterer with genus g. A current on its surface is expanded in RWG functions, with expansion coefficients r. This vector can be expressed in a basis formed by $(N_F - 1)$ RWG stars (Σ), $(N_V - 1)$ RWG local loop (Λ), and $2g$ global RWG loops (H) as defined in [19] :

$$\mathsf{r} = \mathbf{T} \begin{pmatrix} \mathsf{r}^{\Lambda} \\ \mathsf{r}^{H} \\ \mathsf{r}^{\Sigma} \end{pmatrix} . \tag{5.59}$$

The columns of the matrix $\mathbf{T}$ are the RWG coefficients of the basis functions belonging to Λ, H and Σ. The projector operator $\mathbf{P}^{\Sigma}$ then satisfies for all RWG coefficient vectors r

$$\mathbf{P}^{\Sigma}\mathsf{r} = \mathbf{T} \begin{pmatrix} 0 \\ 0 \\ \mathsf{r}^{\Sigma} \end{pmatrix} \Rightarrow \mathbf{P}^{\Sigma}\mathbf{T} = \mathbf{T} \begin{pmatrix} \mathbf{0} & \mathbf{0} & \mathbf{0} \\ \mathbf{0} & \mathbf{0} & \mathbf{0} \\ \mathbf{0} & \mathbf{0} & \mathbf{1} \end{pmatrix} . \tag{5.60}$$

The vectors in Λ give rise to solenoidal functions when they are interpreted as RWG expansion coefficients, while they give rise to non-solenoidal functions when they are interpreted as BC expansion coefficients. Similarly, vectors in Σ give rise to non-solenoidal functions when they are interpreted as RWG expansion coefficients, while they give rise to solenoidal functions when they are interpreted as BC expansion functions. Vectors in H give rise to solenoidal

functions both when they are interpreted as RWG or BC coefficients. As a consequence, for a random vector of BC expansion coefficients,

$$\mathsf{b} = \mathbf{T} \begin{pmatrix} \mathsf{b}^{\Lambda} \\ \mathsf{b}^{H} \\ \mathsf{b}^{\Sigma} \end{pmatrix} \tag{5.61}$$

the projector operator $\mathbb{P}^{\Lambda}$ satisfies (similar to (5.60))

$$\mathbb{P}^{\Lambda}\mathsf{b} = \mathbf{T} \begin{pmatrix} \mathsf{b}^{\Lambda} \\ 0 \\ 0 \end{pmatrix} \Rightarrow \mathbb{P}^{\Lambda}\mathbf{T} = \mathbf{T} \begin{pmatrix} \mathbf{1} & \mathbf{0} & \mathbf{0} \\ \mathbf{0} & \mathbf{0} & \mathbf{0} \\ \mathbf{0} & \mathbf{0} & \mathbf{0} \end{pmatrix}. \tag{5.62}$$

Next, consider an element of the Gram matrix $\mathbf{G}_{\mathrm{mx}}$:

$$\begin{aligned} x &= \mathsf{r}^{T}\mathbf{G}_{\mathrm{mx}}\mathsf{b} \\ &= \int_{\Gamma} (\hat{\boldsymbol{n}} \times \boldsymbol{f}(\boldsymbol{r})) \cdot \boldsymbol{g}(\boldsymbol{r}) ds \\ \boldsymbol{f}(\boldsymbol{r}) &= \sum_{m} \mathsf{r}_m \boldsymbol{f}_m(\boldsymbol{r}) \\ \boldsymbol{g}(\boldsymbol{r}) &= \sum_{m} \mathsf{b}_m \boldsymbol{g}_m(\boldsymbol{r}). \end{aligned} \tag{5.63}$$

If $\boldsymbol{f}(\boldsymbol{r})$ is a local RWG loop on Γ, it can be written as the surface curl of a potential:

$$\boldsymbol{f}(\boldsymbol{r}) = \hat{\boldsymbol{n}} \times \mathrm{grad}_{\Gamma}\psi(\boldsymbol{r}). \tag{5.64}$$

Further suppose that $\boldsymbol{g}(\boldsymbol{r})$ is solenoidal (either a global or a local BC loop). Then,

$$x = -\int_{\Gamma} (\mathrm{grad}_{\Gamma}\psi(\boldsymbol{r})) \cdot \boldsymbol{g}(\boldsymbol{r}) ds \tag{5.65}$$

$$= \int_{\Gamma} \psi(\boldsymbol{r}) \left(\mathrm{div}_{\Gamma} \cdot \boldsymbol{g}(\boldsymbol{r})\right) ds \tag{5.66}$$

$$= 0. \tag{5.67}$$

The same reasoning can also be applied when $\boldsymbol{g}(\boldsymbol{r})$ is a local BC loop, and $\boldsymbol{f}(\boldsymbol{r})$ is solenoidal (either a global or a local RWG loop).

Therefore,

$$\mathbf{G}_{\mathrm{mx}} = \left(\mathbf{T}^{T}\right)^{-1} \begin{pmatrix} \square & \mathbf{0} & \mathbf{0} \\ \square & \square & \mathbf{0} \\ \square & \square & \square \end{pmatrix} (\mathbf{T})^{-1}, \tag{5.68}$$

where $\square$ represents a nonzero block.The inverse Gram matrix exhibits the same algebraic structure:

$$\mathbf{G}_{\mathrm{mx}}^{-1} = \mathbf{T} \begin{pmatrix} \square & \mathbf{0} & \mathbf{0} \\ \square & \square & \mathbf{0} \\ \square & \square & \square \end{pmatrix} \mathbf{T}^{T}. \tag{5.69}$$

Now,

$$\begin{aligned}
& \mathbb{P}^{\Lambda}\mathbf{G}_{\mathrm{mx}}^{-1}\mathbf{P}^{\Sigma} \\
= \;& \mathbb{P}^{\Lambda}\mathbf{G}_{\mathrm{mx}}^{-1}\left(\mathbf{P}^{\Sigma}\right)^{T} \\
= \;& \mathbb{P}^{\Lambda}\mathbf{T}\begin{pmatrix}\square & \mathbf{0} & \mathbf{0}\\ \square & \square & \mathbf{0}\\ \square & \square & \square\end{pmatrix}\left(\mathbf{P}^{\Sigma}\mathbf{T}\right)^{T} \\
= \;& \mathbf{T}\begin{pmatrix}\mathbf{1} & \mathbf{0} & \mathbf{0}\\ \mathbf{0} & \mathbf{0} & \mathbf{0}\\ \mathbf{0} & \mathbf{0} & \mathbf{0}\end{pmatrix}\begin{pmatrix}\square & \mathbf{0} & \mathbf{0}\\ \square & \square & \mathbf{0}\\ \square & \square & \square\end{pmatrix}\begin{pmatrix}\mathbf{0} & \mathbf{0} & \mathbf{0}\\ \mathbf{0} & \mathbf{0} & \mathbf{0}\\ \mathbf{0} & \mathbf{0} & \mathbf{1}\end{pmatrix}\mathbf{T}^{T} \\
= \;& \mathbf{0}. \qquad (5.70)
\end{aligned}$$

References

[1] Y. Beghein, K. Cools, and F. P. Andriulli, "A DC-stable, well balanced, Calderón preconditioned time domain electric field integral equation", *IEEE Transactions on Antennas and Propagation*, accepted for publication on October 1st, 2015.

[2] K. Cools, F. P. Andriulli, F. Olyslager, and E. Michielssen, "Time domain Calderón identities and their application to the integral equation analysis of scattering by PEC objects part I: Preconditioning", *IEEE Transactions on Antennas and Propagation*, vol. 57, no. 8, pp. 2352–2364, Aug. 2009.

[3] F. P. Andriulli, K. Cools, H. Bağcı, F. Olyslager, A. Buffa, S. Christiansen, and E. Michielssen, "A multiplicative Calderón preconditioner for the electric field integral equation", *IEEE Transactions on Antennas and Propagation*, vol. 56, no. 8, pp. 2398–2412, Aug. 2008.

[4] F. P. Andriulli, A. Tabacco, and G. Vecchi, "Solving the EFIE at low frequencies with a conditioning that grows only logarithmically with the number of unknowns", *IEEE Transactions on Antennas and Propagation*, vol. 58, no. 5, pp. 1614–1624, May 2010.

[5] Z. G. Qian and W. C. Chew, "A quantitative study on the low frequency breakdown of EFIE", *Microwave and Optical Technology Letters*, vol. 50, no. 5, pp. 1159–1162, May 2008.

[6] F. P. Andriulli, H. Bağcı, F. Vipiana, G. Vecchi, and E. Michielssen, "Analysis and regularization of the TD-EFIE low-frequency breakdown", *IEEE Transactions on Antennas and Propagation*, vol. 57, no. 7, pp. 2034–2046, Jul. 2009.

[7] N.-W. Chen, K. Aygun, and E. Michielssen, "Integral-equation-based analysis of transient scattering and radiation from conducting bodies at very low frequencies", *IEE Proceedings Microwaves, Antennas and Propagation*, vol. 148, no. 6, pp. 381–387, Dec. 2001.

[8] F. P. Andriulli, K. Cools, F. Olyslager, and E. Michielssen, "Time domain Calderón identities and their application to the integral equation analysis of scattering by PEC objects part II: Stability", *IEEE Transactions on Antennas and Propagation*, vol. 57, no. 8, pp. 2365–2375, Aug. 2009.

[9] M.-D. Zhu, X.-L. Zhou, and W.-Y. Yin, "Efficient evaluation of double surface integrals in time-domain integral equation formulations", *IEEE Transactions on Antennas and Propagation*, vol. 61, no. 9, pp. 4653–4664, Sep. 2013.

[10] B. Shanker, M. Lu, J. Yuan, and E. Michielssen, "Time domain integral equation analysis of scattering from composite bodies via exact evaluation of radiation fields", *IEEE Transactions on Antennas and Propagation*, vol. 57, no. 5, pp. 1506–1520, May 2009.

[11] A. Yucel and A. Ergin, "Exact evaluation of retarded-time potential integrals for the RWG bases", *IEEE Transactions on Antennas and Propagation*, vol. 54, no. 5, pp. 1496–1502, May 2006.

[12] Y. Shi, M.-Y. Xia, R. shan Chen, E. Michielssen, and M. Lu, "Stable electric field TDIE solvers via quasi-exact evaluation of MOT matrix elements", *IEEE Transactions on Antennas and Propagation*, vol. 59, no. 2, pp. 574–585, Feb. 2011.

[13] Y. Shi, H. Bağcı, and M. Lu, "On the static loop modes in the marching-on-in-time solution of the time-domain electric field integral equation", *IEEE Antennas and Wireless Propagation Letters*, vol. 13, pp. 317–320, 2014.

[14] K. Cools, F. P. Andriulli, F. Olyslager, and E. Michielssen, "Nullspaces of MFIE and Calderón preconditioned EFIE operators applied to toroidal surfaces", *IEEE Transactions on Antennas and Propagation*, vol. 57, no. 10, pp. 3205–3215, Oct. 2009.

[15] G. Vecchi, "Loop-star decomposition of basis functions in the discretization of the EFIE", *IEEE Transactions on Antennas and Propagation*, vol. 47, no. 2, pp. 339–346, Feb. 1999.

[16] J.-S. Zhao and W. C. Chew, "Integral equation solution of Maxwell's equations from zero frequency to microwave frequencies", *IEEE Transactions on Antennas and Propagation*, vol. 48, no. 10, pp. 1635–1645, Oct. 2000.

[17] J.-F. Lee and R. Burkholder, "Loop star basis functions and a robust preconditioner for EFIE scattering problems", *IEEE Transactions on Antennas and Propagation*, vol. 51, no. 8, pp. 1855–1863, Aug. 2003.

[18] T. Eibert, "Iterative-solver convergence for loop-star and loop-tree decompositions in method-of-moments solutions of the electric-field integral equation", *Antennas and Propagation Magazine, IEEE*, vol. 46, no. 3, pp. 80–85, Jun. 2004.

[19] F. P. Andriulli, K. Cools, I. Bogaert, and E. Michielssen, "On a well-conditioned electric field integral operator for multiply connected geometries", *IEEE Transactions on Antennas and Propagation*, vol. 61, no. 4, pp. 2077–2087, Apr. 2013.

[20] F. Valdes, M. Ghaffari-Miab, F. P. Andriulli, K. Cools, J. Kotulski, and E. Michielssen, "High-order Calderón multiplicative preconditioner for time domain electric field integral equations", in *2011 IEEE International Symposium on Antennas and Propagation (APSURSI)*, Jul. 2011, pp. 2362–2362.

[21] S. Rao, D. Wilton, and A. Glisson, "Electromagnetic scattering by surfaces of arbitrary shape", *IEEE Transactions on Antennas and Propagation*, vol. 30, no. 3, pp. 409 –418, May 1982.

[22] A. Buffa and S. H. Christiansen, "A dual finite element complex on the barycentric refinement", *Comptes Rendus Mathematique*, vol. 340, no. 6, pp. 461 –464, 2005.

[23] M. Bebendorf, "Approximation of boundary element matrices", *Numerische Mathematik*, vol. 86, no. 4, pp. 565–589, 2000.

Part II

Scattering by Penetrable Media

This second part is concerned with scattering problems involving penetrable media. Chapter 6 extends the techniques of part I to the time domain PMCHWT equation. In chapter 7, a Calderón preconditioner for the frequency domain chiral PMCWHT equation is studied.

6

The qHP-PMCHWT Equation

Y. Beghein

This chapter is in part based on a contribution to the *International Conference on Electromagnetics in Advanced Applications (ICEAA)* (September 2015) [1], but also contains additional unpublished results.

★ ★ ★

The time domain PMCHWT equation models transient scattering by piecewise homogeneous penetrable objects. Like the TD-EFIE, it can be solved numerically using the MOT method. However, it has been notoriously difficult to obtain stable MOT schemes from this equation. Theoretically, the TD-PMCHWT equation suffers from DC instability: it supports static sourceless regime solutions. In practice, these regime solutions correspond to exponentially increasing solutions of the discretized system. This is due to numerical errors in the computation of the interaction matrix elements. In this chapter, the qHP-PMCHWT equation is developed, an alternative formulation of the TD-PMCHWT equation which is immune to DC instability. As such, it does not support static regime solutions which can become exponentially increasing due to numerical errors. As a result, a stable MOT scheme can be developed. Furthermore, the proposed equation is immune to low frequency breakdown, and its dense discretization breakdown is solved by developing a suitable Calderón preconditioner.

6.1 Introduction

The time domain Poggio-Miller-Chan-Harrington-Wu-Tsai (TD-PMCHWT) equation models transient scattering by piecewise homogeneous dielectrics. Like the time domain electric field integral equation (TD-EFIE), which is applicable to perfect conductors, it can be solved using the marching-on-in-time (MOT) algorithm. It has, however, proven more difficult to develop a stable MOT system for the TD-PMCHWT equation than for the TD-EFIE, as noted in [2].

As will be shown further in this chapter, the main problem plaguing the TD-PMCHWT equation is DC instability. This phenomenon was previously encountered in the TD-EFIE in chapter 4. It originates from the existence of sourceless regime solutions, which reside in the null space of the TD-EFIE operator and inevitably show up in the numerical solution. In the case of the TD-EFIE, these spurious currents are static (i.e., constant or at most linear in time). This is true even when the interaction integrals are computed with limited precision, because the spatial and temporal differentiations that lead to the cancellation of such solutions appear explicitly in the equation and can be performed up to machine precision.

The TD-PMCHWT equation also supports static regime solutions. However, the null space of the PMCHWT operator is less robust under the discretization, especially in the presence of numerical errors such as quadrature errors: the (theoretically static) regime solutions then become exponentially increasing. As a result, standard TD-PMCHWT MOT simulations can only be stable if all interaction integrals are computed with extremely high accuracy, which is very challenging especially when the algorithm is required to be extended to allow for curvilinear elements and higher order spaces. Even then, TD-PMCHWT MOT simulations would be plagued by spurious static currents.

In chapter 4, the quasi-Helmholtz projected TD-EFIE or qHP-TDEFIE has been introduced, a TD-EFIE formulation which is immune to DC instability. Unfortunately, the stabilization method used in chapter 4 cannot be applied directly to the TD-PMCHWT equation. The reason for this is that while the order of temporal differentiation of the TD-EFIE operator applied to local and global solenoidal currents is the same, the TD-PMCHWT operator does discriminate between them. Therefore, the stabilization method of chapter 4 would not correctly handle global loops if it were applied to the TD-PMCHWT equation.

In this chapter, an alternative stabilization method is developed for the TD-PMCHWT equation. The resulting equation, termed the qHP-PMCHWT equation, is immune to DC instability. In other words, it does not support static regime solutions which can become unstable due to numerical errors. This solves the TD-PMCHWT equation's stability problem on a fundamental level, for both simply and multiply connected geometries, without requiring the detection of global topological loops.

Once a stable MOT scheme is obtained, the condition number of the MOT system matrix must be investigated. Just like the TD-EFIE, the TD-PMCHWT equation suffers from both low frequency breakdown and dense discretization breakdown. Just like the qHP-TDEFIE, the qHP-PMCHWT equation is immune to low frequency breakdown. Furthermore, a Calderón preconditioner can be developed in order to combat dense discretization breakdown.

This chapter is organized as follows. In section 6.2, the TD-PMCHWT is discretized in space. In section 6.3, the resulting semi-discrete equation is further manipulated in order to obtain a DC stable and low frequency stable equation. The low frequency limit of this formulation is investigated in section 6.4. It is then discretized in time in section 6.5, resulting in the discrete qHP-PMCHWT equation. A Calderón preconditioner for this equation is constructed in section 6.6. Then, some implementation details are discussed in section 6.7. Finally, numerical results are presented in section 6.8.

6.2 Spatial Discretization

Consider a scattering problem as in section 1.2.10, involving a dielectric body Ω with boundary Γ and exterior normal vector $\hat{\boldsymbol{n}}$. The permittivity of this body is denoted ϵ', and its permeability μ'. It is embedded in a medium (e.g., vacuum) with permittivity ϵ and permeability μ. When an incident electromagnetic field $\boldsymbol{e}^{\text{inc}}, \boldsymbol{h}^{\text{inc}}$ illuminates Ω, the equivalent electric and magnetic current densities $\boldsymbol{j}, \boldsymbol{m}$ on Γ satisfy the TD-PMCHWT equation (1.55):

$$\begin{pmatrix} \frac{1}{\eta}\mathcal{T} + \frac{1}{\eta'}\mathcal{T}' & -\mathcal{K} - \mathcal{K}' \\ \mathcal{K} + \mathcal{K}' & \eta\mathcal{T} + \eta'\mathcal{T}' \end{pmatrix} \begin{pmatrix} \boldsymbol{m} \\ \boldsymbol{j} \end{pmatrix} = - \begin{pmatrix} \hat{\boldsymbol{n}} \times \boldsymbol{h}^{\text{inc}} \\ \hat{\boldsymbol{n}} \times \boldsymbol{e}^{\text{inc}} \end{pmatrix} \tag{6.1}$$

where the operators $\mathcal{T}$ and $\mathcal{K}$ are defined as in (1.33) and (1.36), respectively, and $\eta = \sqrt{\mu/\epsilon}$. The operators and quantities with a prime ($\mathcal{K}'$, $\mathcal{T}'$, η') are defined similarly, with material parameters ϵ' and μ'.

In order to discretize (6.1), define

$$\begin{pmatrix} \boldsymbol{j}' \\ \boldsymbol{m}' \end{pmatrix} := \begin{pmatrix} \frac{1}{\eta}\mathcal{T} + \frac{1}{\eta'}\mathcal{T}' & -\mathcal{K} - \mathcal{K}' \\ \mathcal{K} + \mathcal{K}' & \eta\mathcal{T} + \eta'\mathcal{T}' \end{pmatrix} \begin{pmatrix} \boldsymbol{m} \\ \boldsymbol{j} \end{pmatrix}. \tag{6.2}$$

The unknowns $\boldsymbol{j}$ and $\boldsymbol{m}$ are discretized in space using the Rao-Wilton-Glisson (RWG) functions $\boldsymbol{f}_l(\boldsymbol{r})$ (defined without edge length normalization, as in (2.2)), while $\boldsymbol{j}'$ and $\boldsymbol{m}'$ are discretized using Buffa-Christiansen (BC) functions $\boldsymbol{g}_l(\boldsymbol{r})$:

$$\boldsymbol{m}(\boldsymbol{r}, t) \approx \sum_{l=1}^{N_S} \mathsf{m}_l(t) \boldsymbol{f}_l(\boldsymbol{r}) \tag{6.3}$$

$$\boldsymbol{j}(\boldsymbol{r}, t) \approx \sum_{l=1}^{N_S} \mathsf{j}_l(t) \boldsymbol{f}_l(\boldsymbol{r}) \tag{6.4}$$

$$\boldsymbol{m}'(\boldsymbol{r},t) \approx \sum_{l=1}^{N_S} \mathsf{m}'_l(t)\boldsymbol{g}_l(\boldsymbol{r}) \tag{6.5}$$

$$\boldsymbol{j}'(\boldsymbol{r},t) \approx \sum_{l=1}^{N_S} \mathsf{j}'_l(t)\boldsymbol{g}_l(\boldsymbol{r}). \tag{6.6}$$

A relation between $(\mathsf{m}'(t),\mathsf{j}'(t))$ and $(\mathsf{m}(t),\mathsf{j}(t))$ can be obtained by spatially testing both lines of (6.2) with the rotated RWG functions $\hat{\boldsymbol{n}} \times \boldsymbol{f}_m(\boldsymbol{r})$:

$$\begin{pmatrix} \mathsf{j}'(t) \\ \mathsf{m}'(t) \end{pmatrix} = \begin{pmatrix} \mathsf{G}_{fg}^{-1} & \mathbf{0} \\ \mathbf{0} & \mathsf{G}_{fg}^{-1} \end{pmatrix} \begin{pmatrix} \mathcal{Q}_{11} & \mathcal{Q}_{12} \\ \mathcal{Q}_{21} & \mathcal{Q}_{22} \end{pmatrix} \begin{pmatrix} \mathsf{m}(t) \\ \mathsf{j}(t) \end{pmatrix} \tag{6.7}$$

where

$$[\mathcal{Q}_{11}\mathsf{m}(t)]_k = \sum_{l=1}^{N_S} \left(\hat{\boldsymbol{n}} \times \boldsymbol{f}_k, \left(\frac{1}{\eta}\mathcal{T} + \frac{1}{\eta'}\mathcal{T}' \right) \{\mathsf{m}_l(t)\boldsymbol{f}_l(\boldsymbol{r})\} \right) \tag{6.8a}$$

$$[\mathcal{Q}_{12}\mathsf{j}(t)]_k = -\sum_{l=1}^{N_S} \left(\hat{\boldsymbol{n}} \times \boldsymbol{f}_k, (\mathcal{K} + \mathcal{K}') \{\mathsf{j}_l(t)\boldsymbol{f}_l(\boldsymbol{r})\} \right) \tag{6.8b}$$

$$[\mathcal{Q}_{21}\mathsf{m}(t)]_k = \sum_{l=1}^{N_S} \left(\hat{\boldsymbol{n}} \times \boldsymbol{f}_k, (\mathcal{K} + \mathcal{K}') \{\mathsf{m}_l(t)\boldsymbol{f}_l(\boldsymbol{r})\} \right) \tag{6.8c}$$

$$[\mathcal{Q}_{22}\mathsf{j}(t)]_k = \sum_{l=1}^{N_S} \left(\hat{\boldsymbol{n}} \times \boldsymbol{f}_k, (\eta\mathcal{T} + \eta'\mathcal{T}') \{\mathsf{j}_l(t)\boldsymbol{f}_l(\boldsymbol{r})\} \right) \tag{6.8d}$$

$$[\mathsf{G}_{fg}]_{mn} = \left(\hat{\boldsymbol{n}} \times \boldsymbol{f}_m, \boldsymbol{g}_n \right). \tag{6.8e}$$

The operators $\mathcal{Q}_{ij}$ map a time-dependent vector of RWG expansion coefficients onto a time-dependent vector of RWG testing coefficients.

In terms of $\mathsf{m}'(t)$ and $\mathsf{j}'(t)$, the PMCHWT equation (6.1) becomes

$$\begin{pmatrix} \mathsf{j}'(t) \\ \mathsf{m}'(t) \end{pmatrix} = -\begin{pmatrix} \mathsf{G}_{fg}^{-1} & \mathbf{0} \\ \mathbf{0} & \mathsf{G}_{fg}^{-1} \end{pmatrix} \begin{pmatrix} \mathsf{h}(t) \\ \mathsf{e}(t) \end{pmatrix} \tag{6.9}$$

with

$$[\mathsf{h}(t)]_m = \int_\Gamma \boldsymbol{f}_m(\boldsymbol{r}) \cdot \boldsymbol{h}^{\mathrm{inc}}(\boldsymbol{r},t)ds \tag{6.10}$$

$$[\mathsf{e}(t)]_m = \int_\Gamma \boldsymbol{f}_m(\boldsymbol{r}) \cdot \boldsymbol{e}^{\mathrm{inc}}(\boldsymbol{r},t)ds. \tag{6.11}$$

Note that the inverse Gram matrices in the left and right hand side of (6.9) cancel out. However, they are included here in order to facilitate the construction of the qHP-PMCHWT equation in the next sections.

6.3 Rescaling

Temporally discretizing (6.9) would lead to a system of equations that supports static regime solutions. In order to eliminate these solutions, define the auxiliary unknowns

$$\mathsf{x}(t) = \left(\mathbf{P}^{\Lambda H} + \frac{1}{T_0}\partial_t^{-1}\mathbf{P}^{\Sigma}\right)\mathsf{m}(t) \tag{6.12}$$

$$\mathsf{y}(t) = \left(\mathbf{P}^{\Lambda H} + \frac{1}{T_0}\partial_t^{-1}\mathbf{P}^{\Sigma}\right)\mathsf{j}(t) \tag{6.13}$$

$$\mathsf{x}'(t) = \left(\mathbb{P}^{\Sigma H} + \frac{1}{T_0}\partial_t^{-1}\mathbb{P}^{\Lambda}\right)\mathsf{m}'(t) \tag{6.14}$$

$$\mathsf{y}'(t) = \left(\mathbb{P}^{\Lambda} + \frac{1}{T_0}\partial_t^{-1}\mathbb{P}^{\Lambda}\right)\mathsf{j}'(t). \tag{6.15}$$

The projectors $\mathbf{P}^{\Sigma}$ and $\mathbf{P}^{\Lambda H}$ [3] are defined in section 4.3.1 (equations (4.21) and (4.21)), and project an arbitrary RWG coefficient vector onto the space of (local and global) RWG loops, and onto the space of RWG stars, respectively. Likewise, the projectors $\mathbb{P}^{\Lambda}$ and $\mathbb{P}^{\Sigma H}$ are defined in section 5.2.4 (equations (5.14) and (5.16)) and project an arbitrary BC coefficient vector onto the space of (local and global) BC loops, and onto the space of BC stars, respectively. When applied to multiply connected geometries, these projectors do not require the detection or construction of global topological loops.

The quantity T_0 is a scaling factor with the dimension of time. It is introduced to obtain a scale invariant and dimensionally consistent equation, and will be set to $T_0 = D/c$, where D is the diameter of the scatterer, and c is the speed of light in the surrounding medium.

In terms of the auxiliary unknowns, (6.7) becomes

$$\begin{pmatrix}\mathsf{y}'(t)\\ \mathsf{x}'(t)\end{pmatrix} = \begin{pmatrix}\mathcal{Q}'_{11} & \mathcal{Q}'_{12}\\ \mathcal{Q}'_{21} & \mathcal{Q}'_{22}\end{pmatrix}\begin{pmatrix}\mathsf{x}(t)\\ \mathsf{y}(t)\end{pmatrix} \tag{6.16}$$

with

$$\mathcal{Q}'_{ij} = \left(\mathbb{P}^{\Sigma H} + \tfrac{1}{T_0}\partial_t^{-1}\mathbb{P}^{\Lambda}\right)\mathbf{G}_{fg}^{-1}\ \mathcal{Q}_{ij}\left(\mathbf{P}^{\Lambda H} + T_0\partial_t\mathbf{P}^{\Sigma}\right). \tag{6.17}$$

A similar treatment of the right hand side of (6.1) leads to the semi-discrete qHP-PMCHWT equation

$$\begin{pmatrix}\mathcal{Q}'_{11} & \mathcal{Q}'_{12}\\ \mathcal{Q}'_{21} & \mathcal{Q}'_{22}\end{pmatrix}\begin{pmatrix}\mathsf{x}(t)\\ \mathsf{y}(t)\end{pmatrix} = -\begin{pmatrix}\mathsf{h}'(t)\\ \mathsf{e}'(t)\end{pmatrix} \tag{6.18}$$

where

$$\mathsf{h}'(t) = \left(\mathbb{P}^{\Sigma H} + \frac{1}{T_0}\partial_t^{-1}\mathbb{P}^{\Lambda}\right)\mathbf{G}_{fg}^{-1}\mathsf{h}(t) \tag{6.19}$$

$$\mathsf{e}'(t) = \left(\mathbb{P}^{\Sigma H} + \frac{1}{T_0}\partial_t^{-1}\mathbb{P}^{\Lambda}\right)\mathbf{G}_{fg}^{-1}\mathsf{e}(t). \tag{6.20}$$

6.4 Low Frequency Behavior

Before proceeding to the temporal discretization of (6.18), its low frequency behavior is investigated.

The spaces of RWG and BC expansion and testing coefficients can be decomposed into the following subspaces [3]:

- Λ: RWG local loops and BC stars,
- H: global loops in both RWG and BC space,
- Σ: RWG stars and BC local loops.

An explicit basis transform then transforms an RWG or BC coefficient vector into the following form:

$$\mathsf{x} \to \begin{pmatrix} \mathsf{x}_\Lambda \\ \mathsf{x}_H \\ \mathsf{x}_\Sigma \end{pmatrix} \tag{6.21}$$

where x_Λ contains the coefficients of the local RWG loops (or BC stars), x_H the coefficients of the global RWG loops (or global BC loops), and x_Σ the coefficients of the RWG stars (or local BC loops). In such a basis, the inverse Gram matrices take the following form:

$$\mathsf{G}_{gf}^{-1} \to \begin{pmatrix} \square & \square & \square \\ \mathbf{0} & \square & \square \\ \mathbf{0} & \mathbf{0} & \square \end{pmatrix} \qquad \mathsf{G}_{fg}^{-1} \to \begin{pmatrix} \square & \mathbf{0} & \mathbf{0} \\ \square & \square & \mathbf{0} \\ \square & \square & \square \end{pmatrix} \tag{6.22}$$

where $\square$ represents a nonzero block – see section 5.A. The projectors become

$$\mathsf{P}^{\Lambda H} \to \begin{pmatrix} \mathbf{1} & \mathbf{0} & \mathbf{0} \\ \mathbf{0} & \mathbf{1} & \mathbf{0} \\ \mathbf{0} & \mathbf{0} & \mathbf{0} \end{pmatrix} \qquad \mathsf{P}^{\Sigma} \to \begin{pmatrix} \mathbf{0} & \mathbf{0} & \mathbf{0} \\ \mathbf{0} & \mathbf{0} & \mathbf{0} \\ \mathbf{0} & \mathbf{0} & \mathbf{1} \end{pmatrix} \tag{6.23}$$

$$\mathbb{P}^{\Lambda} \to \begin{pmatrix} \mathbf{1} & \mathbf{0} & \mathbf{0} \\ \mathbf{0} & \mathbf{0} & \mathbf{0} \\ \mathbf{0} & \mathbf{0} & \mathbf{0} \end{pmatrix} \qquad \mathbb{P}^{\Sigma H} \to \begin{pmatrix} \mathbf{0} & \mathbf{0} & \mathbf{0} \\ \mathbf{0} & \mathbf{1} & \mathbf{0} \\ \mathbf{0} & \mathbf{0} & \mathbf{1} \end{pmatrix}. \tag{6.24}$$

In order to study the behavior of (6.18) for slowly varying fields, it is first Fourier transformed (yielding the frequency domain PMCHWT operator) and expressed in the basis of (Λ, H, Σ). It is known that the discretized frequency domain EFIE and MFIE components scale as [4], [5]

$$\mathcal{T} \quad \to \quad \begin{pmatrix} \omega & \omega & \omega \\ \omega & \omega & \omega \\ \omega & \omega & \omega^{-1} \end{pmatrix} \tag{6.25}$$

$$\pm\frac{1}{2} + \mathcal{K} \quad \to \quad \begin{pmatrix} \omega^2 & \omega^2 & 1 \\ \omega^2 & 1 & 1 \\ 1 & 1 & 1 \end{pmatrix}. \tag{6.26}$$

Keeping in mind that $\mathcal{K}+\mathcal{K}' = \left(\frac{1}{2}+\mathcal{K}\right)+\left(-\frac{1}{2}+\mathcal{K}'\right)$, it can easily be seen that the complete PMCHWT operator scales as[1]

$$\begin{pmatrix} \mathcal{Q}_{11} & \mathcal{Q}_{12} \\ \mathcal{Q}_{21} & \mathcal{Q}_{22} \end{pmatrix} \quad \rightarrow \quad \begin{pmatrix} \omega & \omega & \omega & \omega^2 & \omega^2 & 1 \\ \omega & \omega & \omega & \omega^2 & 1 & 1 \\ \omega & \omega & \omega^{-1} & 1 & 1 & 1 \\ \omega^2 & \omega^2 & 1 & \omega & \omega & \omega \\ \omega^2 & 1 & 1 & \omega & \omega & \omega \\ 1 & 1 & 1 & \omega & \omega & \omega^{-1} \end{pmatrix}. \tag{6.27}$$

This operator is ill-defined at low frequencies due to the presence of terms of $\mathcal{O}(\omega^{-1})$. As a result, (6.9) does not possess a well-defined limit for slowly varying fields. On the other hand,

$$\begin{pmatrix} \mathcal{Q}'_{11} & \mathcal{Q}'_{12} \\ \mathcal{Q}'_{21} & \mathcal{Q}'_{22} \end{pmatrix} \quad \rightarrow \quad \begin{pmatrix} 1 & 1 & \omega & \omega & \omega & 1 \\ \omega & \omega & \omega^2 & \omega^2 & 1 & \omega \\ \omega & \omega & 1 & 1 & 1 & \omega \\ \omega & \omega & 1 & 1 & 1 & \omega \\ \omega^2 & 1 & \omega & \omega & \omega & \omega^2 \\ 1 & 1 & \omega & \omega & \omega & 1 \end{pmatrix}. \tag{6.28}$$

In contrast to (6.27), (6.28) is well-behaved for low frequencies in the sense that it does not contain any divergent terms of $\mathcal{O}(\omega^{-1})$, or vanishing rows or columns of $\mathcal{O}(\omega)$. As a result, (6.18) does possess a well-defined limit for slowly varying electromagnetic fields.

6.5 Temporal Discretization

Now, a temporal Galerkin method is applied to the semi-discrete qHP-PMCHWT equation (6.18). The correct choice of basis and testing functions is essential for the stability of the MOT scheme. Following the procedure in chapter 4 , the loop and star parts of the auxiliary unknowns are expanded in different basis functions:

$$\mathsf{x}(t) = \sum_{i=1}^{N_T} \left(p(t-i\Delta t)\mathbf{P}^{\Lambda H} + h(t-i\Delta t)\mathbf{P}^{\Sigma} \right) \mathsf{x}^i \tag{6.29}$$

$$\mathsf{y}(t) = \sum_{i=1}^{N_T} \left(p(t-i\Delta t)\mathbf{P}^{\Lambda H} + h(t-i\Delta t)\mathbf{P}^{\Sigma} \right) \mathsf{y}^i \tag{6.30}$$

[1] Technically, it is possible that, e.g., two $\mathcal{O}(1)$ terms cancel out to an $\mathcal{O}(\omega)$ term. While it has not been proven that such cancellations do not occur, (6.27) and (6.28) describe the scaling that is encountered in practice.

where $p(t)$ are the pulse functions and $h(t)$ are the hat functions, as defined in chapter 2 (equation (2.56)–(2.57), figure 2.7). Similarly,

$$\mathsf{x}'(t) = \sum_{i=1}^{N_T} \left(p(t-i\Delta t)\mathbb{P}^{\Sigma H} + h(t-i\Delta t)\mathbb{P}^{\Lambda}\right)\mathsf{x}'^{i} \tag{6.31}$$

$$\mathsf{y}'(t) = \sum_{i=1}^{N_T} \left(p(t-i\Delta t)\mathbb{P}^{\Sigma H} + h(t-i\Delta t)\mathbb{P}^{\Lambda}\right)\mathsf{y}'^{i}. \tag{6.32}$$

Next, the following temporal Galerkin test procedure is applied to both lines of (6.16):

$$\int_{\mathbb{R}} \left(\tfrac{1}{\Delta t}p(t-j\Delta t)\mathbb{P}^{\Sigma H} + \delta(t-j\Delta t)\mathbb{P}^{\Lambda}\right)(\text{equation (6.16)})\,dt, \tag{6.33}$$

for $j = 1, 2, ..., N_T$, where $\delta(t)$ is the Dirac delta distribution, leading to

$$\begin{pmatrix}\mathsf{y}'^{j}\\ \mathsf{x}'^{j}\end{pmatrix} = \sum_{i=0}^{j}\begin{pmatrix}\mathbf{Q}'^{i}_{11} & \mathbf{Q}'^{i}_{12}\\ \mathbf{Q}'^{i}_{21} & \mathbf{Q}'^{i}_{22}\end{pmatrix}\begin{pmatrix}\mathsf{x}^{j-i}\\ \mathsf{y}^{j-i}\end{pmatrix} \tag{6.34}$$

with

$$\begin{aligned}\left[\mathbf{Q}'^{i}_{ab}\right]_{mn} &= \frac{1}{\Delta t}\int_{\mathbb{R}} p(t-i\Delta t)\mathbb{P}^{\Sigma H}\left[\mathcal{Q}'_{ab}\left\{\mathbf{P}^{\Lambda H}\mathbb{1}_n p(t)\right\}\right]_m(t)dt\\ &+ \frac{1}{\Delta t}\int_{\mathbb{R}} p(t-i\Delta t)\mathbb{P}^{\Sigma H}\left[\mathcal{Q}'_{ab}\left\{\mathbf{P}^{\Sigma}\mathbb{1}_n h(t)\right\}\right]_m(t)dt\\ &+ \int_{\mathbb{R}} \delta(t-i\Delta t)\mathbb{P}^{\Lambda}\left[\mathcal{Q}'_{ab}\left\{\mathbf{P}^{\Lambda H}\mathbb{1}_n p(t)\right\}\right]_m(t)dt\\ &+ \int_{\mathbb{R}} \delta(t-i\Delta t)\mathbb{P}^{\Lambda}\left[\mathcal{Q}'_{ab}\left\{\mathbf{P}^{\Sigma}\mathbb{1}_n h(t)\right\}\right]_m(t)dt\end{aligned} \tag{6.35}$$

or

$$\begin{aligned}\left[\mathbf{Q}'^{i}_{ab}\right]_{mn} &= \mathbb{P}^{\Sigma H}\mathbf{G}^{-1}_{fg}\left[\mathcal{Q}_{ab}\left\{\mathbf{P}^{\Lambda H}\mathbb{1}_n h(t)\right\}\right]_m(i\Delta t)\\ &+ T_0\mathbb{P}^{\Sigma H}\mathbf{G}^{-1}_{fg}\left[\partial_t\mathcal{Q}_{ab}\left\{\mathbf{P}^{\Sigma}\mathbb{1}_n q(t)\right\}\right]_m(i\Delta t)\\ &+ \frac{1}{T_0}\mathbb{P}^{\Lambda}\mathbf{G}^{-1}_{fg}\left[\partial_t^{-1}\mathcal{Q}_{ab}\left\{\mathbf{P}^{\Lambda H}\mathbb{1}_n p(t)\right\}\right]_m(i\Delta t)\\ &+ \mathbb{P}^{\Lambda}\mathbf{G}^{-1}_{fg}\left[\mathcal{Q}_{ab}\left\{\mathbf{P}^{\Sigma}\mathbb{1}_n h(t)\right\}\right]_m(i\Delta t)\end{aligned} \tag{6.36}$$

where the $N_S \times 1$ column vector $\mathbb{1}_n$ is defined by

$$\left[\mathbb{1}_n\right]_m = \delta_{nm}. \tag{6.37}$$

A similar treatment of the right hand side of (6.18) leads to the qHP-PMCHWT equation:

$$\sum_{i=0}^{j}\begin{pmatrix}\mathbf{Q}'^{i}_{11} & \mathbf{Q}'^{i}_{12}\\ \mathbf{Q}'^{i}_{21} & \mathbf{Q}'^{i}_{22}\end{pmatrix}\begin{pmatrix}\mathsf{x}^{j-i}\\ \mathsf{y}^{j-i}\end{pmatrix} = -\begin{pmatrix}\mathsf{h}'^{j}\\ \mathsf{e}'^{j}\end{pmatrix} \tag{6.38}$$

where

$$\mathsf{h}'^{j} = \int_{\mathbb{R}} \left(\frac{1}{\Delta t} p(t - j\Delta t)\mathbb{P}^{\Sigma H} + \delta(t - j\Delta t)\mathbb{P}^{\Lambda} \right) \mathsf{h}'(t)dt \tag{6.39}$$

$$\mathsf{e}'^{j} = \int_{\mathbb{R}} \left(\frac{1}{\Delta t} p(t - j\Delta t)\mathbb{P}^{\Sigma H} + \delta(t - j\Delta t)\mathbb{P}^{\Lambda} \right) \mathsf{e}'(t)dt. \tag{6.40}$$

Equation (6.38) can again be solved using the MOT algorithm:

$$-\begin{pmatrix} \mathbf{Q}'^{0}_{11} & \mathbf{Q}'^{0}_{12} \\ \mathbf{Q}'^{0}_{21} & \mathbf{Q}'^{0}_{22} \end{pmatrix} \begin{pmatrix} \mathsf{x}^{j} \\ \mathsf{y}^{j} \end{pmatrix} = \sum_{i=1}^{j} \begin{pmatrix} \mathbf{Q}'^{i}_{11} & \mathbf{Q}'^{i}_{12} \\ \mathbf{Q}'^{i}_{21} & \mathbf{Q}'^{i}_{22} \end{pmatrix} \begin{pmatrix} \mathsf{x}^{j-i} \\ \mathsf{y}^{j-i} \end{pmatrix} + \begin{pmatrix} \mathsf{h}'^{j} \\ \mathsf{e}'^{j} \end{pmatrix}. \tag{6.41}$$

In contrast to the standard TD-PMCHWT equation, the system (6.41) does not support static regime solutions that can become unstable due to numerical errors. This will be shown in the numerical results in section 6.8.

Also in contrast to the standard TD-PMCHWT scheme, the condition number of the MOT system matrix (i.e., the matrix in the left hand side of (6.41)) does not grow when the time step Δt is increased. This will be demonstrated numerically in section 6.8.

Equation (6.41) does suffer from dense discretization breakdown: the MOT system
order to remedy this, a Calderón preconditioner is constructed in section 6.6.

6.6 Calderón Preconditioning

The origin of dense discretization breakdown lies in the spectral properties of the PMCHWT operator. As discussed in [6], the PMCHWT operator's spectrum is bounded neither from below nor from above. However, by using the Calderón identities (1.43)–(1.44), it can be shown that the operator

$$\begin{pmatrix} \eta\mathcal{T} + \eta'\mathcal{T}' & -\mathcal{K} - \mathcal{K}' \\ \mathcal{K} + \mathcal{K}' & \frac{1}{\eta}\mathcal{T} + \frac{1}{\eta'}\mathcal{T}' \end{pmatrix} \begin{pmatrix} \frac{1}{\eta}\mathcal{T} + \frac{1}{\eta'}\mathcal{T}' & -\mathcal{K} - \mathcal{K}' \\ \mathcal{K} + \mathcal{K}' & \eta\mathcal{T} + \eta'\mathcal{T}' \end{pmatrix} \tag{6.42}$$

does possess a bounded spectrum. This has been proven in the frequency domain in [6], and can easily be extended to the time domain.

In order to construct a multiplicative preconditioner for the qHP-PMCHWT MOT equation (6.41), the continuous Calderón preconditioned PMCHWT equation

$$\begin{aligned} &\begin{pmatrix} \eta\mathcal{T} + \eta'\mathcal{T}' & -\mathcal{K} - \mathcal{K}' \\ \mathcal{K} + \mathcal{K}' & \frac{1}{\eta}\mathcal{T} + \frac{1}{\eta'}\mathcal{T}' \end{pmatrix} \begin{pmatrix} \frac{1}{\eta}\mathcal{T} + \frac{1}{\eta'}\mathcal{T}' & -\mathcal{K} - \mathcal{K}' \\ \mathcal{K} + \mathcal{K}' & \eta\mathcal{T} + \eta'\mathcal{T}' \end{pmatrix} \begin{pmatrix} \boldsymbol{m} \\ \boldsymbol{j} \end{pmatrix} \\ = \; &-\begin{pmatrix} \eta\mathcal{T} + \eta'\mathcal{T}' & -\mathcal{K} - \mathcal{K}' \\ \mathcal{K} + \mathcal{K}' & \frac{1}{\eta}\mathcal{T} + \frac{1}{\eta'}\mathcal{T}' \end{pmatrix} \begin{pmatrix} \hat{\boldsymbol{n}} \times \boldsymbol{h}^{\mathrm{inc}} \\ \hat{\boldsymbol{n}} \times \boldsymbol{e}^{\mathrm{inc}} \end{pmatrix} \end{aligned} \tag{6.43}$$

is used as a starting point. Analogously to (6.16), define

$$\begin{pmatrix} \boldsymbol{m}'' \\ \boldsymbol{j}'' \end{pmatrix} := \begin{pmatrix} \eta\mathcal{T} + \eta'\mathcal{T}' & \mathcal{K} + \mathcal{K}' \\ -\mathcal{K} - \mathcal{K}' & \frac{1}{\eta}\mathcal{T} + \frac{1}{\eta'}\mathcal{T}' \end{pmatrix} \begin{pmatrix} \boldsymbol{j}' \\ \boldsymbol{m}' \end{pmatrix}. \tag{6.44}$$

These auxiliary unknowns are discretized using RWG functions:

$$\boldsymbol{m}''(\boldsymbol{r},t) \approx \sum_{l=1}^{N_S} \mathsf{m}_l''(t)\boldsymbol{f}_l(\boldsymbol{r}) \tag{6.45}$$

$$\boldsymbol{j}''(\boldsymbol{r},t) \approx \sum_{l=1}^{N_S} \mathsf{j}_l''(t)\boldsymbol{f}_l(\boldsymbol{r}). \tag{6.46}$$

Testing both lines of (6.44) with the rotated BC functions $\hat{\boldsymbol{n}} \times \boldsymbol{g}_m$ leads to

$$\begin{pmatrix} \mathsf{G}_{gf} & \mathsf{0} \\ \mathsf{0} & \mathsf{G}_{gf} \end{pmatrix} \begin{pmatrix} \mathsf{m}''(t) \\ \mathsf{j}''(t) \end{pmatrix} = \begin{pmatrix} \mathcal{R}_{11} & \mathcal{R}_{12} \\ \mathcal{R}_{21} & \mathcal{R}_{22} \end{pmatrix} \begin{pmatrix} \mathsf{j}'(t) \\ \mathsf{m}'(t) \end{pmatrix} \tag{6.47}$$

where

$$[\mathcal{R}_{11}\mathsf{j}'(t)]_k = \sum_{l=1}^{N_S} (\hat{\boldsymbol{n}} \times \boldsymbol{g}_k, (\eta\mathcal{T} + \eta'\mathcal{T}') \{\mathsf{j}_l'(t)\boldsymbol{g}_l(\boldsymbol{r})\}) \tag{6.48}$$

$$[\mathcal{R}_{12}\mathsf{m}'(t)]_k = -\sum_{l=1}^{N_S} (\hat{\boldsymbol{n}} \times \boldsymbol{g}_k, (\mathcal{K} + \mathcal{K}') \{\mathsf{m}_l'(t)\boldsymbol{g}_l(\boldsymbol{r})\}) \tag{6.49}$$

$$[\mathcal{R}_{21}\mathsf{j}'(t)]_k = \sum_{l=1}^{N_S} (\hat{\boldsymbol{n}} \times \boldsymbol{g}_k, (\mathcal{K} + \mathcal{K}') \{\mathsf{j}_l'(t)\boldsymbol{g}_l(\boldsymbol{r})\}) \tag{6.50}$$

$$[\mathcal{R}_{22}\mathsf{m}'(t)]_k = \sum_{l=1}^{N_S} \left(\hat{\boldsymbol{n}} \times \boldsymbol{g}_k, \left(\frac{1}{\eta}\mathcal{T} + \frac{1}{\eta'}\mathcal{T}'\right) \{\mathsf{m}_l'(t)\boldsymbol{g}_l(\boldsymbol{r})\}\right) \tag{6.51}$$

$$[\mathsf{G}_{gf}]_{mn} = (\hat{\boldsymbol{n}} \times \boldsymbol{g}_m, \boldsymbol{f}_n). \tag{6.52}$$

In terms of the rescaled quantities

$$\mathsf{x}''(t) = \left(\mathsf{P}^{\Lambda H} + \frac{1}{T_0}\partial_t^{-1}\mathsf{P}^{\Sigma}\right) \mathsf{m}''(t) \tag{6.53}$$

$$\mathsf{y}''(t) = \left(\mathsf{P}^{\Lambda H} + \frac{1}{T_0}\partial_t^{-1}\mathsf{P}^{\Sigma}\right) \mathsf{j}''(t) \tag{6.54}$$

equation (6.47) is rewritten as

$$\begin{pmatrix} \mathsf{x}''(t) \\ \mathsf{y}''(t) \end{pmatrix} = \begin{pmatrix} \mathcal{R}_{11}' & \mathcal{R}_{12}' \\ \mathcal{R}_{21}' & \mathcal{R}_{22}' \end{pmatrix} \begin{pmatrix} \mathsf{y}'(t) \\ \mathsf{x}'(t) \end{pmatrix} \tag{6.55}$$

where

$$\mathcal{R}_{ij}' = \left(\mathsf{P}^{\Lambda H} + \frac{1}{T_0}\partial_t^{-1}\mathsf{P}^{\Sigma}\right) \mathsf{G}_{gf}^{-1}\mathcal{R}_{ij} \left(\mathbb{P}^{\Sigma H} + T_0\partial_t\mathbb{P}^{\Lambda}\right). \tag{6.56}$$

Analogously to (6.29)–(6.30), the unknowns $\mathsf{x}''(t)$ and $\mathsf{y}''(t)$ are expanded as

$$\mathsf{x}''(t) = \sum_{i=1}^{N_T} \left(p(t-i\Delta t)\mathbf{P}^{\Lambda H} + h(t-i\Delta t)\mathbf{P}^{\Sigma} \right) \mathsf{x}''^{i} \tag{6.57}$$

$$\mathsf{y}''(t) = \sum_{i=1}^{N_T} \left(p(t-i\Delta t)\mathbf{P}^{\Lambda H} + h(t-i\Delta t)\mathbf{P}^{\Sigma} \right) \mathsf{y}''^{i}. \tag{6.58}$$

Next, a temporal Galerkin method is applied to both lines of (6.55):

$$\int_{\mathbb{R}} \left(\frac{1}{\Delta t} p(t-j\Delta t)\mathbf{P}^{\Lambda H} + \delta(t-j\Delta t)\mathbf{P}^{\Sigma} \right) (\text{equation (6.55)})\, dt \tag{6.59}$$

leading to

$$\begin{pmatrix} \mathsf{y}''^{j} \\ \mathsf{x}''^{j} \end{pmatrix} = \sum_{i=0}^{j} \begin{pmatrix} \mathbf{R}'^{i}_{11} & \mathbf{R}'^{i}_{12} \\ \mathbf{R}'^{i}_{21} & \mathbf{R}'^{i}_{22} \end{pmatrix} \begin{pmatrix} \mathsf{x}'^{j-i} \\ \mathsf{y}'^{j-i} \end{pmatrix} \tag{6.60}$$

with

$$\begin{aligned} \left[\mathbf{R}'^{j}_{ab}\right]_{mn} &= \frac{1}{\Delta t} \int_{\mathbb{R}} p(t-j\Delta t)\mathbf{P}^{\Lambda H} \left[\mathcal{R}'_{ab} \left\{ \mathbb{P}^{\Sigma H} \mathbb{1}_n p(t) \right\}\right]_m (t) dt \\ &+ \frac{1}{\Delta t} \int_{\mathbb{R}} p(t-j\Delta t)\mathbf{P}^{\Lambda H} \left[\mathcal{R}'_{ab} \left\{ \mathbb{P}^{\Lambda} \mathbb{1}_n h(t) \right\}\right]_m (t) dt \\ &+ \int_{\mathbb{R}} \delta(t-j\Delta t)\mathbf{P}^{\Sigma} \left[\mathcal{R}'_{ab} \left\{ \mathbb{P}^{\Sigma H} \mathbb{1}_n p(t) \right\}\right]_m (t) dt \\ &+ \int_{\mathbb{R}} \delta(t-j\Delta t)\mathbf{P}^{\Sigma} \left[\mathcal{R}'_{ab} \left\{ \mathbb{P}^{\Lambda} \mathbb{1}_n h(t) \right\}\right]_m (t) dt \end{aligned} \tag{6.61}$$

or, analogously to (6.36),

$$\begin{aligned} \left[\mathbf{R}'^{j}_{ab}\right]_{mn} &= \mathbf{P}^{\Lambda H} \mathbf{G}^{-1}_{gf} \left[\mathcal{R}_{ab} \left\{ \mathbb{P}^{\Sigma H} \mathbb{1}_n h(t) \right\}\right]_m (j\Delta t) \\ &+ T_0 \mathbf{P}^{\Lambda H} \mathbf{G}^{-1}_{gf} \left[\partial_t \mathcal{R}_{ab} \left\{ \mathbb{P}^{\Lambda} \mathbb{1}_n q(t) \right\}\right]_m (j\Delta t) \\ &+ \frac{1}{T_0} \mathbf{P}^{\Sigma} \mathbf{G}^{-1}_{gf} \left[\partial_t^{-1} \mathcal{R}_{ab} \left\{ \mathbb{P}^{\Sigma H} \mathbb{1}_n p(t) \right\}\right]_m (j\Delta t) \\ &+ \mathbf{P}^{\Sigma} \mathbf{G}^{-1}_{gf} \left[\mathcal{R}_{ab} \left\{ \mathbb{P}^{\Lambda} \mathbb{1}_n h(t) \right\}\right]_m (j\Delta t). \end{aligned} \tag{6.62}$$

The right hand side of (6.43) is treated similarly, leading to

$$\sum_{i=0}^{j} \begin{pmatrix} \mathbf{R}'^{i}_{11} & \mathbf{R}'^{i}_{12} \\ \mathbf{R}'^{i}_{21} & \mathbf{R}'^{i}_{22} \end{pmatrix} \sum_{k=0}^{j-i} \begin{pmatrix} \mathbf{Q}'^{k}_{11} & \mathbf{Q}'^{k}_{12} \\ \mathbf{Q}'^{k}_{21} & \mathbf{Q}'^{k}_{22} \end{pmatrix} \begin{pmatrix} \mathsf{x}^{j-i-k} \\ \mathsf{y}^{j-i-k} \end{pmatrix} = -\sum_{i=0}^{j} \begin{pmatrix} \mathbf{R}'^{i}_{11} & \mathbf{R}'^{i}_{12} \\ \mathbf{R}'^{i}_{21} & \mathbf{R}'^{i}_{22} \end{pmatrix} \begin{pmatrix} \mathsf{h}'^{j-i}_{\text{inc}} \\ \mathsf{e}'^{j-i}_{\text{inc}} \end{pmatrix}. \tag{6.63}$$

This equation can be regarded as the Calderón preconditioned version of (6.38). It can again be solved using the marching-on-in-time algorithm, where the

matrix to be inverted at each time step is

$$\begin{pmatrix} \mathsf{R}'^0_{11} & \mathsf{R}'^0_{12} \\ \mathsf{R}'^0_{21} & \mathsf{R}'^0_{22} \end{pmatrix} \begin{pmatrix} \mathsf{Q}'^0_{11} & \mathsf{Q}'^0_{12} \\ \mathsf{Q}'^0_{21} & \mathsf{Q}'^0_{22} \end{pmatrix}. \tag{6.64}$$

As will be shown in section 6.8, this matrix remains well-conditioned for both dense discretizations and large time steps. This motivates the use of the matrix

$$\begin{pmatrix} \mathsf{R}'^0_{11} & \mathsf{R}'^0_{12} \\ \mathsf{R}'^0_{21} & \mathsf{R}'^0_{22} \end{pmatrix} \tag{6.65}$$

as a multiplicative preconditioner for the qHP-PMCHWT MOT equation (6.41):

$$\begin{aligned} &-\begin{pmatrix} \mathsf{R}'^0_{11} & \mathsf{R}'^0_{12} \\ \mathsf{R}'^0_{21} & \mathsf{R}'^0_{22} \end{pmatrix} \begin{pmatrix} \mathsf{Q}'^0_{11} & \mathsf{Q}'^0_{12} \\ \mathsf{Q}'^0_{21} & \mathsf{Q}'^0_{22} \end{pmatrix} \begin{pmatrix} \mathsf{x}^j \\ \mathsf{y}^j \end{pmatrix} \\ = \;& \begin{pmatrix} \mathsf{R}'^0_{11} & \mathsf{R}'^0_{12} \\ \mathsf{R}'^0_{21} & \mathsf{R}'^0_{22} \end{pmatrix} \sum_{i=1}^{j} \begin{pmatrix} \mathsf{Q}'^i_{11} & \mathsf{Q}'^i_{12} \\ \mathsf{Q}'^i_{21} & \mathsf{Q}'^i_{22} \end{pmatrix} \begin{pmatrix} \mathsf{x}^{j-i} \\ \mathsf{y}^{j-i} \end{pmatrix} + \begin{pmatrix} \mathsf{R}'^0_{11} & \mathsf{R}'^0_{12} \\ \mathsf{R}'^0_{21} & \mathsf{R}'^0_{22} \end{pmatrix} \begin{pmatrix} \mathsf{h}^j \\ \mathsf{e}^j \end{pmatrix}. \end{aligned} \tag{6.66}$$

Equation (6.66) is the Calderón preconditioned qHP-PMCHWT (CP qHP-PMCHWT) equation. As will be shown in section 6.8, it is immune to DC instability, low frequency breakdown, and dense discretization breakdown.

6.7 Computation of the Matrix Elements

Implementing the qHP-PMCHWT equation requires the computation of interaction elements such as (6.17). Although these elements look more complex than those encountered in standard PMCHWT computations, they contain a fundamental structure.

By switching to the subspaces (Λ, H, Σ), as in section 6.4, the terms of (6.17) can be interpreted as

$$\begin{aligned} \mathsf{x}^T \mathbb{P}^{\Lambda} \mathsf{G}_{fg}^{-1} \mathcal{Q}_{ij} \mathsf{P}^{\Lambda H} y &= \tilde{\mathsf{x}}^T \mathcal{Q}_{ij} \tilde{\mathsf{y}}, \quad \tilde{\mathsf{x}} \in \Lambda, \quad \tilde{\mathsf{y}} \in \Lambda \times H \\ \mathsf{x}^T \mathbb{P}^{\Lambda} \mathsf{G}_{fg}^{-1} \mathcal{Q}_{ij} \mathsf{P}^{\Sigma} y &= \tilde{\mathsf{x}}^T \mathcal{Q}_{ij} \tilde{\mathsf{y}}, \quad \tilde{\mathsf{x}} \in \Lambda, \quad \tilde{\mathsf{y}} \in \Sigma \end{aligned}$$

and similar for the terms of (6.56). In other words, the basis and testing spaces are restricted to specific subspaces for each term. This restriction does not have to be enforced explicitly, but it can be used to simplify the implementation of the qHP-PMCHWT equation.

6.7.1 Diagonal Blocks

The operators $\mathcal{Q}'_{11}$ and $\mathcal{Q}'_{22}$ are linear combinations of the $\mathcal{T}$ operators. For example, consider

$$\begin{aligned} \mathcal{Q}'_{11} = \;& \frac{1}{T_0} \mathbb{P}^{\Lambda} \mathsf{G}_{fg}^{-1} \left(\partial_t^{-1} \mathcal{Q}_{11} \right) \mathsf{P}^{\Lambda H} + \mathbb{P}^{\Sigma H} \mathsf{G}_{fg}^{-1} \mathcal{Q}_{11} \mathsf{P}^{\Lambda H} \\ & + \mathbb{P}^{\Lambda} \mathsf{G}_{fg}^{-1} \mathcal{Q}_{11} \mathsf{P}^{\Sigma} + T_0 \mathbb{P}^{\Sigma H} \mathsf{G}_{fg}^{-1} \left(\partial_t \mathcal{Q}_{11} \right) \mathsf{P}^{\Sigma}. \end{aligned} \tag{6.67}$$

The hypersingular operator $\mathcal{T}_h$ vanishes when it is applied to, or tested with, solenoidal currents (i.e., RWG currents which reside in $\Lambda \times H$ or BC currents which reside in $\Sigma \times H$). The first term therefore contains only the operators $\partial_t^{-1}\mathcal{T}_s$ and $\partial_t^{-1}\mathcal{T}'_s$, but not $\partial_t^{-1}\mathcal{T}_h$ and $\partial_t^{-1}\mathcal{T}'_h$. For the same reason, the second and the third term contain only the operators $\mathcal{T}_s$ and $\mathcal{T}'_s$, but not $\mathcal{T}_h$ and $\mathcal{T}'_h$.

In the first term, the temporal integral ∂_t^{-1} is canceled by the temporal derivative in $\mathcal{T}_s$. In the last term, the temporal derivative ∂_t cancels the temporal integral in $\mathcal{T}_h$. Therefore, $\mathcal{Q}'_{11}$ and $\mathcal{Q}'_{22}$ do not contain any temporal integrals. After temporal discretization, this results in a finite number of nonzero matrices $\mathbf{Q}'^{j}_{11}$ and $\mathbf{Q}'^{j}_{22}$ (6.35).

With these considerations in mind, the numerical evaluation of $\mathbf{Q}'^{j}_{11}$ and $\mathbf{Q}'^{j}_{22}$ can be done using the same methods as for standard TD-PMCHWT (and TD-EFIE) computations. The same conclusion holds for the BC discretized operators $\mathcal{R}'_{11}$ and $\mathcal{R}'_{22}$ and the matrices $\mathbf{R}'^{j}_{11}$ and $\mathbf{R}'^{j}_{22}$.

6.7.2 Off-Diagonal Blocks

The operators $\mathcal{Q}'_{12}$ and $\mathcal{Q}'_{21}$ are linear combinations of the $\mathcal{K}$ operators, but can also be considered as combinations of the inner and outer MFIE operators (see section 1.2.9):

$$\mathcal{K} + \mathcal{K}' = \left(\frac{1}{2} + \mathcal{K}\right) + \left(-\frac{1}{2} + \mathcal{K}'\right) = \left(-\frac{1}{2} + \mathcal{K}\right) + \left(\frac{1}{2} + \mathcal{K}'\right). \tag{6.68}$$

For example, consider

$$\begin{aligned} \mathcal{Q}'_{12} \quad = \quad & \frac{1}{T_0}\mathbb{P}^{\Lambda}\mathbf{G}_{fg}^{-1}\left(\partial_t^{-1}\mathcal{Q}_{12}\right)\mathbf{P}^{\Lambda H} + \mathbb{P}^{\Sigma H}\mathbf{G}_{fg}^{-1}\mathcal{Q}_{12}\mathbf{P}^{\Lambda H} \\ & + \mathbb{P}^{\Lambda}\mathbf{G}_{fg}^{-1}\mathcal{Q}_{12}\mathbf{P}^{\Sigma} + T_0\mathbb{P}^{\Sigma H}\mathbf{G}_{fg}^{-1}\left(\partial_t\mathcal{Q}_{12}\right)\mathbf{P}^{\Sigma}. \end{aligned} \tag{6.69}$$

The second, third and fourth term involve the computation of the $\mathcal{K}$ (or MFIE) operators and their temporal derivatives. After temporal discretization, this corresponds to standard time domain PMCHWT operator evaluations, see (6.36).

The first term requires some additional manipulations. After discretization (see

(6.36)), the following term is obtained:

$$\begin{aligned}
\tilde{\mathbf{M}}^j_{mn} &= \frac{1}{T_0}\mathbb{P}^{\Lambda}\mathbf{G}^{-1}_{fg}\left[\partial_t^{-1}\mathcal{Q}_{12}\left\{\mathbf{P}^{\Lambda H}\mathbb{1}_n p(t)\right\}\right]_m(j\Delta t) \\
&= \frac{1}{T_0}\int_{-\Delta t}^{j\Delta t}\mathbb{P}^{\Lambda}\mathbf{G}^{-1}_{fg}\left[\mathcal{Q}_{12}\left\{\mathbf{P}^{\Lambda H}\mathbb{1}_n p(t)\right\}\right]_m(t)dt \qquad (6.70)\\
&= \frac{1}{T_0}\sum_{i=0}^{j}\int_{\mathbb{R}} p(t-i\Delta t)\mathbb{P}^{\Lambda}\mathbf{G}^{-1}_{fg}\left[\mathcal{Q}_{12}\left\{\mathbf{P}^{\Lambda H}\mathbb{1}_n p(t)\right\}\right]_m(t)dt \qquad (6.71)\\
&= \frac{\Delta t}{T_0}\sum_{i=0}^{j}\mathbb{P}^{\Lambda}\mathbf{G}^{-1}_{fg}\left[\mathcal{Q}_{12}\left\{\mathbf{P}^{\Lambda H}\mathbb{1}_n h(t)\right\}\right]_m(i\Delta t) \qquad (6.72)\\
&= \frac{\Delta t}{T_0}\sum_{i=0}^{j}\mathbf{M}^i_{mn}. \qquad (6.73)
\end{aligned}$$

The term $\mathbf{M}^i_{mn}$ represents a field generated by a solenoidal RWG current, with time dependency $h(t)$, tested at $t = i\Delta t$ with a local RWG loop. In the frequency domain, the MFIE operator applied to a solenoidal current and tested with a local loop scales as $\mathcal{O}(\omega^2)$. In the time domain, this corresponds to a double temporal differentiation. As a result, the operator has a finite range, determined by the diameter D of the scatterer:

$$\mathbf{M}^i_{mn} = 0 \qquad \forall i > i_{max} = \left\lfloor \frac{D}{c_{\min}\Delta t} \right\rfloor \qquad (6.74)$$

with $c_{\min} = \min(c, c')$. Therefore, the summation in (6.73) can be truncated.

The term $\tilde{\mathbf{M}}^j_{mn}$ represents the temporal integral of a field generated by a solenoidal RWG current, with time dependency $p(t)$, tested at $t = j\Delta t$ with a local RWG loop. In the frequency domain, this term scales as $\mathcal{O}(\omega)$. In the time domain, this corresponds to a single temporal differentiation. As a result, this operator also has a finite range:

$$\tilde{\mathbf{M}}^j_{mn} = 0 \qquad \forall j \geq i_{max} \qquad (6.75)$$

Although the sum in (6.73) might not converge to zero due to numerical errors in the computation of $\mathbf{M}^i_{mn}$, it is permitted to explicitly enforce (6.75). One can even argue that this is necessary since the contributions that are left out are guaranteed to be the result of quadrature error.

If the time step is sufficiently large, i.e., $c_{\min}\Delta t > D$, $i_{max} = 0$. As a result, $\tilde{\mathbf{M}}^0_{mn} = 0$. Equation (6.73) then implies that also $\mathbf{M}^0_{mn} = 0$.

In this reasoning, it is essential to note that $\mathbb{P}^{\Lambda}\mathbf{G}^{-1}_{fg}$ limits the testing space to the local RWG loops. The MFIE operator applied to a global loop and tested

with a global loop is $\mathcal{O}(1)$ rather than $\mathcal{O}(\omega^2)$. Therefore, the truncation of the matrices could not be done if global loops were present in the testing space.

Again, similar conclusions hold for the BC discretized operators $\mathcal{R}'_{12}$ and $\mathcal{R}'_{21}$ and the matrices $\mathbf{R}'^{ij}_{12}$ and $\mathbf{R}'^{ij}_{21}$.

6.8 Numerical Results

6.8.1 Scattering by a Sphere

Consider the spherical triangle mesh in figure 6.1. The medium inside the sphere is characterized by $\epsilon' = 2\epsilon_0$ and $\mu' = \mu_0$. The surrounding medium has material parameters $\epsilon = \epsilon_0$ and $\mu = \mu_0$. This structure is illuminated by a Gaussian wave. This scattering problem is simulated using the MOT algorithm applied to both the standard TD-PMCHWT equation and the qHP-PMCHWT equation, with $c\Delta t = 2\ m$.

The current expansion coefficient $\mathrm{j}_1(t)$ obtained with both methods is shown in figure 6.2. The two solutions match up to $ct \approx 110$ m. After that, the qHP-PMCHWT solution continues to decay, while the standard PMCHWT solution remains approximately constant up to at least $ct = 250$ m. This is DC instability.

However, upon closer inspection, this residual current is not constant-in-time, but grows exponentially. The rate at which the current grows depends on the accuracy of the numerical computation of the interaction integrals. In our implementation, this is mainly determined by the number of quadrature points per triangle (denoted G) used to evaluate the outer spatial integrals in (6.8). In figure 6.3, the currents resulting from simulations with $G = 13$, $G = 36$ (as in figure 6.2), $G = 78$ and $G = 400$ are compared. While late-time instability can be delayed by more accurate quadrature methods, it can not be avoided.

Next, a stability analysis is performed as in section 2.3.3: the stability of the MOT algorithm is defined by the eigenvalues of the so-called companion matrix. Eigenvalues located outside the unit circle indicate instability, whereas eigenvalues equal to one correspond to static regime solutions. In figure 6.4, these eigenvalues are plotted for the standard TD-PMCHWT method with $G = 13$ (left), the standard TD-PMCHWT method with $G = 400$ (middle) and the qHP-PMCHWT method with $G = 36$ (right). The standard TD-PMCHWT equation exhibits eigenvalues that are clustered around 1. By employing more accurate quadrature methods, these eigenvalues can be brought closer to 1. However, even with $G = 400$, a number of eigenvalues are located outside of the unit circle, leading to instability. The qHP-PMCHWT equation on the other hand does not exhibit eigenvalues clustered around 1. All eigenvalues are located inside the unit circle, indicating that the scheme is stable.

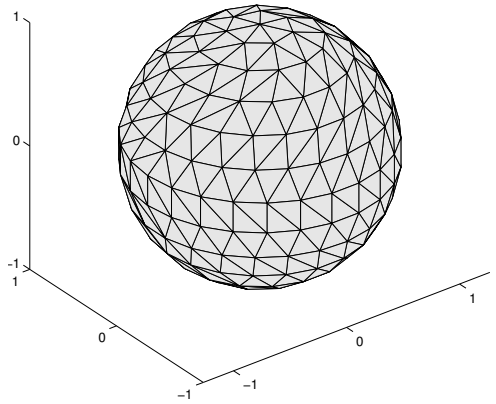

Figure 6.1: A sphere with radius $r = 1$ m, $\epsilon' = 2\epsilon_0$, $\mu' = \mu_0$ is discretized using 444 triangles.

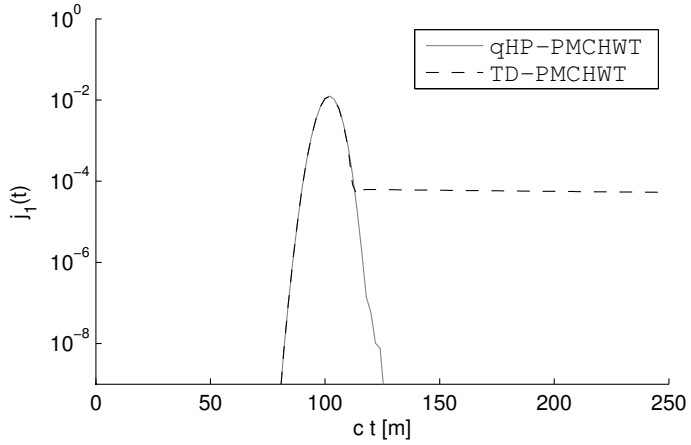

Figure 6.2: The current expansion coefficient $j_1(t)$ on the sphere in figure 6.1, obtained with the standard TD-PMCHWT method and with the qHP-PMCHWT method.

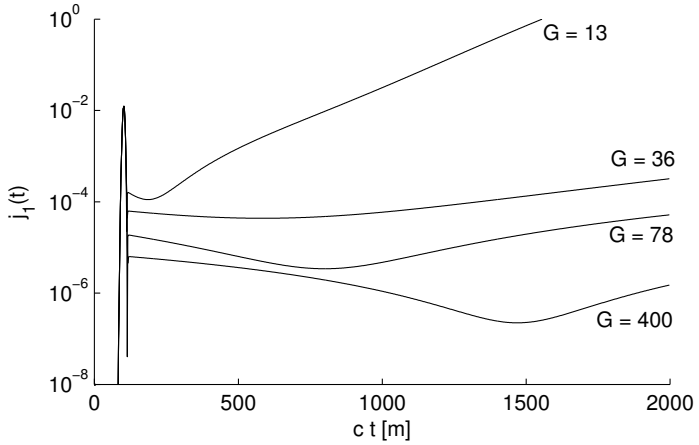

Figure 6.3: The current expansion coefficient $\mathrm{j}_1(t)$ on the sphere in figure 6.1, obtained with the standard TD-PMCHWT method, with different numerical quadrature methods.

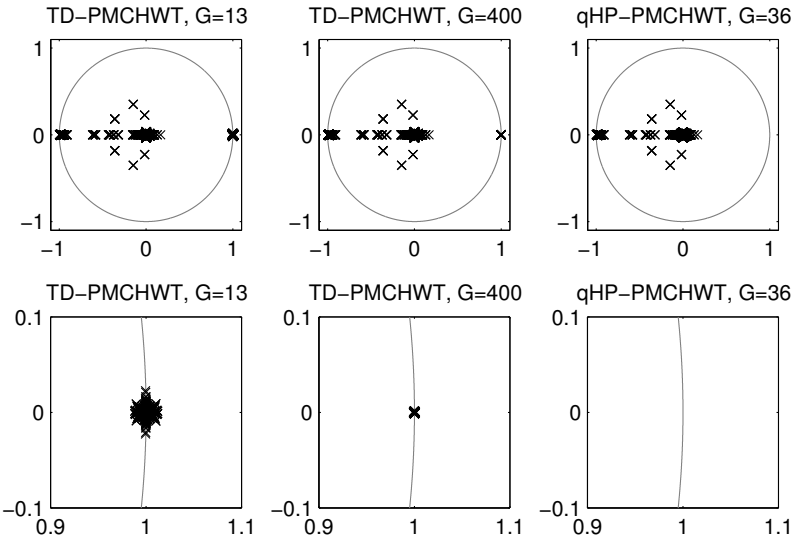

Figure 6.4: The eigenvalues of the companion matrix (see section 2.3.3) for the standard PMCHWT equation with $G = 13$ (left), the standard PMCHWT equation with $G = 400$ (middle), and the qHP-PMCHWT equation with $G = 36$ (right). The top rows show all eigenvalues, whereas the bottom rows zoom in on the eigenvalues clustered around 1 (if any).

6.8.2 Scattering by a Square Torus

The experiment in the previous section is now repeated with the same parameters for the triangle mesh of a square torus in figure 6.5. The current expansion coefficient $\mathsf{j}_1(t)$ is shown in figure 6.6. The standard PMCHWT and the qHP-PMCHWT results match for $ct < 100\ m$, but after that, the current obtained from the standard TD-PMCHWT equation grows exponentially: the simulation method is unstable. The qHP-PMCHWT equation, on the other hand, remains stable.

Next, a stability analysis is performed as in section 2.3.3. The eigenvalues of the companion matrix for the standard TD-PMCHWT equation are shown in figure 6.7, left. Part of the eigenvalues are scattered around 1, both inside and outside the unit circle. This indicates instability. The eigenvalues for the qHP-PMCHWT equation are shown in figure 6.7, right. Here, all eigenvalues are located inside the unit circle. The qHP-PMCHWT simulation is therefore stable. This shows that the conclusions of the previous section also apply to multiply connected geometries, as well as geometries with sharp corners.

Finally, the condition number of the MOT system matrix is computed for time steps ranging from $c\Delta t = 1\ m$ up to $c\Delta t = 1024\ m$ (figure 6.8). The condition number of the standard TD-PMCHWT equation grows proportionally to Δt^2. This is low frequency breakdown. The condition number of the qHP-PMCHWT equation, on the other hand, remains constant. This shows that the qHP-PMCHWT equation does not suffer from low frequency breakdown.

6.8.3 Scattering by a Torus

Consider the toroidal mesh in figure 6.9, middle. Its mesh parameter is $h = 0.15$ m and it contains $N_S = 828$ edges. First, the standard TD-PMCHWT equation, the qHP-PMCHWT equation and the Calderón preconditioned qHP-PMCHWT equation are applied to this mesh, with time step sizes varying from $c\Delta t = 0.125$ m to $c\Delta t = 1024$ m. The condition number of the MOT system matrix as a function of the time step is shown in figure 6.10. The condition number of the standard TD-PMCHWT equation scales proportionally to Δt^2. The condition of the qHP-PMCHWT equation, with or without preconditioner, remains constant.

Next, the time step is fixed at $c\Delta t = 1$ m, and the mesh parameter is varied from $h = 0.08$ m ($N_S = 3105$, figure 6.9, left) to $h = 0.22$ m ($N_S = 384$, figure 6.9, right). The condition number of the system matrices obtained with each of the three simulation techniques is plotted in figure 6.11. The standard TD-PMCHWT and the qHP-PMCHWT formulations suffer from dense discretization breakdown: the condition number of the MOT system matrices grow proportionally to h^{-2}. The Calderón preconditioner solves this problem: the condition number of the preconditioned system matrices remains constant as the mesh density is increased.

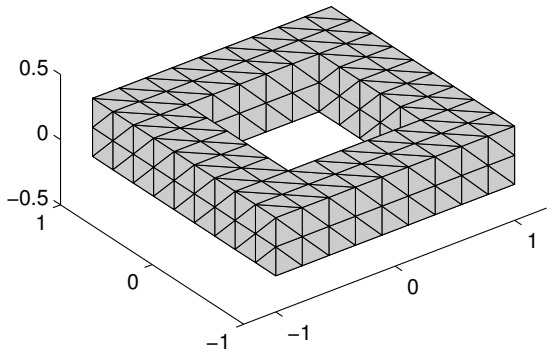

Figure 6.5: A square torus with $\epsilon' = 2\epsilon_0$, $\mu' = \mu_0$ is discretized using 448 triangles.

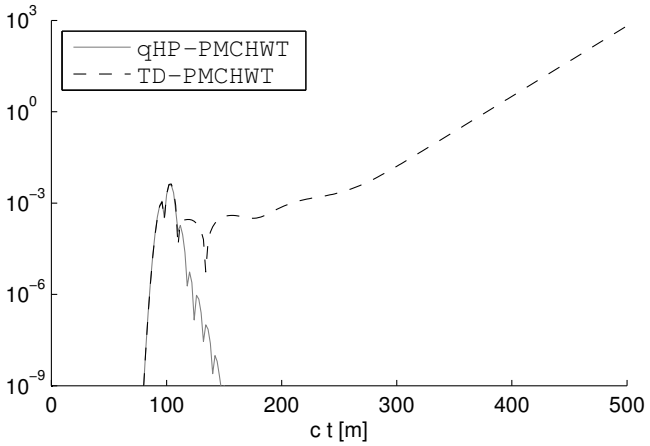

Figure 6.6: The current obtained from a standard TD-PMCHWT simulation (dashed line), and from a qHP-PMCHWT simulation (solid line), for the square torus in figure 6.5.

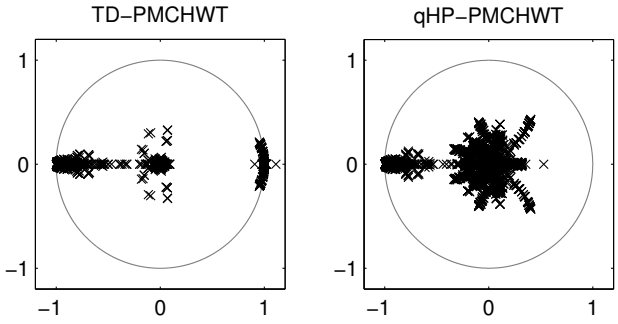

Figure 6.7: The eigenvalues of the companion matrix (see section 2.3.3) for the TD-PMCHWT equation (left) and for the qHP-PMCHWT equation (right), applied to the square torus in figure 6.5.

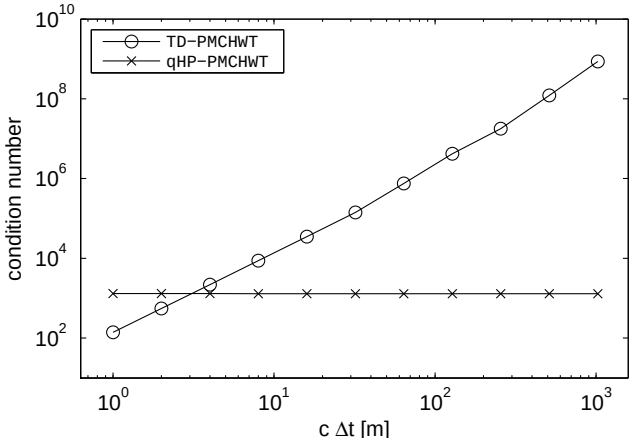

Figure 6.8: Condition number of the MOT system matrix for the square torus in figure 6.5 as a function of the time step size Δt.

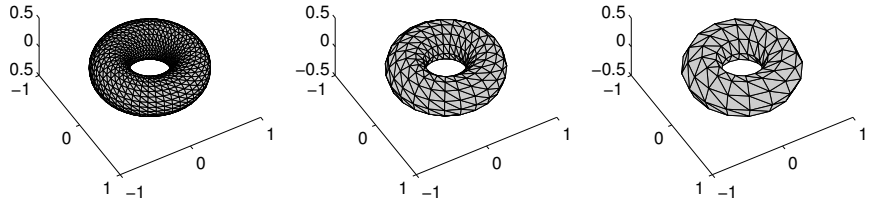

Figure 6.9: Meshes of a torus with large radius 1 m and small radius 0.25 m. Left: $h = 0.08$ m, $N_S = 3105$. Middle: $h = 0.15$ m, $N_S = 828$. Right: $h = 0.22$ m, $N_S = 384$.

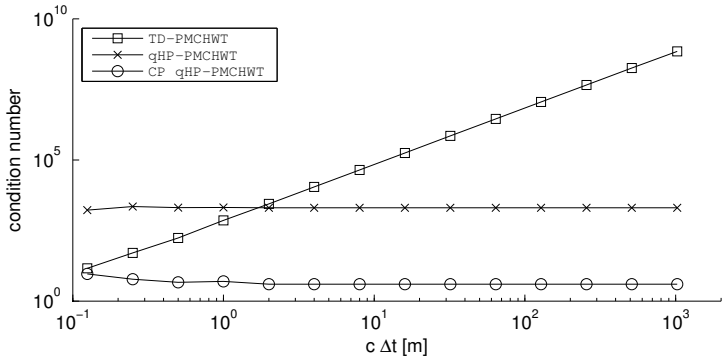

Figure 6.10: Condition number of the MOT system matrix obtained from the standard TD-PMCHWT equation, the qHP-PMCHWT equation and the Calderón preconditioned qHP-PMCHWT equation, as a function of the time step size, for the torus in figure 6.9.

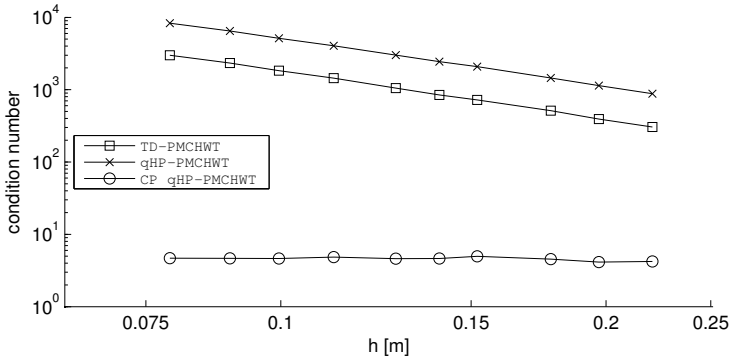

Figure 6.11: Condition number of the MOT system matrix obtained from the standard TD-PMCHWT equation, the qHP-PMCHWT equation and the Calderón preconditioned qHP-PMCHWT equation, as a function of the mesh parameter h, for the torus in figure 6.9.

6.9 Conclusions

The TD-PMCHWT equation suffers from DC instability. Furthermore, it is not robust, in the sense that in the presence of small numerical errors, the spurious static currents become exponentially increasing, rendering the MOT scheme unstable. In this chapter, the qHP-PMCHWT equation was developed. This TD-PMCHWT formulation is immune to DC instability, and as a result, it can be solved using a stable MOT scheme. Additionally, the qHP-PMCHWT equation is immune to low frequency breakdown, and can be Calderón preconditioned in order to solve dense discretization breakdown. This formulation can thus efficiently solve scattering problems involving homogeneous penetrable media, regardless of the chosen time step and mesh parameter. It can be applied directly to multiply connected geometries, without requiring the detection of global loops.

References

[1] Y. Beghein, K. Cools, and F. P. Andriulli, "A robust and low frequency stable time domain PMCHWT equation", in *International Conference on Electromagnetics in Advanced Applications (ICEAA)*, Sep. 2015, pp. 954–957.

[2] B. Shanker, M. Lu, J. Yuan, and E. Michielssen, "Time domain integral equation analysis of scattering from composite bodies via exact evaluation of radiation fields", *IEEE Transactions on Antennas and Propagation*, vol. 57, no. 5, pp. 1506–1520, May 2009.

[3] F. P. Andriulli, K. Cools, I. Bogaert, and E. Michielssen, "On a well-conditioned electric field integral operator for multiply connected geometries", *IEEE Transactions on Antennas and Propagation*, vol. 61, no. 4, pp. 2077–2087, Apr. 2013.

[4] S. Chen, W. C. Chew, J. Song, and J.-S. Zhao, "Analysis of low frequency scattering from penetrable scatterers", *IEEE Transactions on Geoscience and Remote Sensing*, vol. 39, no. 4, pp. 726–735, Apr. 2001.

[5] I. Bogaert, K. Cools, F. Andriulli, and D. De Zutter, "Low frequency scaling of the mixed MFIE for scatterers with a non-simply connected surface", in *International Conference on Electromagnetics in Advanced Applications (ICEAA)*, IEEE, Sep. 2011, pp. 951–954.

[6] K. Cools, F. Andriulli, and E. Michielssen, "A Calderón multiplicative preconditioner for the PMCHWT integral equation", *IEEE Transactions on Antennas and Propagation*, vol. 59, no. 12, pp. 4579–4587, Dec. 2011.

7

A Calderón Multiplicative Preconditioner for the Chiral PMCHWT Equation

Y. Beghein, K. Cools, F.P. Andriulli, D. De Zutter and E. Michielssen

This chapter is based on an article published in
IEEE Transactions on Antennas and Propagation [1].

★ ★ ★

Scattering of time-harmonic electromagnetic waves by chiral structures can be modeled via an extension of the PMCHWT boundary integral equation for analyzing scattering by dielectric objects. The classical PMCHWT equation however suffers from dense discretization breakdown: the matrices resulting from its discretization become increasingly ill-conditioned when the mesh density increases. This contribution revisits the PMCHWT equation for chiral media. It is demonstrated that it also suffers from dense discretization breakdown. This dense discretization breakdown is mitigated by the construction of a Calderón multiplicative preconditioner. A stable discretization scheme is introduced, and the resulting algorithm's accuracy and efficiency are corroborated by numerical examples.

7.1 Introduction

Scattering of time-harmonic electromagnetic fields by homogeneous objects often is modeled using boundary integral equations (BIEs). The best-known BIEs that apply to scattering by perfect electric conductors are the electric and magnetic field integral equations (EFIE and MFIE). Prototypical BIEs that apply to penetrable objects are the Poggio-Miller-Chan-Harrington-Wu-Tsai (PMCHWT) [2] and Müller equations [3]. These equations can be regarded as analogues of the EFIE and MFIE, respectively, in that they exhibit similar spectral properties. More precisely, the spectra of the EFIE's and the PMCHWT equation's operators comprise two branches, one accumulating at zero, and the other at infinity. The spectra of the MFIE's and the Müller equation's operators, on the other hand, accumulate at a finite non-zero value.

All of the above BIEs can be solved numerically using the boundary element method: the surface of the scatterer is approximated by a mesh, and the unknown field quantities are expanded in a finite number of basis functions defined on this mesh. This approach reduces the BIE to a finite set of linear equations in the field expansion coefficients, which often is solved using iterative methods. Because the EFIE's and PMCHWT equation's operators have unbounded spectra, the corresponding system matrices have very large condition numbers when the mesh parameter (i.e. the length of the shortest edge) decreases. This phenomenon is called dense discretization breakdown and can be resolved by applying Calderón multiplicative preconditioners (CMPs) [4]–[6].

In [7], the authors have presented the successful application of the CMP to the chiral extension of the PMCHWT equation. It is the aim of this chapter to elaborate on the theoretical fundamentals of the chiral CMP, and to present further numerical experiments corroborating the accuracy and the efficiency of the technique.

Section 7.2 offers a quick overview of electromagnetic fields in chiral media. Following this, the PMCHWT equation for chiral media is presented in section 7.3. While this is not new material, it is included for self-containedness and to introduce the notations used throughout the following sections.

In section 7.4, the self-regularizing property of the chiral PMCHWT operator is studied. While this is analogous to the nonchiral case, two difficulties arise: the spectral properties of a composite operator involving three different wavenumbers must be studied, and the chiral PMCHWT operator requires a diagonalization. Once it is established that the operator is indeed self-regularizing, the CMP is formed by applying a suitable discretization scheme.

In the last section, numerical experiments testify to the success of the CMP. The accuracy is tested by comparing the results to the Mie series and to ab initio simulations of chiral metamaterials. The efficiency is shown by comparing the condition number of the system matrix with and without CMP, and the required number of iterations.

7.2 Electromagnetic Fields in Chiral Media

For time-harmonic electromagnetic fields, the electric and magnetic field (resp. $\boldsymbol{E}$ and $\boldsymbol{H}$) are linked to the electric and magnetic displacement field (resp. $\boldsymbol{D}$ and $\boldsymbol{B}$) by the Maxwell equations (1.59a)–(1.59b)

$$\nabla \times \boldsymbol{E} = -j\omega \boldsymbol{B} - \boldsymbol{M} \tag{7.1}$$
$$\nabla \times \boldsymbol{H} = j\omega \boldsymbol{D} + \boldsymbol{J} \tag{7.2}$$

where $\omega = 2\pi f$ is the angular frequency, $\boldsymbol{J}$ is the electric current density, and $\boldsymbol{M}$ is the magnetic current density.

The interaction of the electromagnetic fields with the medium in which they propagate is modeled by constitutive equations, as discussed in section 1.4.1. The lack of reflection symmetry, which is the defining characteristic for chiral media, must therefore be incorporated into the constitutive equations. This can be done using the Drude-Born-Fedorov (DBF) model [8]. However, for notational simplicity, the following equivalent constitutive equations are assumed [9]:

$$\begin{pmatrix} \boldsymbol{D} \\ \boldsymbol{B} \end{pmatrix} = \begin{pmatrix} \epsilon & -j\kappa\sqrt{\epsilon\mu} \\ j\kappa\sqrt{\epsilon\mu} & \mu \end{pmatrix} \begin{pmatrix} \boldsymbol{E} \\ \boldsymbol{H} \end{pmatrix} \tag{7.3}$$

where ϵ is the permittivity, μ is the permeability and κ is the dimensionless chirality parameter. The constitutive equations (7.3) introduce extra coupling between electric and magnetic field quantities. This coupling can be removed, however, by application of the so-called Bohren transform (see section 1.4.2):

$$\begin{pmatrix} \mathcal{E}_\pm \\ \mathcal{H}_\pm \end{pmatrix} = P^\pm \begin{pmatrix} \boldsymbol{E} \\ \boldsymbol{H} \end{pmatrix} \quad , \quad P^\pm = \frac{1}{2} \begin{pmatrix} 1 & \mp j\eta \\ \pm \frac{j}{\eta} & 1 \end{pmatrix}. \tag{7.4}$$

Here $\eta = \sqrt{\mu/\epsilon}$ is the characteristic impedance of the medium. The matrices $P^\pm$ are projection matrices, satisfying $P^+ + P^- = 1$. The inverse Bohren transform is

$$\boldsymbol{E} = \mathcal{E}_+ + \mathcal{E}_- \qquad \boldsymbol{H} = \mathcal{H}_+ + \mathcal{H}_-. \tag{7.5}$$

A similar transformation applies to the electric and magnetic sources:

$$\begin{pmatrix} \mathcal{J}_\pm \\ \mathcal{M}_\pm \end{pmatrix} = \frac{1}{2} \begin{pmatrix} 1 & \mp \frac{j}{\eta} \\ \pm j\eta & 1 \end{pmatrix} \begin{pmatrix} \boldsymbol{J} \\ \boldsymbol{M} \end{pmatrix}. \tag{7.6}$$

The fields resulting from the Bohren transforms (7.4) and (7.6) are governed by equations formally identical to Maxwell equations in the absence of chirality:

$$\nabla \times \mathcal{E}_\pm = -j\omega\mu(1 \pm \kappa)\mathcal{H}_\pm - \mathcal{M}_\pm \tag{7.7}$$
$$\nabla \times \mathcal{H}_\pm = j\omega\epsilon(1 \pm \kappa)\mathcal{E}_\pm + \mathcal{J}_\pm. \tag{7.8}$$

Equation (7.4) decomposes the electromagnetic fields $(\boldsymbol{E}, \boldsymbol{H})$ into two contributions: $(\mathcal{E}_+, \mathcal{H}_+)$ and $(\mathcal{E}_-, \mathcal{H}_-)$. In the absence of external sources,

$$\nabla \times \mathcal{E}_\pm = \pm\gamma_\pm \mathcal{E}_\pm \tag{7.9}$$

$$\gamma_\pm = \omega\sqrt{\epsilon\mu}(1 \pm \kappa). \tag{7.10}$$

Therefore, $\mathcal{E}_+$ and $\mathcal{E}_-$ are Beltrami fields. For $-1 < \kappa < 1$ (which is the case for realistic materials), the two "modes" $\mathcal{E}_+$ and $\mathcal{E}_-$ have opposite helicity, and the operators P^+ and P^- project the electromagnetic fields upon their components with positive and negative helicity, respectively. When applied to plane wave solutions, the component with positive helicity $(\mathcal{E}_+, \mathcal{H}_+)$ is right-handed circularly polarized, while the component with negative helicity $(\mathcal{E}_-, \mathcal{H}_-)$ is left-handed circularly polarized. If the chirality parameter κ is nonzero, these components propagate with different wavenumbers $\gamma_\pm$. This is the cause of the well-known phenomenon of optical activity.

7.3 The Chiral PMCHWT Equation

The Bohren transform allows for the expansion of the electromagnetic field in a chiral medium into two components, each fulfilling the Maxwell equations in a nonchiral medium. These components thus obey all the usual equations and identities of electromagnetics. This property can be exploited to construct BIEs describing scattering by chiral objects – see section 1.4.3. In this section, the extension of the PMCHWT equation for the modeling of scattering by nonchiral objects to the chiral PMCHWT equation for the modeling of scattering by chiral structures is revisited.

7.3.1 The Stratton-Chu Representation Theorem

Consider a homogeneous, isotropic, penetrable object Ω characterized by permittivity ϵ, permeability μ, impedance $\eta = \sqrt{\mu/\epsilon}$ and wavenumber $k = \omega\sqrt{\mu\epsilon}$. It is embedded in a background medium with permittivity ϵ_0, permeability μ_0, impedance $\eta_0 = \sqrt{\mu_0/\epsilon_0}$ and wavenumber $k_0 = \omega\sqrt{\mu_0\epsilon_0}$. The boundary of Ω is denoted Γ, and its exterior normal vector is denoted $\hat{\boldsymbol{n}}$. An external electromagnetic field $(\boldsymbol{E}^i, \boldsymbol{H}^i)$ is applied. The tangential traces of the electromagnetic field just inside Ω, denoted $(\boldsymbol{E}^-, \boldsymbol{H}^-)$, satisfy the Stratton-Chu representation formula [10]:

$$\begin{pmatrix} -\hat{\boldsymbol{n}} \times \boldsymbol{E}^- \\ \hat{\boldsymbol{n}} \times \boldsymbol{H}^- \end{pmatrix} = \mathcal{S}^{\text{int}}(\eta, k) \begin{pmatrix} -\hat{\boldsymbol{n}} \times \boldsymbol{E}^- \\ \hat{\boldsymbol{n}} \times \boldsymbol{H}^- \end{pmatrix} \tag{7.11}$$

where

$$\mathcal{S}^{\text{int}}(\eta, k) = \begin{pmatrix} \frac{1}{2} + \mathcal{K}_k & \eta\mathcal{T}_k \\ -\mathcal{T}_k/\eta & \frac{1}{2} + \mathcal{K}_k \end{pmatrix} \tag{7.12}$$

is the internal Stratton-Chu operator. A similar result holds for the traces of the electromagnetic field just outside Ω, denoted $(\boldsymbol{E}^+, \boldsymbol{H}^+)$:

$$\begin{pmatrix} -\hat{\boldsymbol{n}} \times \boldsymbol{E}^+ \\ \hat{\boldsymbol{n}} \times \boldsymbol{H}^+ \end{pmatrix} = \mathcal{S}^{\text{ext}}(\eta_0, k_0) \begin{pmatrix} -\hat{\boldsymbol{n}} \times \boldsymbol{E}^+ \\ \hat{\boldsymbol{n}} \times \boldsymbol{H}^+ \end{pmatrix} + \begin{pmatrix} -\hat{\boldsymbol{n}} \times \boldsymbol{E}^i \\ \hat{\boldsymbol{n}} \times \boldsymbol{H}^i \end{pmatrix} \tag{7.13}$$

where

$$\mathcal{S}^{\text{ext}}(\eta_0, k_0) = \begin{pmatrix} \frac{1}{2} - \mathcal{K}_{k_0} & -\eta_0 \mathcal{T}_{k_0} \\ \mathcal{T}_{k_0}/\eta_0 & \frac{1}{2} - \mathcal{K}_{k_0} \end{pmatrix} \tag{7.14}$$

is the external Stratton-Chu operator. The EFIE operator $\mathcal{T}_k$ (which is the sum of a weakly singular part $\mathcal{T}_s$ and a hypersingular part $\mathcal{T}_h$) and the MFIE operator $\mathcal{K}_k$ are

$$\left(\mathcal{T}_k \boldsymbol{f}\right)(\boldsymbol{r}) = \left(\mathcal{T}_{S,k} \boldsymbol{f}\right)(\boldsymbol{r}) + \left(\mathcal{T}_{H,k} \boldsymbol{f}\right)(\boldsymbol{r}) \tag{7.15}$$

$$\left(\mathcal{T}_{S,k} \boldsymbol{f}\right)(\boldsymbol{r}) = -jk\hat{\boldsymbol{n}} \times \int_\Gamma \frac{e^{-jkR}}{4\pi R} \boldsymbol{f}(\boldsymbol{r'}) d\mathbf{s'} \tag{7.16}$$

$$\left(\mathcal{T}_{H,k} \boldsymbol{f}\right)(\boldsymbol{r}) = \frac{1}{jk}\hat{\boldsymbol{n}} \times p.v. \int_\Gamma \nabla \frac{e^{-jkR}}{4\pi R} \nabla' \cdot \boldsymbol{f}(\boldsymbol{r'}) d\mathbf{s'} \tag{7.17}$$

$$\left(\mathcal{K}_k \boldsymbol{f}\left(\boldsymbol{r}\right)\right) = -\hat{\boldsymbol{n}} \times p.v. \int_\Gamma \nabla \times \frac{e^{-jkR}}{4\pi R} \boldsymbol{f}(\boldsymbol{r}') d\mathbf{s}' \tag{7.18}$$

where $p.v.$ indicates that the integral should be interpreted as a Cauchy principal value, and $R = |\boldsymbol{r} - \boldsymbol{r}'|$.

By imposing continuity of the tangential traces of $(\boldsymbol{E}^-, \boldsymbol{H}^-)$ and $(\boldsymbol{E}^+, \boldsymbol{H}^+)$, and subtracting (7.11) from (7.13), the PMCHWT equation [2] is obtained:

$$\mathcal{Q}(\eta_0, k_0; \eta, k) \begin{pmatrix} -\hat{\boldsymbol{n}} \times \boldsymbol{E} \\ \hat{\boldsymbol{n}} \times \boldsymbol{H} \end{pmatrix} = \begin{pmatrix} -\hat{\boldsymbol{n}} \times \boldsymbol{E}^i \\ \hat{\boldsymbol{n}} \times \boldsymbol{H}^i \end{pmatrix} \tag{7.19}$$

where the PMCHWT operator is

$$\begin{aligned} \mathcal{Q}(\eta_0, k_0; \eta, k) &= \mathcal{S}^{\text{int}}(\eta, k) - \mathcal{S}^{\text{ext}}(\eta_0, k_0) \\ &= \begin{pmatrix} \mathcal{K}_{\text{k}_0} + \mathcal{K}_k & \eta_0 \mathcal{T}_{\text{k}_0} + \eta \mathcal{T}_k \\ -\mathcal{T}_{\text{k}_0}/\eta_0 - \mathcal{T}_k/\eta & \mathcal{K}_{\text{k}_0} + \mathcal{K}_k \end{pmatrix}. \end{aligned} \tag{7.20}$$

7.3.2 The PMCHWT Equation for Chiral Media

If the medium filling Ω is chiral, equation (7.11) does not hold. However, the Bohren transform has shown that in chiral media, the field comprises two components $(\mathcal{E}_\pm, \mathcal{H}_\pm)$ that do not couple (except at boundaries). They act as though they propagate through a nonchiral medium with characteristic

impedance η and wavenumbers $\gamma_\pm$. Therefore, they obey the Stratton-Chu representation formula (7.11):

$$\begin{pmatrix} -\hat{\boldsymbol{n}} \times \mathcal{E}_\pm \\ \hat{\boldsymbol{n}} \times \mathcal{H}_\pm \end{pmatrix} = \mathcal{S}^{\text{int}}(\eta, \gamma_\pm) \begin{pmatrix} -\hat{\boldsymbol{n}} \times \mathcal{E}_\pm \\ \hat{\boldsymbol{n}} \times \mathcal{H}_\pm \end{pmatrix}. \tag{7.21}$$

Transforming this back to $\boldsymbol{E}$ and $\boldsymbol{H}$ using (7.4) and (7.5) results in

$$\begin{aligned} \begin{pmatrix} -\hat{\boldsymbol{n}} \times \boldsymbol{E}^- \\ \hat{\boldsymbol{n}} \times \boldsymbol{H}^- \end{pmatrix} &= \mathcal{S}_c^{\text{int}}(\eta, \gamma_-, \gamma_+) \begin{pmatrix} -\hat{\boldsymbol{n}} \times \boldsymbol{E}^- \\ \hat{\boldsymbol{n}} \times \boldsymbol{H}^- \end{pmatrix} \qquad (7.22) \\ \mathcal{S}_c^{\text{int}}(\eta, \gamma_-, \gamma_+) &= \mathcal{S}^{\text{int}}(\eta, \gamma_+) P^- + \mathcal{S}^{\text{int}}(\eta, \gamma_-) P^+. \end{aligned}$$

The pairing of γ_+ with P^- and γ_- with P^+ stems from

$$\begin{pmatrix} \mathcal{E}^\pm \\ \mathcal{H}^\pm \end{pmatrix} = P^\pm \begin{pmatrix} \boldsymbol{E} \\ \boldsymbol{H} \end{pmatrix} \Rightarrow \begin{pmatrix} -\hat{\boldsymbol{n}} \times \mathcal{E}^\pm \\ \hat{\boldsymbol{n}} \times \mathcal{H}^\pm \end{pmatrix} = P^\mp \begin{pmatrix} -\hat{\boldsymbol{n}} \times \boldsymbol{E} \\ \hat{\boldsymbol{n}} \times \boldsymbol{H} \end{pmatrix}. \tag{7.23}$$

The chiral PMCHWT equation is obtained by again imposing continuity of the tangential traces of $(\boldsymbol{E}^-, \boldsymbol{H}^-)$ and $(\boldsymbol{E}^+, \boldsymbol{H}^+)$, and subtracting (7.13) from (7.22):

$$\mathcal{Q}_c(\eta_0, k_0; \eta, \gamma_-, \gamma_+) \begin{pmatrix} -\hat{\boldsymbol{n}} \times \boldsymbol{E} \\ \hat{\boldsymbol{n}} \times \boldsymbol{H} \end{pmatrix} = \begin{pmatrix} -\hat{\boldsymbol{n}} \times \boldsymbol{E}^i \\ \hat{\boldsymbol{n}} \times \boldsymbol{H}^i \end{pmatrix} \tag{7.24}$$

where the chiral PMCHWT operator is

$$\begin{aligned} & \mathcal{Q}_c(\eta_0, k_0; \eta, \gamma_-, \gamma_+) \\ = \; & \mathcal{S}^{\text{int}}(\eta, \gamma_+) P^- + \mathcal{S}^{\text{int}}(\eta, \gamma_-) P^+ - \mathcal{S}^{\text{ext}}(\eta_0, k_0) \\ = \; & \mathcal{Q}(\eta_0, k_0; \eta, \gamma_+) P^- + \mathcal{Q}(\eta_0, k_0; \eta, \gamma_-) P^+ \qquad (7.25) \\ = \; & \begin{pmatrix} \mathcal{Q}_{11} & \mathcal{Q}_{12} \\ \mathcal{Q}_{21} & \mathcal{Q}_{22} \end{pmatrix}. \qquad (7.26) \end{aligned}$$

Expressions for the operators $\mathcal{Q}_{11}$, $\mathcal{Q}_{12}$, $\mathcal{Q}_{21}$ and $\mathcal{Q}_{22}$ are obtained by combining (7.4), (7.12) and (7.14):

$$\begin{aligned} \mathcal{Q}_{11} = \mathcal{Q}_{22} &= \mathcal{K}_{\text{k}_0} + \mathcal{K}^+ - j\mathcal{T}^- \\ \mathcal{Q}_{12} &= \eta_0 \mathcal{T}_{\text{k}_0} + \eta \left(\mathcal{T}^+ + j\mathcal{K}^- \right) \\ \mathcal{Q}_{21} &= -\mathcal{T}_{\text{k}_0}/\eta_0 - \left(\mathcal{T}^+ + j\mathcal{K}^- \right)/\eta. \end{aligned}$$

Here the notation

$$\mathcal{K}^\pm = \frac{1}{2} \left(\mathcal{K}_{\gamma_-} \pm \mathcal{K}_{\gamma_+} \right), \qquad \mathcal{T}^\pm = \frac{1}{2} \left(\mathcal{T}_{\gamma_-} \pm \mathcal{T}_{\gamma_+} \right)$$

was used.

The chiral PMCHWT equation is obtained by performing the following substitution in the nonchiral PMCHWT equation:

$$\mathcal{K}_k \to \mathcal{K}^+ - j\mathcal{T}^-, \qquad \mathcal{T}_k \to \mathcal{T}^+ + j\mathcal{K}^-.$$

Note that the compact contributions $\mathcal{K}_k$ from the nonchiral PMCHWT equation are perturbed by discontinuous contributions $j\mathcal{T}^-$. This implies that no matter how small the chirality parameter κ, there always is a mesh parameter h_0 such that when the actual mesh parameter h is smaller than h_0, the spectra of the matrices resulting upon discretization of the nonchiral and chiral PMCHWT equation will differ qualitatively. This is symptomatic to the introduction of "new physics" in the system.

The chiral PMCHWT equation (7.24) is equivalent to that presented in [11], and is a special case of the integral equations constructed for inhomogeneous chiral structures in [12]. A similar boundary integral equation has been derived for scattering by chiral objects above a lossy half space [13], [14]. The chiral PMCHWT equation can also be applied to chiral scatterers in chiral background media [15].

7.3.3 Numerical Solution of the Chiral PMCHWT equation

To solve (7.24) via the boundary element method, the unknown quantities $-\hat{\boldsymbol{n}} \times \boldsymbol{E}$ and $\hat{\boldsymbol{n}} \times \boldsymbol{H}$ are expanded in a set of N_S basis functions $\boldsymbol{f}_i$:

$$-\hat{\boldsymbol{n}} \times \boldsymbol{E} = \sum_{i=1}^{N_S} \mathsf{c}_i \boldsymbol{f}_i \quad , \quad \hat{\boldsymbol{n}} \times \boldsymbol{H} = \sum_{i=1}^{N_S} \mathsf{d}_i \boldsymbol{f}_i. \tag{7.27}$$

These expansions are inserted into (7.24), and the resulting equations are tested with a set of N_S testing functions $\tilde{\boldsymbol{f}}_i$ (i.e., multiplied by $\tilde{\boldsymbol{f}}_i$ and integrated over Γ). This results in the following set of linear equations (in matrix form):

$$\begin{pmatrix} \mathbf{Q}_{11} & \mathbf{Q}_{12} \\ \mathbf{Q}_{21} & \mathbf{Q}_{22} \end{pmatrix} \begin{pmatrix} \mathsf{c} \\ \mathsf{d} \end{pmatrix} = \begin{pmatrix} \mathsf{e}^i \\ -\mathsf{h}^i \end{pmatrix} \tag{7.28}$$

with

$$\begin{aligned} \left(\mathbf{Q}_{ij}\right)_{mn} &= \left(\tilde{\boldsymbol{f}}_m, \mathcal{Q}_{ij} \boldsymbol{f}_n\right) \\ \mathsf{e}^i_m &= \left(\tilde{\boldsymbol{f}}_m, \hat{\boldsymbol{n}} \times \boldsymbol{E}^i\right) \\ \mathsf{h}^i_m &= \left(\tilde{\boldsymbol{f}}_m, \hat{\boldsymbol{n}} \times \boldsymbol{H}^i\right) \\ (\boldsymbol{x}, \boldsymbol{y}) &= \int_\Gamma \boldsymbol{x}(\boldsymbol{r}) \cdot \boldsymbol{y}(\boldsymbol{r}) ds. \end{aligned}$$

This set of $2N_S$ linear equations can be solved using a Krylov iterative solver.

The accuracy of the solution obtained by the boundary element method depends upon the spectral properties of the PMCHWT operator, as well as the choice of expansion and testing functions [16]. In our implementation, following standard practice [4], [5], the surface Γ is approximated by a triangle mesh. The expansion functions $\boldsymbol{f}_i$ are chosen to be divergence-conforming RWG functions [17], while the testing functions $\tilde{\boldsymbol{f}}_i$ are chosen to be curl-conforming rotated RWG functions

$\hat{\boldsymbol{n}} \times \boldsymbol{f}_i$. The accuracy of the solution (7.27) then depends upon the density of the triangle mesh, which is measured by the mesh parameter (i.e. the minimum edge length).

7.4 The Calderón Multiplicative Preconditioner

7.4.1 Dense Discretization Breakdown

The numerical solution of the EFIE suffers from dense discretization breakdown: when the mesh is made denser, the condition number of the system matrix grows quadratically as a function of the inverse of the mesh parameter. This renders the iterative solution of the discretized EFIE increasingly hard and time-consuming.

As discussed in section 2.2.5, the cause of this phenomenon is rooted in the mathematical properties of the EFIE operator. Its spectrum comprises two branches: one accumulating at zero, the other at infinity. As the discretization is made denser, eigenfunctions corresponding to eigenvalues accumulating at zero and infinity both can be resolved. This renders the system matrix ill-conditioned, and the iterative solution inefficient.

As the nonchiral PMCHWT operator (7.20) contains the EFIE operator as one of its constituents, it is not surprising that it too is susceptible to dense discretization breakdown [5].

Equation (7.25) indicates that the chiral PMCHWT operator is intimately connected with the nonchiral PMCHWT operator. Its spectrum can therefore also be expected to be unbounded, resulting in dense discretization breakdown.

To mitigate this problem, the EFIE and the PMCHWT equation have been regularized by Calderón multiplicative preconditioners (CMPs) [5], [6], [18]. In the next sections, this regularization procedure is elucidated and extended to the chiral PMCHWT equation.

7.4.2 Regularizing the EFIE

Dense discretization breakdown of the EFIE is caused by the unbounded spectrum of the EFIE operator $\mathcal{T}_k$. However, it is known that for smooth surfaces Γ, the eigenvalues of the MFIE operator $\mathcal{K}_k$ accumulate at zero (i.e. the operator is compact) [19]. The Calderón identities

$$\mathcal{K}_{\mathrm{k}}^2 - \mathcal{T}_{\mathrm{k}}^2 = \frac{1}{4} \tag{7.29}$$

$$\mathcal{T}_{\mathrm{k}}\mathcal{K}_{\mathrm{k}} + \mathcal{K}_{\mathrm{k}}\mathcal{T}_{\mathrm{k}} = 0 \tag{7.30}$$

imply that the EFIE operator is self-regularizing: the eigenvalues of its square accumulate at $-\frac{1}{4}$, and its spectrum therefore is bounded. Moreover, if the

scatterer does not support an internal resonance at the wave number k, the spectrum is bounded away from zero. Upon discretization, such an operator results in a well-conditioned set of equations, even when the discretization is made denser. This fact inspired the introduction of the CMP EFIE in [18]:

$$\eta \mathcal{T}_k^2 (\boldsymbol{J}) = -\mathcal{T}_k \left(\hat{\boldsymbol{n}} \times \boldsymbol{E}^i \right). \tag{7.31}$$

In [4], it has been shown that this equation, which involves a product of two operators, can be discretized in a conforming and stable manner by leveraging both RWG and BC functions and the introduction of the corresponding inverse Gram matrix.

7.4.3 Regularizing the Nonchiral PMCHWT Equation

In [5], it has been shown that the PMCHWT equation's operator too exhibits a self-regularizing property. In particular, it has been show that the CMP PMCHWT equation

$$\mathcal{Q}(\eta_0, k_0; \eta, k)^2 \begin{pmatrix} -\hat{\boldsymbol{n}} \times \boldsymbol{E} \\ \hat{\boldsymbol{n}} \times \boldsymbol{H} \end{pmatrix} = \mathcal{Q}(\eta_0, k_0; \eta, k) \begin{pmatrix} -\hat{\boldsymbol{n}} \times \boldsymbol{E}^i \\ \hat{\boldsymbol{n}} \times \boldsymbol{H}^i \end{pmatrix} \tag{7.32}$$

involves an operator whose spectrum accumulates at finite non-zero values. In addition to the Calderón identities, the proof requires the determination of the accumulation points of the spectra of the following two-wavenumber operators:

$$\begin{aligned} \mathcal{T}_{k_1} \mathcal{T}_{k_2} &\rightarrow -\frac{k_1}{4k_2} \text{ and } -\frac{k_2}{4k_1} \\ \mathcal{T}_{k_2} \mathcal{K}_{k_1} + \mathcal{K}_{k_1} \mathcal{T}_{k_2} &\rightarrow 0. \end{aligned}$$

For $k_1 = k_2$, this simply follows from the Calderón identities (7.29), (7.30). Ignoring all compact operators, it is then found that

$$\mathcal{Q}(\eta_0, k_0; \eta, k)^2 \rightarrow \left(\frac{1}{2} - \frac{\eta}{\eta_0} \mathcal{T}_{k_0} \mathcal{T}_k - \frac{\eta_0}{\eta} \mathcal{T}_k \mathcal{T}_{k_0} \right) \begin{pmatrix} 1 & 0 \\ 0 & 1 \end{pmatrix} \tag{7.33}$$

where the arrow "$\rightarrow$" must be understood as an equality modulo compact contribution. This shows that the eigenvalues of the squared nonchiral PMCHWT operator will accumulate at finite nonzero values. Thus, upon discretization, the system matrix will be well-conditioned, uniformly with regard to the mesh parameter.

7.4.4 Regularizing the Chiral PMCHWT Equation

The results in [4], [5] suggest the introduction of the following CMP for the chiral PMCHWT equation (7.24):

$$\begin{aligned} &\mathcal{Q}_c(\eta_0, k_0; \eta, \gamma_-, \gamma_+)^2 \begin{pmatrix} -\hat{\boldsymbol{n}} \times \boldsymbol{E} \\ \hat{\boldsymbol{n}} \times \boldsymbol{H} \end{pmatrix} \\ &= \mathcal{Q}_c(\eta_0, k_0; \eta, \gamma_-, \gamma_+) \begin{pmatrix} -\hat{\boldsymbol{n}} \times \boldsymbol{E}^i \\ \hat{\boldsymbol{n}} \times \boldsymbol{H}^i \end{pmatrix}. \end{aligned} \tag{7.34}$$

The occurrence of a nonzero chirality parameter however complicates the spectral analysis. Two difficulties arise:

- Explicit computation of the operators in the operator block matrix $\mathcal{Q}_c^2$ reveals the presence of a new type of operator: the three-wavenumber operator $\mathcal{T}_{k_0}\mathcal{K}^- - \mathcal{K}^-\mathcal{T}_{k_0}$. To characterize the spectrum of $\mathcal{Q}_c^2$, the spectrum of this three-wavenumber operator needs to be understood. In section 7.4.4, it will be shown that the three-wavenumber operator is compact. This operator therefore does not qualitatively affect the spectrum of $\mathcal{Q}_c^2$.
- The explicit expression of $\mathcal{Q}_c^2$ contains noncompact contributions in both the on- and off-diagonal blocks, complicating the study of the spectrum of the operator as a whole. To alleviate this difficulty, a suitable diagonalizing transformation (up to compact contributions) will be introduced in section 7.4.4.

Spectrum of the three-wavenumber operator

Compactness of the three-wavenumber operator $\mathcal{T}_{k_0}\mathcal{K}^- - \mathcal{K}^-\mathcal{T}_{k_0}$ can be demonstrated for spherical scatterers of unit radius. It is known that the operators $\mathcal{T}_k$ and $\mathcal{K}_k$ are (skew-)diagonal in the basis of vector spherical harmonics $\boldsymbol{X}_{lm} = \mathrm{curl}_S Y_{lm}$ and $\boldsymbol{Y}_{lm} = \mathrm{grad}_S Y_{lm}$, with curl_S and grad_S the surface curl and surface gradient, respectively, and Y_{lm} the spherical harmonics [18]:

$$\begin{aligned}
\mathcal{T}_k \boldsymbol{X}_{lm} &= -\mathbb{J}_l(k)\mathbb{H}_l(k)\boldsymbol{Y}_{lm} && (7.35a)\\
\mathcal{T}_k \boldsymbol{Y}_{lm} &= \mathbb{J}_l'(k)\mathbb{H}_l'(k)\boldsymbol{X}_{lm} && (7.35b)\\
\mathcal{K}_k \boldsymbol{X}_{lm} &= \left(\frac{1}{2} - j\mathbb{J}_l'(k)\mathbb{H}_l(k)\right)\boldsymbol{X}_{lm} && (7.35c)\\
\mathcal{K}_k \boldsymbol{Y}_{lm} &= \left(\frac{1}{2} + j\mathbb{J}_l(k)\mathbb{H}_l'(k)\right)\boldsymbol{Y}_{lm} && (7.35d)
\end{aligned}$$

where $\mathbb{J}_l(k)$ and $\mathbb{H}_l(k)$ are the Riccati Bessel and Hankel functions, respectively. They are related to the spherical Bessel function $j_l(k)$ and the spherical Hankel function of the first kind $h_l^{(1)}(k)$ as

$$\begin{aligned}
\mathbb{J}_l(k) &= k j_l(k)\\
\mathbb{H}_l(k) &= k h_l^{(1)}(k).
\end{aligned}$$

Using (7.35), it is found that

$$\left(\mathcal{T}_{k_0}\mathcal{K}^- - \mathcal{K}^-\mathcal{T}_{k_0}\right)\begin{pmatrix}\boldsymbol{X}_{lm}\\ \boldsymbol{Y}_{lm}\end{pmatrix} = \begin{pmatrix}0 & a_{lm}\\ b_{lm} & 0\end{pmatrix}\begin{pmatrix}\boldsymbol{X}_{lm}\\ \boldsymbol{Y}_{lm}\end{pmatrix} \tag{7.36}$$

with

$$\begin{pmatrix}a_{lm}\\ b_{lm}\end{pmatrix} = \frac{j}{2}\left(\mathbb{J}_l(\gamma_1)\mathbb{H}_l(\gamma_1) - \mathbb{J}_l(\gamma_2)\mathbb{H}_l(\gamma_2)\right)'\begin{pmatrix}\mathbb{J}_l(k_0)\mathbb{H}_l(k_0)\\ \mathbb{J}_l'(k_0)\mathbb{H}_l'(k_0)\end{pmatrix}.$$

From (7.36), it follows that the eigenvalues of $\mathcal{T}_{k_0}\mathcal{K}^- - \mathcal{K}^-\mathcal{T}_{k_0}$ are $\pm\sqrt{a_{lm}b_{lm}}$. For large l, these eigenvalues tend to [20]

$$\pm\sqrt{a_{lm}b_{lm}} \to \pm\frac{k^2\kappa}{4l^3} + \mathcal{O}(l^{-4}) \tag{7.37}$$

and hence accumulate at zero. The operator $\mathcal{T}_{k_0}\mathcal{K}^- - \mathcal{K}^-\mathcal{T}_{k_0}$ therefore is compact. This conclusion is not limited to spherical objects: the numerical examples at the end of this chapter will show that it also holds for non-spherical ones.

Diagonalization of the squared PMCHWT operator

Non-compact operators appear in the off-diagonal elements of $\mathcal{Q}_c(\eta_0, k_0; \eta, \gamma_-, \gamma_+)^2$, which makes it difficult to make conclusive statements regarding the behavior of its spectrum. This complication can be resolved by expressing the chiral CMP PMCHWT equation (7.34) in terms of the circularly polarized components of the electromagnetic fields outside the scatterer, $\boldsymbol{E}_1$ and $\boldsymbol{E}_2$, as

$$\begin{pmatrix}\boldsymbol{E}\\ \boldsymbol{H}\end{pmatrix} = \begin{pmatrix}1 & 1\\ -\frac{\jmath}{\eta_0} & \frac{\jmath}{\eta_0}\end{pmatrix}\begin{pmatrix}\boldsymbol{E}_1\\ \boldsymbol{E}_2\end{pmatrix}. \tag{7.38}$$

(Note the difference between (7.38) and the Bohren transform (7.4): in (7.38) the vacuum impedance η_0 is used instead of the impedance of the chiral medium η.) Transformation (7.38) on the fields induces the following transformation on the traces:

$$\begin{pmatrix}-\hat{\boldsymbol{n}}\times\boldsymbol{E}\\ \hat{\boldsymbol{n}}\times\boldsymbol{H}\end{pmatrix} = -\begin{pmatrix}1 & 1\\ \frac{\jmath}{\eta_0} & -\frac{\jmath}{\eta_0}\end{pmatrix}\begin{pmatrix}\hat{\boldsymbol{n}}\times\boldsymbol{E}_1\\ \hat{\boldsymbol{n}}\times\boldsymbol{E}_2\end{pmatrix}.$$

The chiral CMP PMCHWT equation (7.34) can therefore be expressed as

$$\begin{aligned}&\begin{pmatrix}1 & 1\\ \frac{\jmath}{\eta_0} & -\frac{\jmath}{\eta_0}\end{pmatrix}^{-1}\mathcal{Q}_c^2\begin{pmatrix}1 & 1\\ \frac{\jmath}{\eta_0} & -\frac{\jmath}{\eta_0}\end{pmatrix}\begin{pmatrix}\hat{\boldsymbol{n}}\times\boldsymbol{E}_1\\ \hat{\boldsymbol{n}}\times\boldsymbol{E}_2\end{pmatrix}\\ =&\begin{pmatrix}1 & 1\\ \frac{\jmath}{\eta_0} & -\frac{\jmath}{\eta_0}\end{pmatrix}^{-1}\mathcal{Q}_c\begin{pmatrix}1 & 1\\ \frac{\jmath}{\eta_0} & -\frac{\jmath}{\eta_0}\end{pmatrix}\begin{pmatrix}\hat{\boldsymbol{n}}\times\boldsymbol{E}_1^i\\ \hat{\boldsymbol{n}}\times\boldsymbol{E}_2^i\end{pmatrix}\end{aligned}$$

where the dependence of $\mathcal{Q}_c$ on material parameters has been left out to simplify the notation.

From a physical point of view, it is clear that this reformulation cannot change the essential properties of the PMCHWT operator. From an algebraic point of view, the matrix

$$\mathcal{R} = \begin{pmatrix}\mathcal{R}_{11} & \mathcal{R}_{12}\\ \mathcal{R}_{21} & \mathcal{R}_{22}\end{pmatrix} = \begin{pmatrix}1 & 1\\ \frac{\jmath}{\eta_0} & -\frac{\jmath}{\eta_0}\end{pmatrix}^{-1}\mathcal{Q}_c^2\begin{pmatrix}1 & 1\\ \frac{\jmath}{\eta_0} & -\frac{\jmath}{\eta_0}\end{pmatrix}$$

is connected to $\mathcal{Q}_c^2$ by a similarity transformation, and therefore has an identical spectrum. Up to compact contributions (such as the three-wavenumber operator

Table 7.1: Overview of spectral accumulation points

Operator	Spectral accumulation points
$\mathcal{T}_k^2$	$-\frac{1}{4}$
$\mathcal{T}_{k_1}\mathcal{T}_{k_2}$	$-\frac{k_1}{4k_2}, -\frac{k_2}{4k_1}$
$\mathcal{K}_{k_1}\mathcal{K}_{k_2}$	0
$\mathcal{T}_{k_1}\mathcal{K}_{k_2} + \mathcal{K}_{k_2}\mathcal{T}_{k_1}$	0
$\mathcal{T}_{k_0}\mathcal{K}^- - \mathcal{K}^-\mathcal{T}_{k_0}$	0

discussed in the previous subsection), it is found that

$$\begin{aligned}
\mathcal{R}_{11} &\to \frac{1}{2} - \left(\frac{\eta_0}{\eta}\mathcal{T}_{k_0}\mathcal{T}^+ + \frac{\eta}{\eta_0}\mathcal{T}^+\mathcal{T}_{k_0}\right) + \left(\mathcal{T}^-\mathcal{T}_{k_0} + \mathcal{T}_{k_0}\mathcal{T}^-\right) \\
\mathcal{R}_{12} &\to 0 \\
\mathcal{R}_{21} &\to 0 \\
\mathcal{R}_{22} &\to \frac{1}{2} - \left(\frac{\eta_0}{\eta}\mathcal{T}_{k_0}\mathcal{T}^+ + \frac{\eta}{\eta_0}\mathcal{T}^+\mathcal{T}_{k_0}\right) - \left(\mathcal{T}^-\mathcal{T}_{k_0} + \mathcal{T}_{k_0}\mathcal{T}^-\right).
\end{aligned}$$

The eigenvalues of the diagonal elements accumulate at a finite number of finite nonzero values, while the off-diagonal elements are compact (for an overview of the accumulation points, see table 7.1). Therefore, it can be concluded that the spectrum of $\mathcal{R}$, and thus the spectrum of the squared chiral PMCHWT operator, is bounded from above and below and thus allows an unconditionally stable discretization, which will be discussed in the next subsection.

7.4.5 Stable Discretization

The chiral CMP PMCHWT equation is formed by action of the block operator $\mathcal{Q}_c$ on the left and right hand sides of the chiral PMCHWT equation (7.24):

$$\begin{pmatrix} \mathcal{Q}_{11} & \mathcal{Q}_{12} \\ \mathcal{Q}_{21} & \mathcal{Q}_{22} \end{pmatrix}^2 \begin{pmatrix} -\hat{\boldsymbol{n}} \times \boldsymbol{E} \\ \hat{\boldsymbol{n}} \times \boldsymbol{H} \end{pmatrix} = \begin{pmatrix} \mathcal{Q}_{11} & \mathcal{Q}_{12} \\ \mathcal{Q}_{21} & \mathcal{Q}_{22} \end{pmatrix} \begin{pmatrix} -\hat{\boldsymbol{n}} \times \boldsymbol{E}^i \\ \hat{\boldsymbol{n}} \times \boldsymbol{H}^i \end{pmatrix}. \tag{7.39}$$

The squared PMCHWT operator can be discretized elegantly by introducing a second set of expansion functions $\boldsymbol{g}_i$ and testing functions $\tilde{\boldsymbol{g}}_i$. The following system is obtained (in block matrix form):

$$\begin{aligned}
&\begin{pmatrix} \mathbf{Q}'_{11} & \mathbf{Q}'_{12} \\ \mathbf{Q}'_{21} & \mathbf{Q}'_{22} \end{pmatrix} \begin{pmatrix} \mathbf{G}^{-1} & 0 \\ 0 & \mathbf{G}^{-1} \end{pmatrix} \begin{pmatrix} \mathbf{Q}_{11} & \mathbf{Q}_{12} \\ \mathbf{Q}_{21} & \mathbf{Q}_{22} \end{pmatrix} \begin{pmatrix} \mathsf{c} \\ \mathsf{d} \end{pmatrix} \\
= &\begin{pmatrix} \mathbf{Q}'_{11} & \mathbf{Q}'_{12} \\ \mathbf{Q}'_{21} & \mathbf{Q}'_{22} \end{pmatrix} \begin{pmatrix} \mathbf{G}^{-1} & 0 \\ 0 & \mathbf{G}^{-1} \end{pmatrix} \begin{pmatrix} -\mathsf{e}^i \\ \mathsf{h}^i \end{pmatrix}
\end{aligned} \tag{7.40}$$

with

$$\begin{aligned}(\mathbf{Q}_{ij})_{mn} &= (\tilde{\boldsymbol{f}}_m, \mathcal{Q}_{ij}\boldsymbol{f}_n)\\ (\mathbf{Q'}_{ij})_{mn} &= (\tilde{\boldsymbol{g}}_m, \mathcal{Q}_{ij}\boldsymbol{g}_n)\\ \mathbf{G}_{mn} &= (\tilde{\boldsymbol{f}}_m, \boldsymbol{g}_n)\,.\end{aligned}$$

The matrix $\mathbf{Q}_{ij}$ results from discretizing the operator with the first set of basis and testing functions, and $\mathbf{Q'}_{ij}$ is obtained using the second set. The Gram matrix $\mathbf{G}$ relates the first set of testing functions to the second set of expansion functions. The matrix $\mathbf{Q'G}^{-1}$ acts as a multiplicative preconditioner.

In order to obtain accurate results, both sets of expansion functions must be div-conforming, and both sets of testing functions must be curl-conforming. Secondly, the Gram matrix $\mathbf{G}$ must be well-conditioned. Finally, the operators $\mathcal{Q}_{ij}$ must be well-tested in $\mathbf{Q}_{ij}$ as well as $\mathbf{Q}'_{ij}$.

For a triangular mesh, a suitable choice was presented in [4] and [5]. There, $\mathbf{Q}$ is computed using divergence-conforming RWG functions $\boldsymbol{f}_i$ and curl-conforming rotated RWG functions $\hat{\boldsymbol{n}} \times \boldsymbol{f}_i$ [17]. $\mathbf{Q'}$ is computed using div-conforming Buffa-Christiansen (BC) functions $\boldsymbol{g}_i$ and curl-conforming rotated BC functions $\hat{\boldsymbol{n}} \times \boldsymbol{g}_i$ [21]. This discretization scheme will also be used in the numerical examples in the following section.

This discretization scheme can be extended to curvilinear [22] as well as higher-order triangular elements [23]. A general procedure not restricted to triangular meshes is described in [24].

In the next section, the beneficial properties of the CMP will be corroborated by numerical examples.

7.5 Numerical Examples

7.5.1 Scattering by a Chiral Sphere

As presented in [7], the accuracy of the chiral CMP PMCHWT equation and the proposed discretization scheme can be tested by comparing numerical results to analytical solutions for scattering by a chiral sphere [25]. For example, consider a sphere with radius 1 meter and material parameters $\epsilon = 2\epsilon_0$, $\mu = \mu_0$, and $\kappa = 0.5$. It is embedded in vacuum, and illuminated by a circularly polarized plane wave propagating along the z axis with frequency 90 MHz:

$$\begin{aligned}\boldsymbol{E}^{\pm}(x,y,z) &= \boldsymbol{P}\exp\left(-jk_0 z\right)\\ \boldsymbol{H}^{\pm}(x,y,z) &= \pm\frac{j}{\eta_0}\boldsymbol{E}^{\pm}(x,y,z)\\ \boldsymbol{p} &= \hat{\mathbf{1}}_x \mp j\hat{\mathbf{1}}_y.\end{aligned}$$

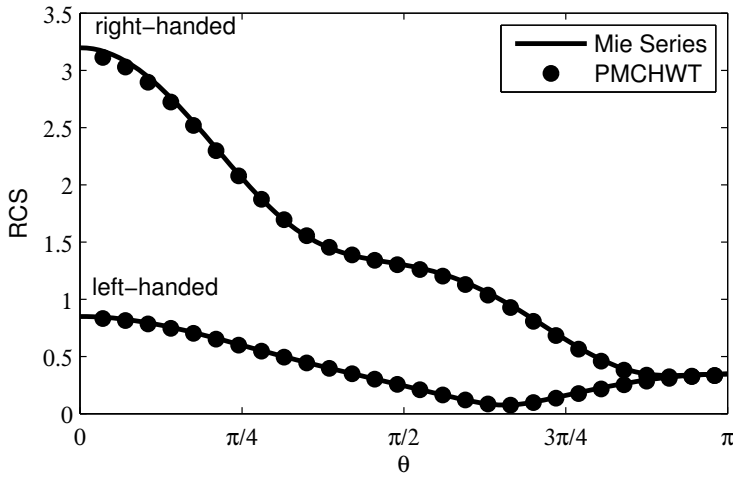

Figure 7.1: Comparison of the chiral CMP PMCHWT method to the Mie series: the Radar Cross Section (RCS) in the xz plane, with θ being the angle between the observed direction and the z axis.

$(\boldsymbol{E}^+, \boldsymbol{H}^+)$ corresponds to a right-hand circularly polarized wave, while $(\boldsymbol{E}^-, \boldsymbol{H}^-)$ corresponds to a left-hand circularly polarized wave. The radar cross section (RCS) obtained using the chiral CMP PMCHWT method (with $N = 1398$ RWG expansion functions) is compared to the results from the Mie series in figure 7.1, and seen to be in excellent agreement.

While the sphere is geometrically fully symmetrical, left-right symmetry in the scattered field is broken by the microscopic chiral structure of the material. This causes the sphere to react differently upon illumination by left- and right-handed circularly polarized waves. This asymmetry is only exhibited when $\kappa \neq 0$.

When solving the chiral PMCHWT method without the CMP, dense discretization breakdown occurs. To illustrate this, the condition number of the system matrix in (7.28) is plotted in figure 7.2 for increasingly dense discretizations alongside the number of iterations needed to reach convergence (arbitrarily defined as a relative residual smaller than 10^{-6} using the TFQMR method) when the sphere is illuminated by a linearly polarized plane wave.

However, when employing the CMP, the system matrix remains well-conditioned, no matter how small the mesh parameter. The condition number of the system matrix of (7.40) and the number of iterations needed to reach convergence for this scattering problem are shown in figure 7.3. It is clear that dense discretization breakdown is effectively cured by the CMP.

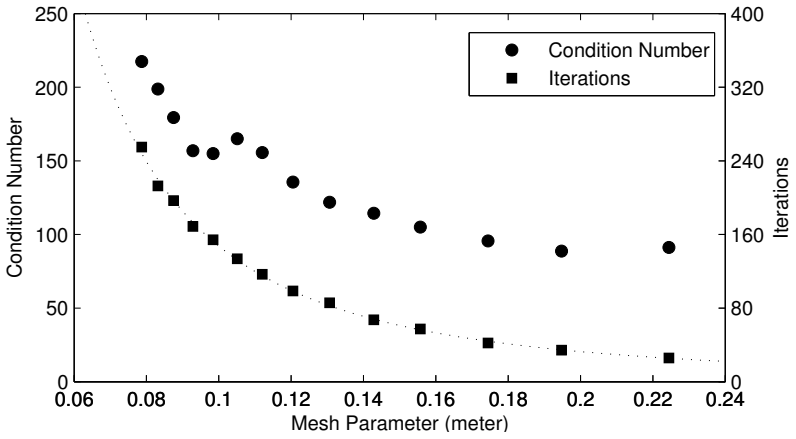

Figure 7.2: The condition number of the system matrix and the number of iterations required to reach convergence without the CMP, as a function of the mesh parameter (in meters).

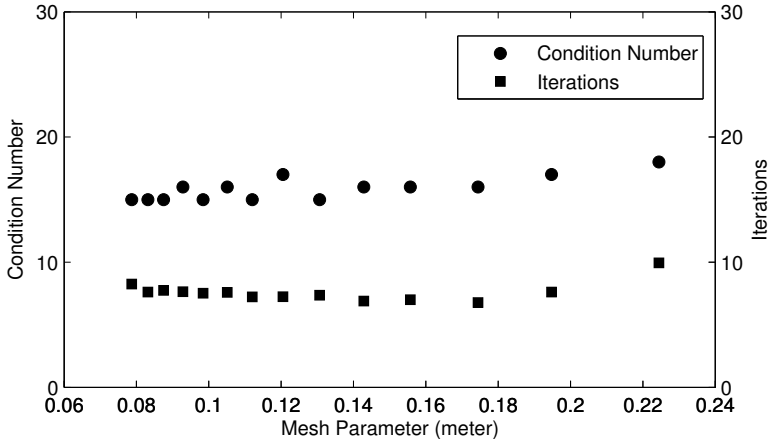

Figure 7.3: The condition number of the system matrix and the number of iterations required to reach convergence with the CMP, as a function of the mesh parameter (in meters).

7.5.2 Compactness of the three-wavenumber operator

In section 7.4.4, we claimed that the three-wavenumber operator $\mathcal{T}_{k_0}\mathcal{K}^- - \mathcal{K}^-\mathcal{T}_{k_0}$ is compact, and proved this assertion for spherical scatterers. Now, the spectrum of this operator applied to a cube will be calculated by solving the eigenvalue equation

$$\left(\mathcal{T}_{k_0}\mathcal{K}^- - \mathcal{K}^-\mathcal{T}_{k_0}\right)\boldsymbol{f}^{(\lambda)} = \lambda \boldsymbol{f}^{(\lambda)}. \tag{7.41}$$

The eigenfunctions $\boldsymbol{f}^{(\lambda)}$ are approximated using RWG expansion functions:

$$\boldsymbol{f}^{(\lambda)} = \sum_{i=1}^{N} \mathsf{a}_i^{(\lambda)} \boldsymbol{f}_i. \tag{7.42}$$

By applying the discretization scheme used for the construction of the CMP, the eigenvalue equation (7.41) becomes

$$\left(\mathbf{T'}_{k_0}\mathbf{G}^{-1}\mathbf{K}^- - \mathbf{K'}^-\mathbf{G}^{-1}\mathbf{T}_{k_0}\right)\mathsf{a}^{(\lambda)} = -\lambda \mathbf{G}^T \mathsf{a}^{(\lambda)} \tag{7.43}$$

with

$$\begin{aligned}
\left(\mathbf{T}_{k_0}\right)_{mn} &= (\hat{\boldsymbol{n}} \times \boldsymbol{f}_m, \mathcal{T}_{k_0}\boldsymbol{f}_n) \\
\left(\mathbf{T'}_{k_0}\right)_{mn} &= (\hat{\boldsymbol{n}} \times \boldsymbol{g}_m, \mathcal{T}_{k_0}\boldsymbol{g}_n) \\
\left(\mathbf{K}^-\right)_{mn} &= \left(\hat{\boldsymbol{n}} \times \boldsymbol{f}_m, \mathcal{K}^-\boldsymbol{f}_n\right) \\
\left(\mathbf{K'}^-\right)_{mn} &= \left(\hat{\boldsymbol{n}} \times \boldsymbol{g}_m, \mathcal{K}^-\boldsymbol{g}_n\right) \\
\mathbf{G}_{mn} &= (\hat{\boldsymbol{n}} \times \boldsymbol{f}_n, \boldsymbol{g}_m)\,.
\end{aligned}$$

Thus, the spectrum of the operator $\mathcal{T}_{k_0}\mathcal{K}^- - \mathcal{K}^-\mathcal{T}_{k_0}$ is approximated by the spectrum of the matrix

$$-\left(\mathbf{G}^T\right)^{-1}\left(\mathbf{T'}_{k_0}\mathbf{G}^{-1}\mathbf{K}^- - \mathbf{K'}^-\mathbf{G}^{-1}\mathbf{T}_{k_0}\right) \tag{7.44}$$

which can easily be calculated numerically.

For example, consider a cube with side 1 meter, $\epsilon = 2\epsilon_0$, $\mu = \mu_0$, and $\kappa = 0.5$. The surface of the cube is discretized using 1800 expansion functions. The matrix (7.44) and its eigenvalues are computed for a frequency of 150 MHz (figure 7.4). The eigenvalues accumulate at zero, thus supporting the assertion that $\mathcal{T}_{k_0}\mathcal{K}^- - \mathcal{K}^-\mathcal{T}_{k_0}$ is compact.

7.5.3 Application of the PMCHWT Equation to a Chiral Meta-material

As a last example, the chiral CMP PMCHWT simulation technique is applied to the chiral metamaterial presented in [26]. Chiral particles (figure 7.5) with diameter 2.202 mm are mixed randomly to create an isotropic chiral metamaterial. The inclusion density is 34.5 cm^{-3}.

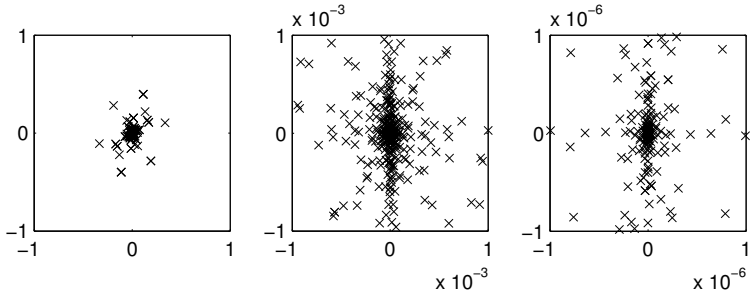

Figure 7.4: Location of the eigenvalues of the three-wavenumber operator $\mathcal{T}_{k_0}\mathcal{K}^- - \mathcal{K}^-\mathcal{T}_{k_0}$ in the complex plane, applied to a cube. The left panel contains all eigenvalues. The middle and right panel are zoomed in around 0, where the eigenvalues are seen to accumulate.

Figure 7.5: A chiral particle [26].

When the T-matrix of a spherical ensemble of chiral particles is known, it is possible to derive a closed form expression of the material parameters of an equivalent homogeneous sphere. Using this technique, the authors found that at a frequency of 5.98 GHz (corresponding to a wavelength $\lambda = 5$ cm), this metamaterial can be described by the following parameters: $\epsilon = 1.6347\epsilon_0$, $\mu = 1.1072\mu_0$, and $\kappa = 0.1511$.

The bistatic radar cross section of a cuboid of this material with dimensions 10 cm $\times$ 10 cm $\times$ 5 cm is computed in the xy-plane (figure 7.7). The incoming electric field is linearly polarized along the z axis and propagates along the directions $\phi^{inc} = 0$ and $\phi^{inc} = \pi/4$. The comparison of the condition number and the required number of iterations (averaged over the dipole and the plane wave excitations) with and without CMP again testifies to the success of the CMP (figure 7.8). Without CMP, dense discretization breakdown occurs for mesh parameters $h \leq \lambda/8$. With CMP, the condition number as well as the

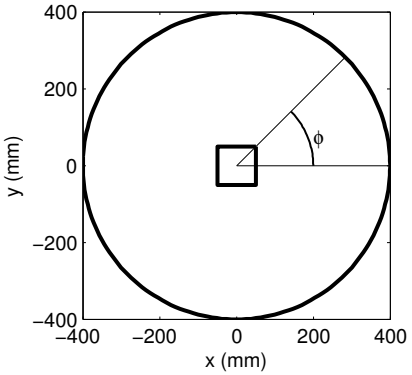

Figure 7.6: Definition of the angle ϕ.

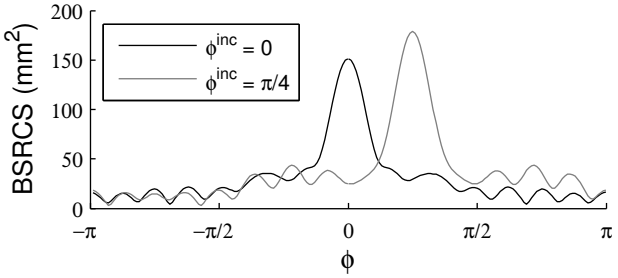

Figure 7.7: Bistatic radar cross section in the xy-plane, computed for incoming plane waves propagating along the directions $\phi^{inc} = 0$ and $\phi^{inc} = \pi/4$. The angle ϕ is defined in figure 7.6.

required number of iterations remain constant.

Next, the cuboid is excited by two different sources: a dipole located in the symmetry plane of the block, and one residing in its top plane (figure 7.9). In [26], the field scattered by this configuration was computed “ab initio", that is by accounting for each and every spiral by using the NSPW-MLFMA T-matrix method. This approach required the solution of a set of linear equations with 347,400 unknowns.

The calculation is now repeated using both the classic chiral PMCHWT and the chiral CMP PMCHWT method by modeling the block as a homogeneous chiral medium, and covering its surface with 2048 expansion functions (the mesh parameter being $\lambda/8$). As is to be expected, the use of the CMP does not alter the results (up to numerical precision). The efficiency of the CMP is once again proven: for the symmetrical excitation, the required number of iterations to reach a relative residual of 10^{-6} is reduced from 247 to 16, and for

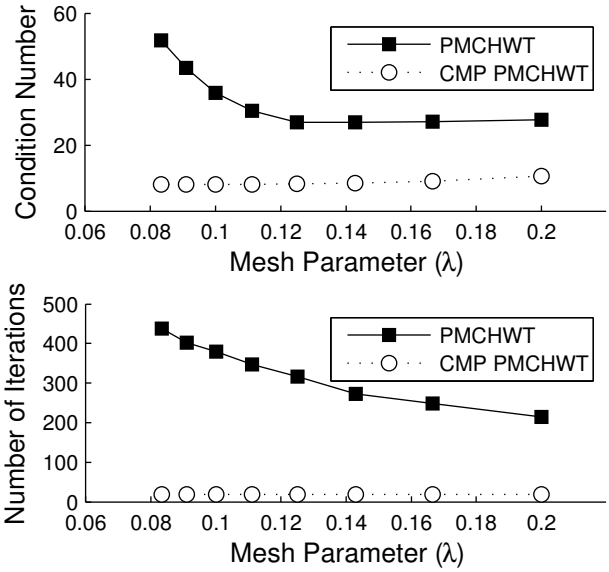

Figure 7.8: Condition number of the system matrix (top) and average number of iterations (bottom) for the cuboid, with and without CMP.

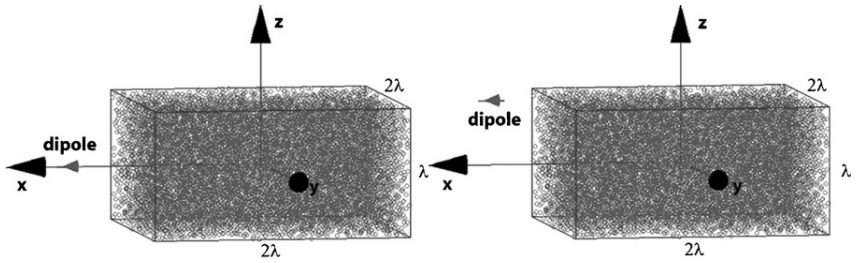

Figure 7.9: Position of the dipole source for symmetric (left) and asymmetric (right) excitation [26].

the asymmetric one from 254 to 17.

In order to compare the results to the ab initio simulation data provided by the authors of [26], the electromagnetic fields are calculated at a distance of 40 cm from the center of the block (figure 7.6). The $\boldsymbol{H}_x$-component is shown in the top and middle panels of figures 7.10 and 7.11 for the symmetric and the asymmetric excitations, respectively.

A remark concerning the approximate agreement between the results of the ab initio simulation and the chiral PMCHWT method is in order. The constitutive equations (7.3) describe a homogeneous, continuous medium. However, in this

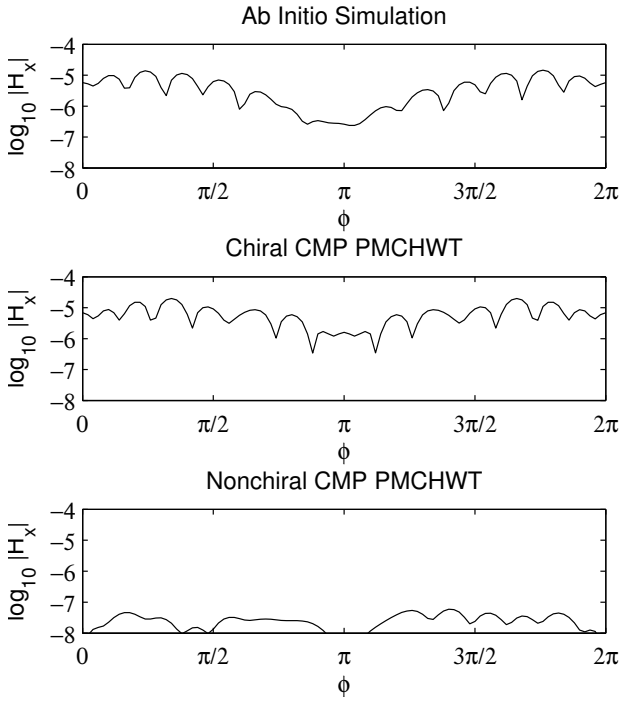

Figure 7.10: The scattered field $\log_{10}(|\boldsymbol{H}_x|)$ due to the symmetric excitation.

particular example, the microscopic building blocks are relatively large (with dimensions of about $\lambda/20$). Therefore, constitutive equations can only provide an approximate model of the medium. When characterization of the chiral medium by a macroscopic parameter κ is warranted, however, the modeling of scattering by such chiral objects obviously can be performed much more efficiently by the chiral CMP PMCHWT than by an ab initio simulation which takes into account the microscopic structure of the material.

The inclusion of a nonzero chirality parameter however does provide a good prediction of the order of magnitude of the different field components. The scattered field computed using the nonchiral PMCHWT method (with the same permittivity and permeability) is shown in the bottom panel of Figs. 7.10 and 7.11. For the symmetric excitation, the $\boldsymbol{H}_x$-component vanishes (up to the iterative solver's tolerance) for all ϕ. For the asymmetric excitation, it vanishes at $\phi = 0$ and $\phi = \pi$. This is due to incorrect assumptions about the symmetry of the medium. This error is corrected by the inclusion of a nonzero chirality parameter.

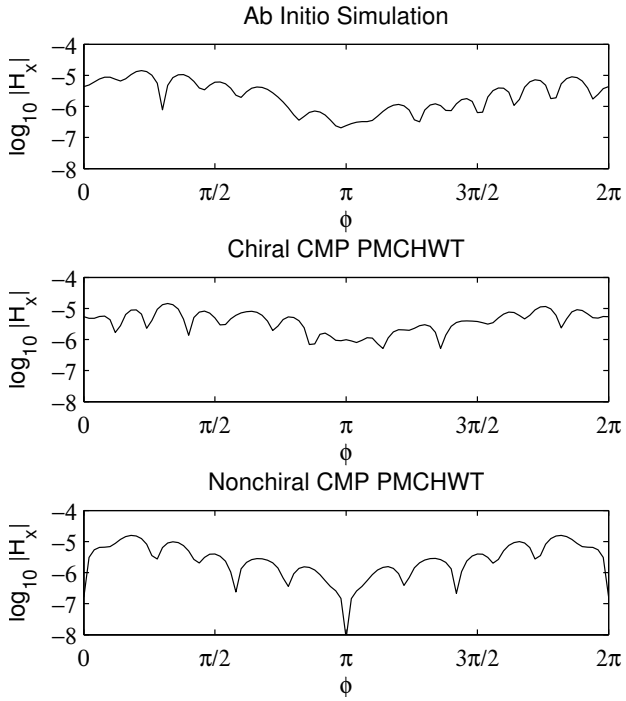

Figure 7.11: The scattered field $\log_{10}(|\boldsymbol{H}_x|)$ due to the asymmetric excitation.

7.6 Conclusions

In this chapter, numerical methods for analyzing scattering of electromagnetic fields by chiral media were studied. The main theoretical tool is the Bohren transform, which allows for a far-reaching analogy between chiral media and nonchiral dielectrics. By exploiting this analogy, boundary integral equations for dielectric structures can be extended to chiral objects. The extension of the PMCHWT equation was revisited in detail.

An accurate numerical solution of the chiral PMCHWT equation can be obtained with straightforward discretization schemes using RWG expansion functions. However, as is the case for the nonchiral PMCHWT equation and the EFIE, the condition number of the resulting set of equations quickly grows as the discretization becomes denser; that is, dense discretization breakdown occurs.

By studying two- and three-wavenumber extensions to the Calderón identities used in the Calderón preconditioning of the EFIE for analyzing PEC scattering, it is shown that the square of the chiral PMCHWT operator possesses a bounded spectrum and is therefore not susceptible to dense discretization breakdown. By applying a stable discretization scheme involving both RWG and BC functions to the squared chiral PMCHWT operator, a Calderón multiplicative preconditioner

for the chiral PMCHWT equation, which effectively resolves the problem of dense discretization breakdown, was constructed.

Finally, three numerical experiments were performed. First, the accuracy of the chiral PMCHWT method and the efficacy of the CMP were corroborated by comparison of the result they yield, to the analytical solution for scattering by a spherical object. Second, the spectrum of the chiral PMCHWT operator was studied for nonsmooth surfaces. Third, the chiral CMP PMCHWT method was applied to the analysis of scattering by a metamaterial. These experiments show that the CMP PMCHWT method is able to efficiently and accurately solve scattering problems involving chiral media, provided that these media can be described using constitutive equations, i.e. if they can be considered as homogeneous and isotropic.

References

[1] Y. Beghein, K. Cools, F. P. Andriulli, D. De Zutter, and E. Michielssen, "A Calderón multiplicative preconditioner for the PMCHWT equation for scattering by chiral objects", *IEEE Transactions on Antennas and Propagation*, vol. 60, no. 9, pp. 4239–4248, Sep. 2012.

[2] A. Poggio and E. Miller, *Computer Techniques for Electromagnetics*. Oxford UK: Pergamon Press, 1973, ch. IV Integral Equation Solutions of Three-dimensional Scattering Problems.

[3] C. Müller, *Foundations of the Mathematical Theory of Electromagnetic Waves*. Springer, 1969.

[4] F. P. Andriulli, K. Cools, H. Bağci, F. Olyslager, A. Buffa, S. Christiansen, and E. Michielssen, "A multiplicative Calderón preconditioner for the electric field integral equation", *IEEE Transactions on Antennas and Propagation*, vol. 56, pp. 2398–1930, Aug. 2008.

[5] K. Cools, F. Andriulli, and E. Michielssen, "A Calderón multiplicative preconditioner for the PMCHWT integral equation", *IEEE Transactions on Antennas and Propagation*, vol. 59, no. 12, pp. 4579–4587, Dec. 2011.

[6] S. Yan, J.-M. Jin, and Z. Nie, "A comparative study of Calderón preconditioners for PMCHWT equations", *IEEE Transactions on Antennas and Propagation*, vol. 58, no. 7, pp. 2375 –2383, Jul. 2010.

[7] Y. Beghein, K. Cools, F. P. Andriulli, D. De Zutter, and E. Michielssen, "Calderon multiplicative preconditioner for the PMCHWT equation applied to chiral media", in *2011 IEEE International Symposium on Antennas and Propagation (APSURSI)*, Jul. 2011, pp. 3203 –3206.

[8] H. Ammari, K. Hamdache, and J.-C. Nédélec, "Chirality in the Maxwell equations by the dipole approximation", *SIAM J. Appl. Math.*, vol. 59, pp. 2045–2059, 6 Aug. 1999.

[9] A. Lakhtakia, V. Varadan, and V. Varadan, *Time-Harmonic Electromagnetic Fields in Chiral Media*. Springer-Verlag, 1989.

[10] D. Colton and R.Kress, *Integral Equation Methods in Scattering Theory*. Wiley, 1983.

[11] D. Worasawate, J. Mautz, and E. Arvas, "Electromagnetic scattering from an arbitrarily shaped three-dimensional homogeneous chiral body", *IEEE Transactions on Antennas and Propagation*, vol. 51, no. 5, pp. 1077 –1084, May 2003.

[12] H. Ammari and J. Nédélec, *Time-harmonic electromagnetic fields in chiral media*, http://citeseerx.ist.psu.edu/viewdoc/summary?doi=10.1.1.38.3073, 1996.

[13] X. Wang, D. Werner, L.-W. Li, and Y.-B. Gan, "Interaction of electromagnetic waves with 3-D arbitrarily shaped homogeneous chiral targets in the presence of a lossy half space", *IEEE Transactions on Antennas and Propagation*, vol. 55, no. 12, pp. 3647 –3655, Dec. 2007.

[14] R. S. Chen, Y. Q. Hu, Z. H. Fan, D. Z. Ding, D. X. Wang, and E. Yung, "An efficient surface integral equation solution to EM scattering by chiral objects above a lossy half space", *IEEE Transactions on Antennas and Propagation*, vol. 57, no. 11, pp. 3586 –3593, Nov. 2009.

[15] C Athanasiadis, G Costakis, and I. Stratis, "Electromagnetic scattering by a homogeneous chiral obstacle in a chiral environment", *IMA Journal of Applied Mathematics*, vol. 64, no. 3, pp. 245–258, 2000. [Online]. Available: `http://imamat.oxfordjournals.org/content/64/3/245.abstract`.

[16] S. Sauter and C. Schwab, *Boundary Element Methods*. Springer, 2010, isbn: 3540680926.

[17] S. Rao, D. Wilton, and A. Glisson, "Electromagnetic scattering by surfaces of arbitrary shape", *IEEE Transactions on Antennas and Propagation*, vol. 30, no. 3, pp. 409 –418, May 1982.

[18] H. Contopanagos, B. Dembart, M. Epton, J. Ottusch, V. Rokhlin, J. Visher, and S. Wandzura, "Well-conditioned boundary integral equations for three-dimensional electromagnetic scattering", *IEEE Transactions on Antennas and Propagation*, vol. 50, pp. 1824–1930, Dec. 2002.

[19] G. Hanson and A. Yakolev, *Operator Theory for Electromagnetics*. Springer, 2001.

[20] M. Abramowitz and I. Stegun, *Handbook of Mathematical Functions with Formulas, Graphs, and Mathematical Tables*, ninth Dover printing, tenth GPO printing. New York: Dover, 1964.

[21] A. Buffa and S. H. Christiansen, "A dual finite element complex on the barycentric refinement", *Comptes Rendus Mathematique*, vol. 340, no. 6, pp. 461 –464, 2005.

[22] S. Yan, J.-M. Jin, and Z. Nie, "Implementation of the Calderón multiplicative preconditioner for the efie solution with curvilinear triangular patches", in *Antennas and Propagation Society International Symposium, 2009. APSURSI '09. IEEE*, Jun. 2009, pp. 1 –4.

[23] F. Valdes, F. P. Andriulli, K. Cools, and E. Michielssen, "High-order div- and quasi curl-conforming basis functions for Calderón multiplicative preconditioning of the EFIE", *IEEE Transactions on Antennas and Propagation*, vol. 59, no. 4, pp. 1321 –1337, Apr. 2011.

[24] F. P. Andriulli, F. Valdés, K. Cools, and E. Michielssen, "A generalized Calderón preconditioner for the electric field integral equation", in *Antennas and Propagation Society International Symposium (APSURSI), 2010 IEEE*, Jul. 2010, pp. 1 –4.

[25] C. F. Bohren, "Light scattering by an optically active sphere", *Chemical Physics Letters*, vol. 29, no. 3, pp. 458 –462, 1974.

[26] I. Bogaert, J. Peeters, and F. Olyslager, "Homogenization of metamaterials using full-wave simulations", *Metamaterials*, vol. 2, no. 2-3, pp. 101–112, Sep. 2008.

8 Conclusions and Future Work

8.1 Conclusions

In this PhD thesis, significant advancements have been presented concerning the accuracy, the stability and the applicability of both time domain and frequency domain electromagnetic boundary integral equation methods.

Most of the research presented in this work has focused on time domain boundary integral equations, which are solved numerically using the marching-on-in-time method. The primary concern of these methods is their stability, which depends on two factors: the choice of the temporal discretization method, and the accurate computation of the interaction matrix elements.

A lot of research has been performed on the topic of temporal discretization methods, resulting in a wide variety of schemes. In section 2.3.3, a set of related temporal discretization methods was discussed. Many examples in this work as well as in other independent research papers indicate that these methods yield stable MOT schemes when applied to the TD-EFIE, the TD-MFIE or the TD-CFIE, if the interaction matrix elements can be computed with sufficient accuracy.

These stable MOT schemes form the basis of the research presented in part I. In chapter 3, a set of higher-order temporal basis functions was constructed. These functions lead to a more accurate representation of the temporal variation of the electromagnetic fields, without damaging the stability of the MOT scheme. Related schemes have been presented in [1] and [2].

Although the fields and currents can accurately be represented using the aforementioned basis functions, the TD-EFIE and the TD-MFIE still suffer from a fundamental issue: they support static (constant-in-time or, depending on the exact formulation, linear-in-time) regime solutions which inevitably show

up in the MOT method, even though they are physically not allowed. This phenomenon is termed DC instability. In chapter 4, these spurious modes are eliminated by judiciously integrating or differentiating the quasi-Helmholtz components of the TD-EFIE with respect to time. Applying standard temporal discretization techniques to this equation leads to unstable MOT schemes. In chapter 4, a mixed temporal Galerkin method was proposed that does lead to a stable MOT scheme. The resulting equation, termed the qHP-TDEFIE, is immune to DC instability on both simply and multiply connected geometries.

The performance of the MOT algorithm hinges on the condition number of the MOT system matrix. If this matrix is ill-conditioned, the equation cannot be solved efficiently. Unfortunately, the TD-EFIE and the TD-CFIE suffer from low frequency breakdown as well as dense discretization breakdown: the MOT system matrix becomes ill-conditioned for large time step sizes and for dense spatial meshes, respectively. The qHP-TDEFIE is immune to low frequency breakdown, as shown in chapter 4, but not to dense discretization breakdown. In chapter 5, this problem was solved by constructing an appropriate Calderón preconditioner.

The techniques developed in part I improve the accuracy and the efficiency of MOT simulations involving only perfect conductors. In part II, the focus is shifted to penetrable media.

Transient scattering by homogeneous penetrable objects is modeled by the TD-PMCHWT equation. However, it is notoriously harder to obtain a stable MOT scheme from the TD-PMCHWT equation than from the TD-EFIE. In chapter 6, this was traced back to DC instability: although the PMCHWT equation theoretically only allows static regime solutions, these modes become exponentially increasing in the presence of numerical quadrature errors. This problem cannot be solved as in chapter 4, due to the differences between the TD-PMCHWT and the TD-EFIE operators. An alternative stabilization method is developed in chapter 6, leading to the qHP-PMCHWT equation. This equation is immune to DC instability and low frequency breakdown, and can be made immune to dense discretization breakdown by employing a suitable Calderón preconditioner.

In chapter 7, scattering by chiral media is studied. Since phenomena associated with chirality, such as optical activity, are only found in relatively small frequency bands, the discussion is restricted to the frequency domain. Like the standard PMCHWT-equation, the chiral PMCHWT-equation suffers from dense discretization breakdown. In chapter 7, a Calderón preconditioner is constructed for this equation.

Together, these results contribute to a deeper understanding of boundary integral equation methods, and lead to more efficient and more accurate simulations of scattering problems involving piecewise homogeneous media.

8.2 Future Work

The techniques presented in this thesis solve some of the issues that have been holding back the widespread use of TD-BIE methods. However, some questions still need answering before these methods can be labeled as fully mature:

- How can the temporal higher-order methods developed in chapter 3 be applied to the qHP-TDEFIE and the qHP-PMCHWT equation?
- Are the qHP-TDEFIE and the qHP-PMCHWT equation compatible with spatial higher order methods?
- In this thesis, penetrable media were modeled using the PMCHWT equation. Alternatively, the Müller equation can be used. How do these methods compare?
- When applied to closed structures, the TD-EFIE is prone to internal resonances. This problem can be solved by employing the TD-CFIE. Can a similar approach be used for the qHP-TDEFIE, in order to obtain an equation that (i) does not support spurious static or resonant modes; (ii) is low frequency stable; and (iii) can be Calderón preconditioned? In the frequency domain, such a formulation was presented in [3]. It is however not straightforward to adapt it to the time domain.
- The rescaling strategies leading to the qHP-TDEFIE and the qHP-PMCHWT equation are incompatible. How can scattering problems involving both dielectrics and perfect conductors be handled correctly?
- The research presented in this thesis is restricted to perfect conductors and lossless dielectrics. How should media with a finite conductivity be incorporated?
- Furthermore, only interfaces between two homogeneous regions were studied. How can these results be generalized to junctions, i.e. interfaces between three or more homogeneous regions?
- Time domain boundary element methods allow the efficient modeling of piecewise homogeneous media. For inhomogeneous media, other methods such as the finite difference time domain (FDTD) method or the time domain finite element method (TD-FEM) are better suited. In order to treat more intricate scattering problems, hybrid methods must be developed.
- As noted in section 2.3.7, solving large problems requires the use of acceleration methods. Although such techniques exist for time domain BIE methods, they are less mature and widespread than their frequency domain counterparts. More research into these methods, and their parallel implementation, would broaden the applicability of TD-BIE methods.
- The MOT systems studied in this work are derived from temporal Petrov-Galerkin discretization methods. As discussed in section 2.3.9, MOT systems can also be obtained using the convolution quadrature (CQ) method. To what extent can the techniques developed in this work be extended to CQ MOT methods?

Many of these issues are also encountered in FD-BIE methods, and have either already been solved or are receiving attention from the scientific community. Therefore, it is reasonable to believe that, with sufficient research effort, TD-BIE methods can be developed into fully mature simulation techniques that complement or even rival their frequency domain counterparts.

References

[1] A. J. Pray, Y. Beghein, N. V. Nair, K. Cools, H. Bağcı, and B. Shanker, "A higher order space-time Galerkin scheme for time domain integral equations", *IEEE Transactions on Antennas and Propagation*, vol. 62, no. 12, pp. 6183–6191, Dec. 2014.

[2] Y. Beghein, K. Cools, and D. De Zutter, "A temporal Galerkin discretization of the charge-current continuity equation", in *2013 International Conference on Electromagnetics in Advanced Applications (ICEAA)*, Sep. 2013, pp. 628–631.

[3] F. P. Andriulli, I. Bogaert, K. Cools, and E. Michielssen, "A well-conditioned combined field integral equation based on quasi-Helmholtz projectors", in *2013 International Conference on Electromagnetics in Advanced Applications (ICEAA)*, IEEE, 2013, pp. 644–647.